



HAL
open science

Contributions to real-time multi-messenger searches for the origin of high-energy cosmic rays

Fabian Schüssler

► **To cite this version:**

Fabian Schüssler. Contributions to real-time multi-messenger searches for the origin of high-energy cosmic rays. High Energy Astrophysical Phenomena [astro-ph.HE]. Sorbonne Université, 2019. tel-02175309

HAL Id: tel-02175309

<https://theses.hal.science/tel-02175309>

Submitted on 5 Jul 2019

HAL is a multi-disciplinary open access archive for the deposit and dissemination of scientific research documents, whether they are published or not. The documents may come from teaching and research institutions in France or abroad, or from public or private research centers.

L'archive ouverte pluridisciplinaire **HAL**, est destinée au dépôt et à la diffusion de documents scientifiques de niveau recherche, publiés ou non, émanant des établissements d'enseignement et de recherche français ou étrangers, des laboratoires publics ou privés.

Habilitation à Diriger des Recherches

**Contributions to real-time multi-messenger searches for the
origin of high-energy cosmic rays**

Fabian Schüssler
CEA Paris-Saclay

Soutenu le 4 juillet 2019 devant le jury composé de:

- Nicolas Leroy (LAL)
- Kumiko Kotera (IAP)
- Ioana Maris (ULB, Rapportrice)
- Tanguy Pierog (KIT)
- Jerome Rodriguez (DAP/ AIM, Rapporteur)
- Antoino Stamerra (INAF, Rapporteur)

Abstract

Cosmic rays are one of the most mysterious phenomena in the high-energy universe. These fundamental particles arrive at Earth with energies orders of magnitude above those produced in man-made accelerators but their origin remains illusive. The key question to resolve this century old mystery is to locate their astrophysical sources and study the acceleration mechanisms able to produce the fantastic energies observed. Over the last years it has become increasingly obvious that multiple messengers and novel techniques will be needed to achieve this task. Fortunately, several of these new messengers have allowed opening new windows to the high-energy universe recently: high-energy gamma rays, neutrinos and gravitational waves are now providing unprecedented insights into the most violent phenomena ever observed.

Using mainly data from the ANTARES neutrino telescope and the H.E.S.S. gamma-ray observatory combined with observations across all electromagnetic wavelengths ranging from the Parkes radio telescope to gamma rays detected by Fermi-LAT and including gravitational waves detected by Virgo/Ligo, I will discuss various searches exploiting the individual particularities of the used particles (e.g. full sky coverage of neutrino telescopes and gravitational wave interferometers, high sensitivity of gamma-ray observatories, etc.) before presenting first multi-messenger analyses at VHE energies, illustrating the potential of this new domain of astrophysics.

Contents

1	Introduction	3
1.1	The quest for the source of high-energy cosmic rays	3
1.2	Overview of my contributions to multi-messenger astrophysics	4
2	High-energy neutrinos	7
2.1	Introduction	7
2.1.1	Astrophysical neutrinos	7
2.2	The ANTARES neutrino telescope	8
2.2.1	Evolution of the detector sensitivity with time	9
2.2.2	AntDSTs: a high level physics analysis data format	11
2.2.3	Verification of the directional reconstruction accuracy	11
2.3	Estimation of the neutrino energy	13
2.3.1	From dE/dX to energy estimation	14
2.3.2	Data vs. Monte Carlo comparison, performance, and systematic uncertainties .	16
2.3.3	Application of the energy estimator: measurement of the atmospheric neutrino spectrum	17
2.4	Searches for clustering in the neutrino sky	18
2.4.1	An improved 2pt correlation analysis	18
2.4.2	Reference autocorrelation distribution and comparison with data	19
2.4.3	Sensitivity	20
2.4.4	Autocorrelation results and discussion	21
2.5	Multi-messenger links: two-point cross-correlation with external catalogues	22
2.5.1	High-energy gamma rays	22
2.5.2	The local universe	23
2.5.3	Massive black holes	23
2.5.4	Summary and outlook on neutrino 2pt-correlations	24
2.6	TAToO: multi-messenger alerts	24
2.6.1	Searches for fast optical and X-ray transients with TAToO	26
2.6.2	ANT150901A: a X-ray transient detected following a TAToO neutrino alert . .	27
2.7	Future prospects of neutrino astronomy	29
2.7.1	Personal comments on neutrino telescopes and their multi-messenger links . .	30
3	High-energy gamma rays	31
3.1	Introduction	31
3.2	Multi-messenger connections	32
3.2.1	High-energy neutrinos	32
3.2.2	Gravitational waves	34
3.2.3	The H.E.S.S. multi-messenger alert system	38
3.3	Connecting VHE gamma-rays with high-energy neutrinos	39
3.3.1	H.E.S.S. follow-up of an ANTARES neutrino excess	39

3.3.2	IceCube high-energy neutrinos	41
3.3.3	Entering the time domain: H.E.S.S. follow-up of high-energy neutrino alerts	45
3.3.4	IceCube-170922A and TXS 0506+056	49
3.3.5	Further developments of the H.E.S.S. high-energy neutrino program	50
3.4	Fast Radio Bursts	52
3.4.1	FRB150215	53
3.4.2	FRB150418	54
3.5	Gravitational Waves	55
3.5.1	Scheduling follow-up observations of gravitational waves	55
3.5.2	GW170814: the first complete VHE gamma-ray follow-up	58
3.5.3	GW170817: the first binary neutron star merger	59
3.6	The Cherenkov Telescope Array	61
3.6.1	Preparations for the CTA transient program	62
3.7	The High Altitude Water Cherenkov Observatory (HAWC)	64
3.7.1	Coincidences of sub-threshold events of Virgo/Ligo and HAWC	65
3.8	The Southern Gamma-ray Survey Observatory (SGSO)	67
4	Summary, outlook and acknowledgements	71
4.1	Acknowledgements	72
	Appendices	83
	A Curriculum Vitae	84
	B Major publications	90

*Souvenez-vous que dans les champs de l'observation
le hasard ne favorise que les esprits préparés.*

Louis Pasteur
(Université de Lille, 1854)

1

Introduction

1.1 The quest for the source of high-energy cosmic rays

Cosmic rays (CRs), high-energy fundamental particles reaching Earth from space, are known since the pioneering observations of Victor Hess more than hundred years ago. We know today that the CR energy spectrum spans many orders of magnitude from a few MeV to above 10^{20} eV (see Fig. 1.1). Whereas the low energy particles are known to be emitted by the Sun, the sources of the higher energy particles remain, despite tremendous theoretical and experimental efforts over the last hundred years, elusive until today. Many considerations on the potential accelerators have been put forward over the last decades. The most straightforward one is called the Hillas criterion [89]. In order to be able to accelerate charged particles they have to be at least partially confined into some *acceleration region* and the maximum achievable energy E_{\max} is given by $E_{\max} \sim \beta \times Z \times B \times L$, with β being the characteristic velocity of particles or fields driving the acceleration in a shock front, Z being the charge of the accelerated particle and B the magnetic field needed to keep the particles inside the acceleration region of size L . This relation is the basis for the diagram shown in Fig. 1.2. Possible UHECR accelerators have to lie above the diagonal line and therefore only a few astrophysical objects like cores of active galactic nuclei (AGN), large lobes in radio galaxies, gamma ray bursts (GRBs) or pulsars remain as viable candidates. Most of these remaining source candidates show strong time dependent emission and transient behavior. Even in this simplified picture it becomes clear that transient phenomena play a crucial role in the high-energy universe and especially as potential CR accelerators. This important point already hints to the importance of the time domain, which is at the core of the MultiTimeTeV project. This is further underlined by a puzzling coincidence: the energy production rate density of CRs across an enormous energy range spanning 10 orders of magnitude is surprisingly similar (about $10^{44-45} \text{ erg Mpc}^{-3} \text{ yr}^{-1}$ [96]) and consistent with a universal E^{-2} spectrum. This fact can be interpreted as signature of a universal source population across the full energy range. Various features of the CR energy spectrum like the flux suppression above the knee (cf. Fig. 1.1) can in this scenario be readily explained by the transient nature of the sources.

In addition to their possible transient nature, various effects hamper the search for the sources of high-energy CRs. Their flux is rapidly decreasing with increasing energy (see Fig. 1.1) and direct detection is possible only below around a TeV, the maximum energy reached with the currently largest CR detector, AMS-II on the International Space Station. At higher energies one has to rely on the observations of extensive air showers induced in the Earth's atmosphere. Consequently the

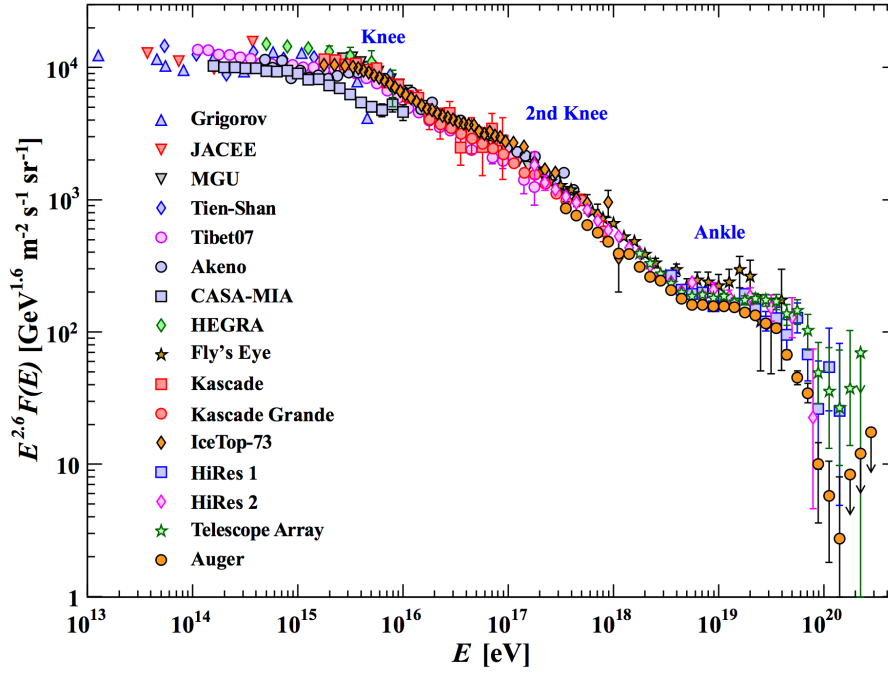


Figure 1.1: The energy spectrum of high-energy cosmic rays is spanning many orders of magnitude in energy and flux and reaches to extreme energies above 10^{20} eV. From [126].

obtained angular resolutions are limited. Even more important is the influence of astrophysical magnetic fields. Although being ultra-relativistic, CRs are being deflected by magnetic fields present throughout the universe. The distribution and strength of these fields remains largely unknown, but most available models predict deflections that remain at the level of several degrees for extragalactic sources emitting UHECRs ($E > 10^{18}$ eV). Obviously lower energy particles are even stronger deflected. The net result of magnetic deflections is two-fold:

- Charged CRs arriving at Earth do not clearly point back to their source.
- The time structure of the underlying acceleration mechanism (e.g. bursts, flares, etc.) is completely washed out after the propagation.

These fundamental problems have hindered the identification of the sources of high-energy cosmic rays so far. I therefore believe that new methods and new messengers are necessary to attack this century old problem. This approach will be discussed in the following sections.

1.2 Overview of my contributions to multi-messenger astrophysics

Astroparticle physics joins the two extremes in fundamental physics: the very large scales of astrophysics and the very small scales of particle physics. By exploiting the fundamental particle interactions that provide unique links between various high-energy particles we hope to obtain the missing pieces of information about the violent phenomena potentially at the origin of high-energy cosmic rays.

The links between the various particles (or messengers) that can be exploited with this aim are illustrated in Fig. 1.3. At first approximation and without the necessity of detailed knowledge of the underlying acceleration mechanisms, several clear correlations can be established. It becomes obvious that high-energy gamma rays play a leading role in this context. They are abundantly produced

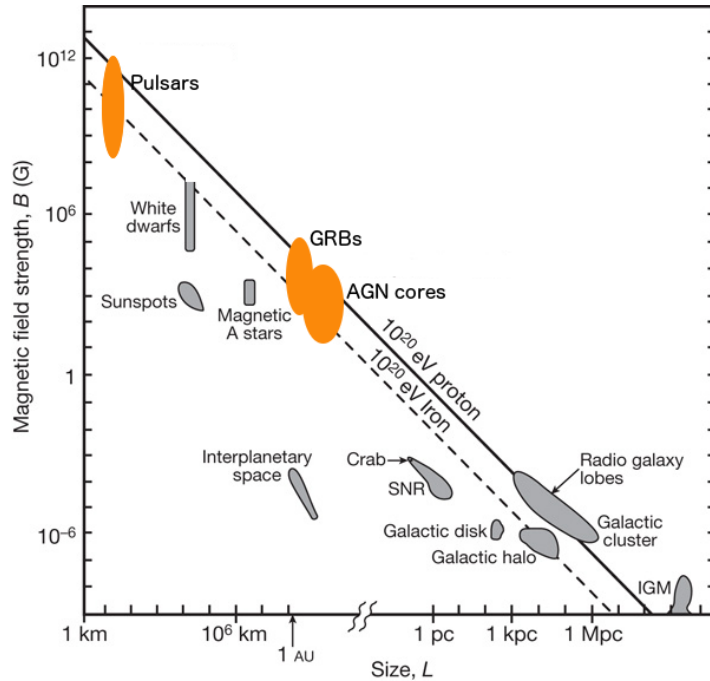


Figure 1.2: Particle acceleration requires (at least partial) confinement within the source of size L and having a magnetic field B . The approximate maximal achievable energy is therefore given by $E_{\max} \sim L \times B$ (diagonal lines). Many of the potential sources are known to show transient behavior (orange regions). Modified from [59].

in all high-energy processes and provide a wealth of information like detailed measurements of the source morphologies, energy spectra, etc. One can also realize that most of the analyses would benefit greatly by information brought about by coincident detection of other messengers like high-energy neutrinos and gravitational waves. If achieved, this combination would allow lifting ambiguities due to background contributions and thus determine the origin of the observed radiation. I'll here present my main contributions to searches for these multi-messenger signals.

I first focus on the detection of high-energy neutrinos (cf. Sec. 2) in which I am involved since 2009 at Irfu/CEA Paris-Saclay. I describe my contributions to the various steps in the data analysis chain of the ANTARES neutrino telescope: a laboratory setup to study the evolution of the detector efficiency over time (cf. Sec. 2.2.1), the introduction of a versatile data format for high-level physics analysis (cf. Sec. 2.2.2), a simulation independent check of the angular resolution of the experiment (cf. Sec. 2.2.3), and the development of an energy estimator in order to suppress background contributions in Sec. 2.3.

Building on these crucial low level studies, I was able to introduce a novel high-level analysis technique: a 2-point correlation analysis method that is using the estimated energy of the neutrino candidates to significantly reduce the influence of atmospheric backgrounds (cf. Sec. 2.4). I used this method to search for sources of high-energy neutrinos in two ways: by analyzing the intrinsic clustering of the recorded neutrino events (cf. Sec. 2.4.4) and via a multi-messenger cross-correlation study between neutrinos and high-energy gamma rays (cf. Sec. 2.5). The latter study could then be extended to search for correlations between neutrinos and very generic source candidates like the distribution of matter in the local universe and, more specifically, massive black holes.

Introducing the time domain to multi-messenger searches I describe in Sec. 2.6 the ANTARES alert network TAToO which is analyzing the ANTARES data in real-time to send alerts to a variety of observatories around the world, before discussing a few recent analyses exploiting the TAToO

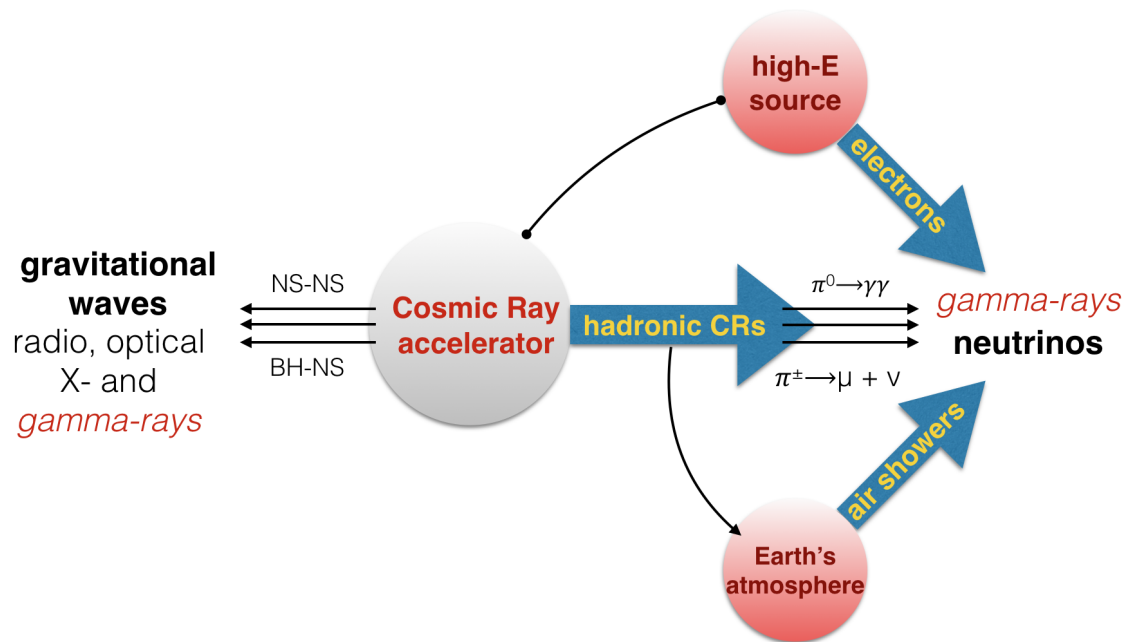


Figure 1.3: In the search of the CR acceleration sites, gamma rays provide the link between various emission scenarios and connect new messengers like neutrinos and gravitational waves. The background contributions from astrophysical, high-energy electrons and atmospheric neutrinos can be removed by space and time correlation between the different messengers.

system.

I then move on to describe a few aspects of searches employing high-energy gamma rays in Sec. 3, where I mainly focus on contributions to the H.E.S.S. gamma-ray observatory. Starting by combining observations of high-energy neutrinos and high-energy gamma rays, I was able to implement and lead the H.E.S.S. multi-messenger program. In a roughly chronological order I outline how I started the program with searches for persistent neutrino-gamma ray sources (cf. Sec. 3.3.1 and Sec. 3.3.2) and describe how it transformed into a fully operational real-time multi-messenger system (cf. Sec. 3.3.3). I'll present details of recent analysis searching for transient neutrino-gamma ray sources including the first detection of a high-energy neutrino in coincidence with a blazar in a high flux state.

The H.E.S.S. transient program also includes multi-wavelength searches for high-energy gamma-ray afterglows of gamma-ray bursts, flaring AGN as well as novel phenomena like searches for afterglows from Fast Radio Bursts (FRBs, cf. Sec. 3.4). A major extension to the program was the inclusion of gravitational waves that I describe in Sec. 3.5 before reporting on the first H.E.S.S. follow-up observations of sources detected by the Advanced Ligo and Virgo interferometers, including the first binary black hole merger observed by all three interferometers (GW170814, cf. Sec. 3.5.2) and the first binary neutron star merger (GW170817, cf. Sec. 3.5.3).

Using the experience gained with searches for transient sources with H.E.S.S., I conclude by briefly outlining preparations for the transient program of the next-generation gamma-ray observatories, the Cherenkov Telescope Array (CTA, cf. Sec. 3.6.1) and the Southern Gamma-ray Survey Observatory (SGSO, cf. Sec. 3.8).

2

High-energy neutrinos

2.1 Introduction

Neutrinos interact only weakly with matter, which makes them insensitive to radiation fields and they thus provide access to cosmological distance scales. Unfortunately the low cross-section is at the same time making their detection challenging. Several very sensitive instruments searching for astrophysical neutrino sources are currently in operation: IceCube at the South Pole is the largest neutrino telescope worldwide. It is complemented by ANTARES, a smaller detector in the Mediterranean Sea and the Baikal Neutrino Telescope now called Giant Volume Detector (GVD) in Lake Baikal. Despite the enormous size of the instrumented volumes available event statistics are still relatively low. In addition, high-energy neutrinos are produced copiously in the Earth's atmosphere via CR induced extensive air showers. These atmospheric neutrinos are an important background for the search of astrophysical neutrino sources. Their influence can be reduced thanks to their soft energy spectrum following $E^{-3.7}$ (compared to the harder E^{-2} spectrum expected from Fermi acceleration processes in astrophysical sources).

Over the last years and together with students and postdoctoral researchers I supervised, I actively participated in the exploitation of this feature. We developed a way to estimate the energy of neutrinos interacting outside the detector volume of a neutrino telescope (see Sec. 2.3 and [146]). Energy estimators can also be used to enhance the sensitivity of searches for clustering of the neutrino arrival directions. Over the last years various analyses searched for point-like or extended neutrino sources. Typically, these searches use maximum likelihood scans of the distribution of neutrino events on the sky and/or correlations with the positions of known, high-energy gamma ray emitters. Complementing these searches I developed an improved 2pt-correlation method that uses the estimated energy of the neutrino events to reduce the influence of atmospheric backgrounds [138, 145]. So far none of the neutrino telescopes has found any significant localized excess which would hint to a steady neutrino source (e.g. [4, 9, 11, 53, 135]).

2.1.1 Astrophysical neutrinos

Yet, a significant breakthrough in the search for astrophysical neutrinos has been made by the IceCube collaboration. The initial analysis in 2013 [3] used three years of data and was able to single out 37 neutrinos with energies in the range of 30TeV to 2 PeV that interacted within the instrumented

volume. The measured flux was found somewhat steeper than E^{-2} . Adding a third year of data the excess over the atmospheric backgrounds already reached a statistical significance of 5.7σ [5]. Follow-up studies were able to confirm this excess also at a lower the energy threshold (below 10 TeV), providing for example 87_{-10}^{+14} astrophysical neutrinos detected in 2 years of data [6]. However, the astrophysical origin of these neutrinos is still unknown and no significant clustering or excess at small angular scales has been found so far. This fact increases the probability that the underlying sources are either very faint but numerous or of transient nature and emit neutrinos only for a limited amount of time.

The detection of the astrophysical neutrino flux paves the way for further detailed analysis with the final aim to localize the astrophysical sources emitting the detected TeV-PeV neutrinos. Based on well-understood particle physics, one can conclude that the same sources should be able to accelerate hadronic CRs (in the simplest case protons) to energies in the 1-100 PeV range. It is also important to note that the observed neutrino flux matches a bound predicted from the well measured CR energy spectrum, the Waxman-Bahcall bound [170], in both intensity and spectral shape. This hints to a close connection between the observed neutrinos and UHECRs and might point the way for future advances in the quest for the CR origin.

I believe that in this context the reduction of the time between multi-wavelength and multi-messenger observations is crucial. Around the time of the detection of the astrophysical flux, the state of the art searches for space and time coincidences were performed offline, i.e. for example the timing and localizations of GRBs were compared with neutrino event lists months or years after the data taking (e.g. [137]). A major leap forward in this domain was the real-time analysis of neutrino data streams and online multi-messenger correlations. Only by triggering deep follow-up observations of significant neutrino events rapidly after their occurrence one can be sure to obtain complete multi-messenger and multi-wavelength coverage, which is necessary for the unequivocal proof of a common origin of potentially observed transient events. In contrast to most gamma-ray observatories, neutrino telescopes have the capability to observe large portions of the sky without the necessity of scheduled observations. They are therefore ideally suited to monitor the high-energy universe and provide alerts on interesting events for detailed follow-up observations by other instruments. Implementing these opportunities within the ANTARES and H.E.S.S. collaboration will be described in Sec. 2.6 and Sec. 3.3.3).

2.2 The ANTARES neutrino telescope

The ANTARES telescope [110] became fully operational in 2008. The detector comprises twelve detection lines anchored at a depth of 2475 m and 40 km off the French coast near Toulon. The detector lines are about 450 m long and host a total of 885 optical modules (OMs), each comprising a 17" glass sphere which houses a 10" photomultiplier tube. The OMs are mounted in groups of three on optical storeys including also the local readout electronics. The OMs look downward at 45° in order to optimise the detection of upgoing, i.e. neutrino induced, tracks. The geometry and size of the detector make it sensitive to extraterrestrial neutrinos in the TeV-PeV energy range. A schematic layout of the telescope is shown in Figure 2.1.

The main neutrino detection channel is based on the Cherenkov light induced by high-energy muons originating from charged current neutrino interactions inside or near the instrumented volume. All detected light pulses (*hits*) are transmitted via an optical cable to a shore station, where a computer farm filters the data for coincident signals in several adjacent OMs. The muon direction is then determined by maximizing a likelihood which compares the time of the hits with the expectation from the Cherenkov signal of a muon track. Details on the event reconstruction are given in Ref. [135, 136].

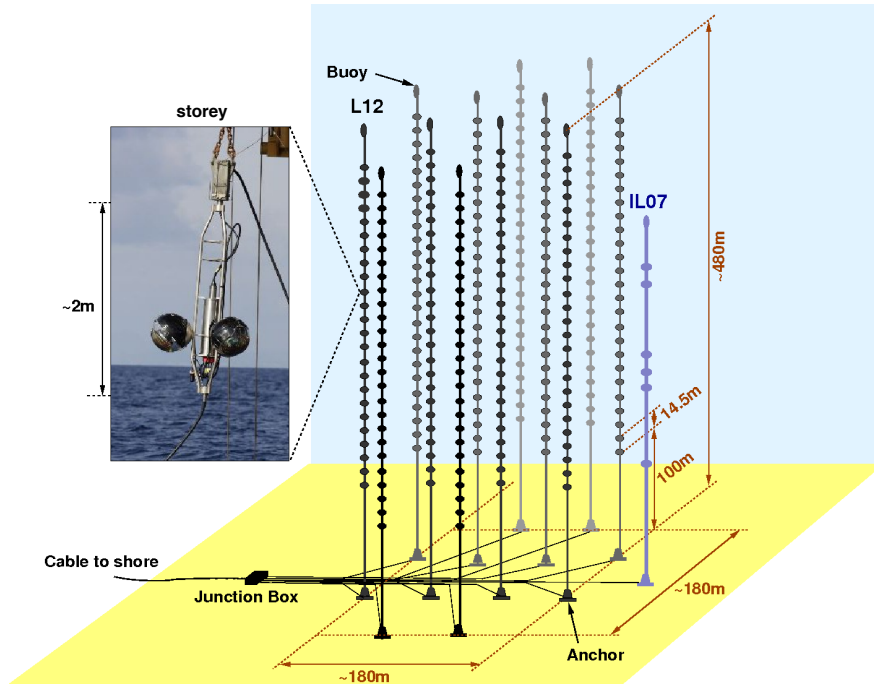


Figure 2.1: Schematic view of the ANTARES telescope. The inset shows a photograph of an optical storey.

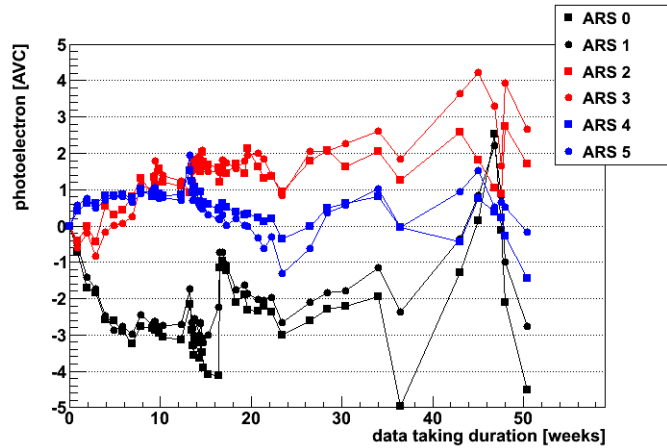
Two main backgrounds for the search for astrophysical neutrinos can be identified: down-going atmospheric muons which have been mis-reconstructed as up-going and atmospheric neutrinos originating in cosmic ray induced air showers at the opposite side of the Earth. Depending on the requirements of the analysis both backgrounds can, at least partially, be discriminated using various parameters such as the quality of the event reconstruction or an estimator of the energy of the muon, e.g. the number of hits used in the track reconstruction. The latter, being strongly correlated with the energy of the original neutrino, helps to discriminate events of atmospheric origin from neutrinos produced in astrophysical sources. Atmospheric neutrinos have a much softer energy spectrum ($\propto E^{-3.7}$) compared to the generic E^{-2} spectrum expected from Fermi acceleration in astrophysical sources. As illustrated in Figure 2.9 this difference affects the distribution of energy dependent parameters (or *energy estimators*) and can therefore be used to enhance the background discrimination. In addition, analyzing the reconstructed arrival directions of the events allows to search for an excess over the isotropic atmospheric backgrounds. Over the past years I have developed novel methods to exploit both features. They will be discussed in Sec. 2.2.3 and Sec. 2.3.

2.2.1 Evolution of the detector sensitivity with time

The optical modules of the ANTARES detector are operated constantly in an environment not fully void of light sources: bioluminescence, radioactive decays of ^{40}K in the sea water and the glass-spheres housing the photomultipliers cause an average rate around 100 kHz (using a charge threshold of around 1/3 of the average photoelectron peak). These continuous exposures may influence the performance and sensitivity of the instrument and has therefore to be studied in detail. The main method is using the evolution of the ^{40}K rates over time [1]. Another attempt was a laboratory study of the time evolution of the response of ANTARES PMTs and the associated readout electronics. For



(a) OM ageing testbench



(b) Evolution of the single electron charge

Figure 2.2: A laboratory setup has been used to detect potential ageing effects of the ANTARES PMTs and electronics. The testbench (left figure) was able to illuminate three optical modules simultaneously. The results (right figure) are not conclusive and no hint of a systemic ageing process could be found.

this purpose a dedicated test bench has been set up at Irfu/CEA Paris-Saclay [67]. The setup replicated the in-situ instrumentation of the ANTARES experiment and is shown in Fig. 2.2a.

Three standard ANTARES optical modules have been housed in a "dark box". A light source consisting of a blue LED (470 nm) ran in continuous mode, with the ability to tune the LED intensity for a resulting OM rate varying from 2 MHz to 4 MHz. The LED light went through an optical light splitter (1:16), from which three optical fibres brought the light towards the photocathode through diffusers at the bottom of each dark box. The photoelectron charge was measured using the standard ANTARES tools and software, as done in-situ and the measurements were therefore affected by the same features as the ANTARES data (e.g. limited charge resolution, ADC differential nonlinearity, etc.). A reference optical device was required to monitor the LED intensity during irradiation. It consisted of a reference optical module receiving the LED light through a fourth optical fibre, powered periodically for short durations and read out independently, so that the LED monitoring did not interfere with the ageing operations. Simulating the ANTARES data taking, the OMs were illuminated almost continuously over 16 months, accumulating a total of 394.4 active days. During the tests, the PMT gains have been monitored based on several quantities: the observed rate of the PMTs above a fixed threshold as measured by the ANTARES DAQ, and the charge corresponding to a single photoelectron and the pedestal as measured periodically by the ARS front-end chip.

The studies performed on the data, lead to integrated charges similar to what may be expected for ANTARES over a span of about 15 years. Although the irradiation rate was higher, the gain was at most 5×10^7 as currently used in ANTARES. As illustrated in Fig. 2.2b, out of the three optical modules, one showed a substantial gain increase, another one showed a limited gain drop, and the third module showed a very substantial gain drop. In this last case, the ageing affected both the PMT and the active base itself. Nevertheless, there was no destruction of any PMT, and the nominal gain could be recovered by readjustment of the high voltage well within the margins of the ANTARES specifications. Although inconclusive with respect to the initial goal of the tests, the results reproduced the behavior observed in ANTARES, where some modules are very stable, while others require punctual positive or negative high voltage adjustments to regain a stable response throughout the detector.

2.2.2 AntDSTs: a high level physics analysis data format

When I joined the Antares Collaboration several standalone event reconstruction tools were used in parallel. Each tool brought with it its own file format summarizing the reconstructed parameters of the events used as input for high level physics analyses (e.g. *PhysicsAnalysis* for CalReal, *aNTuple* for BBFit, *TreeGen* and *I3* for SeaTray). To allow for easier comparisons between the various frameworks, algorithms and analyses and to ease the maintenance of the data analysis software packages, I developed a standalone, ROOT based file format which can be used with all common data analysis frameworks of the ANTARES Collaboration. In reminiscence of the *Data Summary Tapes* once popular in high energy physics experiments, it is called *AntDST* standing for *ANTARES Data Summary Tree* [79]. The presented data format has been derived from a very similar project which I co-developed within the Pierre Auger Collaboration and which forms the basis for adapted formats now used in various high-energy and astroparticle physics experiments (e.g. NA61/SHINE, Nemo, IceCube/IceTop).

The AntDSTs were designed to contain high level variables needed for physics analysis and (if desired) a fair amount of low level data to facilitate the development of new data selection cuts and to debug the reconstruction. Choosing ROOT over a simple ASCII format allows to handle more complicated data structures like several reconstructions of the same event using different strategies, etc. While all variables within the AntDST files are accessible within a plain ROOT session via access to the underlying TTrees, the AntDST library permits to centralize common tasks (event access, etc.) and facilitates some more sophisticated tasks like the extraction of a given event. In addition to the definition of the format itself. Tools and interfaces to convert the output of all reconstruction and simulation programs used within ANTARES have been made available to the collaboration and the AntDST format rapidly became the standard physics analysis format.

AntDST-Analysis: a tool package for physics analyses

As addition to the AntDST data summary format, I introduced the *AntDST-Analysis* package [78] as a bundle of software to facilitate high level event selection and comparisons between different algorithms and reconstruction frameworks. It helped to increase the exchangeability of high level analysis code like event selection algorithms between collaborators and provides a standardized way of performing routing high-level physics analysis tasks as well as the definition and maintenance of standardized data quality control plots that are automatically created along with the event selection procedure. The standardized way of performing these tasks helped to significantly reduce the efforts required to debug and maintain high level analysis code within the collaboration.

The developed tools enabled an extended period of comparisons between the different analysis frameworks before the ANTARES Collaboration adopted the SeaTray framework for data reconstruction supplemented by the AntDST data format and high-level analysis tools as common and standard solution in 2010/2011.

2.2.3 Verification of the directional reconstruction accuracy

The angular resolution of an observatory and its data reconstruction algorithm(s) is an important ingredient to all searches for a localized excess of events and the fundamental parameter in searches of point-like sources. Neutrino telescopes suffer from the inherent problem of not being able to derive their intrinsic angular resolution from the neutrino data itself. As no high-energy neutrino source has been detected so far, the determination of the detector performances have to rely on indirect measurements. Several different possibilities can be exploited for this purpose:

Moon shadow The moon is blocking cosmic rays from reaching Earth and thus causes a shadowing effect in the, otherwise isotropic, distribution of CR arrival directions. By reconstructing the

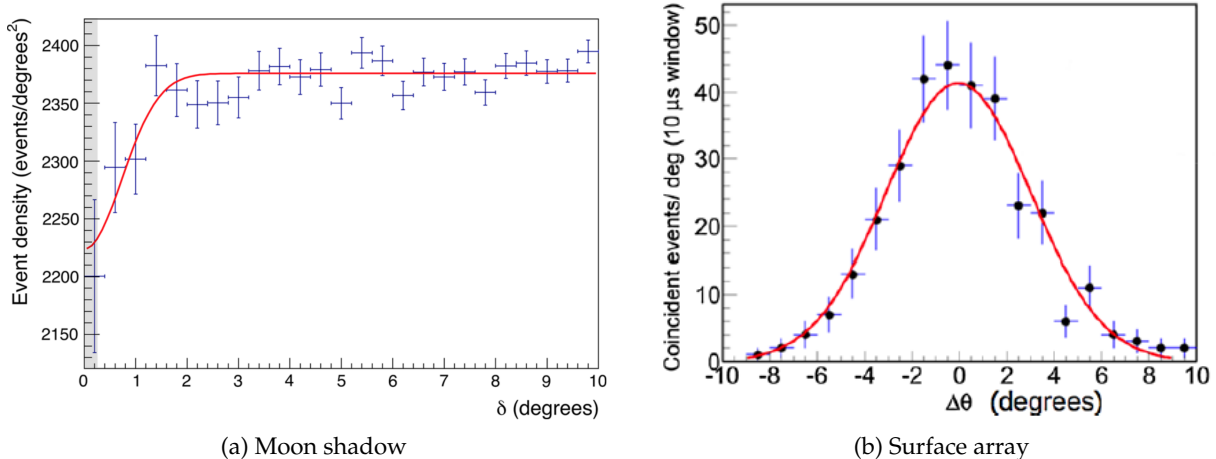


Figure 2.3: Methods to verify the angular resolution of the ANTARES neutrino telescope. Left plot: Event deficit towards the direction of the Moon. Right plot: Zenith angle differences of coincident events detected by ANTARES and a surface air shower detector array. From [2].

distribution of muons created in CR induced air showers above the detector, this effect can be used to estimate the pointing accuracy of the telescope. The moon shadow measured by ANTARES using 5 years of data has a significance of 3.1σ and is shown in Fig. 2.3a. Fitting the observed deficit (cf. Fig. 2.3a) towards the Moon by a Gaussian, the average angular resolution for downgoing muons has been derived to $\Delta\Omega_{moon} = 0.73 \pm 0.14\text{deg}$ [2, 139].

Surface array The angular pointing accuracy of the detector can be also be derived and cross-checked with an independent device observing the same events. For ANTARES this has been realized by a particle detector array on the surface detecting air showers that give rise to high-energy muons detected by the ANTARES telescope. Due to the location of the ANTARES detector, the surface array has been installed on a boat circling the detector site during two measurement campaigns with a total livetime of 6+7 days. During these campaigns a number of events have been observed in coincidence between the two instruments and a comparison between the directions of the shower axis and the reconstructed muon underwater allows to confirm the pointing accuracy of the moon-shadow analysis (cf. Fig. 2.3b [2]).

An additional and novel option has been explored by a Master student in 2012 under my supervision (Nicolas Renault, SupOptique). The driving idea was to develop a measurement of the angular resolution based solely on the ANTARES neutrino data used in searches for the sources of astrophysical neutrinos, i.e. without the need to rely on Monte Carlo simulations nor on atmospheric muon events with their significantly different properties. This goal has been reached by a *checkerboard analysis* which splits large events into two equal parts without any bias between them. Several methods of this crucial step have been tested before settling on a division being done on each detector line using both the altitude and the time of the recorded hits. The two sub-events created in the division step can then be passed through the standard event reconstruction algorithms individually in order to derive two estimates of the incoming direction \vec{p}_i of the particle responsible for the recorded event. By comparing the two reconstructions, a measured of the intrinsic angular resolution $\Delta\Omega$ can be derived as:

$$\Delta\Omega = (\vec{p}_1 - \vec{p}_2) / \sqrt{2}$$

The implemented method has been extensively tested and verified on Monte Carlo simulations. It

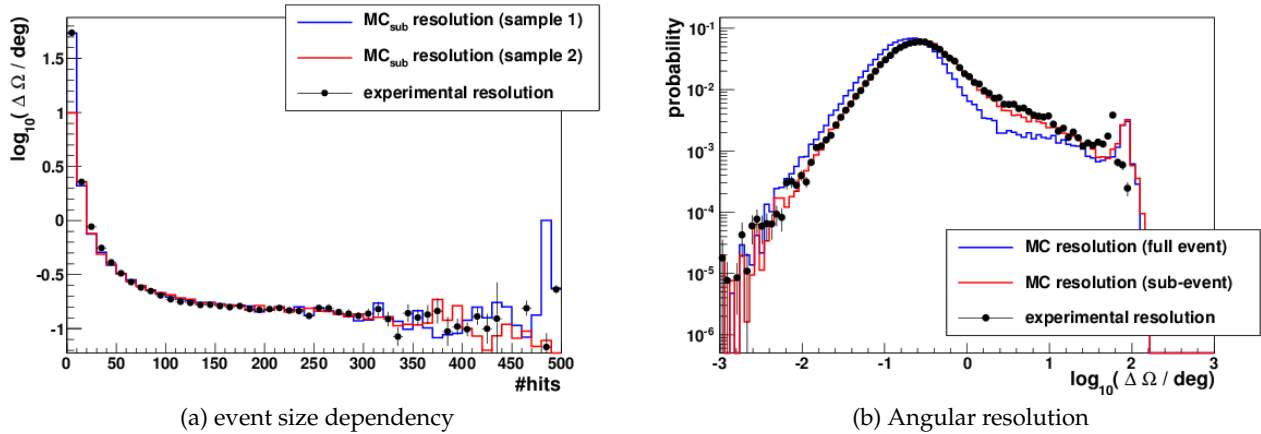


Figure 2.4: Verification of the angular resolution of the ANTARES neutrino telescope. Good agreement between the novel method (*exp. resolution*) with expectations from Monte Carlo simulations. Left plot: dependence on the size of the neutrino event. Right plot: distribution of the derived angular resolution.

became clear that it requires rather large events that can be reconstructed reliably also after having removed half of the available information. Due to lack of available statistics, the method could therefore unfortunately not be applied on an event-by-event basis to the bulk of the neutrino data. On the other hand it was used to verify the angular resolution derived from Monte Carlos simulations with real data. Examples for these comparisons are shown in Fig. 2.4a. The successful verification between data and Monte Carlo on the highest level, i.e. the angular resolution, allowed to validate the MC based values and distributions used within the collaboration. This verification could later be confirmed by the other methods mentioned above (e.g. moon shadow and surface array) and provides a solid basis for various analyses like the search for point-like sources of astrophysical neutrinos [135, 53], which rely on a precise modeling of the angular resolution as input to the likelihood employed in the analyses.

2.3 Estimation of the neutrino energy

The vast majority of the neutrino candidates recorded by neutrino telescopes are of atmospheric origin. To discriminate and select events of potential astrophysical origin, the energy of the events is the prime parameter. It is expected that the astrophysical neutrino flux follows a harder spectrum (typically described by an E^{-2} energy dependence), whereas the atmospheric flux is falling more rapidly with increasing energy ($E^{-3.7}$ in the energy range typically accessible with current neutrino telescopes [43]).

Within the ANTARES collaboration we developed an algorithm to reconstruct the energy of both the muon traversing the detector and the primary neutrino using the energy deposited in the instrumented volume. Its use in several analyses lead to significant increase of their sensitivities [136]. The underlying principles are valid for all neutrino telescopes and similar algorithms are being developed for example within the IceCube Collaboration [131]. The description given here closely follows the one provided to the ANTARES Collaboration as internal note [77] and to the larger community in [146].

The different neutrino interaction modes lead to different experimental signatures in neutrino

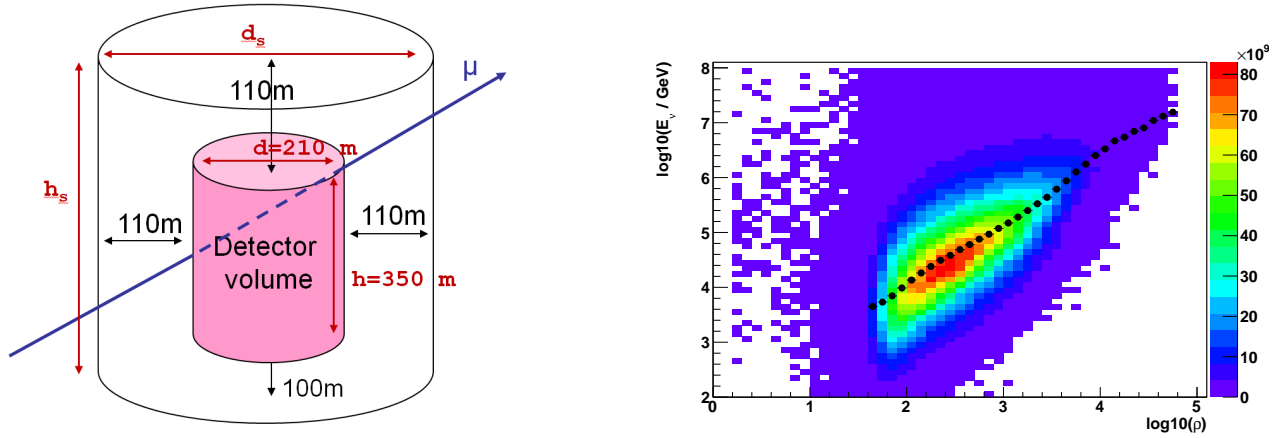


Figure 2.5: Left plot: Definition of the fiducial volume used to calculate the length of the muon track L_μ . The total size of the volume is given by $d_s = 430$ m and $h_s = 560$ m. Right plot: The correlation between the reconstructed dE/dX and the true energy is used to calibrate the energy estimator. The black markers denotes the derived calibration table, i.e. the average true energy per dE/dX bin.

telescopes. The signature of neutral current interactions of all neutrino flavors and charged current interactions of electron or tau neutrinos are particle showers, i.e. very localized energy deposits and light emission. The rate of these events is limited by the available instrumented volume which acts as interaction volume. On the other hand their energy reconstruction is possible with good precision as they are usually fully contained in the instrumented region. Muons emerging from charged current interactions of muon neutrinos provide the bulk of the neutrino induced data of ANTARES and other neutrino telescopes due to the extension of the fiducial volume beyond the instrumented volume. Whereas the direction of the muon track can be reconstructed with good precision, the reconstruction of its energy however is, due to the intrinsic fluctuations of the energy deposited within the detector volume, less obvious and the subject of the algorithm discussed here.

The fundamental idea behind the presented algorithm is to exploit the correlation between the energy of a charged particle in a medium and its energy loss. The latter is deposited along the muon track and can be denoted as energy deposit dE per track-length dX . At energies above the critical energy of a few hundred GeV, energy losses due to Bremsstrahlung become more important with respect to ionisation losses and a clear correlation between dE/dX and the particle energy can be expected. If a significant amount of this energy deposit happens within or close to the instrumented volume of a neutrino telescope it can be detected via the recording of the emitted light along the muon track. One will then be able to reconstruct a measure of the (local) energy loss by dividing the measured amount of energy deposit by the reconstructed length of the track within the fiducial volume. In a final step detailed Monte Carlo simulations are used to estimate the energy of the muon and the incident neutrino.

2.3.1 From dE/dX to energy estimation

We approximate the total muon energy deposit dE/dX by an estimator ρ which can be derived on an event-by-event basis from quantities measured by the ANTARES detector:

$$dE/dX \approx \rho = \frac{\sum^{n\text{Hits}} Q_i}{\epsilon(\vec{x})} \cdot \frac{1}{L_\mu(\vec{x})} \quad (2.1)$$

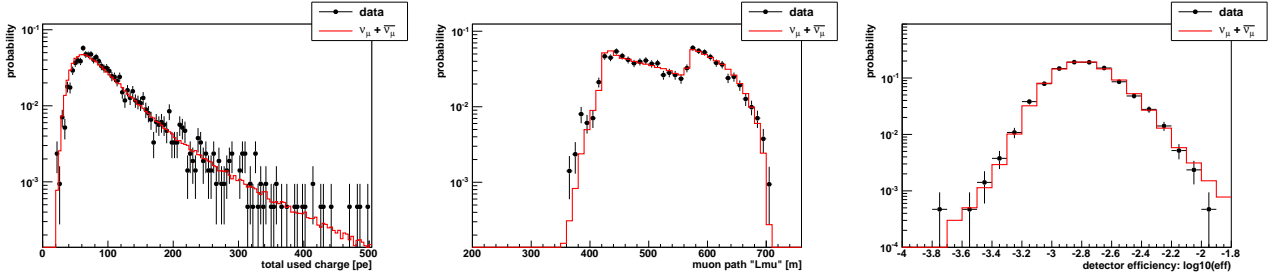


Figure 2.6: Comparison between data (black markers) and Monte Carlo (red histogram) for events selected for the determination of the atmospheric neutrino spectrum [136] for the main input variables to the energy estimator (cf. Eq. 2.1). Left plot: The total charge of all used hits $\sum^{\text{nHits}} Q_i$. Middle plot: The track-length within the fiducial volume $L_\mu(\vec{x})$. Right plot: The detection efficiency $\epsilon(\vec{x})$.

$\epsilon(\vec{x})$ is the light detection efficiency and will be described in detailed below. Q_i denotes the charge recorded by a given photomultiplier tube i of the ANTARES detector. To suppress the influence of background light, we only consider the hits that remain after a hit selection based on the causality criterion assuming a Cherenkov light cone and that have been selected for the final step of the track reconstruction. The track length L_μ is taken as the length of the reconstructed muon path within a sensitive volume. This volume has been defined as the cylinder of the ANTARES instrumented volume extended by twice the approximate light attenuation length ($L_{\text{att}} = 55 \text{ m}$) to take into account the possibility of light entering the instrumented volume from the outside. It is depicted in Fig. 2.5, left plot.

The ANTARES light detection efficiency is depending on the geometrical position and direction of the muon track \vec{x} . This efficiency ϵ can be derived on an event-by-event basis as:

$$\epsilon(\vec{x}) = \sum^{\text{nOMs}} \exp\left(-\frac{r_i}{L_{\text{abs}}}\right) \cdot \frac{\alpha_i(\theta_i)}{r_i} \quad (2.2)$$

Here, the sum runs over all optical modules (OMs) that were active at the time the event was recorded. Modules become inactive for short periods of time, due to localized bioluminescence bursts which cause the data acquisition for modules close by to be stopped, or permanently, due to mechanical or electronics failures. The distance to the muon track r and the angle of incidence θ of the Cherenkov light is calculated for all nOM active modules. The latter is used to derive the angular acceptance $\alpha(\theta)$ of the optical modules. r is used to correct for light absorption in the water, with L_{abs} being the light absorption length. Finally a factor $1/r$ is applied to take into account the light distribution within the Cherenkov cone.

Charged current muon neutrino simulations in combination with a time dependent detector simulation reproducing the actual data taking conditions of the ANTARES detector have been used to correlate the dE/dX values calculated following Eq. 2.1 with the true energy of the incident neutrino or of the muon passing through the detector. These correlations are shown in the right plot of Fig. 2.5. Averaging the result in small dE/dX bins ($\Delta(\log(dE/dX)) = 0.1$), the distributions have been condensed into the final calibration tables. Given a dE/dX value, these tables can be used easily to derive the corresponding estimated energy. Linear interpolations in log-log scale are used between the discrete bins of the tables. As baseline, this calibration step is performed using neutrino simulations fulfilling the quality cuts described in [135]. It should be noted that, depending on the intended application of the energy estimator, a dedicated calibration might become necessary (e.g. energy reconstruction of atmospheric muons, etc.).

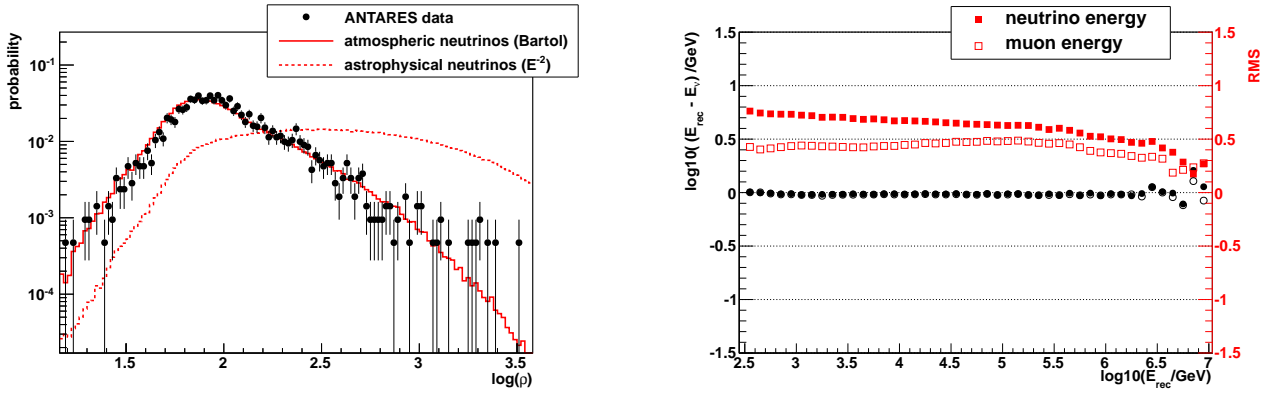


Figure 2.7: Left plot: Distributions of the ρ parameter showing the good agreement between data (black markers) and Monte Carlo simulations (solid, red line). For illustration the expectation for an astrophysical neutrino flux is also shown (dotted, red line). Right plot: The stability of the mean (black markers) and the evolution of the RMS (red markers) of the difference between reconstructed and true energy as function of the reconstructed energy. Filled (open) markers denote the reconstruction of the neutrino (muon) energy.

2.3.2 Data vs. Monte Carlo comparison, performance, and systematic uncertainties

To make sure that the energy estimation will be as reliable for real data as it is for simulated events, a detailed data vs. Monte Carlo comparison has been performed. This comparison has been conducted at several levels, ranging from the input parameters that are used for the energy estimation as given in Eq. 2.1 and 2.2 to the distribution of the final reconstructed energies and for the main event signatures available with sufficient statistics: atmospheric muons and muon neutrinos. Several event selection criteria have been tested and all distributions show a very satisfactory agreement between data and simulations. Examples are shown in Fig. 2.6. It can therefore be expected to obtain results similar to those for Monte Carlo simulations when the estimator is applied to real data. As final example, the distribution of the ρ estimator (see Eq. 2.1) is shown in the left plot of Fig. 2.7 for events fulfilling the high quality event selection criteria used for the determination of the atmospheric neutrino spectrum [136]. It should be noted that the total number of events selected from data is commonly about 25 % higher with respect to the expectations from flux parameterizations (see for example [144]). As we are only interested in the agreement of the shape, the distributions have therefore been normalized to unity.

After the verification of agreement between data and Monte Carlo, the performance of the energy estimator can be derived from Monte Carlo simulations. The described method has therefore been applied to charge current neutrino simulations reproducing the ANTARES data taken in the period 2008-2012. As an example, the event selection criteria follow the ones developed during the search for point like sources [135]. To improve the energy reconstruction quality, two additional criteria based on internal parameters of the energy estimator have been developed:

- $\log(\rho) > 1.6$
- $L_\mu > 380$ m

Events with path lengths within the fiducial volume L_μ shorter than 380 m are dominated by events passing outside the instrumented volume which leads to an overestimation of the energy. The cut at the limit of the $\rho - E_{\text{MC}}$ table ($\log(\rho) > 1.6$) is necessary to define the validity of the energy estimator: the correlation between energy and energy deposit practically disappears at low energies (cf. Fig. 2.5).

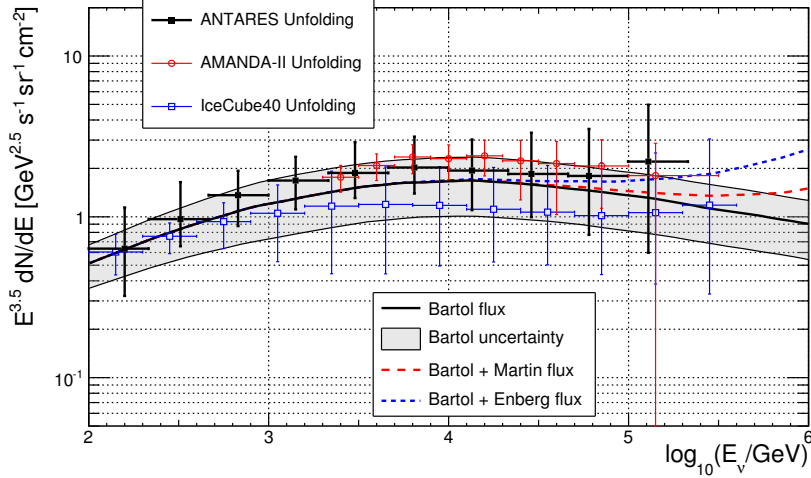


Figure 2.8: The energy spectrum of atmospheric $\nu_{\mu} + \bar{\nu}_{\mu}$ neutrinos as measured by ANTARES using the developed dE/dX energy estimator in comparison to previous observations and phenomenological models. From [136]

The efficiency of the algorithm has been estimated with the help of the above mentioned Monte Carlo simulations. An efficiency of 1 is found over a wide range of energies for events fulfilling the reconstruction quality cuts. Applying all selection criteria and weighting the neutrino simulations to follow an astrophysical E^{-2} energy spectrum, the performance of the energy estimator has been derived. As can be seen in Fig. 2.7, an average resolution of $\log(E) \approx 0.45$ ($\log(E) \approx 0.7$) has been achieved for the reconstruction of the muon (neutrino) energy.

The main limitation to the energy resolution is the limited size of the detector, which, combined with the statistical nature of the energy loss processes, leads to an insufficient sampling of the energy losses along the muon track. The reconstruction of the neutrino energy suffers in addition from the fluctuations induced in the charged current interaction. Minor additional contributions are related to the uncertainties of the directional reconstruction and the selection of the hits used as input for the energy estimation.

As for any physics analysis and novel analysis method, a discussion of the related systematic uncertainties is of utmost importance. For the developed energy estimator various effects have been studied and quantified in detail. A summary is given in Tab. 2.1.

Table 2.1: Systematic uncertainties of the dE/dX energy estimator

origin	sys. uncertainty [$\Delta \log(E)$]
detector description	0.1
bioluminescence noise level	< 0.01
event selection criteria	< 0.1
spectral assumptions	< 0.05

2.3.3 Application of the energy estimator: measurement of the atmospheric neutrino spectrum

The developed energy estimator has been used in various physics analysis within the ANTARES collaboration. A notable first application is for example the measurement of the energy spectrum

of atmospheric neutrinos ($\nu_\mu + \bar{\nu}_\mu$) in the energy range 0.1 – 200 TeV [136] from data collected by the ANTARES neutrino telescope from 2008 to 2011. The result is depicted in Fig. 2.8. The flux is compatible with a single power-law dependence with spectral index $\Gamma_{\text{meas}} = 3.58 \pm 0.12$. With the available statistics an additional contribution of prompt neutrinos could not be established.

2.4 Searches for clustering in the neutrino sky

Despite significant effort, no clear signature for point-like sources of astrophysical neutrinos has been found so far by any of the past and current neutrino telescopes [4, 9, 11, 53, 135, 149] and both the spatial distribution as well as the morphologies of sources potentially emitting neutrinos in the TeV energy range are unknown. Similar to the distribution of observed sources emitting high energy gamma rays, they are supposed to be distributed very in-homogeneously throughout our cosmic neighborhood. A significant fraction of them may be located in the Galactic disk and could be spatially extended (e.g. shell-type supernova remnants). It is therefore interesting to study the intrinsic clustering of the arrival directions of neutrino candidates.

2.4.1 An improved 2pt correlation analysis

In the analysis described here, an improved autocorrelation method is used for these searches. One of the main advantages of autocorrelation searches is that no prior information about the potential sources is required. Potential biases are thus naturally reduced. Since it covers a large angular range, i.e. neutrino emission regions of very different sizes, this study is complementary to searches for point-like sources and could provide hints for underlying, yet unresolved, source morphologies and source distributions. Exploiting the expected multi-messenger signatures of potential sources the introduced method is extended to searches for correlations between the arrival directions of neutrino candidates and other classes of astrophysical objects: sources of high energy gamma rays, massive black holes and nearby galaxies. The novel autocorrelation analysis method introduced here as well as its application to ANTARES data is also described in detail in [145, 138].

The most commonly used method to detect intrinsic clusters within a set of N events is the standard two-point autocorrelation distribution. It is defined as the differential distribution of the number of observed event pairs, N_p , in the dataset as a function of their mutual angular distance, $\Delta\Omega$. I adapted this technique to the ANTARES data and applied it to the first two years of ANTARES data. No significant clustering has been detected [143].

Continuing the development I introduced a significant improvement of the method by using an estimator of the neutrino energy. This novel method will be described in the following.

To suppress statistical fluctuations that would reduce the sensitivity of the method, the cumulative autocorrelation distribution is used. It is defined as

$$\mathcal{N}_{\hat{E}}(\Delta\Omega) = \sum_{i=1}^N \sum_{j=i+1}^N w_{ij} \cdot [1 - H(\Delta\Omega_{ij} - \Delta\Omega)], \quad (2.3)$$

where H is the Heaviside step function. The weights $w_{ij} = w_i \cdot w_j$ are calculated using the individual event weights $w_i = \int_0^{\hat{E}_i} f(\hat{E}) d\hat{E}$, where $f(\hat{E})$ is the cumulative distribution of the energy estimator \hat{E} for the background. Astrophysical neutrinos are more likely to produce events with a higher value of the energy estimator \hat{E}_i than atmospheric neutrinos. This is represented by a higher event weight w_i . The used distribution is built from large statistics Monte Carlo simulations reproducing the actual data taking conditions, including, for example, the time dependent background fluctuations induced by bioluminescence. These simulations have been validated by extensive comparisons with data. An

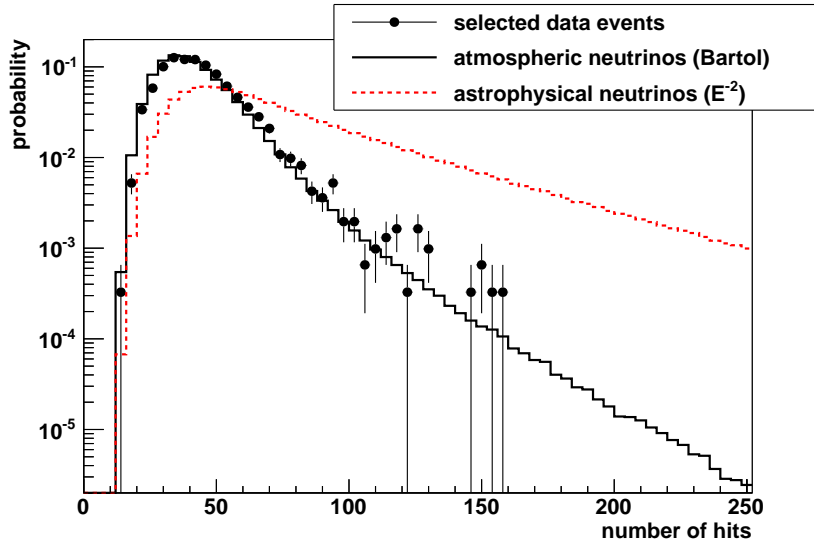


Figure 2.9: Normalized distribution of the number of hits used in the event reconstruction for data (black markers) and Monte Carlo simulations (atmospheric neutrinos following the parametrization from Ref. [43]: black histogram; astrophysical neutrinos: red, dotted histogram).

example is shown in Figure 2.9, where the number of hits used in the event reconstruction is depicted (see [135, 136] for further details). The simulated events used to build the $f(\hat{E})$ distribution follow an energy spectrum as expected for atmospheric neutrinos [43] (black histogram in Figure 2.9). Modifying the standard autocorrelation by these weights leads to a significant increase of the sensitivity to detect clustering of (astrophysical) events following a harder energy spectrum. This improvement is illustrated in Figure 2.10. Various possibilities exist for the estimation of the energy and the definition of the weights. As crosscheck of the stability and performance of the method, the full analysis has been performed using two different energy estimators: the number of hits used during the final step of the event reconstruction, n_{Hit} , as in the search for point-like sources [135], as well as a recently developed estimator exploiting the correlation between the energy deposit, dE/dX , and the primary energy [146, 136]. Both provide very similar results. As shown in Figure 2.10, the n_{Hit} energy estimator shows a slightly better performance for weak sources and is therefore retained for the final analysis.

Pseudo-experiments have been used to determine the optimal size of the angular steps $\Delta\Omega$. Increasing the number of angular steps enhances the angular resolution of the method but degrades the sensitivity due to the increasing number of trials (*look-elsewhere-effect* [87]). Taking into account the median angular resolution of 0.5° [135], an optimum has been found for angular steps of about 0.1° .

2.4.2 Reference autocorrelation distribution and comparison with data

To detect structures in the sky distribution of the selected events, a reference autocorrelation distribution to compare with is needed. This reference is determined by scrambling the data themselves, a method which allows the reduction of systematic uncertainties potentially introduced by the use of Monte Carlo simulations. The scrambling is performed keeping the pairs of local coordinates (zenith, azimuth) in order to avoid losing information about possible correlations between them. The detection time is drawn randomly from another event within the same detector configuration to keep track of the changing layout of the detector due to its construction and maintenance. This method is

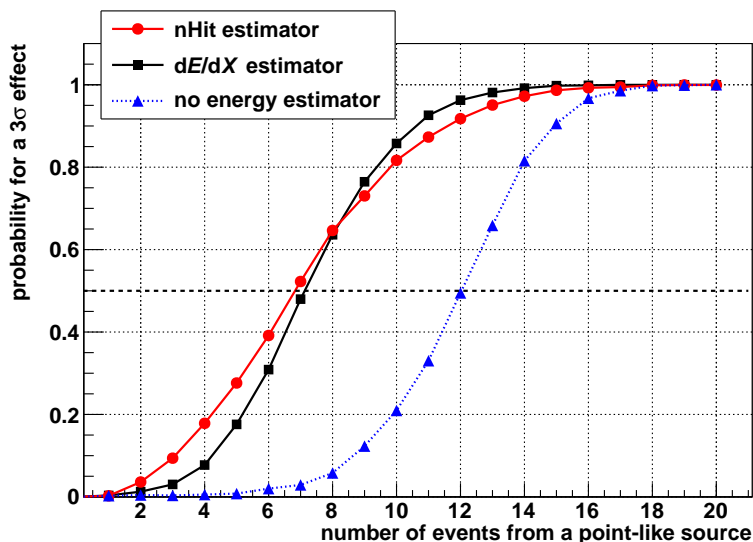


Figure 2.10: Probability to detect with a 3σ significance a single point-like source following an E^{-2} energy spectrum as a function of its neutrino luminosity, i.e. the number of detected neutrinos. The blue triangles denote the standard autocorrelation method without an energy estimator. The black squares show the performance including the dE/dX energy estimator [146] and the red circles denote the finally used method using the n_{Hit} estimator.

applied to all selected events and a randomized sky map naturally reproducing the coverage of the unscrambled ANTARES data is constructed.

This randomized sky is then analyzed in exactly the same way as the data to derive the autocorrelation function. The randomisation process is performed about 10^6 times and the derived autocorrelation distributions are averaged in order to reduce statistical fluctuations.

Structures in the sky distribution of the data will show up as differences between the autocorrelation distribution of the data and the reference distribution. The comparison is performed by using the formalism introduced by Li and Ma [106]. This formalism provides a raw test statistic, t , as a function of the cumulative angular scale. As the comparison is performed bin-by-bin and as the scan is made over different angular scales, this result has to be corrected for the corresponding trial factor. To limit the number of trials the scan is performed only up to 25° , a scale which includes most known extended sources and emission regions.

Finally, the method proposed by Finley and Westerhoff [81] is applied by performing about 10^6 pseudo experiments in which the autocorrelation distributions of randomized sky maps are compared with the reference distribution. For each simulated map the maximum value of the test statistic is calculated. The final p-value of the analysis is then calculated as the probability to obtain the same or a higher value of t from these background-only pseudo-experiments.

2.4.3 Sensitivity

The performance of the novel algorithm has been determined using mock datasets built by scrambling the selected data events as described above. While keeping the total number of events constant, predefined source structures with various sizes and source luminosities are added. The angular resolution of the detector is taken into account by convolving the intrinsic source size with a two dimensional Gaussian with a width of $\sigma = 0.5^\circ$. The energy estimator for the injected signal events

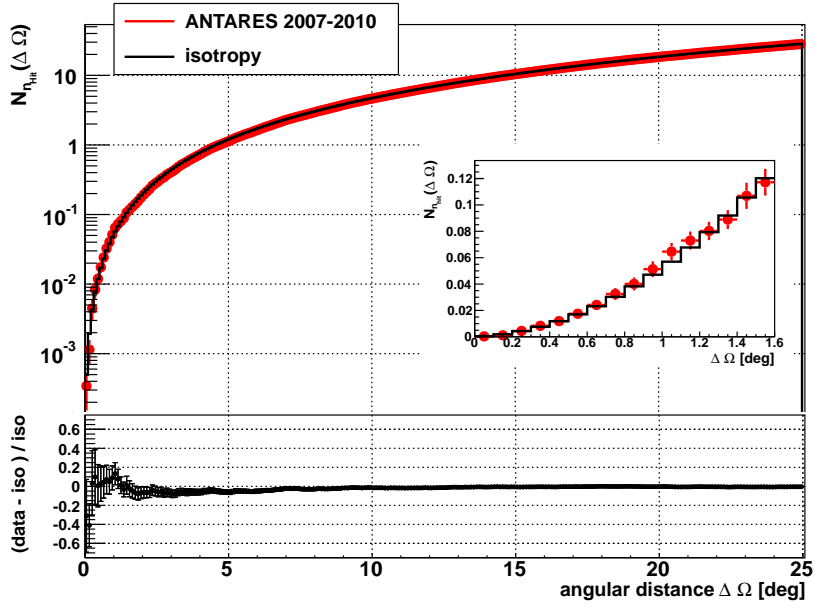


Figure 2.11: Cumulative autocorrelation function of data taken with the ANTARES neutrino telescope in 2007-2010. The red markers denote the ANTARES data and the black histogram represents the reference distribution expected for an isotropic dataset. The inset shows an enlarged view for small angular distances and the lower panel depicts the relative difference between data and reference distribution.

is drawn randomly from distributions weighted to follow an E^{-2} energy spectrum (see red dotted line in Figure 2.9). These mock datasets are then analyzed in exactly the same way as described in Section 2.4.2.

Compared to a dedicated likelihood-based search for a point-like excess in the same dataset [135], the sensitivity of the autocorrelation analysis is slightly worse for a single source. The present method indeed requires about 7 signal events to obtain a 3σ detection with a 50 % probability, compared to about 6 events required in the likelihood search. On the other hand, it outperforms the algorithm optimized for the localisation of point-like sources as soon as several weak sources are present, which underlines the complementarity of the two methods. Another advantage is the sensitivity of the autocorrelation method to extended source regions. The performance of the algorithm for both cases is illustrated in Figure 5 of the corresponding publication (cf. [138], also available in the Appendix [appendix:papers]).

2.4.4 Autocorrelation results and discussion

Following Eq. 2.3, the improved cumulative autocorrelation analysis using the n_{Hit} energy estimator has been applied to 3058 selected neutrino candidate events recorded by the ANTARES neutrino telescope between 2007 and 2010 (813 days of effective lifetime). A skymap in galactic coordinates of these events is shown in the upper left plot of Figure 2.12. The obtained distribution is shown as the red markers in Figure 2.11 and compared with the reference corresponding to the expectation from an isotropic distribution of the arrival directions (black histogram). The maximum deviation between the data and the reference distribution is found for an angular scale $\leq 1.1^\circ$. Correcting for the scanning trial factor this corresponds to a p-value of 9.6 % and is therefore not significant. In addition, it is known that the dataset analyzed here contains a slight excess of events around (R.A., Dec) = $(-46.5^\circ,$

-65.0°), where a cluster of 5 events within one degree has been found [135]. This cluster resulted in a 2.2σ effect. I studied this region in detail using observations in VHE gamma-rays obtained with the H.E.S.S. system. Details are presented in [149] and discussed in Sec. 3.3.1. Replacing these events by randomized events increases the post-trial p-value of the autocorrelation analysis to 35 %. Therefore we concluded that the analyzed ANTARES dataset does not contain significant clusters in addition to the small point-like excess that had already been observed in the dedicated search.

2.5 Multi-messenger links: two-point cross-correlation with external catalogues

One way to improve the sensitivity of searches for sources of high-energy astrophysical neutrinos is to rely on the connection with other messengers. Based on phenomenological source scenarios, observations in certain wavelengths and catalogues of interesting astrophysical objects can provide valuable additional information. This approach is followed here through a first search for a global correlation between neutrinos detected by the ANTARES telescope and high energy gamma rays as well as the matter distribution in the local universe represented by the distribution of galaxies. The latter correlation with extragalactic sources, is complemented by a correlation with a catalogue of massive black holes. A dedicated correlation analysis between ultra-high energy cosmic rays detected by the Pierre Auger Observatory and neutrino candidates recorded by ANTARES has been published in Ref. [40].

For this purpose, the improved autocorrelation function described in Eq. 2.3 is extended to measure the two-point cross-correlation between the N neutrino candidates and an external dataset of n astrophysical objects:

$$\mathcal{N}_p(\Delta\Omega) = \sum_{i=1}^N \sum_{j=1}^n w_i \cdot \hat{w}_j \cdot [1 - H(\Delta\Omega_{ij} - \Delta\Omega)], \quad (2.4)$$

Here, w_i denotes the weights derived for each neutrino candidate event as described above. The weights related to the external dataset, \hat{w}_j , are calculated in a similar way, i.e. by integrating the normalized distribution $f(\hat{x})$ of the discriminant parameter \hat{x} : $\hat{w}_j = \int_0^{\hat{x}_j} f(\hat{x}) d\hat{x}$. The methods for the calculation of the reference distribution expected from an isotropic neutrino dataset, the comparison with the data and the correction for trial factors using pseudo experiments is performed in the same way as described in Section 2.4.4 for the autocorrelation analysis.

2.5.1 High-energy gamma rays

Data from two years of observation of high-energy gamma rays with the Fermi-LAT satellite is used to compile the 2FGL point source catalogue [125]. It is shown in the upper right plot of Figure 2.12. The full catalogue, containing 1873 gamma ray sources, is used for a two-point correlation analysis with the selected ANTARES neutrino candidates. It should be noted that a small subset of these sources are also included in the candidate list used in a dedicated search for point-like sources [135]. Each 2FGL source is weighted with its gamma ray flux $1 - 100$ GeV as given in the Fermi catalogue and the ANTARES events are weighted based on the n_{Hit} energy estimator. The minimum post-trial p-value of 68 % is found for angular scales smaller than 0.6° .

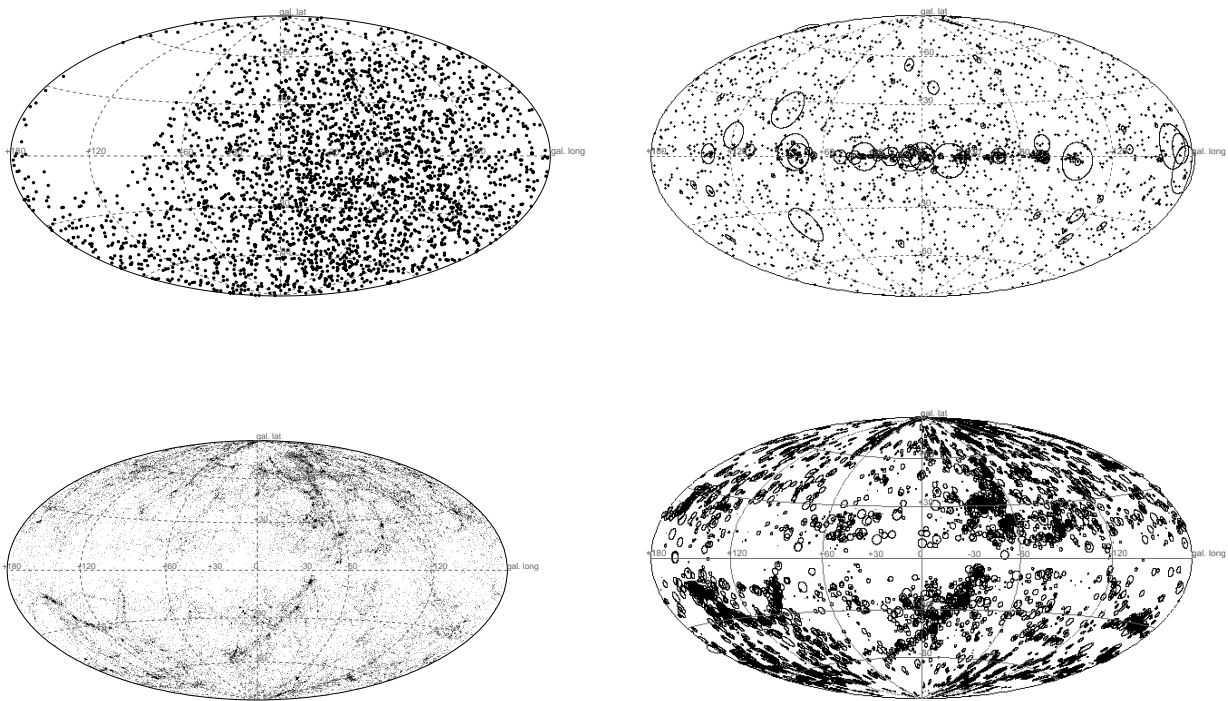


Figure 2.12: Upper left plot: Skymap in galactic coordinates of the 3058 selected neutrino candidates used for this analysis [135]. Upper right plot: High-energy gamma ray sources given in the 2FGL catalogue from Fermi-LAT [125]. The size of the circles indicates the gamma ray flux in the 1 – 100 GeV energy range. Lower left plot: Galaxies within 100 Mpc as given in the GWGC catalogue [172]. Lower right plot: Massive black holes as given in [65]. The size of the circles indicates the mass of the objects.

2.5.2 The local universe

The locations of the cosmic ray accelerators are likely correlated with the matter distribution in the local universe. To exploit this connection, the ‘Gravitational Wave Galaxy Catalogue’ (GWGC) which provides a rather complete set of galaxies within a distance of $D < 100$ Mpc, is used as description of the local extra-galactic matter distribution [172]. Their distribution is shown in the lower left plot Figure 2.12. Assuming the simplest case of equal neutrino luminosity from all given 53295 galaxies, a D^{-2} weighting for the galaxies and the n_{Hit} neutrino weights for the neutrino candidates are used. The two-point correlation analysis finds the most significant clustering at scales smaller than 0.3° with a post-trial p-value of 96 %.

2.5.3 Massive black holes

A refinement of this largely unbiased analysis is the introduction of selection criteria that favour cosmic ray accelerator candidates among the neighbouring galaxies. For example, the sub-class of galaxies housing massive black holes at their centers has been discussed as efficient accelerators of cosmic rays up to ultra-high energies (for a summary of proposed acceleration sites, see e.g. Ref. [163]). Here this scenario is exploited by searching for correlations between the neutrino candidates detected by the ANTARES telescope and massive black holes given in Ref. [65] (see lower right plot of Figure 2.12). The weighting the 5894 objects in the catalogue according to their mass reflects the energetics of the black hole systems and thus their acceleration power. Again, the neutrino events

are weighted using the n_{Hit} estimator. The minimum post-trial p-value of 56 % is found for angles smaller than 8.6° .

2.5.4 Summary and outlook on neutrino 2pt-correlations

In the search for the sources of high-energy cosmic rays, the detection of astrophysical neutrino sources may play a crucial role. Unfortunately searches for identified structures (point-like or extended) in the neutrino sky continue to turn up empty handed. Ever increasing statistics in these searches and the use of novel methods now enable to derive stringent limits. As illustrated above, an interesting strategy is to search for un-localized clusterings, i.e. cumulative effects of potentially many source clusters too weak to be detected individually. Application of the introduced 2-pt correlation method to 813 days of effective lifetime of ANTARES data, the arrival directions of the selected neutrino candidates neither show evidence for clustering of events on top of the isotropic distribution expected for the background of atmospheric neutrinos, nor correlate with catalogues of gamma rays, nearby galaxies or massive black holes. Further details can be found in the corresponding publication [138] available in Sec. B.

The presented analysis has since been transferred to Rodrigo Gracia Ruiz, PhD student at APC/Paris VII between 2013 and 2016 whom I followed as member of his PhD committee. In addition to extending the analyzed dataset (2007-2013, i.e. adding 3 additional years of ANTARES data), he used the autocorrelation analysis to put limits on an astrophysical population of high-energy neutrino emitters in the form of blazars [86].

2.6 TAToO: multi-messenger alerts

A complementary, and in my opinion ever more promising, way to search for the sources of high-energy neutrinos is the search for *spatial and temporal correlations* with other astrophysical messengers (cf. Sec.2.1.1). We successfully implemented this idea within the TAToO collaboration, which I joined in 2010. TAToO is composed of a small sub-group of ANTARES members and collaborators from various, initially mainly optical, observatories. Over the last years, the range of partners could be extended to cover the full wavelength range of electromagnetic radiation from the radio domain to high-energy gamma rays. An overview of the various partner observatories is shown in Fig. 2.13.

TAToO was initially relying on an online reconstruction of the ANTARES neutrino candidates based on a fast and robust algorithm [44], which uses an idealized detector geometry and is thus independent of the dynamical positioning calibration, which is available only after dedicated offline analyses. This reconstruction, and a subsequent quality selection ($N_{\text{line}} \geq 2$, zenith angle $\theta < 0$ and the total recorded charge $Q \leq 1.3 + [0.04 \times (N_{\text{hits}} - 5)]^2$, see [42] for details) allows the rate of events to be reduced from few Hz down to few mHz. In close collaboration with Manuela Vecchi (Postdoc at CPPM/Marseille, now at University of Sao Paolo and Groningen) and Michel Ageron (CPPM/Marseille) I implemented an additional reconstruction of the events passing these criteria using the more precise reconstruction tool used in offline analyses (e.g. [39]). The implemented method allows the neutrino nature of the event to be confirmed and the angular resolution to be improved. The online system of ANTARES now reaches a resolution similar to that of offline searches for point-like neutrino sources (≈ 0.3 deg [39]) and thus facilitates the follow-up at other wavelengths allowing to add new follow-up observatories with smaller field-of-views like the Zadko facility in Australia or the instruments onboard the SWIFT satellite (cf. Fig. 2.13).

The criteria for the TAToO triggers are based on the features expected from astrophysical sources. Several models predict the production of neutrinos with energy greater than 1 TeV from GRBs [169, 117, 74, 132], CCSNe [50] and AGN [62]. A basic requirement for the near coincident observa-

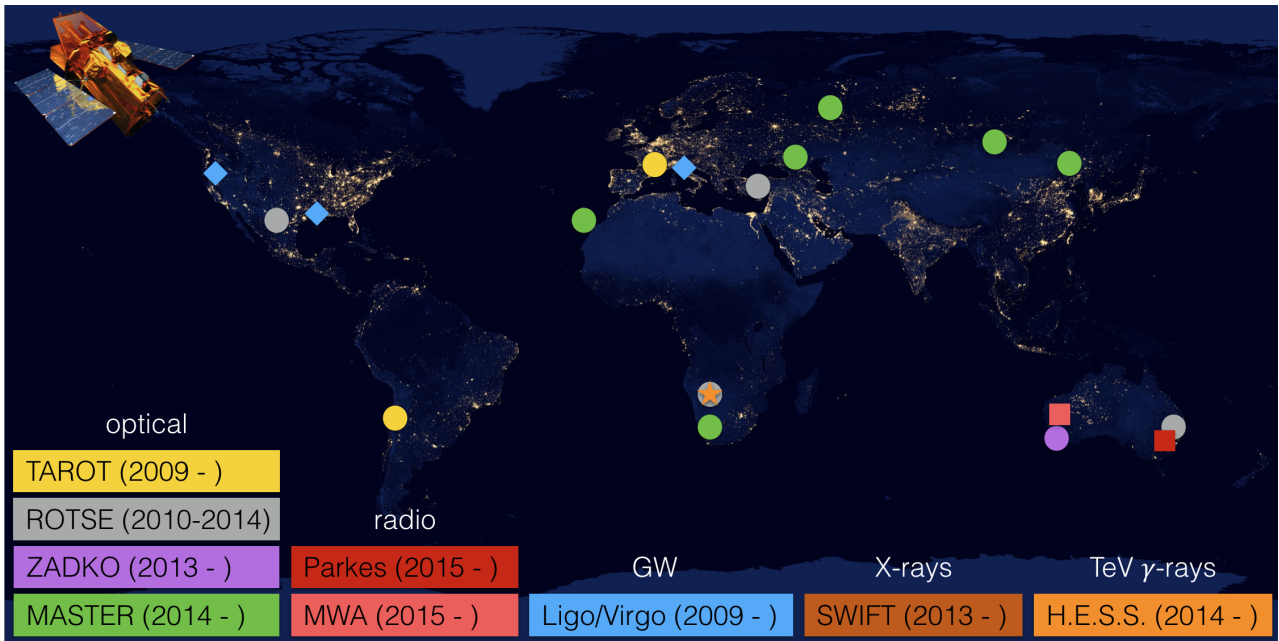


Figure 2.13: Overview of the multi-wavelength and multi-messenger partners of the ANTARES/TAToO online analysis and alert program, illustrating the achieved full-sky and large MWL coverage.

tion of a neutrino and an optical counterpart is that the pointing accuracy of the neutrino telescope should be at least comparable to the field of view of optical telescopes ($\approx 2 \text{ deg} \times 2 \text{ deg}$ for TAROT/ROTSE). After the selection of up-going events, which removes the majority of atmospheric muons, the ANTARES/TAToO neutrino sample consists mainly of atmospheric neutrinos. Several criteria are used to select candidates with an increased probability to be of cosmic origin [42]. Three online neutrino trigger criteria are currently implemented in the TAToO alert system:

- Doublet trigger: the detection of at least two neutrino-induced muons coming from similar directions ($< 3 \text{ deg}$) within a predefined time window ($< 15 \text{ minutes}$).
- High-energy trigger: the detection of a single high-energy ($\geq 7 \text{ TeV}$) neutrino-induced muon.
- Directional trigger: the detection of a single neutrino-induced muon for which the direction points towards a local galaxy within $< 0.5 \text{ deg}$. The coordinates of the galaxies are selected from the GWGC catalogue [172] with a distance cut at 20 Mpc.

In agreement with the optical telescopes, the total trigger rate has been tuned initially to 25 per year. This rate is dominated by high-energy and directional triggers, as until now no doublet trigger has been sent to the network. The accidental coincidence rate due to two uncorrelated events is estimated to be 7×10^{-3} per year. The high-energy trigger typically requires more than 70 photomultiplier hits and a total amplitude greater than 150 photoelectrons. To comply with lower rate requirements (e.g. 6 alerts per year are accepted by the Swift satellite), a subset of the high-energy trigger, denoted as the very high-energy trigger, provides a dedicated trigger for several additional follow-up instruments. It typically requires more than 80 hits and 300 photoelectrons. These triggers are since early 2016 also sent to the H.E.S.S. gamma ray observatory (see Sec. 3.3.3 for details). The bi-dimensional distribution of variables used for the selection of both high-energy and very high-energy triggers is illustrated in Fig. 2.14a for neutrino candidates recorded from 2012 to March 2015.

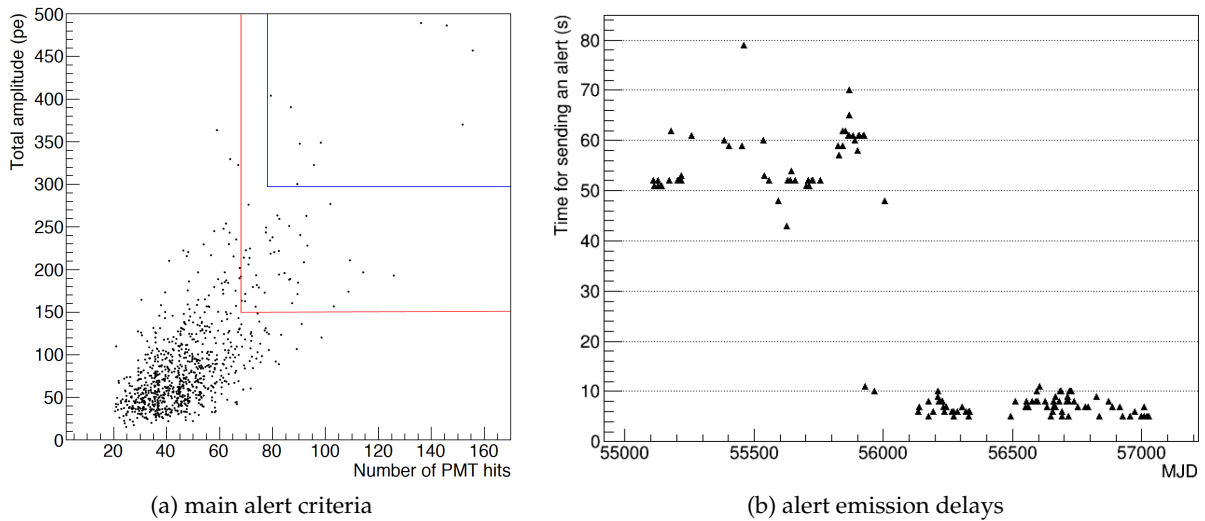


Figure 2.14: Alerts emitted by the TAToO online analysis and alert program are mainly based on events with a high number of triggered PMTs and a high total charge (left plot, right top corner). After a DAQ re-organisation the delays until the alert emissions could be reduced significantly (right plot). From [41].

Neutrinos falling outside the red box can lead to an alert if they fulfill the directional or the doublet trigger. The directional trigger was implemented in late 2011.

Before 2012, the alert system was able to send alerts about 50 seconds after the neutrino events. Since 2012, a major DAQ system improvement allows us to send alerts only a few seconds ($\sim 3 - 5$ seconds) after the detection of the neutrinos. Fig. 2.14b displays this latency for the first 150 alerts collected since the commissioning of the TAToO alert system until March 2015.

2.6.1 Searches for fast optical and X-ray transients with TAToO

After several years of successful operations of the ANTARES alert system, analyses of the obtained optical and X-ray follow-up observations were performed. The analyses were led by Aurore Mathieu (Phd student at CPPM/Marseille), the resulting publication [41] was jointly prepared by all members of the TAToO group. A short summary is given in the following.

The work focused on transient sources active at relatively short timescales such as gamma-ray bursts, core-collapse supernovae, or active galactic nuclei. We therefore selected only those alerts which had optical or X-ray images taken with a maximum delay of 24 hours after the neutrino trigger. The optical follow-up of TAToO alerts used for the analysis was performed using several ground-based telescopes dedicated to early observations of GRBs. Six such telescopes are involved: ROTSE-III (USA, Namibia, Australia, Turkey) and TAROT (France and Chile). They are shown in Fig. 2.13. ROTSE-III was a network of four identical 0.45 m telescopes [45] and TAROT is a network of two identical 0.25 m telescopes [102]. ROTSE has stopped its activity progressively over the last years: ROTSE 3a (Australia), 3b (Texas), 3c (Namibia) and 3d (Turkey) have been stopped in 07/2011, 09/2014, 12/2010 and 12/2012, respectively. These telescopes had a field of view of 1.9×1.9 and a spatial sampling of 3.3 arcsec/pixel. The sensitivity of the TAROT and ROTSE telescopes is about the same: for a signal to noise ratio of 5, an exposure time of 180 seconds and a clear filter, the limiting magnitude is 18.5. Between 2009-2015, out of about 150 alerts emitted by the TAToO program, 42 could be followed successfully within 24h and were therefore selected for the analysis. For 11 alerts the time between the neutrino detection and the start of the acquisition of the first image was less

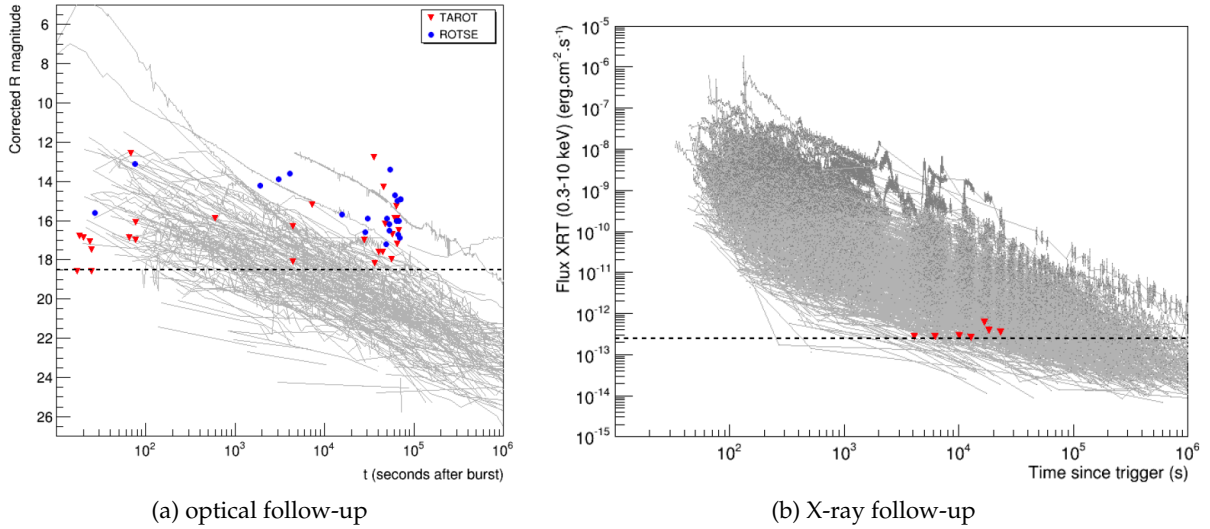


Figure 2.15: Left plot: Limiting magnitudes obtained from TAToO follow-up with the ROTSE and TAROT optical telescopes (color markers) compared to measured GRB afterglows (grey lines). Right plot: Limits on the X-ray flux from Swift-XRT (red triangles) compared to measured GRB afterglows. From [41].

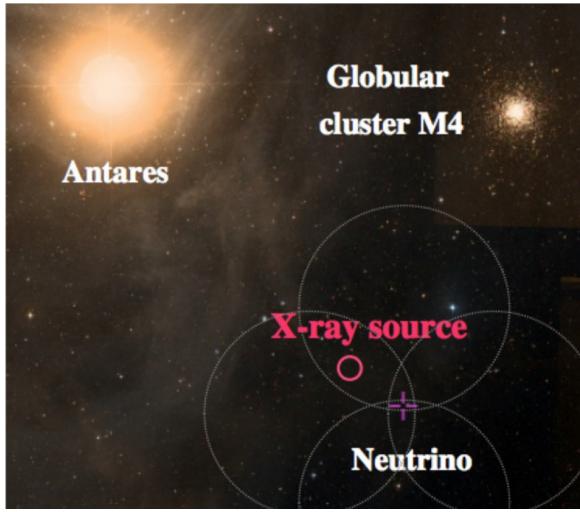
than 1.2 minutes while being as low as 25 seconds for 7 alerts.

In addition to the optical follow-up, a subset of the alerts were sent to the Swift satellite [83] to be followed with its XRT instrument [63] since 2013. The detection sensitivity of the XRT is $5 \times 10^{-13} \text{ erg cm}^{-2} \text{ s}^{-1}$ in 1 ks, with an energy band covering from 0.3 to 10 keV. Due to the small field of view (radius 0.2 deg) of the XRT and the typical error radius of an ANTARES alert (0.3 – 0.4 deg), each observation is composed of 4 tiles up to 2ks exposure each. This mapping covers about 72% of the ANTARES PSF for an event fulfilling the ‘high-energy’ selection outlined above.

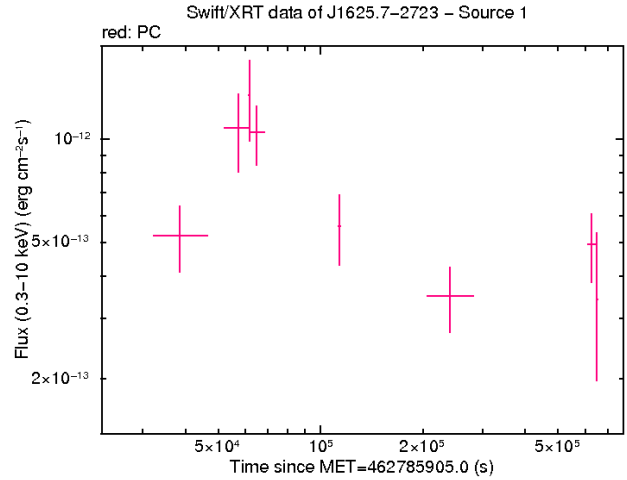
No optical or X-ray counterparts associated to the neutrino triggers have been found in the analyzed observations and upper limits on transient source magnitudes have been derived. Using archival optical and X-ray GRB afterglow observations we calculated the probability to reject the gamma-ray burst origin hypothesis has been computed for each alert. The comparison between our upper limits and the archival light curves are illustrated in Fig. 2.15a for the optical observations and similarly in Fig. 2.15b for the X-ray follow-up. Compared to detected GRB afterglow light curves, the very rapid response time of the full TAToO system has allowed to place stringent constraints on the GRB origin of individual neutrinos. Even though the response time of the XRT follow-up is larger, the early observations of the neutrino alerts have allowed to exclude the GRB origin for the followed neutrinos with a high confidence level as well. Further details can be found in the corresponding publication [41].

2.6.2 ANT150901A: a X-ray transient detected following a TAToO neutrino alert

One noticeable alert emitted by the TAToO system happened on 2015-09-01. After the detection of a very high-energy energy neutrino event, an alert has been distributed among the optical follow-up partners and the Swift X-ray satellite. Swift-XRT observations took place the same and the following day. The automatic data analysis pipeline, verified by the multi-messenger ToO advocate (P.A. Evans, U. Leicester), detected a strong and variable X-ray source within the error box of the ANTARES neutrino event. The X-ray light-curve is shown in Fig. 2.16b. This detection was announced to the community via an Astronomer’s Telegram [76]. This announcement, the first emit-



(a) optical



(b) X-ray light-curve

Figure 2.16: Follow-up of the TAToO alert ANT150901A. Left plot: Optical image of the region around the ANTARES-TAToO alert showing the reconstructed neutrino direction, the four initial Swift-XRT pointings and the location of the newly detected X-ray source (image from MASTER, ATEL#8000). Right plot: Light-curve of the previously unknown X-ray source detected after an high-energy neutrino alert from ANTARES (image from Swift-XRT, ATEL#7987).

ted by ANTARES/TAToO, triggered an impressive follow-up campaign covering the full wavelength range from radio (e.g. Jansky VLA [88]), optical (e.g. SALT [75], NOT [73]) up to VHE gamma-rays (MAGIC [121] and H.E.S.S. [148], see also detailed discussion in Sec. 3.3.3). Combining the obtained results allowed finally to conclude that the observed X-ray flare originated in a young star (e.g. E. Mamajek, ATel #8124) and seems thus unrelated to the high-energy neutrino observed by ANTARES.

Even though the scientific result might seem disappointing, the excitement caused by the ANTARES alert in the astrophysical community thanks to its public announcement led to an increased awareness within the ANTARES collaboration. It allowed for example to implement well defined rules on how to rapidly announce interesting observations to the wider community. Since then, also several follow-up observations of alerts emitted by other observatories could be announced in this way. These include ANTARES observations following the detection of high-energy neutrinos by Ice-Cube [54] and finally led to the participation of ANTARES in the global multi-observatory follow-up efforts of alerts by gravitational wave observatories (e.g. [52]).

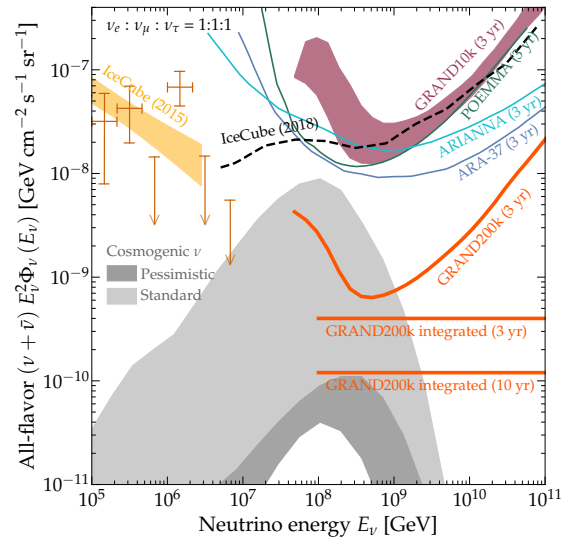
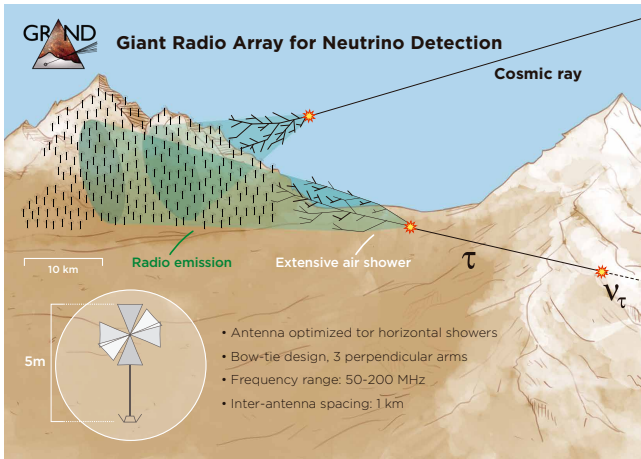


Figure 2.17: Left: Schematic view of the technique used in the GRAND observatory to detect cosmogenic neutrinos. Right: Sensitivity of current and proposed observatories compared to predictions of the cosmogenic neutrino flux. Figures from [49].

2.7 Future prospects of neutrino astronomy

Neutrino astronomy is technically challenging but a crucial ingredient in the search for the sources of high and ultra-high energy cosmic rays. After more than a decade of observations by ANTARES, and 8 years (at the end of 2018) of observations by IceCube, a cubic kilometer sized instrument, no excess is accumulating in the neutrino skymaps [9, 53]. A simplifying and rough conclusion would therefore be that current neutrino telescopes are not sensitive enough to detect neutrino (and thus CR) sources. Technological breakthroughs that would allow to instrument significantly larger volumes (while keeping the density of the instrumentation high to allow for \approx TeV energy thresholds) and thus provide a sizable chance to detect neutrino point-sources with reasonable scales for both cost and construction efforts are not within sight at the moment. Although projects like IceCube-Gen2 [10] and the full-sized KM3NeT-ARCA [56] detector would provide about an order of magnitude improvement over existing datasets, funding scenarios and the necessary installation time seem to push these next-generation observatories more and more towards the end of the coming decade.

In this context, radio detection of neutrino induced air showers appears as interesting option. Experiments like ARA [48], ARIANNA [57] and ANITA [85] use the Antarctic ice-sheet at interaction medium and search for radio pulse by τ -lepton induced air showers. Typically they are sensitive to neutrinos in the EeV (10^{18} eV) energy range (cf. Fig. 2.17). While the main goal is the detection of the cosmogenic neutrinos that are created in the interaction of UHECRs with photons of the Cosmic Microwave Background, these observatories have also some sensitivity to the high-energy end of the flux detected by IceCube [3]. One of the most ambitious projects in this energy range is the Giant Radio Array for Neutrino Detection (GRAND, [49]). Following a staged approach, radio antenna arrays of increasing size are foreseen to be installed in radio quiet region(s) in China and potentially around the globe. An illustration of the detection technique, which is mainly sensitive to Earth skimming air showers induced by ultra-high energy neutrinos, is given in Fig. 2.17. In its final configuration GRAND will comprise 200.000 radio antennas spread over 200.000 km^2 in one or several sites. In addition to its search for cosmogenic neutrinos, GRAND will also provide highly significant measurements in domains ranging from Fast Radio Bursts to large statistics observations

of UHECRs. A white paper describing the physics potential as well as the status and plans for the necessary technical developments has been published recently [49].

2.7.1 Personal comments on neutrino telescopes and their multi-messenger links

While no neutrino point source has been identified in the data of the large neutrino telescopes so far, the detection of the astrophysical diffuse flux by IceCube [3] provides some indications about the relevant fluxes and opens the way for other, complementary and in my personal view very promising analyses: searches for real-time multi-messenger coincidences. As discussed above, I had the chance to contribute to this field during its very infancy. The TAToO program of the ANTARES neutrino telescope [42], able to emit alerts to the astronomical community within seconds, and the very similar program operated by the IceCube collaboration [7] allow to obtain complementary informations across the full electromagnetic spectrum and thus increase the sensitivity of the searches. In these configurations, the neutrino detection and subsequent alert emission is certainly the main input and trigger for the EM observations and analyses. On the other hand, the bulk of the data is being collected by external partners operating telescopes across the electromagnetic spectrum. Due to the accessible energy range, the closest link to high-energy neutrinos is certainly the high-energy gamma-ray domain. This is main reason of my increasing involvement over the last years in instruments observing in this domain. The detection of a blazar flaring in VHE gamma-rays in coincidence with one or more high-energy neutrinos is illustrating the potential of this time domain multi-messenger approach (cf. Sec. 3.3.4).

While my involvement in ANTARES allowed me to obtain a detailed understanding of the advantages but also the systematic uncertainties of neutrino detectors, the extension of my research into the multi-messenger field via searches for high-energy gamma-ray counterparts to neutrino events allowed to significantly broaden my perspective and (in my opinion) increased the chances of success. Driven by the scientific opportunities and prospects, the extension of my work towards high-energy gamma-ray observations obviously came at the cost of a reduction of my direct involvement in neutrino telescopes. While I was able to keep my activities within the ANTARES collaboration at somewhat relevant levels, the high-energy neutrino group at IRFU internally reflected and reviewed the prospects of the next-generation observatory KM3NeT for several months in 2011/2012. In a joint decision, the group decided to not participate in the next phases of preparation and construction of KM3NeT, i.e. beyond the EU funded Preparatory Phase which ended in spring 2012. This decision had wide-ranging consequences all members of the group at IRFU as well as the KM3NeT project itself. The reflection period leading up to the decision allowed me personally to envision a direct implication in high-energy gamma ray experiments and, drawing from the experience with ANTARES, multi-wavelength and multi-messenger astronomy. In hindsight, this was one of the turning points of my career and I have never regretted the taken decision ever since. A summary of my contributions to VHE gamma-ray astronomy will be given in the following sections.

3

High-energy gamma rays

3.1 Introduction

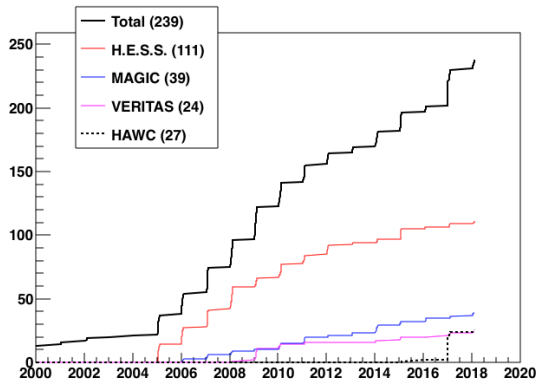
Astronomy with high-energy gamma rays is one of the most recent but also one of the fastest growing domains in astronomy. Less than 30 years after the first detection of an astrophysical high-energy gamma-ray source, the Crab nebula in 1989 by the Whipple telescope [171], there are now more than 200 gamma-ray emitting sources known in the sky. The rapid increase (cf. Fig. 3.1a) can clearly be related to the construction and successful operation of the current generation of observatories exploiting the Imaging Air Cherenkov technique: H.E.S.S., MAGIC and VERITAS. Very recently significant contributions have also been brought about by HAWC, the second generation of high-altitude water Cherenkov observatories.

In the following I outline my major activities in the domain of gamma-ray astronomy. I'll focus on the searches for transient phenomena with multi-messenger and multi-wavelength links, a domain I'll briefly introduce in Sec. 3.2.

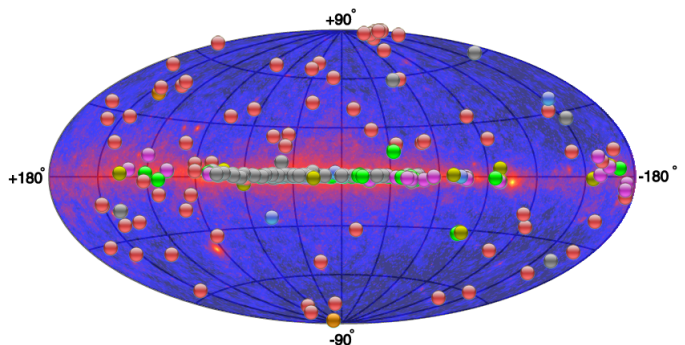
In addition to this main field of research I was able to contribute to several complementary analyses. For example, in 2016 I led studies of the systematic uncertainties of the IACT technique related to seasonal changes of the molecular atmospheric profile. While we did not find significant influence of the seasonal fluctuations in the density overburden in which the air showers develop, to the gamma-ray measurements, we were able to derive new and time dependent parameterizations of the atmosphere above the H.E.S.S. observatory. Details have been presented by M. Seglar-Arroyo as results of her Master thesis under my supervision [158].

Additional projects that I won't be able to detail here included the search for VHE gamma-ray emission from Galactic binaries and especially microquasars. I presented the analysis of H.E.S.S. and RXTE observations on the microquasars GRS 1915+105, Circinus X-1, and V4641 Sgr at conferences (e.g. [147]). The corresponding publication [25] is also available in the Appendix B.

Moving from microquasars to full-fledged, extragalactic blazars, I became an active member of the H.E.S.S. core team on AGN Target of Opportunity (ToO) observations and recently presented a summary report on activities of this field jointly with M. Seglar-Arroyo (PhD student under my supervision) [141]. I currently also lead analyses of several H.E.S.S. observations on extragalactic objects like Mrk 421 [114] and am involved in the joint publication of the VHE detection of PKS 1749+096 by MAGIC [119] and H.E.S.S. [141].



(a) Gamma-ray history



(b) Gamma-ray sky

Figure 3.1: Left plot: Historical evolution of detected VHE gamma-ray sources over the last years. Right plot: Sky map of GeV gamma rays detected by Fermi-LAT (background) and TeV gamma ray sources (markers) detected by ground-based instruments. Source: TeVCat [168].

3.2 Multi-messenger connections

Gamma-ray astronomy in the GeV-TeV range is able to provide a wealth of information on astrophysical sources. Observations of nearby, i.e. Galactic, sources allow to study details in the source morphology, the large accessible energy range allows to derive high precision spectra and the high sensitivity allows following the time evolution of the emission.

On the other hand, the detection of gamma-rays is usually not sufficient proof for the presence of accelerated hadronic CRs as gamma-ray radiation can also be induced by accelerated electrons (via Bremsstrahlung or inverse Compton scattering of low energy photons). In fact, the emission of most TeV gamma-ray sources can be described well by both leptonic (accelerating mainly electrons) as well as hadronic (accelerating predominantly hadronic CRs) models. Attempts to distinguish between these competing explanations are usually based on the spectral shape of the GeV-TeV emission, which makes these attempts dependent on the assumptions and parameters used in the phenomenological models. One can mention two counter-examples which show the presence of accelerated hadronic particles: the discovery of the pion decay signature (*pion-bump*) in high energy gamma rays from two supernova remnants by Fermi [38] and the inference of the existence of a powerful accelerator emitting protons at PeV energies in the Galactic center from H.E.S.S. observations [35]. For many other cases, multi-messenger information could provide the necessary additional information (i.e. the *smoking gun*) on the origin of the detected radiation.

3.2.1 High-energy neutrinos

The most obvious messenger for these searches are high-energy ($> \text{GeV}$) neutrinos. Their emission from astrophysical sources can be directly attributed to hadronic interactions of high-energy protons or nuclei with ambient material (pp interactions, [101]) or radiation fields ($p-\gamma$, [100]). In these collisions, both neutrinos and gamma rays are produced in the decay of mesons via:

$$\begin{aligned}
p + p/\gamma &\rightarrow X + \pi^0 \rightarrow \gamma\gamma \\
X + \pi^+ &\rightarrow \mu^+ + \nu_\mu \\
&\rightarrow \mu^+ \rightarrow e^+ + \nu_e + \bar{\nu}_\mu
\end{aligned}
\tag{3.1}$$

The $\nu_e : \nu_\mu : \nu_\tau$ neutrino flavor ratio of 1:2:0 at emission oscillates to equipartition (1:1:1) as neutrinos propagate over astrophysical distances. The spectral production rates of neutrinos and gamma rays are related by

$$\frac{1}{3} \sum E_\nu^2 \frac{dN_\nu}{dE_\nu} \approx \frac{K_\pi}{4} E_\gamma^2 \frac{dN_\gamma}{dE_\gamma}
\tag{3.2}$$

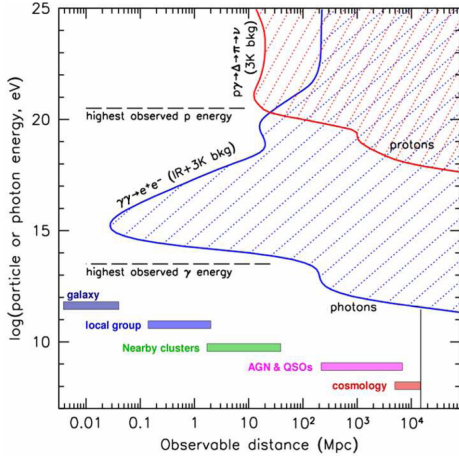
where $K_\pi = 1(2)$ for $p\gamma$ (pp) interactions and ν denotes the neutrino flavor. Due to their low interaction cross-sections, neutrinos easily escape their production sites and then propagate nearly undisturbed over cosmological distances. On the other hand, the flux of gamma rays detected at Earth will depend on the VHE opacity of the source and the propagation medium. This limitation of the gamma-ray propagation distance is induced through interactions with intergalactic radiation fields (extragalactic background light, EBL). As can be seen in Fig. 3.2a the accessible source distance gets reduced rapidly above 10 TeV (see Sec. 3.3.1 for details). It is therefore clear that a search for potentially very distant sources requires an instrument that is most sensitive in the crucial energy range between about 100GeV and 10TeV. The upgraded array of Cherenkov telescopes H.E.S.S.-II provides just this. Interestingly one can note that similar interactions also limit the horizon of the highest-energy cosmic rays to the approximate same range of about 100Mpc.

On the other hand, the strong time variability observed in many sources offers an additional handle to improve our understanding of the underlying mechanisms and establish causal connections between different observations. Extra-galactic sources like AGNs show variability at all timescales accessible by current instruments. Extreme cases like gamma ray bursts vary in seconds to minutes. I'll discuss in the following my attempts at making these timescale accessible for multi-messenger analyses. Again, the fundamental idea is that for example the observation of high-energy neutrinos in spatial and temporal coincidence with transient gamma-ray emission would provide the smoking gun of hadronic processes being responsible for both emissions (cf. Fig. 1.3).

In summary, high-energy gamma rays have several drawbacks that (with few exceptions) until now prevent the clear identification of hadronic acceleration to high energies taking place in astrophysical objects (confusion between leptonic and hadronic emission, limited horizon). On the other hand, gamma rays are comparably easy to detect with current and future instruments like H.E.S.S. and CTA and therefore remain one of the cornerstones for the search of cosmic ray accelerators.

With the successful commissioning of the second phase of the H.E.S.S. experiment, the detection of an astrophysical neutrino flux by IceCube and the beginning of data taking of gravitational wave interferometers Virgo and Ligo in their advanced configuration, the last years were the perfect time to introduce a fundamentally new way of performing these searches: multi-messenger astronomy in real-time. The new H.E.S.S.-II 28m telescope ("CT5") is the largest Cherenkov telescope in the world and provides the lowest energy threshold of ground based gamma-ray detectors worldwide (≈ 30 GeV). Another major goal for this new phase of H.E.S.S. was the reduction of the response time of the system in order to increase the capabilities for the detection of transient phenomena. As discussed in Sec. 3.2.3, this goal has been achieved both on the hardware level of the instrument and on the software and DAQ side.

The H.E.S.S. program of H.E.S.S. observations related to observations of high-energy neutrinos is described in Sec. 3.3.



(a) Gamma-ray horizon



(b) The H.E.S.S. observatory

Figure 3.2: Left plot: The limitations on the accessible distance for high-energy gamma rays (and ultra-high energy cosmic rays) induced by interactions with extragalactic radiation fields. From [90]. Right plot: The five telescopes of the H.E.S.S. observatory in Namibia (photo from C. Medina).

3.2.2 Gravitational waves

In the framework of General Relativity space-time can be considered a fabric that bends or curves under the gravitational influence of masses. In the absence of gravity (and thus mass), space-time is flat and its curvature g can be characterised by the four-dimensional Minkowski metric $\eta_{\mu\nu}$:

$$\eta = \begin{bmatrix} -1 & 0 & 0 & 0 \\ 0 & 1 & 0 & 0 \\ 0 & 0 & 1 & 0 \\ 0 & 0 & 0 & 1 \end{bmatrix} \quad (3.3)$$

A weak gravitational field can be considered as a small 'perturbation' to this flat space, the curvature then becomes:

$$g_{\mu\nu} = \eta_{\mu\nu} + h_{\mu\nu} \quad \text{with} \quad |h_{\mu\nu}| \ll 1 \quad (3.4)$$

The relationship between the metric tensor g and the energy-momentum tensor T is defined by the Einstein Field Equations:

$$R_{\mu\nu} - \frac{1}{2}Rg_{\mu\nu} = 8\pi GT^{\mu\nu} \quad (3.5)$$

The energy-momentum tensor T is a measure of the presence of matter and energy in the local space. $R_{\mu\nu}$ is the Ricci tensor, and R is the scalar curvature. Given that the gravitational perturbation can be assumed to be small, one can expand Einstein's field equations in h . After linearization, one can find a relation between $h_{\mu\nu}$ and the energy-momentum tensor T (see [66] for a detailed derivation):

$$\square \bar{h}_{\mu\nu} = -16\pi GT^{\mu\nu} \quad (3.6)$$

In the limit of flat space-time as specified initially, where the perturbation is small and no significant mass is present, $T^{\mu\nu} \approx 0$. The relation above therefore becomes a wave equation:

$$\square \bar{h}_{\mu\nu} = 0 \quad (3.7)$$

Gravitational waves are thus created by moving masses, very similar to electromagnetic waves being created by moving charges. On the other hand, and in contrast to electromagnetism, mass

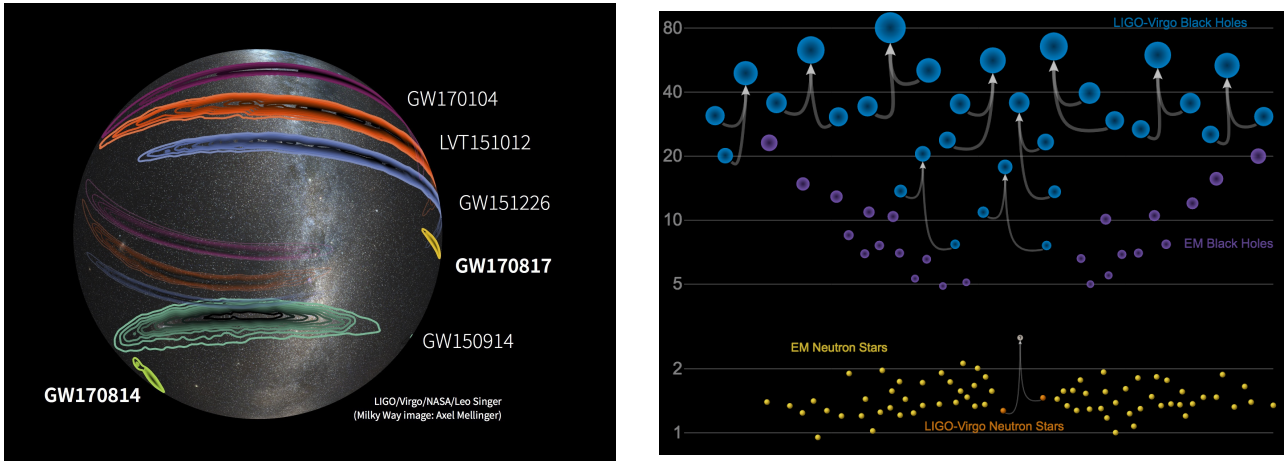


Figure 3.3: Left: Sky localizations of gravitational-wave signals detected by LIGO beginning in 2015 (GW150914, LVT151012, GW151226, GW170104), and, more recently, by the LIGO-Virgo network (GW170814, GW170817). Credits: LIGO/Virgo/NASA/L.Singer (Milky Way image: A. Mellinger). Right: Masses of stellar remnants as measured by gravitational wave observations during the first two runs of Advanced Ligo and Advanced Virgo (arrows) in comparison with previous, electromagnetic observations (markers). Image credits: LIGO-Virgo/Frank Elavsky/Northwestern University

does not come in different signs or ‘charges’. Therefore, gravitational waves can only be produced in asymmetric accelerations of masses. At the lowest order these are quadrupole moments found for example in in-spiralling binary systems or asymmetric mass ejections during supernova explosions. These violent phenomena are predicted to show emission across the full electromagnetic spectrum, motivating the search for counterparts. A prominent example for these scenarios are mergers of binary neutron star systems, that have theoretically been linked to (short) gamma-ray bursts. As GRBs are known emitters of high-energy gamma rays [37], one can expect a detection of these events at high energies accessible by IACTs. These expectations have very recently been fulfilled by the detection of GRB 190114A by the MAGIC observatory [122]. The large effective area of IACTs like MAGIC or H.E.S.S. will enable detailed measurements of light-curves and energy spectra allowing for studies of the underlying particle acceleration mechanism and thus provide significant insight into the NS-NS/GRB mechanisms. In general gravitational wave events offer a unique and novel way to observe the high-energy universe as they provide access to the pre-merger phase of binary coalescence events incl. detailed information about the merging system (e.g. the individual masses and spins of the objects, the inclination of the system, etc.). Binary neutron star mergers have also been linked to kilonovae, a type of a transient event, usually 10-100 times less bright than a classic supernova [118]. This afterglow emission is powered by the radioactive decay of heavy nuclei produced via the so-called r-process, and thus able to explain large portions of elements heavier than iron observed in the Milky Way [95]. These events therefore promised very rich multi-wavelength and multi-messenger emissions.

Detection of gravitational waves

Gravitational waves are modulations of space-time and can be detected as minute distance changes. The waves are polarized, i.e. they compress space in one direction while stretching it in the perpendicular direction. The scale of these changes are tiny: even very massive systems like two orbiting black holes that are about to merge into one, will only produce displacements on the order of 10^{-18} meters, about 1000 times smaller than the diameter of a proton.

Current state-of-the-art gravitational wave detectors are L-shaped and measure the relative lengths

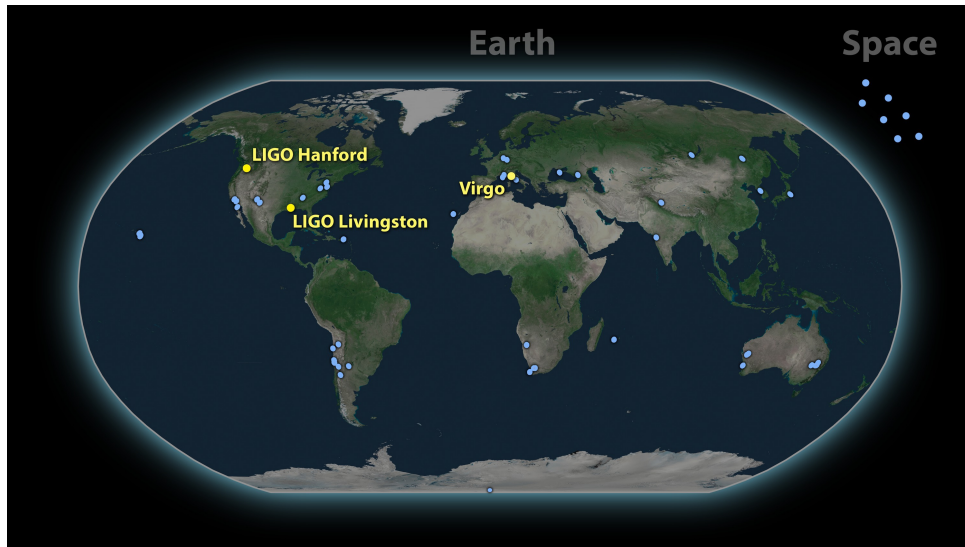


Figure 3.4: Observatories that participated in the follow-up observations of the first binary neutron star merger event, GW170817. Image credits: LIGO-Virgo

of the arms using interferometry. There are three such interferometers in operation at the moment: two in the United States, collectively called LIGO (Laser Interferometer Gravitational-wave Observatory, [20]) and the Virgo interferometer in Italy [36]. Detection of consistent signals by multiple interferometers is necessary to suppress candidate signals that are caused by local noise sources and to locate the sources of the gravitational wave. As gravitational waves travel at finite speed (the speed of light [107]), the arrival times of the waves at the different detectors will be typically separated by about 10 – 30 milliseconds. Using these time differences for triangulation and combining them with the known sensitivity pattern of the individual detectors allows us to localize the origin of the waves. Depending on the signal strength, the associated uncertainties range from tens to several hundred square degrees (cf. Fig.3.3). The efficient scheduling of follow-up observations covering these sizable regions of the sky is thus one of the main challenges and has been a focus of my work (cf. Sec. 3.5.1).

First observations of gravitational waves

After several decades of continuous upgrades and improvements of the interferometers, the era of astronomy and astrophysics with gravitational waves has finally begun on September 14, 2015 at 09:50:45 UTC. At that time the two interferometers of the Advanced LIGO observatory recorded the first direct signal of a gravitational wave [14]. The recorded signal matched expectations derived from general relativity of the inspiral and merger of a binary black hole (BBH) system. The coalescence was reconstructed at a luminosity distance of 410^{+160}_{-180} Mpc. In the source frame, the initial black hole masses are $36^{+5}_{-4} M_{\odot}$ and $29^{+4}_{-4} M_{\odot}$. This first detection of a binary black hole merger demonstrated the existence of binary stellar-mass black hole system and opened the window to gravitational wave multi-messenger astronomy.

After this extremely exciting start of the physics data taking of the LIGO interferometers in their advanced configuration, both detectors have been operated from September 2015 until January 2016 (run O1), allowing for the detection of a second confirmed BBH merger (GW151226 [13]) as well as another, very likely event (LVT151012 [12]). After further upgrades, LIGO resumed data taking in November 2016. It was joined by the Virgo interferometer in August 2017 about one month before

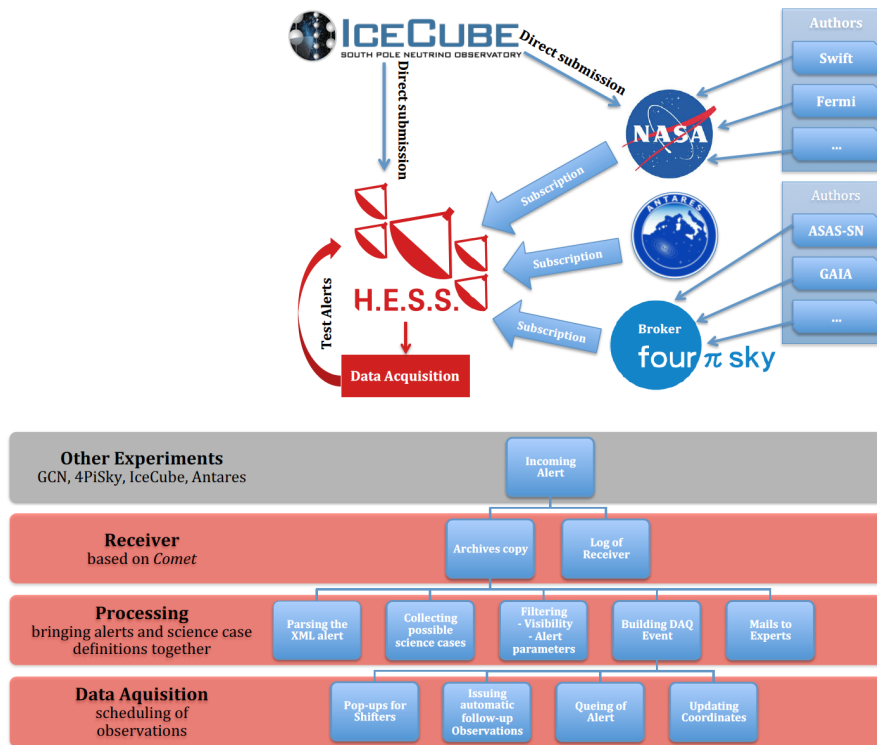


Figure 3.5: Schematic overview of the H.E.S.S. online alert system and its connections to multi-wavelength and multi-messenger observatories (from [92]).

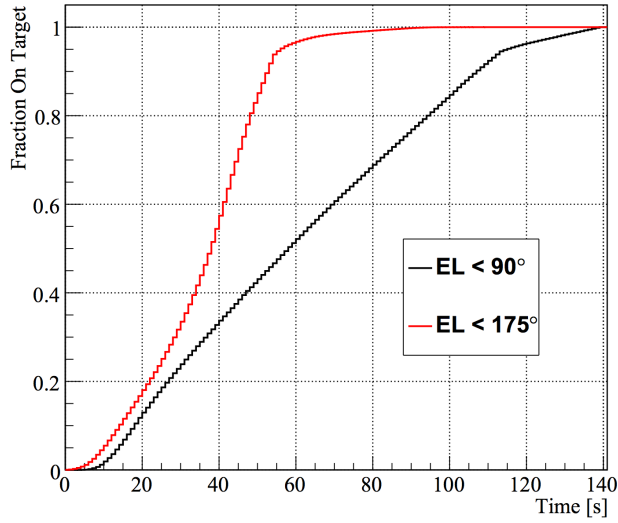
the end of this second physics run (O2). During this run 3 additional BBH mergers (GW170104, GW170608 and GW170814) and the first binary neutron star merger (GW170817) could be detected. An overview over the observed events is given in Fig. 3.3 and a summary of detected GW events is available in [19].

Gravitational wave follow-up observations

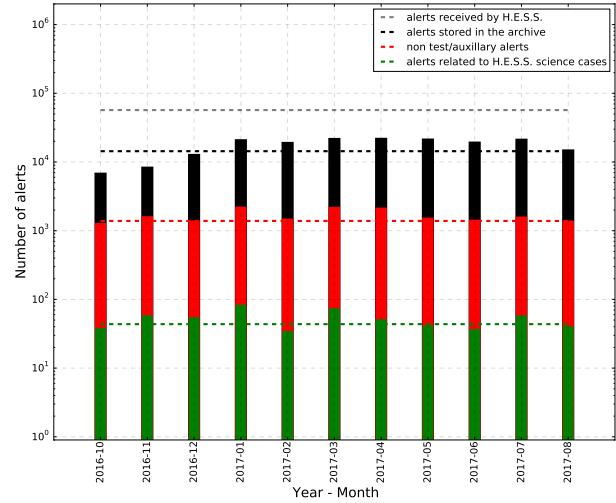
Accompanying the GW observations a global effort tried to identify electromagnetic radiation (as well as high-energy neutrinos) associated to these events. Using data from two detectors, the 90 % uncertainty regions spanned up to several thousand square degrees during O1. At least three observatories were necessary to achieve a localisations to better than hundred square degrees. These conditions were fulfilled only starting August 2017 when the Advanced VIRGO observatory joined the two LIGO interferometers during run O2. The large uncertainty areas, combined with delays in the alert emission induced by the reconstruction and validation of the GW data are therefore the main difficulty for follow-up observations of GW with pointing instruments like IACTs.

Since the beginning of the data taking of the gravitational wave interferometers in their advanced configuration at the end of 2015, all IACT collaborations were part of the electromagnetic follow-up group. During O1 and O2, this group comprised about 70 observatories around the world searching for electromagnetic signals related to GWs. During this early phase of GW searches (i.e. during the LIGO/Virgo runs O1 + O2), IACT follow-up started with individual, exploratory observations of BBH mergers (e.g. observations of the binary black hole merger GW151226 [13] by MAGIC [70] and the follow-up of GW170104 [15] with VERITAS*). During the run O2 these observations evolved

*<https://gcn.gsfc.nasa.gov/gcn3/21153.gcn3>



(a) Slewing speed of H.E.S.S.-II



(b) The H.E.S.S. alert system

Figure 3.6: Left plot: Slewing speed of the H.E.S.S. 28m telescope CT5, illustrated by the time required to arrive on target to a random position on the sky shown with (red line) and without (black line) reverse observation (from [91]). Right plot: The performance and longterm stability of the H.E.S.S. VoAlert system illustrated by the number of alerts processes by the alert receiver (from [93]).

into complete scans of the uncertainty regions (e.g. the first GW event detected by all three interferometers: the binary black hole merger GW170814 [16] followed up by H.E.S.S. (cf. Sec. 3.5.2). These preparations came to fruition during the rapid and deep follow-up of GW170817, the first ever detected merging of two neutron stars (cf. Sec. 3.5.3).

H.E.S.S. participated and, for many aspects led, the VHE follow-up observations of GWs over the last years. After coordinating the successful signature of an MoU between the LIGO/Virgo Scientific Collaboration (LVC) and the H.E.S.S. collaboration, I started to lead the GW follow-up program with H.E.S.S. in 2014. A summary of first results is given in Sec. 3.5.

3.2.3 The H.E.S.S. multi-messenger alert system

With the commissioning of CT5, the 28m telescope in the center of the H.E.S.S. array, the observatory entered a new phase called H.E.S.S.-II. Designed from the start as transient detection machine, the new telescope allows to reach every point on the sky within less than one minute (cf. Fig. 3.6a). This delay can further be reduced by enabling reverse operations during which the telescope is able to slew through zenith instead of mainly azimuthal rotation. As this operation causes some stress to the mechanical systems and temporarily increases the point-spread function, this mode is reserved for extremely time critical observation, especially prompt follow-up observations of GRBs.

The installation of the fifth telescope was accompanied by significant efforts to optimize the alert reception and subsequent reaction scheme. The implemented multi-purpose alert system is now connecting the H.E.S.S. observatory to a large variety of observatories worldwide, covering the full wavelength and multi-messenger domain and thus allowing for an extensive multi-messenger program. A schematic view of the alert system is given in Fig. 3.5, further details can be found in [92]. In my role as multi-messenger contact of the H.E.S.S. collaboration I accompanied these development with the necessary political and administrative support, i.e. working towards setting up agreements

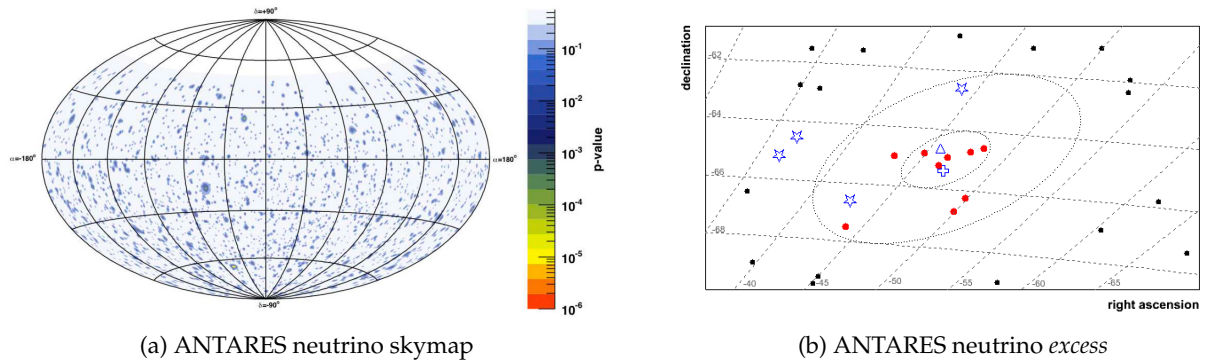


Figure 3.7: Left plot: Skymap in equatorial coordinates showing the pre-trial p-values obtained in the all-sky search for point-like clusters. Figure from [135]. Right plot: Zoom in the location of the most signal like cluster found in the full-sky search. As indicated by the red circles, 5 (9) neutrino candidates are found within 1 (3) degrees of the cluster center as expected for a point-like source. Gamma-ray sources given in the 2nd Fermi-LAT catalogue are indicated by blue stars, PKS 2047-655 is denoted by the blue cross and AC 103 by the blue triangle. Figure from [149].

between the different collaborations to share their confidential data with H.E.S.S. to allow for follow-up observations. For example a Memorandum of Understanding (MoU) has been signed between the H.E.S.S. and IceCube collaborations in 2015. In the following a dedicated real-time link between the IceCube computing facility in Wisconsin/Madison and the H.E.S.S. alert system could be installed. A similar MoU has been signed and a datalink has been established with the ANTARES neutrino telescope, the radio telescopes Parkes and UTMOST (see Sec. 3.4) and the gravitational wave observatories VIRGO and LIGO (see Sec. 3.5). The H.E.S.S. VoAlert system has been running stable since mid 2016. A snapshot of the alerts treated constantly from the various connected external observatories but also test alerts used to monitor the performance of the system is shown in Fig. 3.6b.

3.3 Connecting VHE gamma-rays with high-energy neutrinos

3.3.1 H.E.S.S. follow-up of an ANTARES neutrino excess

Observations with H.E.S.S. are organized via yearly proposal calls that are evaluated by an Observation Committee. The committee considers *external proposals from outside H.E.S.S. to the extent that they add new aspects beyond the physics program [...] discussed and documented by the H.E.S.S. physics working groups*[†]. I used this opportunity in 2012 to propose the first H.E.S.S. multi-messenger observations: searches for a VHE gamma-ray counterpart of a slight excess seen in a search for point-like neutrino sources with the ANTARES neutrino telescope [135].

Applying an unbinned likelihood method to the data recorded by ANTARES between beginning of 2007 and end of 2010 (corresponding to a total lifetime of 813 days and 3058 selected events, see also Sec. 2.4.4) the most significant cluster of events was found at $\alpha, \delta = (-46.5^\circ, -65.0^\circ)$. As can be seen in the right plot of Fig. 3.7b, 9 events have been found within a search cone of 3 degrees. For this cluster the likelihood fit assigns 5.1 as signal events. Their directions are compatible with the signature of a point-like source. Pseudo-experiments taking into account systematic uncertainties of the angular resolution and the acceptance of the detector were used to determine the trial factor corrected p-value of 2.6% (i.e. 2.2σ using the two-sided convention). While being compatible with a

[†]<https://www.mpi-hd.mpg.de/hfm/HESS/pages/home/proposals/>

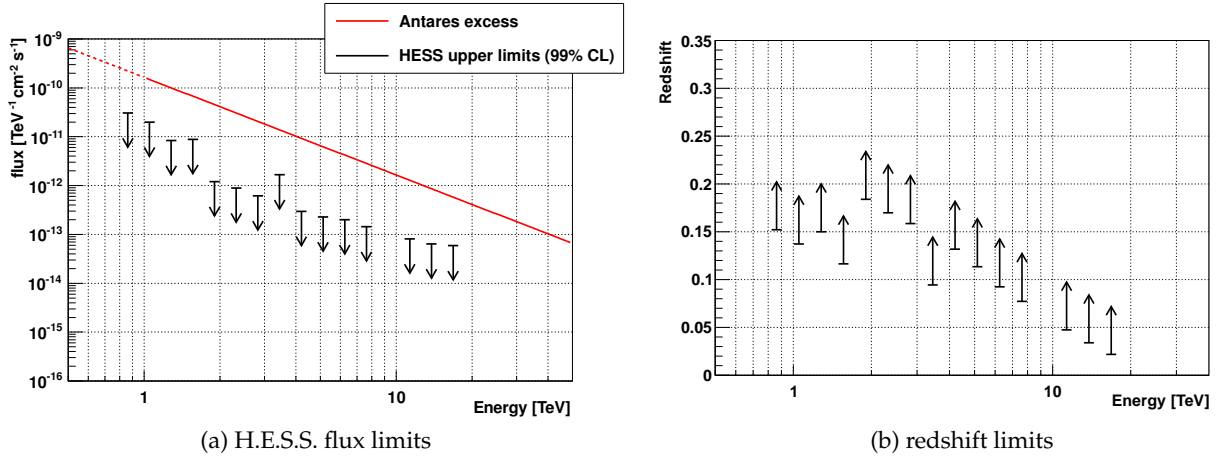


Figure 3.8: Left plot: VHE gamma-ray flux limits Φ_{UL} at 99 % CL derived from the H.E.S.S. observations (black arrows) compared to predictions based on the ANTARES neutrino excess Φ_{γ} (red line). Right plot: 99 % C.L. lower limits on the distance of the potential neutrino and gamma-ray source derived by matching the ANTARES flux with the upper limits obtained with H.E.S.S. Figures from [149].

fluctuation of the atmospheric background (and considered as such by the ANTARES collaboration), the accumulation represented the most significant localized excess in the high energy neutrino sky at that time. I therefore proposed to observe the region with the H.E.S.S. system to search for associated gamma-ray emission.

The observations were granted and the region around the neutrino excess was observed by H.E.S.S. in its original configuration of four telescopes for almost 2h in November 2012. The obtained H.E.S.S. observations do not reveal significant VHE gamma-ray emission. The same holds for a complementary analysis of 4 years of data recorded with the Fermi-LAT instrument. Given the absence of a significant VHE gamma-ray signal in the observed region upper limits on the gamma-ray flux could be derived. The relatively high zenith angle of 45 deg of the observations yielded an energy threshold of around 800 GeV. The obtained flux limits Φ_{UL} have been calculated assuming a generic E^{-2} energy spectrum and following the method introduced by Feldman & Cousins [80]. They are shown as black arrows in Fig. 3.8a. The red line shows the flux expectation from the neutrino candidate events that has been calculated using the observed number of neutrino events and converting the neutrino flux of $\Phi_{\nu} \approx 5.5 \times 10^{-11} \text{ TeV}^{-1} \text{ cm}^{-2} \text{ s}^{-1}$ into an associated flux of gamma rays. This conversion relies on Monte Carlo simulations of the hadronic interactions connecting neutrino and gamma ray fluxes via the decay of charge and neutral pions within or close to a generic hadronic accelerator. Following the assumptions and considerations given in [94], the gamma ray flux produced by the source that produced the ANTARES neutrino signal can be estimated to about $\Phi_{\gamma} \approx 1.4 \times 10^{-10} \text{ TeV}^{-1} \text{ cm}^{-2} \text{ s}^{-1}$ at 1 TeV.

The upper limits derived from the H.E.S.S. observations seem to clearly rule out a source producing both the high-energy neutrino *excess* as well as high-energy gamma rays. But this conclusion only holds for very nearby sources: high energy gamma-ray photons are absorbed by pair production on the extra-galactic background light (EBL, cf. Fig. 3.2a). This process can be described by $\Phi_{\text{obs}} = \Phi_{\text{source}} \times e^{-\tau}$, where the optical depth τ is a function of the energy E_{γ} and the redshift of the source z_s . The photon density $n_z(\epsilon)$ as function of the photon energy ϵ can be taken from EBL models (e.g. [82]). For this analysis the original model has been scaled by $k = 1.27$ to match the H.E.S.S.

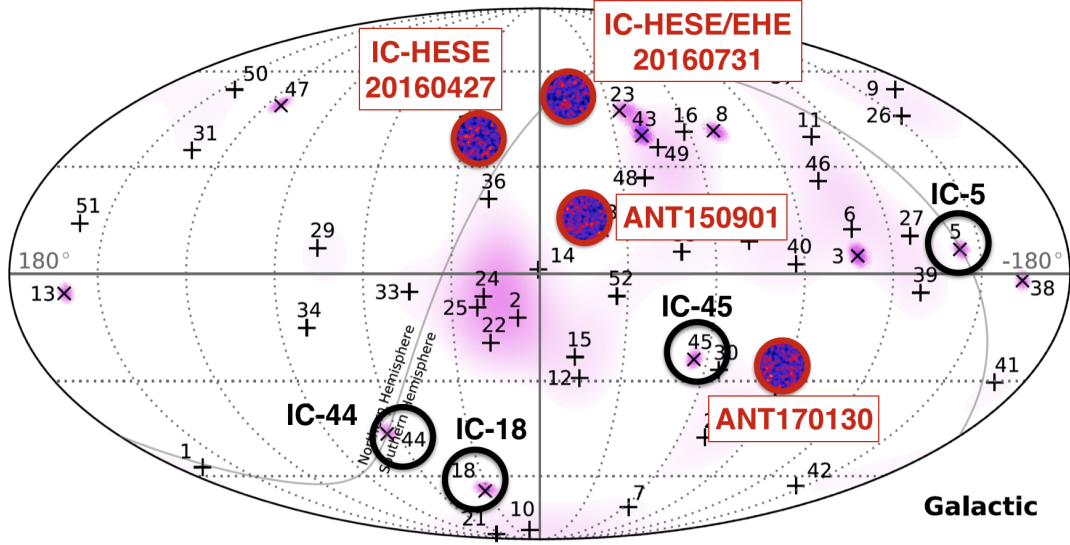


Figure 3.9: Summary of H.E.S.S. observations of high-energy neutrinos. The magenta background and the numbers denote the arrival directions of neutrino events recorded by IceCube (from [103]). The black circles denote archival H.E.S.S. observations searching for continuous emission, whereas the red circles denote H.E.S.S. follow-up observations of neutrino alerts, i.e. searches for transient phenomena. Modified from [152].

measurements in [34]. τ can be written as:

$$\tau(E_\gamma, z_s) = \int_0^{z_s} dl(z) \int_{\epsilon_0}^{\infty} d\epsilon \sigma_{\gamma\gamma}(E_\gamma(z+1), \epsilon) \times k \times n_z(\epsilon)$$

For sufficiently distant sources, i.e. sufficiently large optical depths, the expected gamma-ray flux Φ_γ will get absorbed and will therefore become compatible with the upper limits Φ_{UL} derived from the H.E.S.S. measurements. We exploited this possibility to derive lower limits on the distance to the putative neutrino and gamma-ray sources by solving the following equation for the redshift z_{lim} for all energy bins i :

$$\tau(E_i, z_{lim}) = -\ln \frac{\Phi_{UL,i}}{\Phi_\gamma}$$

The resulting 99 % C.L. limits are shown in Fig. 3.8b. More details of the analyses are available in [149].

Although no gamma-ray coincident with the neutrino excess could be detected, the obtained data and subsequent analysis clearly illustrate the potential of the multi-messenger technique: with less than 2h of H.E.S.S. observations we could (within the caveats mentioned above) conclude that the ANTARES excess was likely due to a background fluctuation and not an astrophysical source. The next step was therefore quite natural: set up a multi-messenger program within the H.E.S.S. collaboration to search for gamma-ray emission related to other high-energy neutrinos.

Subsequent analysis of additional data taken by the ANTARES neutrino telescope did not confirm the early hotspot. To this date, and as discussed above, the neutrino sky remains fully compatible with an isotropic distribution of the arrival directions [53].

3.3.2 IceCube high-energy neutrinos

When IceCube announced the discovery of a high-energy excess of events above the atmospheric neutrino background in 2013 [3], the publication also contained a list with the details of the observed

28 “high-energy starting events” (HESE). For the first time, a list of arrival directions of neutrino events that are, with a reasonably high-probability of around 50 %, of astrophysical origin became available. The sample was composed of events with two different signatures: shower or cascade-like events induced by neutral current interactions and charged current interactions of ν_e and ν_τ as well as track-like events containing a muon track resulting from a charged current ν_μ interaction. While the first provide good estimates of the neutrino energy, only the muons tracks provide good angular resolution around 1° . To select promising track-like HESE events from the published sample the following criteria were applied:

- track-like signature, i.e. good angular resolution
- good visibility from the H.E.S.S. site
- high deposited energy, i.e. high probability for an astrophysical origin

The initial publicly available list of events has been updated several times (e.g. [5, 103]). Applying these selection criteria, the events given in Tab. 3.1 have been selected for searches of gamma-ray counterparts with H.E.S.S. over the last years.

Table 3.1: High-energy neutrino events used for H.E.S.S. searches

	IC-5	IC-18	IC-44	IC-45
IceCube				
Right Ascension [h]	7.37	23.04	22.4	14.59
Declination [$^\circ$]	-0.4	-24.8	0.04	-86.25
Median angular resolution [$^\circ$]	< 1.2	< 1.3	< 1.2	< 1.2
Deposited energy [TeV]	$71.4^{+9.0}_{-9.0}$	$31.5^{+4.6}_{-3.3}$	$84.6^{+7.4}_{-7.9}$	$429.9^{+57.4}_{-49.1}$
H.E.S.S. observations				
Zenith angle range [$^\circ$]	25 - 35	2 - 20	25 - 40	60 - 66
Effective observation time [min]	72	486	432	270

Dedicated observations with H.E.S.S. on several selected HESE events started in 2013/2014 (cf. Fig. 3.9). The region around IC-5 has been observed for about 2 h at a zenith angle of 30° in monoscopic mode with the H.E.S.S.-II 28m telescope, while the region around the neutrino event IC-18 has been observed for almost 12 h with the full array of the five H.E.S.S. telescopes at zenith angles around 10° . Analyzing both dataset using the Model Analysis [72] with standard gamma-hadron separation and event selection cuts no gamma-ray excess could be detected. I complemented the H.E.S.S. observations with an analysis of data recorded by the *Fermi*-LAT gamma-ray instrument, which allowed to extend the covered energy range towards lower energies. Similar to the discussion on the ANTARES excess above, the derived limits on the gamma-ray flux from the regions around the IceCube events, allowed to derive limits on the distance of a potential multi-messenger source emitting neutrinos and gamma-rays via proton-proton interactions. Assuming very conservatively that these potential sources are only emitting in the 100 TeV range around the energies measured by IceCube, i.e. without emission at lower energies and emission, and using the EBL model given in [82], these minimal distances were found to be $z = 0.007$ ($z = 0.012$) at 99 % CL for IC-5 and IC-18 respectively. Extrapolation of the IceCube flux to lower energies would allow to put stronger constraints on the source distance, but would induce a significant dependence on the assumed spectral shapes. Results have been presented at the 34th International Cosmic Ray Conference (ICRC) and details are given in the corresponding proceedings [150].

The observation program of these archival neutrino events continued in 2015 with two additional observations (IC-44 and IC-45). One of them (IC-45) is a particularly interesting neutrino event: it deposited about 430 TeV in the IceCube detector (cf. Tab. 3.1), which makes it one of the most energetic

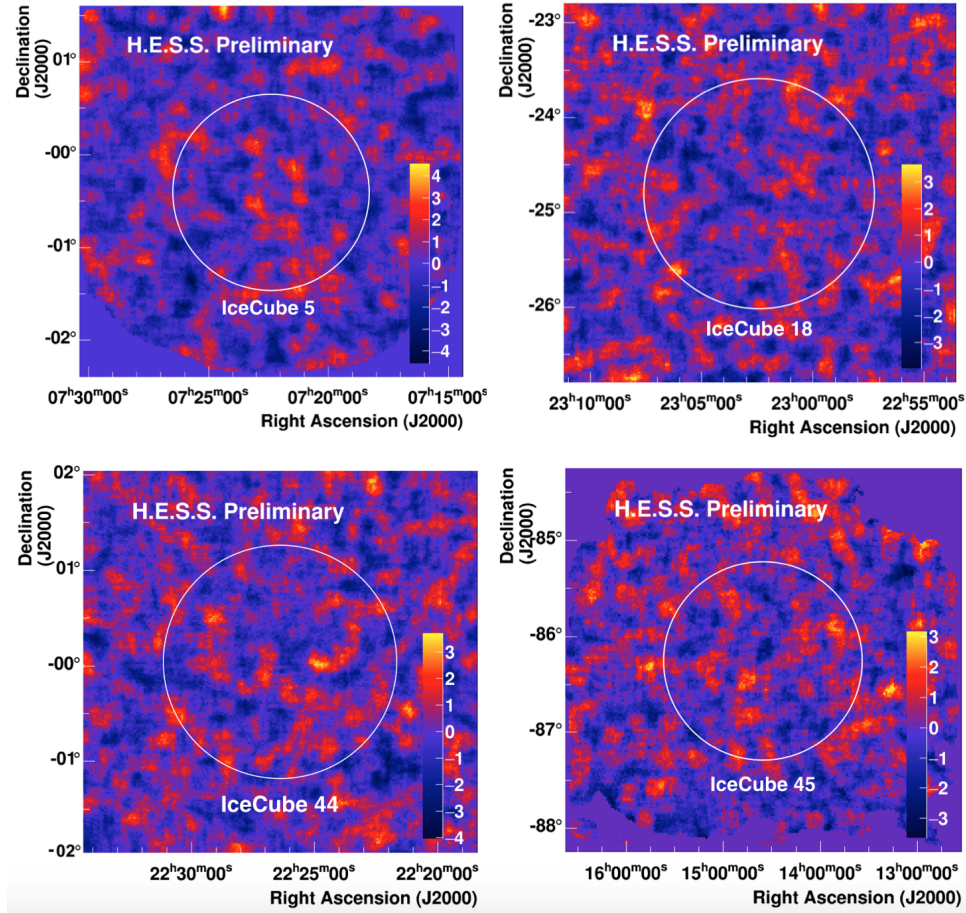


Figure 3.10: Significance maps derived from H.E.S.S. follow-up of the regions around high-energy neutrino events detected by IceCube. The white circles denote the localisation uncertainty of the neutrino events. Modified from [150, 148].

track-like events ever recorded. Even more interesting is the fact that the event has the particularity of being almost vertically down-going at the site of the IceCube detector, but no coincident signal has been recorded by the IceTop air shower array covering the in-ice neutrino telescope. This absence of an extensive air shower accompanying the high-energy neutrino further increases the probability of the event being of astrophysical origin. H.E.S.S. observed the region around the neutrino event IC-45 (IC-44) for almost 4.5 h (7 h) at zenith angles around 63deg (30deg). The relatively high zenith angles for the observations on IC-45 lead to an energy threshold of about $E_{\text{thr}} \approx 1.5$ TeV. No significantly enhanced gamma-ray emission has been detected in any of these observations and the resulting maps (cf. Fig. 3.10) are fully compatible with the background expectation. These analyses have been presented in 2016 at the Neutrino 2016 and the Gamma 2016 conferences [148] and a summary of the events and the obtained observations is given in Table 3.1. Thanks to exchanges in a joint, informal working group between all IACTs and IceCube that I installed and lead since 2015 with support from the french “Programme National Hautes Energies (PNHE)”, the upper limits derived from the H.E.S.S. observations have been combined with similar observations by VERITAS. They are shown in comparison with results from the HAWC observatory in Fig. 3.11 and have been discussed together with results from the MAGIC and FACT programs [111, 156].

Interpretation of these null results is challenging. In addition to the EBL absorption discussion above, one has to take into account the large positional uncertainty related to the neutrino events,

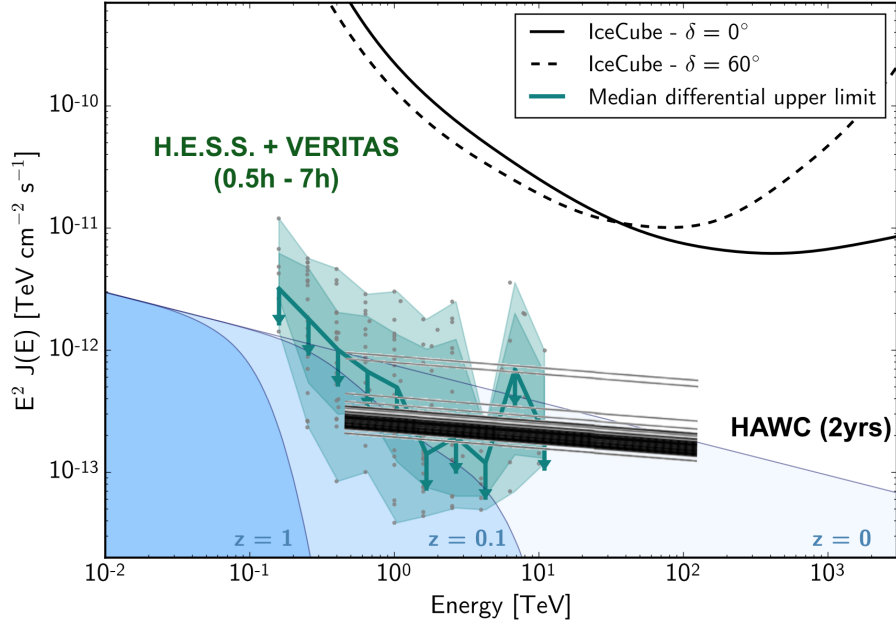


Figure 3.11: Differential upper limits derived from observations searching for persistent gamma-ray sources associated to high-energy neutrino detected by IceCube. Combined limits from H.E.S.S. and VERITAS IACTs (green lines) are shown together with results from the HAWC observatory (black lines). The blue lines illustrate the flux level expected assuming a pp-model of 1000 sources responsible for the astrophysical flux of high-energy neutrinos. From [156].

which is of the order of 1.2 deg. One possibility to present the results in a meaningful way is by calculating maps of integral flux upper limits for the whole region-of-interest. In the current implementation, the limits are derived above an energy threshold E_{thr} defined individually for each observation as the energy where the acceptance is 10% of its maximum value and yielding more than 10 events available to estimate the background. The background level in the field-of-view is determined from the dataset itself using the standard “ring background” technique [61]. In order to build the upper limits maps the general idea as developed for the H.E.S.S. Galactic Plane Survey [22] was followed. The computation is using

$$F = \frac{N_{\gamma}^{\text{UL}}}{N_{\text{exp}}} \int_{E_{\text{min}}}^{E_{\text{max}}} \Phi_{\text{ref}}(E) dE, \quad (3.8)$$

where F is the integral flux computed for each spatial bin of the map between E_{min} and E_{max} . Here we set $E_{\text{min}} = E_{\text{thr}}$ to the energy threshold of each observation (cf. Tab.3.1). N_{γ}^{UL} is the upper limit on the number of gamma-ray events in each bin of the map. It is obtained for a confidence level of 99% [134]. N_{exp} is the total predicted number of events. It is given by

$$N_{\text{exp}} = \sum_{i=0}^{i=N_{\text{runs}}} T_i \int_{E_{\text{thr}}}^{\infty} \Phi_{\text{ref}}(E_{\text{rec}}) A_{\text{eff}}(E_{\text{rec}}, R_i) dE_{\text{rec}}. \quad (3.9)$$

Here, E_{rec} is the reconstructed energy, T_i is the effective live time and R_i symbolizes the observation parameters for run i (zenith, off-axis and azimuth angle, pattern of telescopes participating in the run, optical efficiencies). A_{eff} is the effective area and E_{thr} is the threshold energy appropriate for the observation. The function $\Phi(E)$ is the assumed gamma-ray spectral energy distribution. In absence of commonly agreed models for the general emission we use a generic power law following E^{-2} .

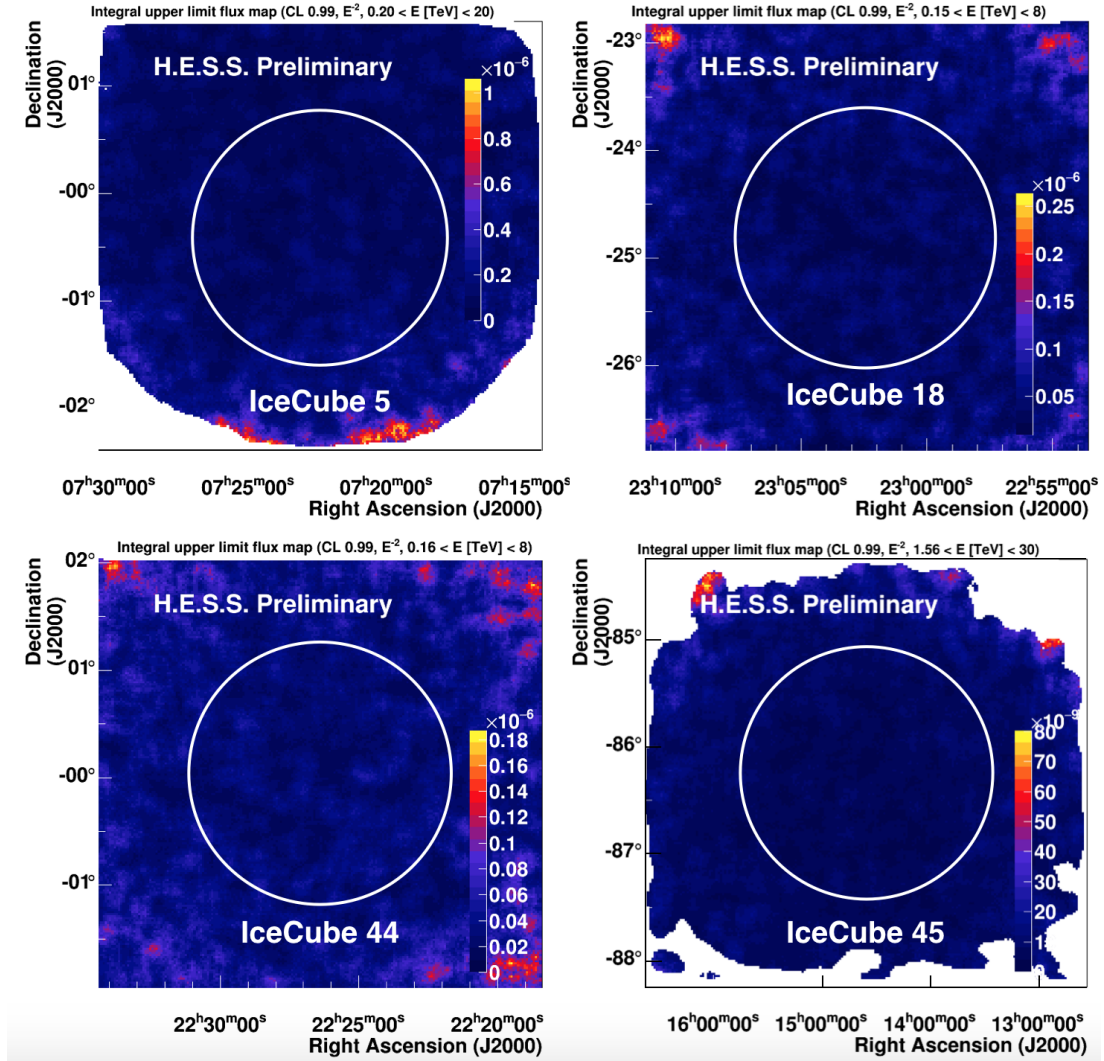


Figure 3.12: Skymaps of regions around high-energy neutrinos recorded by IceCube. The color scale represents upper limits in units of $\text{m}^{-2}\text{s}^{-1}$ on the high-energy gamma-ray flux derived from H.E.S.S. observations. The white circles denote the localisation uncertainty of the neutrino events. Modified from [151].

The resulting upper limit skymaps of the regions around the four selected IceCube HESE events are shown in Fig. 3.12 and are discussed in [151].

3.3.3 Entering the time domain: H.E.S.S. follow-up of high-energy neutrino alerts

The detection of an astrophysical flux of high-energy neutrinos and the continued absence of localized excesses hinting towards the sources of the recorded neutrinos caused over the last years a paradigm shift within the collaboration operating the IceCube detector. Scenarios involving transient sources became more and more likely. As the highest-energy neutrino events did not (and still don't) arrive in bunches, i.e. close in time, the corresponding fluxes emitted by each source have to be assumed to be very low. IceCube therefore realized that a large and multi-messenger observational effort will be required to locate the underlying sources. In contrast to the delayed publications of the parameters of individual high-energy events (see Sec. 3.3.2), timely announcements of preliminary

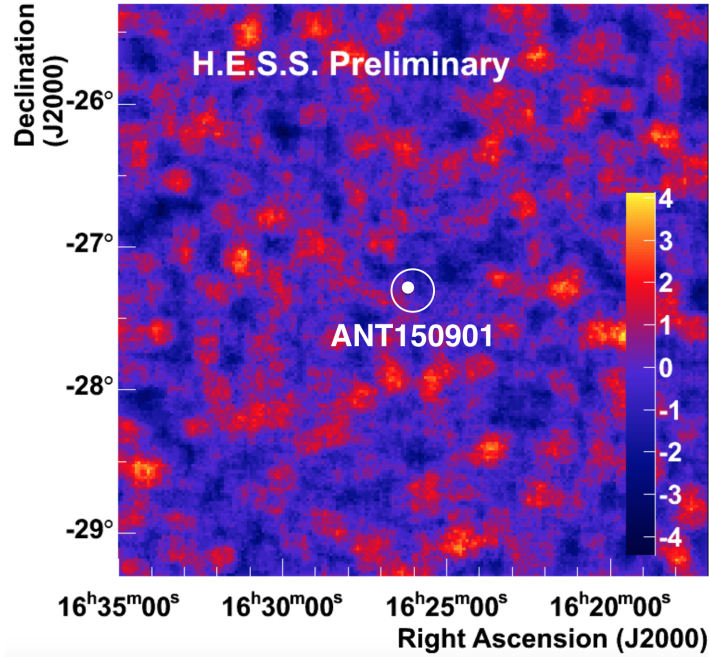


Figure 3.13: Significance map derived from H.E.S.S. observations of the region around the region of the ANTARES high-energy neutrino alert ANT150901A published in ATEL#7987 [76]. The uncertainty of the neutrino direction (0.3 deg) is shown as white circle and the location of the Swift source is indicated by the white marker. From [148]. See also Sec. 2.6.2.

reconstructed parameters of interesting events was necessary to allow for searches of transient phenomena with potentially very short timescales. IceCube therefore installed a performant real-time alert system able to partially circumvent the difficulties of operating an observatory in a remote area like the South Pole with limited computing and network capabilities [7]. This system is very similar to the one operated by the ANTARES/TAToO collaboration since several years (cf. Sec. 2.6). The public and real-time announcements of individual HESE (and later “extremely high-energy (EHE)”) events by IceCube started early 2016. In preparation, the capabilities of H.E.S.S. to receive and react to external alerts had been updated and improved significantly (cf. Sec. 3.2.3). At the same time, and based on the experience gained during the observation campaigns of archival high-energy neutrino events, a program on timely follow-up observations of high-energy neutrinos detected by the IceCube and ANTARES neutrino telescopes could be installed within the H.E.S.S. multi-messenger program. Although without providing a clear detection so far, these observations are now considered a success within and outside the H.E.S.S. collaboration. Over the last years they evolved significantly (e.g. Sec. 3.3.5) and have been repeatedly renewed and approved by the H.E.S.S. Observations Committee.

ANT150901A

One of the first H.E.S.S. searches for transient sources using a multi-messenger approach was performed in September 2015 with the follow-up of the ANTARES neutrino alert ANT150901A. After the detection of a high-energy neutrino by the online reconstruction of the ANTARES neutrino telescope on September 1st, 2015, at 07:38:25 UT, an alert has been issued to a variety of optical telescopes and the Swift X-ray satellite [42]. 10 hours later Swift observed the region around the neutrino direction (RA=246.43 deg, Dec=-27.39 deg with an uncertainty radius of 18 arcmin) and discovered an unknown, relatively bright ($\Phi = 5 \times 10^{-13} - 1.4 \times 10^{-12} \text{ erg cm}^{-2} \text{ s}^{-1}$ at 0.3 – 10 keV) and variable X-ray source. These observations were reported in ATEL#7987 [76] on 3 Sep 2015 at 12:18 UT.

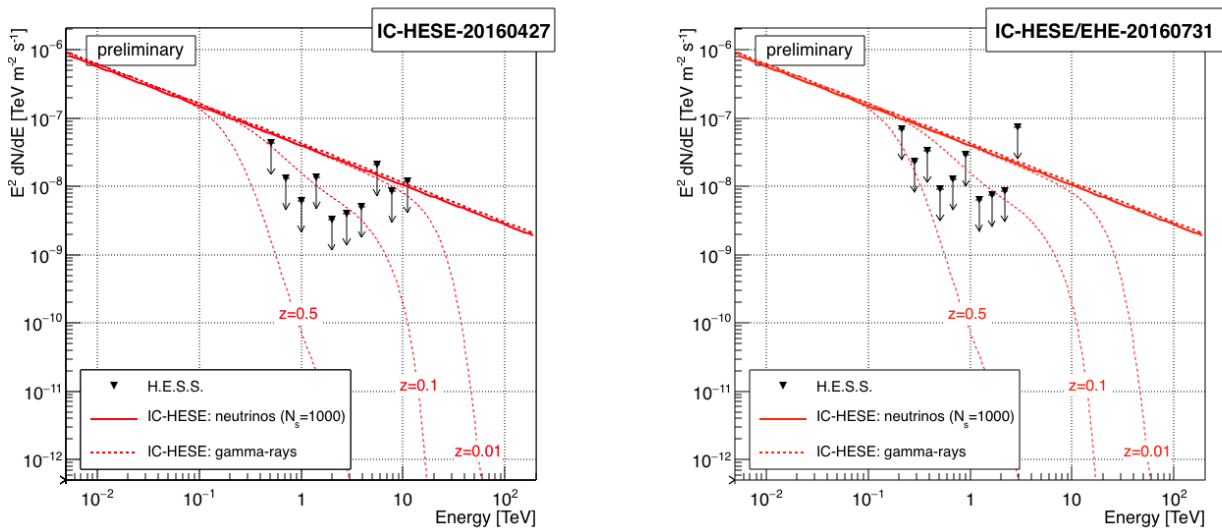


Figure 3.14: VHE gamma-ray flux limits Φ_{UL} at 95 % CL derived from the H.E.S.S. observations (black arrows) assuming a point-like source in the center of neutrino uncertainty region. The estimate of the gamma-ray flux (dashed, red line) has been derived from the IceCube measurement of a diffuse neutrino flux (solid, red line). From [152]

H.E.S.S. follow-up observations were scheduled immediately and started September 1st, 2015, at 18:58 UT as soon as good observation conditions were reached. The significance map derived from 1.5h of observations is shown in Fig. 3.13. The uncertainty on the direction of the high-energy neutrino is shown as white circle and the location of the Swift source is indicated by the white marker. Consequently an upper limit on the gamma-ray flux has been derived as $\Phi(E > 320 \text{ GeV}) < 2.4 \times 10^{-7} \text{ m}^{-2} \text{ s}^{-1}$ (99% C.L.). It should be noted that the extensive multi-wavelength follow-up of ATEL#7987 lead to the conclusion that the Swift X-ray source is due to a young star (USNO-B1.0 0626-0501169) and thus unrelated to the neutrino, which may be of atmospheric origin. Details of the analysis are discussed in [148]. See also Sec. 2.6.2.

First follow-ups of IceCube alerts

On April 27th, 2016, at 05:52:32 UT, IceCube recorded an event fulfilling the HESE criteria and issued an alert soon afterwards. The neutrino has been reconstructed to originate from RA = 16h 02m 16s, Dec = 9.34 deg with an uncertainty of 36arcmin (radius, 90% containment) and a total charge deposited within the detector of about 18900 photoelectrons. Visibility and weather constrains delayed H.E.S.S. observations of the identified region to April 29th, 2016 around 21:07 UTC. The observations were taken with an average zenith angle of around 50 deg, the resulting energy threshold, defined as the energy where the acceptance is 10% of its maximum value, is 350 GeV. Analyzing the total dataset of 1.7h effective livetime, no significant gamma-ray emission could be found. Differential upper limits on the gamma-ray flux from the central position of the covered ROI have thus been calculated. They are shown as black arrows in Fig. 3.14. For illustration, the obtained limits are compared with expectations derived from the IceCube diffuse, all-sky neutrino flux ($E^2 \times \Phi(E) = 2.2 \pm 0.7 \times 10^{-8} (E/100 \text{ TeV})^{-0.58} \text{ GeV cm}^{-2} \text{ s}^{-1} \text{ sr}^{-1}$, [103]) denoted by the solid red lines in Fig. 3.14. The all-sky flux was distributed over 1000 putative sources, a number currently not excluded by the searches for point-like neutrino sources. The derived flux can therefore be considered as an upper-bound on the expected neutrino flux per contributing source. The conversion into a gamma-ray flux (dashed red lines in Fig. 3.14) is relying on the parametrization of pp interactions

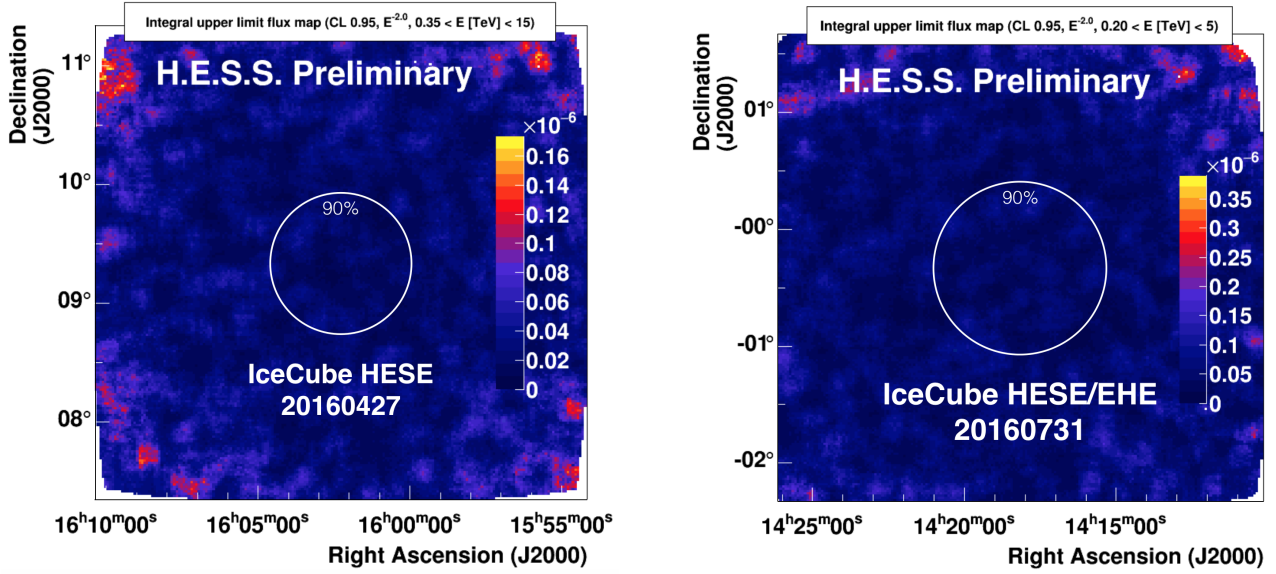


Figure 3.15: Integral VHE gamma-ray flux limits (95 % C.L., assuming a E^{-2} spectrum) in units of $\text{m}^{-2}\text{s}^{-1}$ derived from H.E.S.S. follow-up observations of the first IceCube neutrino alerts. The white circles denote the angular uncertainty (90 % containment) on the neutrino directions. From [152]

within or close to a generic hadronic accelerator as given in [94].

A second observation campaign started after the detection of a neutrino event fulfilling both the HESE and the EHE criteria recorded by IceCube on July 31st, 2016 at 01:55:04 UT with a total deposited charge of about 15800 photoelectrons. H.E.S.S. observations started the same day around 17:50 UTC as soon as the reconstructed neutrino direction (RA = 14h 18m 11s, Dec = -0.33 deg with an uncertainty of $45'$ radius at 90% containment) became visible from the H.E.S.S. site. Again no significant gamma-ray emission has been found. Following the procedure outlined above, differential upper limits on the gamma-ray flux for the central position of the ROI (cf. Fig. 3.14) and integral upper limits on the full region (cf. Fig 3.15) have been derived.

Real-time follow-up: ANT170130A

The performance of the fully automated systems of both, the ANTARES (e.g. data analysis and alert emission) and the H.E.S.S. (e.g. alert reception and follow-up observations) observatories, has been illustrated by an alert received on January 30, 2017. On 00:39:12 ANTARES recorded a single, high-energy neutrino. The automatic event reconstruction triggered a VoEvent notice emitted to partner observatories at 00:39:25. The alert was received at the H.E.S.S. site triggering fully automatic follow-up observations starting at 00:39:44, i.e. only 32 seconds after the neutrino event. About one hour of H.E.S.S. observations could be obtained immediately following the alert before the direction moved outside the visibility window (cf. Fig. 3.16). Another 30min of data was taken during the night after the alert (2017-01-31 at 19:29 UT) in order to search for afterglow and/or delayed emission. A preliminary analysis using monoscopic data from the 28m telescope and time integrating the full dataset did not reveal any significant gamma-ray emission. The significance map of the region around the reconstructed neutrino direction is shown in Fig. 3.16.

Summary of the H.E.S.S. follow-up of high-energy neutrino alerts

The H.E.S.S. alert system (cf. Sec. 3.2.3) has been running stable since 2015. Successful submissions to the yearly call for observing proposals have allowed to follow all neutrino alerts emitted

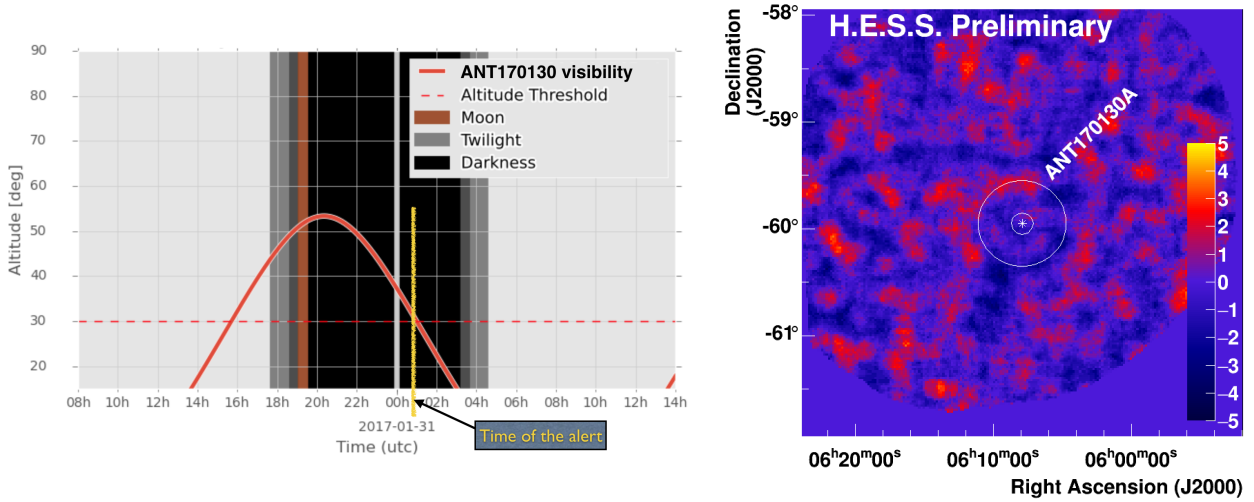


Figure 3.16: Left: Visibility of the ANTARES alert received 2017-01-30 at the H.E.S.S. site. Right: Significance map derived from H.E.S.S. observations of the regions around the ANTARES alert ANT170130A. The inner circle illustrates the size of the H.E.S.S. PSF and the outer circle denotes the 50 % containment angular uncertainty on the neutrino direction of 0.4 deg. From [152]

by IceCube that were visible from the H.E.S.S. site. A summary of the obtained datasets is given in Table 3.2. None of these dataset showed significant VHE gamma-ray emission and stringent limits on the gamma-ray flux could be derived. Details of the observations and the obtained results have been published in [152, 154, 165].

Table 3.2: Summary of neutrino follow-up observations performed by H.E.S.S. (from [165])

Date	Triggering experiment	Alert identifier	Delay of observations	Duration of observations
September 1, 2015	ANTARES	ANT 150901	11h	2h
April 27, 2016	IceCube	HESE 160427	2d 15h	2h
July 31, 2016	IceCube	EHE 160731	16h	2h
November 3, 2016	IceCube	HESE 161103	12h	2h
January 30, 2017	ANTARES	ANT 170130	32s	1h 20m
September 22, 2017	IceCube	EHE 170922	4h	3h14m + 15h

3.3.4 IceCube-170922A and TXS 0506+056

On September 22nd, 2017 IceCube detected another interesting event (EHE 170922 or IceCube-170922A). An alert was emitted by the IceCube real-time system within 43 seconds, triggering follow-up observations across several MWL bands. First among the VHE observatories, H.E.S.S. observations started 4 hours later as soon as the region became visible and continued during the next night. No significant gamma-ray emission was detected [71]. Several days later it was realized that the reconstructed direction of the neutrino event was only 0.1° away and fully compatible with the sky position of the BL Lac object TXS 0506+056, which had shown historically high level of activity in all wavelengths, most notably in GeV gamma-rays monitored by the *Fermi*-LAT [164]) over several months prior to the neutrino alert. Renewed and deeper VHE follow-up observations were obtained by all IACT collaborations over the following days, weeks and months. The source was detected for the first time by the

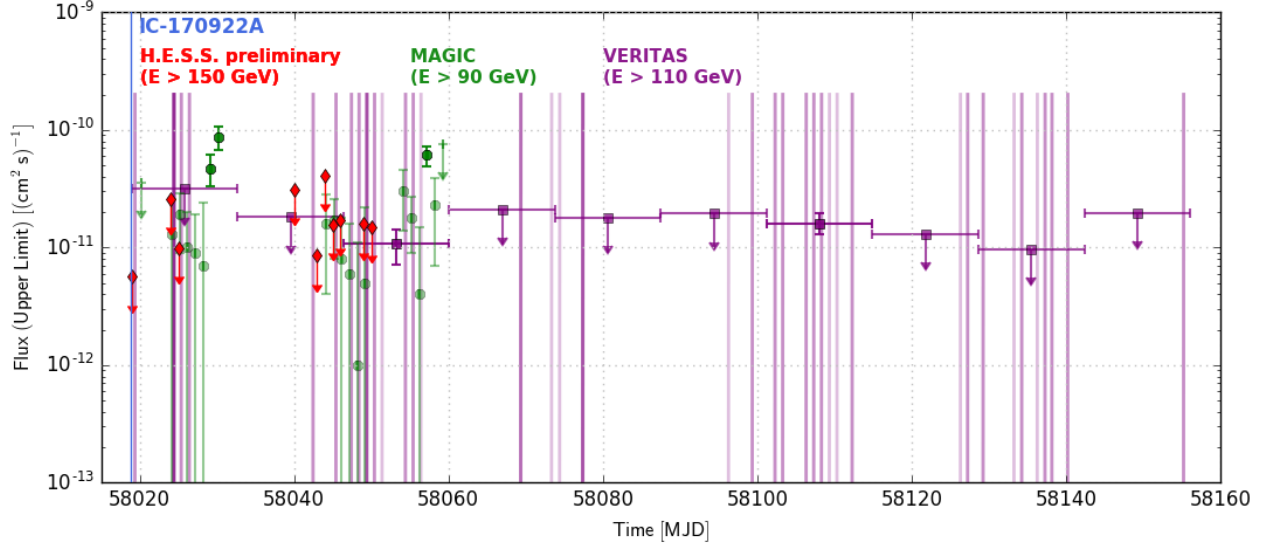


Figure 3.17: Lightcurve of VHE gamma-ray observations of the blazar TXS 0506+056 obtained following the alert on the detection of the high-energy neutrino IceCube-170922A. Red markers denote the upper limits derived from H.E.S.S. observations [154] while the green and magenta markers show the data obtained by the MAGIC [51] and VERITAS [32] IACTs. From [154].

MAGIC telescopes [120, 51], later followed by the VERITAS observatory [32]. Due to the extremely rapid variability of the source at the highest energies and unfavorable observing conditions no VHE gamma-rays have been detected by H.E.S.S. A summary of the observations is given in Fig. 3.17 and discussed in [154].

The chance probability for a high-energy neutrino to be detected in coincidence with a flaring blazar from the *Fermi*-LAT catalogues was found to be disfavored at the 3σ confidence level. It should be noted that this probability does not directly take into account the fact that the neutrino event IceCube-170922A has a $\sim 44\%$ probability to be of atmospheric origin [165]. The significance of the TXS 0506+056 and IC-170922A association is therefore too low to claim the discovery of the first neutrino source. Nevertheless, the event sparked significant interest in the broader community and, thanks to the extensive MWL data, provides a unique opportunity to study the interplay between energetic photons, neutrinos and cosmic rays. Moreover, a search for previous neutrino emission from the identified direction revealed a neutrino flare of several months duration in 2014-2015 in the IceCube data. This flare, which seems not correlated with any increased high-energy electromagnetic emission in *Fermi*-LAT has a significance of about 3.5σ . Currently undisputed theoretical models trying to explain both the correlation of IceCube-170922A and the gamma-ray flare of TXS 0506+056 as well as the *orphan neutrino flare* are still missing (e.g. [99]). Further joint observations of this kind will allow to shed light on the potential association between high-energy neutrinos and flaring blazars and may provide the long-sought hints for the sources of cosmic rays. While the neutrino follow-up programs continue with the current instruments like H.E.S.S., MAGIC and VERITAS, this first exciting result has already strong influence on the preparations of next-generation observatories like the Cherenkov Telescope Array (cf. Sec. 3.6) and the Southern Gamma-ray Survey Observatory (cf. Sec. 3.8).

3.3.5 Further developments of the H.E.S.S. high-energy neutrino program

Given the rapidly evolving field of time domain multi-messenger astrophysics, the H.E.S.S. multi-messenger program is under constant improvement and development. Several new ideas have been

proposed, approved by the collaboration and implemented over the recent years and months. A few highlights are discussed in the following:

The IceCube Gamma-ray Follow-up (GFU) program

After several years of preparation, the IceCube Gamma-ray Follow-up (GFU, [8]) program has been extended in 2018 towards the Southern hemisphere and thus now includes the H.E.S.S. observatory. Started in 2012, the current implementation of the program uses a list of a-priori defined sources that are monitored for an increased rate of neutrino events within the IceCube real-time analysis framework. The search is using an unbiased time-clustering algorithm to search for neutrino flares at all timescales up to several months [140] and the measured long-term background rate as well as real-time data quality assessments to identify significant clusters of neutrino event compatible with one of the monitored sources.

During the preparation of the extension towards the Southern hemisphere a new list of monitored sources has been defined using the following parameters:

- presence in 3FGL or 3FHL catalog
- max. culmination at HESS site: 60 deg
- extragalactic, redshift $z \leq 1.0$
- variability
 - 3FGL: variability index > 77.2
 - 3FHL: at least two Bayesian blocks
- 10 x extrapolated Fermi flux > 100 GeV has to be higher than HESS 5sigma sensitivity for 5h of observations (1% C.U.)

In addition, a list of all extragalactic sources detected by H.E.S.S. has been compiled and added together with SgrA*, the Crab nebula and TXS 0506+056. The list has been approved and implemented in the alert system by the IceCube collaboration end of 2018. Follow-up time with H.E.S.S. has been granted and first alerts and observations have been obtained in early 2019.

The Astrophysical Multi-messenger Observatory Network (AMON)

The Astrophysical Multi-messenger Observatory Network (AMON, [161, 55]) aims at performing real-time correlation analysis across all known astronomical messengers: photons, neutrinos, cosmic rays, and gravitational waves. AMON provides an infrastructure to link multiple, typically high-energy, monitoring instruments as well as follow-up observatories together into a single network. This will enable near real-time coincidence searches for multimessenger astrophysical transients and their electromagnetic counterparts. Candidate and high-confidence multimessenger transient events are identified, characterized, and distributed as alerts within the network and (partially) to interested external observers, enabling follow-up observations across the electromagnetic spectrum. In this way, AMON aims to evoke the discovery of multimessenger transients from within observatory sub-threshold data streams and facilitate the exploitation of these transients for astronomy and fundamental physics. As a central hub of multi-observatory multimessenger science, AMON also enables cross-collaboration analyses of archival datasets in search of rare or exotic astrophysical phenomena and offline searches for correlations between different datasets. An overview of the AMON partner observatories is given in Fig. 3.18.

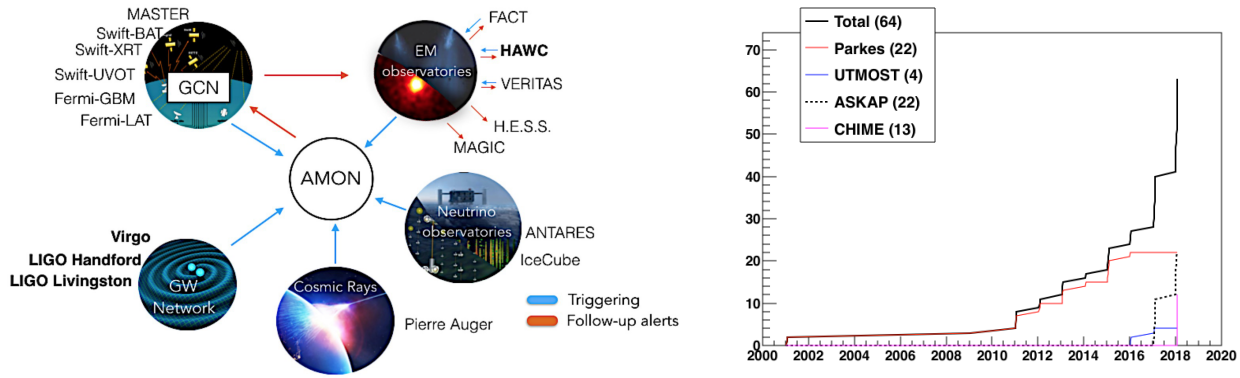


Figure 3.18: Left: Observatories participating in the Astrophysical Multi-messenger Observatory Network (AMON) enabling real-time searches for multi-messenger transients and follow-up observations. From [159]. Right: Number of detected Fast Radio Bursts over the last years. Data from FRBcat [129].

H.E.S.S. joined the AMON network as follow-up instrument in early 2018 under my guidance. H.E.S.S. has therefore access to promising sub-threshold correlations of data from gamma-ray observatories like HAWC and neutrino telescopes like IceCube and ANTARES. I act as AMON contact person within H.E.S.S. and am a member of the AMON executive board. Observation time for H.E.S.S. follow-up observations of AMON alerts (with a priority for HAWC-IceCube coincidences) has been granted starting in 2018. Due to delays in the internal approval process of these alerts by the HAWC and the IceCube collaborations, the start of these observations is currently foreseen in 2019.

In addition, an extension of the AMON network towards gravitational wave observatories and the combination of sub threshold data obtained by HAWC and Virgo/Ligo has been prepared. Details are given in Sec. 3.7.1 below.

3.4 Fast Radio Bursts

Fast radio bursts (FRBs) are one of the major astronomical mysteries that have emerged in the last decade. First noticed in 2007 in archival data taken with the Parkes radio telescope [108], more than 60 of these millisecond-duration bursts have been detected so far [166, 128, 129]. As illustrated in Fig. 3.18, the majority of the early detections were made with the Parkes telescope. Several additional bursts have been detected with the Arecibo telescope [162], the Green Bank Telescope (GBT) [115] as well as with interferometers like UTMOST and CHIME [64] and SKA pathfinders like ASKAP. A summary of known FRBs including the details of the observations can be found in the online catalog FRBCAT[‡] [129].

FRBs release enormous amounts of energy in the radio domain, the only band they have been detected in so far, and their potential origins are thought to be similar to other transients seen in the X-ray and multi-GeV gamma-ray bands such as short and/or long GRBs [173]. Several FRB models have also specifically suggested the existence of flares in the TeV band (e.g., [109, 123]) and proposed follow-ups of FRBs at very high energies.

Using the Parkes telescope, the Survey for Pulsars and Extragalactic Radio Bursts (SUPERB, [98]) collaboration implemented a first quasi-online search for FRBs. Observations started in October 2014 with the Parkes program P858. In preparation, a MoU had been signed with the H.E.S.S. collaboration allowing the sharing of alerts. Dedicated ToO observation time has been allocated via the yearly call for proposals.

[‡]<http://www.frbcats.org>

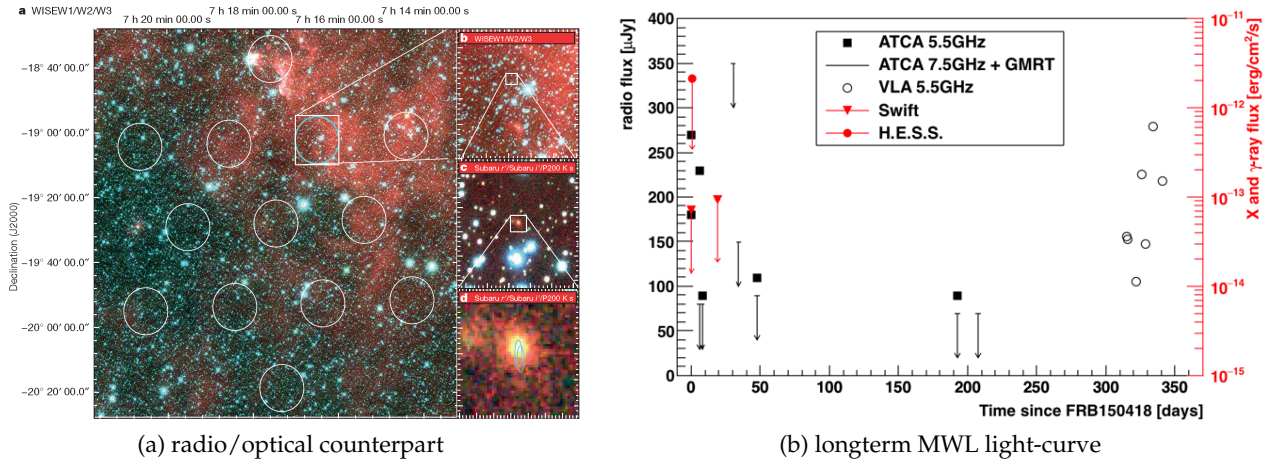


Figure 3.19: Left plot: Optical analysis of the potential host galaxy of FRB150418 showing a wide-field image, overplotted with the half-power beam pattern of the Parkes multi-beam receiver. The smaller panels show successive zooms on the beam 4 region and on the fading ATCA transient location. Figure from [97]. Right plot: Overview of the multi-wavelength follow-up of FRB150418 in the radio, X-rays and the VHE gamma-ray domains. The radio emission detected at late times with the VLA disfavors the *afterglow* interpretation and points to an AGN-like origin of the emission (e.g. [167, 58]). From [148].

3.4.1 FRB150215

A first VHE follow-up observation of an FRB was performed by H.E.S.S. after the SUPERB team announced the detection of FRB150215 [130]. The particularity of this burst is its low galactic latitude ($b = 5.28^\circ$ and only 25° off the Galactic Center). The radio signal was found to be $43 \pm 5\%$ linearly polarized with a rotation measure $-9 < RM < 12 \text{ rad m}^{-2}$ at 95% confidence level, and thus consistent with the Galactic foreground. This implies that rotation measure $\geq 25 \text{ rad m}^{-2}$ in the rest-frame of the host is imparted by the progenitor or a host galaxy, in contrast to FRB 110523 [116] implying that not all FRBs are produced in dense, magnetised regions. At the same time the dispersion measure $DM = 1105.6 \pm 0.8 \text{ pccm}^{-3}$ is more than 2.5 times the expected DM from the Galaxy, which might point to an under-density in the ionized interstellar medium along this sightline.

The location of FRB 150215 became visible at the site of the H.E.S.S. observatory only several days after the burst. A first observation run of 28min started 2015-02-22 at 02:53 UTC, that is 6.3 days after the Parkes detection. A second observation was obtained on 2015-02-25 starting at 02:49 UTC, 9.3 days after the burst. Both observations were performed with a hybrid setup including the 28m H.E.S.S.-II telescope. Combining both observations and after correcting for acceptance effects, a total effective live time of 0.7 h has been obtained under good conditions. No significant gamma-ray flux has been detected from the direction of the burst. In the absence of a significant gamma-ray emission we derive the 99% C.L. upper limit on the gamma-ray flux assuming an E^{-2} energy spectrum as $\Phi_\gamma(E > 1 \text{ TeV}) < 3.98 \times 10^{-14} \text{ cm}^{-2}\text{s}^{-1}$. Although limited in depth and with significant time delays between the burst and the start of the observations, this dataset is the first follow-up observations of fast radio bursts in the very high-energy gamma-ray domain. Details about FRB150215 and the MWL follow-up observations (including also the ANTARES neutrinos telescope) can be found in [130].

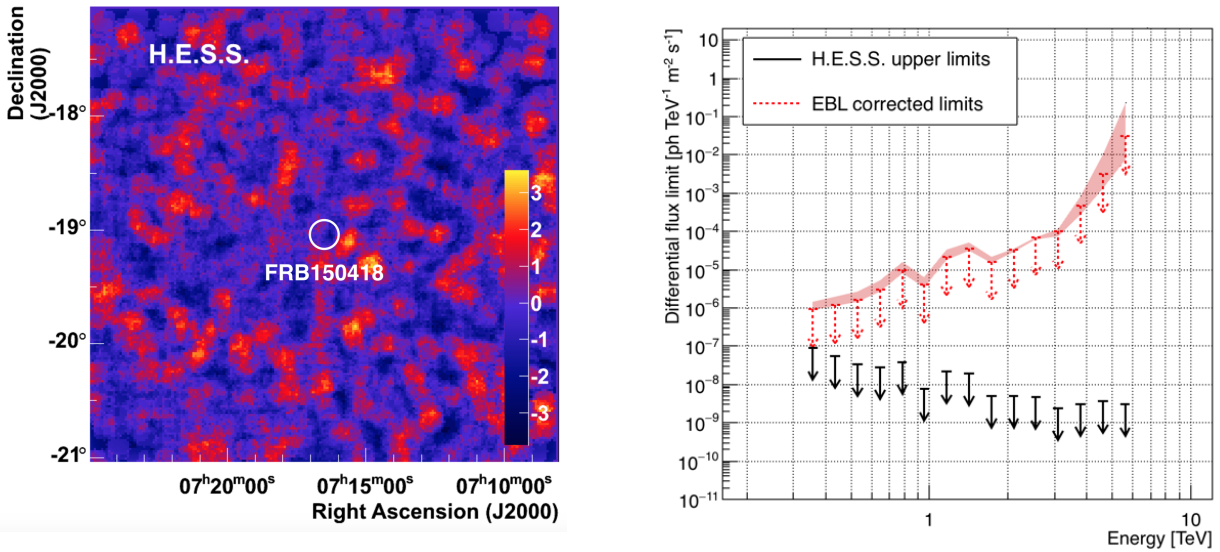


Figure 3.20: Left: Map of significances of the gamma ray emission using the formalism proposed by [106] in the region around FRB150418. The circle in the center has a diameter of 0.24° and denotes the width of the Parkes beam in which the burst was observed. Right: Limits (99% CL) on the very high energy gamma-ray flux derived from the H.E.S.S. follow-up on FRB150418 assuming an E^{-2} energy spectrum. The EBL de-absorption is based on the model from [84] and assumes the FRB distance of $z = 0.492$ [97]. The uncertainty induced by different EBL models is shown as red band. From [21]

3.4.2 FRB150418

Initially considered as a potentially significant advance in our understanding of FRBs came shortly afterwards with the detection of a radio afterglow at the location of FRB150418 with the Australia Telescope Compact Array (ATCA, [97]). The burst FRB150418 was initially detected at Parkes on the 18th April 2015 by the SUPERB team. The fading radio afterglow lasted up to six days after the FRB, and could be linked to an elliptical host galaxy at $z = 0.492 \pm 0.008$ (WISE J071634.59–190039.2). If connected to the afterglow, the energetics of FRB150418 suggest a cataclysmic origin of the bursts [174]. As more data became available, the light curve of the variable radio source became ever better characterized and the statistical significance of the association between the FRB and the galaxy reduced. Further observations with high angular resolution indicate that the supposed afterglow is most likely due to a background AGN [167, 58]. An overview over the multi-wavelength observations following FRB150418 is given in Fig. 3.19.

The notification of FRB150418 was received from the SUPERB team on 2015-04-18 during daytime at the site of the H.E.S.S. experiment, thus prohibiting prompt follow-up observations. The necessary observation conditions were reached the evening of the same day at 17:55 UTC (about 14.5 h after the FRB) and 1.4 h of data could be recorded until the source set below an elevation of 45° . No significant gamma-ray emission has been found (cf. Fig. 3.20). Consequently we derive 99% C.L. upper limits on the gamma-ray flux (assuming a generic E^{-2} energy spectrum for the potential emission and integrating above the threshold of 350 GeV) as $\Phi_\gamma(E > 350 \text{ GeV}) < 1.33 \times 10^{-8} \text{ m}^{-2} \text{ s}^{-1}$. Differential upper limits as function of the energy are shown in the right plot of Fig. 3.20. Taking absorption on the extragalactic background light into account and assuming a distance of $z = 0.492$ based on the radio and optical counterpart studies and consistent with the FRB dispersion, we constrain the gamma-ray luminosity of the afterglow of FRB150418 at 1 TeV to $L < 5.1 \times 10^{47} \text{ erg/s}$ at 99% C.L. Further details are given in the dedicated publication [21], also available in the Appendix B.

3.5 Gravitational Waves

The first direct detections of gravitational waves (cf. Sec. 3.2.2) opened a fundamentally new window to the universe. Exploiting the new opportunities brought by this breakthrough, the joint detection of high-energy gamma-rays and gravitational waves would provide a wealth of information on the fundamental parameters of the system (e.g. GW data allow to infer the fundamental parameter of the system like individual masses, spins, etc.) as well as detailed information on the energetics of the violent phenomena induced by the event (e.g. gamma-ray light curves and energy spectra, etc.). Unfortunately these promising observations are challenging. One of the main difficulties for the identification of gamma-ray counterparts to gravitational wave events is the large uncertainty regions provided by the GW interferometers (cf. Fig. 3.3). Given the relatively small field-of-view of pointing instruments like H.E.S.S., dedicated observation strategies have to be implemented to efficiently scan the provided error boxes.. Several solutions developed for the H.E.S.S. experiment will be discussed in the following. These complex algorithms have already been successfully employed in the follow-up observation of GW events (cf. Sec. 3.5.2 and Sec. 3.5.3) and build a crucial starting point for the multi-messenger program of the next-generation gamma-ray observatory, the Cherenkov Telescope Array (cf. Sec. 3.6.1).

It should be noted that the very recent detection of ≥ 300 GeV gamma-rays from GRB190114C by the MAGIC collaboration [122] is illustrating the potential of these searches. While GRB190114C was categorized as one of the most luminous *long-GRBs* (in contrast to the *short-GRBs* associated to the mergers of compact binary systems that can be detected with GWs), it clearly shows that GRB detection with ground based instruments like IACTs is feasible.

A largely complementary approach to IACT follow-up observations is the use of wide FoV gamma-ray observatories like HAWC. A first study exploiting its capability to continuously monitor the gamma-ray sky at the highest energies for searches for gravitational wave counterparts will be presented in Sec. 3.7.1.

3.5.1 Scheduling follow-up observations of gravitational waves

In preparation of the second physics data taking run O2, the alert reception and subsequent analysis by H.E.S.S. has been significantly improved. The GW localization maps are provided by LIGO/Virgo in form of HealPIX FITS files stored within a database. After the reception of an alert message, these files are now automatically downloaded and analysed to produce a detailed H.E.S.S. follow-up observation schedule within the VoEvent alerter running at the H.E.S.S. site (cf. Sec. 3.2.3). Following the assumption that binary mergers happen predominantly close to matter accumulations (e.g. galaxies) we combine the information of the GW localization maps with a galaxy catalogue. We use the current version of GLADE [69], a catalog that has been constructed (combined and matched) from 4 existing galaxy catalogs: GWGC, 2MPZ, 2MASS XSC and HyperLEDA. Additionally, it has been extended with the SDSS-DR12 quasar catalog. GLADE contains 3,632,300 galaxies, is complete up to about 80Mpc and still reaches a completeness of about 50% at 300Mpc. It thus covers the expected NS-NS merger horizon of Advanced Ligo (< 120 Mpc for O2) and Advanced Virgo (< 60 Mpc for O2). Using the 3D probability map provided with the GW alert messages, we derive the probability density per unit volume P_{Gal} at the position of each of the galaxies listed in the GLADE catalog.

Starting from this point, we optimized the H.E.S.S. follow-up by simulating various scheduling scenarios. For this purpose we used GW localization maps derived from simulated NS-NS merger events. The available dataset contains 250 distinct events representative for run O2, i.e. reproducing the directional dependence of the acceptance of the interferometers, the expected duty cycles and sensitivities. Details are explained in [160]. The size of the 90% uncertainty regions range from 1.3 sq deg to 4570 sq deg.

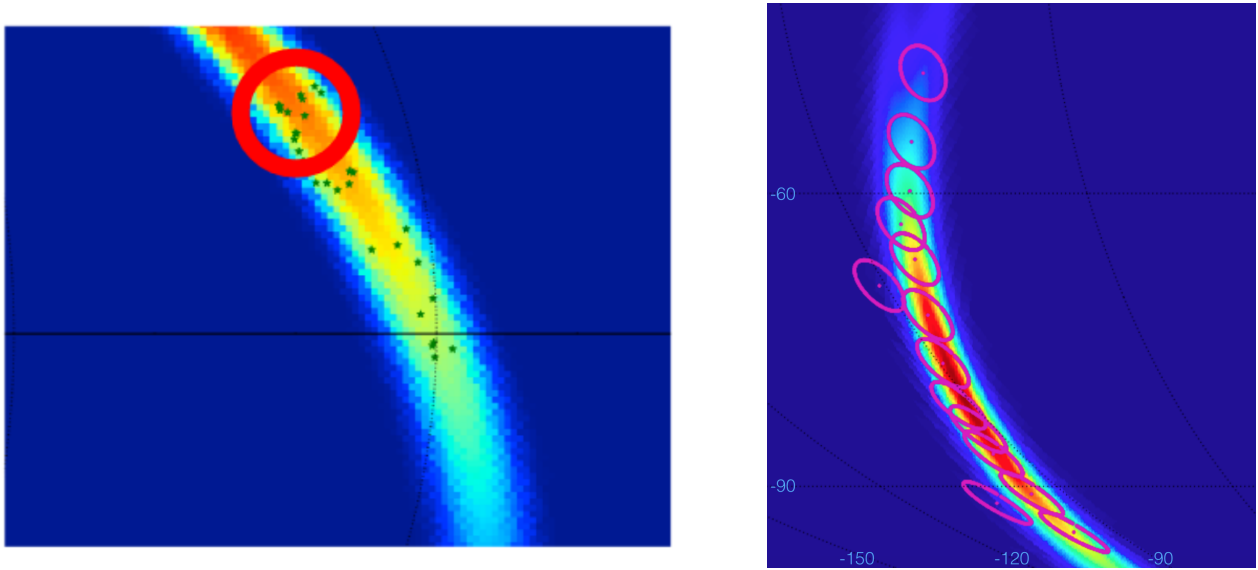


Figure 3.21

Figure 3.22: Left: Example for an individual pointing (red circle) derived from combining the GW uncertainty map (color scale) with a galaxy catalog (blue dots). Right: Example for an optimized H.E.S.S. schedule of follow-up observations of a simulated NS-NS merger event. From [157, 152].

The simulated GW maps have been injected at random times into the developed GW scheduler taking into account a realistic estimate of the duty-cycle for H.E.S.S. observations (e.g. dark time, moon phases, weather, etc.). The proposed follow-up uses a *greedy scheduling*, and can be generalized as:

1. *select the most probable direction* fulfilling the H.E.S.S. observations conditions (e.g. zenith angle range, dark time, etc.)
2. schedule observation for this direction at T_0 with a duration of 30min
3. mask a circular sky region representing the effective H.E.S.S. field-of-view around that region
4. using the modified visibility window at $T_1 = T_0 + 30 \text{ min}$, the direction of the most probable region outside the masked region is selected
5. an observation run is scheduled for this direction at T_1
6. steps 3-5 are repeated until gamma-ray emission is detected by the real-time analysis, the covered probability for the next observations is insignificant or the allocated observation time is used

We implemented several algorithms for the crucial step (1) to *select the most probable direction* of the scheme outlined above. The most generic case would be to select the region with the highest probability in the GW uncertainty map, thus neglecting a-priori and additional information like galaxy catalogs. This approach is very useful for GW events that are not reconstructed in three dimensions (e.g. burst like events that do not fit any of the binary-coalescence templates used in Virgo/LIGO) and for very distant events that occurred outside the completeness range of the available galaxy catalogs. Complementing this baseline scenario, we developed the *One-Galaxy* and the *Galaxies-in-FoV* approach, making use of the full information of both, the GW map and the galaxy catalog.

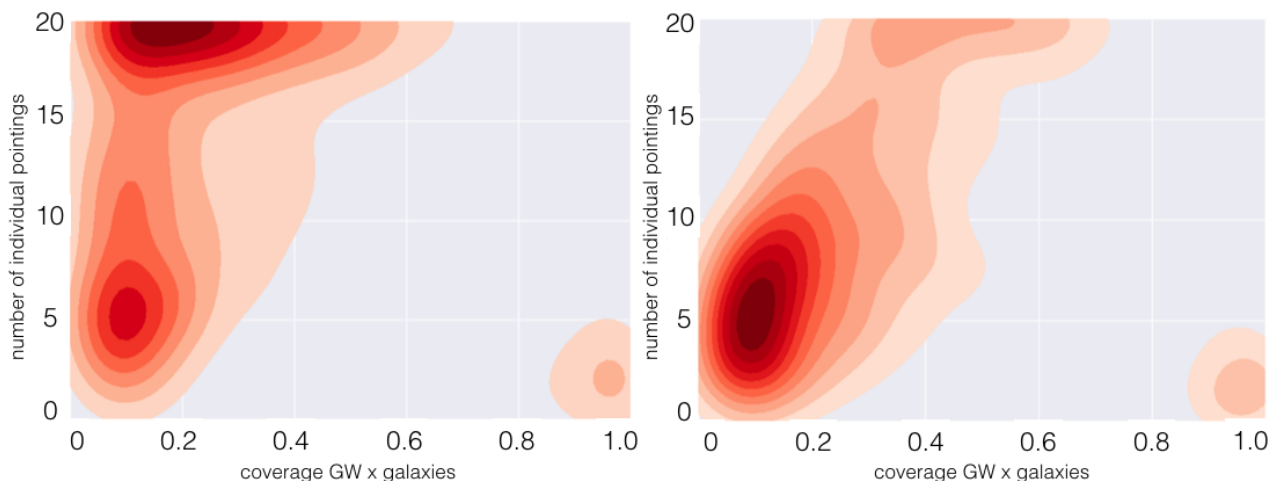


Figure 3.23: Performance of the two main scheduling algorithms developed for H.E.S.S., showing the coverage of simulated NS-NS merger uncertainty regions representative for the O2 run and the necessary pointings. From [152, 157].

One-Galaxy approach

In this strategy we use the probability density P_{Gal} assigned to each galaxy in the catalog to select the most probable individual galaxy as target direction. In each of the iterations outlined above, the galaxies covered by the FoV area are subtracted before re-calculating the following pointing position. The main advantage of this approach is its speed of computation, a key point for transients searches. An efficient sorting algorithm allows to derive a full pointing strategy within only a few seconds. However, the structure of the GW maps and the inhomogeneous distribution of galaxies lead typically to strong clustering of potential targets and the coordinates of the pointing with the highest probability typically end up right next to the edge of the FoV of the previous pointing. The FoVs of these neighboring observations may therefore be overlapping, reducing the achieved final coverage of the GW error map and thus the efficiency of the algorithm.

Galaxies-in-FoV approach

Improving on the original *One-Galaxy* approach, we developed an additional and complementary pointing strategy called *Galaxies-in-FoV*. Here we optimize the pointing strategy in term of a new quantity named P_{GalFoV} . $P_{\text{GalFoV}} = \sum_{\text{FoV}} P_{\text{Gal}}$ denotes the sum of the individual galaxy probabilities P_{Gal} across the full FoV of the IACT. For each pointing we select the center of the direction with the highest P_{GalFoV} compatible with the observational constrains. Again, the algorithm is iterative and in every step the already observed galaxies are removed. This approach is outperforming the initial *One-Galaxy* algorithm since it is optimized for covering the most promising region (and not only the most promising single galaxy). The use of the information on the full FoV also naturally avoids overlapping of subsequent pointings. The drawback of this approach is that it is computational intensive with many sums running over galaxies within each of the potential FoVs.

During the Virgo/Ligo data taking run O2 both outlined algorithms were used in parallel within the H.E.S.S. multi-messenger ToO system. For GW ToO alerts that happen during a period of active observations and for which the GW uncertainty region would be visible at the time of alert reception, the rapid *One-Galaxy* algorithm was used to determine the first pointing. This information was automatically passed on to the H.E.S.S. slow control and data acquisition system, interrupting

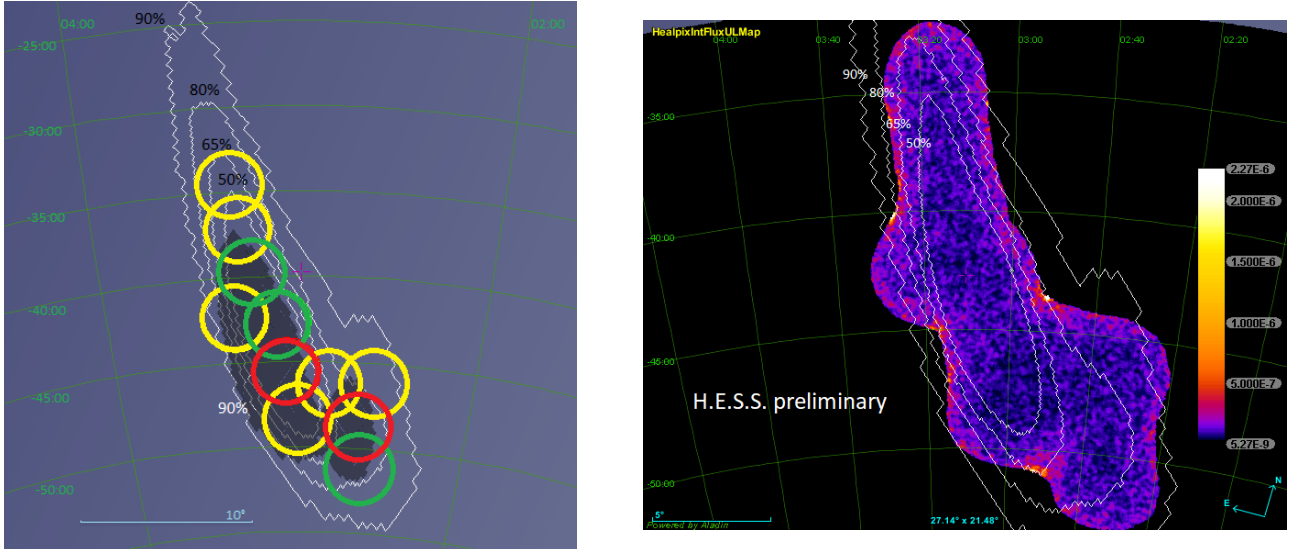


Figure 3.24: Left: H.E.S.S. pointing directions during the follow-up of GW170814. The white contours denote the uncertainty region available at the time of the observations, the shaded area show the final localization region derived from the GW data [16]. The red, green and yellow circles illustrate the H.E.S.S. observations obtained during the first, second and third night of observations. Right: Integral VHE gamma-ray flux limits (95 % C.L., assuming a E^{-2} spectrum) in units of $m^{-2}s^{-1}$ derived from H.E.S.S. follow-up observations. From Master thesis of Halim Ashkar (Obs. Paris / IRFU, CEA Paris-Saclay)

ongoing observations and requesting the slewing to the calculated coordinates and the start of the observations. During this time, the *Galaxies-in-FoV* calculation was launched to derive an updated and extended pointing pattern covering as much of the GW uncertainty region as fast as possible. Updates of the system in preparation of the run O3 which started on April 1st, 2019 extended these capabilities. The system is now for example including the automatic treatment of GW events without 3D information (e.g. detected by un-modeled GW burst searches), dedicated treatment of mergers reconstructed outside the completeness range of the galaxy catalog or events falling into regions with low completeness (e.g. close to the Galactic Plane).

An example for a single H.E.S.S. pointing selected based on this procedure is shown in the left plot of Fig. 3.22. Simulating the GW events expected for the Virgo/LIGO run O2 and injecting all available simulated GW events at random times into the developed GW-Scheduler, we derived the performance of the follow-up. Fig. 3.23 shows the achieved coverage of the GW uncertainty region for all simulated events assuming a follow-up of maximum 10h. On average we are able to cover 32.4% (20.9%) of the GW uncertainty region with hybrid (CT5-mono) observations. Based on the typical H.E.S.S. sensitivity, we reach a sensitivity of $\approx 5\%$ Crab at 5σ throughout the covered region. It should be noted that in reality follow-up observations are only triggered if a minimum percentage of the full GW uncertainty area can be covered. The value of this criterion is depending on the nature of the event, available MWL information, etc. As example, already triggering only on events for which at least $> 5\%$ of the total region can be covered, reduces the number of accepted alerts by 20% but increases the average coverage by about the same margin (i.e. from 26.1% to 32.4%).

3.5.2 GW170814: the first complete VHE gamma-ray follow-up

After several technical trial runs using GW alerts during O1 and O2, the first complete coverage of an uncertainty region provided by the LIGO and VIRGO GW event reconstruction could be performed by H.E.S.S. on August 14, 2017. The binary black hole merger GW170814 was the first GW event

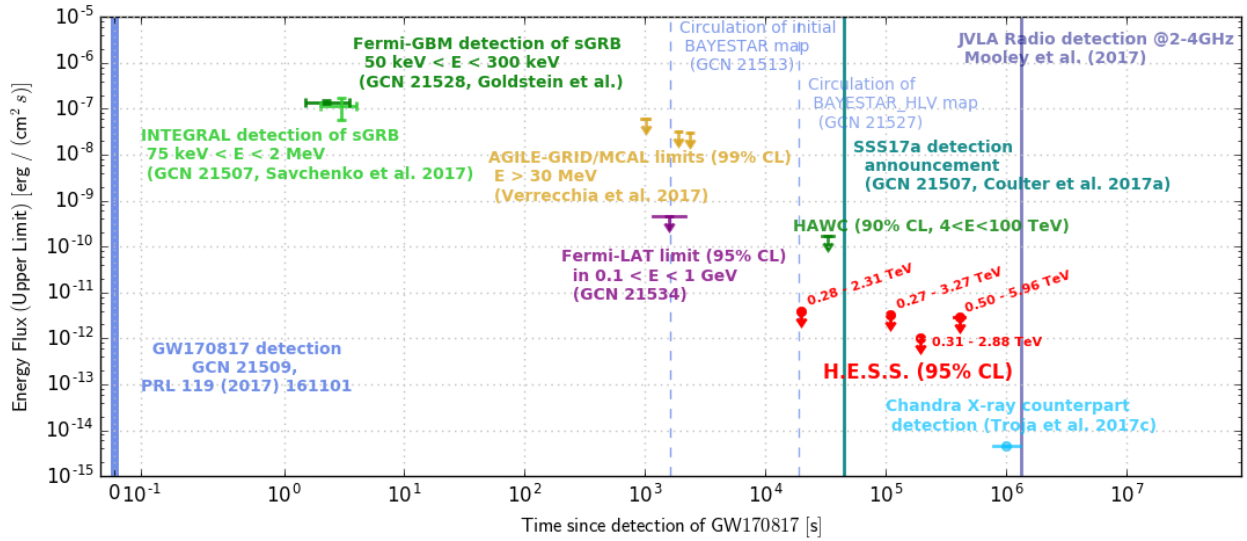


Figure 3.25: Timeline of the discovery of GW170817, GRB 170817A, SSS17a/AT 2017gfo with a focus on the high-energy, non-thermal domain. A more complete picture of the multi-wavelength and multi-messenger campaign is given in [18]. Figure modified from [24].

that was observed by all three interferometers. Its localisation could therefore be improved from $\sim 1160 \text{ deg}^2$ using only the two LIGO detectors to a 90 % credible region spanning only $\sim 60 \text{ deg}^2$ using all three detectors [16]. This regions was covered by thirteen H.E.S.S. observations obtained in three nights (16, 17 and 18 August 2017) maximizing the GW map coverage using the *Galaxies-in-FoV* approach outlined in Sec. 3.5.1. Details of the observations have been shared with the MWL community in [153] and are illustrated in the left part of Fig. 3.24. A real time analysis showed no significant gamma-ray emission. Together with a Master student (Halim Ashkar, Observatoire de Paris/Meudon) we checked the quality of the data by investigating potential hardware malfunctions, calibration problems, trigger rates etc. for each telescope participating in the data acquisition. No apparent problem has been found for any of the taken observations. We proceeded then to analyze the data searching for high-energy gamma-ray emission from the region compatible with the VIRGO/LIGO localization uncertainty. No significant gamma-ray emission has been found and integral flux upper limit maps within the energy range $0.25 \text{ TeV} < E < 20 \text{ TeV}$ could be derived following the method introduced in Sec. 3.3.2. The map is shown in Fig. 3.24 and constrains for the first time VHE gamma-ray emission from a BH-BH merger on a 3-day timescale.

3.5.3 GW170817: the first binary neutron star merger

On August 18, 2017, LIGO and Virgo detected for the first time gravitational-waves from a pair of in-spiralling neutron stars (GW170817 [17]). Mergers of binary neutron stars had been proposed as candidates for the origin of short Gamma-Ray Bursts and associated to kilonova events (see [118] for a recent review). The announcement of the event triggered one of the most extensive follow-up campaigns involving 70 observatories around the world and in space and across all wavelength ranges (cf. Fig. 3.4 and Fig. 3.25). Electromagnetic emission from the collision was observed in multiple wavelength bands and GW170817 is therefore the first cosmic event from which both gravitational waves and light has been observed. The analysis of the obtained wealth of data allowed to confirm the connection between NS-NS mergers and GRBs and kilonovae. Combining information from all three gravitational wave interferometers the event could be localized within a few hours to a region

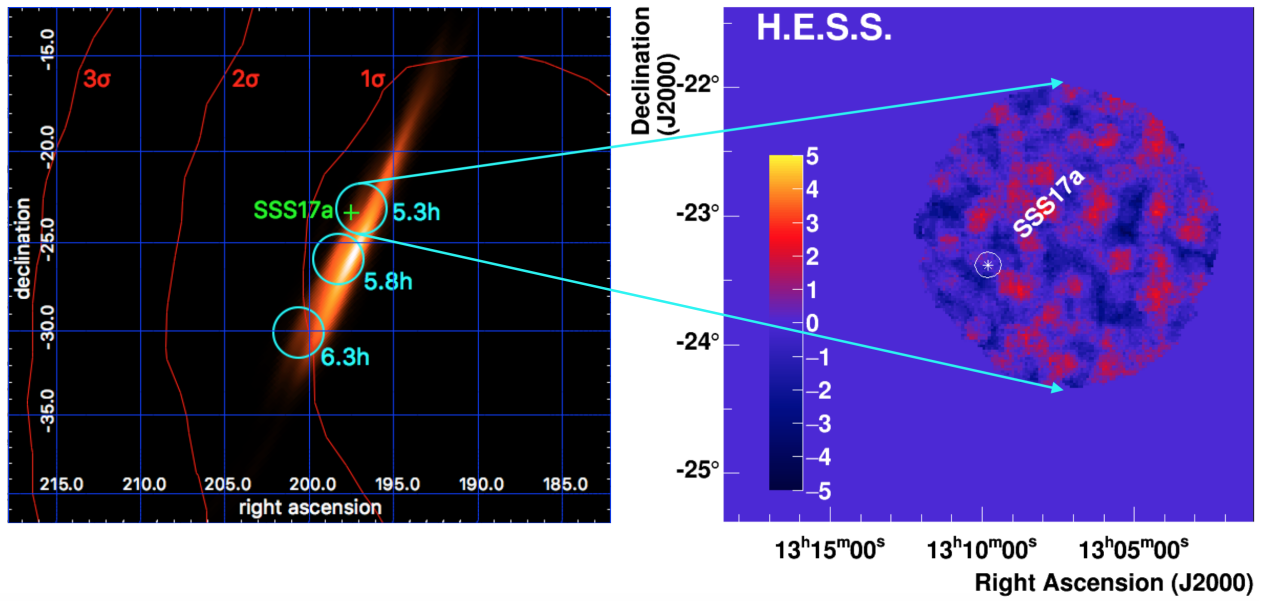


Figure 3.26: Left: Pointing directions of the first night of H.E.S.S. follow-up observations of GW170817 starting 2017-08-17 17:59 UTC. The circles illustrate the H.E.S.S. FoV with radius of 1.5 deg and the shown times are the start times of each observation with respect to GW170817. The localization map of GW170817 derived from the LIGO and Virgo observations is shown as shaded background, the thin lines denote the uncertainty contours of GRB170817A derived from Fermi-GBM observations. Right: Map of significances of the gamma-ray emission in the region around SSS17a obtained during the first observation of GW170817. The circle has a diameter of 0.1deg, corresponding to the H.E.S.S. point spread function. From [24].

spanning $\sim 31 \text{ deg}^2$ at a luminosity distance of 40^{+8}_-8 Mpc , a region compatible with the localization of the short gamma-ray burst (GRB 170817A [107]) detected by *Fermi*-GBM and INTEGRAL $\sim 1.7 \text{ s}$ after the GW event.

Due to the localization of the event to the Southern sky, the H.E.S.S. observatory was the only IACT able to participate in the follow-up campaign. Observations started on August 17, 2017 at 17:59 UTC, only about 5 minutes after the publication of the localisation of the event by LIGO/Virgo [24]. The observations thus started only 5.3h after the detection of the gravitational wave event. The provided uncertainty region comprised about $\sim 31 \text{ deg}^2$ on the sky. Using the full 3D information combined with the GLADE galaxy catalog in the *Galaxies-in-FoV* approach outlined in Sec. 3.5.1, promising regions to host the binary neutron system and thus the merger event could be determined very rapidly. The most probably region that we selected and observed with H.E.S.S. contained the location of the electromagnetic counterpart to the gravitational wave event that has been identified in the optical domain several hours after the H.E.S.S. observations (cf. Fig. 3.26). As a result, H.E.S.S. was the first ground-based pointing instrument to obtain data on the object which turned out to be the afterglow of GRB 170817A and the first confirmed kilonova. The transient source has been named SSS17a by the discovery team, the One-Meter Two-Hemisphere (1M2H) Collaboration using the 1m Swope telescope at Las Campanas Observatory in Chile and was later given the IAU identification AT 2017gfo.

A subsequent monitoring campaign of the kilonova with H.E.S.S. extended over several days, covering timescales from 0.22 to 5.2 days after the merger and an energy range between 270 GeV and 8.55 TeV. No significant gamma-ray emission has been found within this time interval. The derived upper limits on the very-high-energy gamma-ray flux for the first time constrain non-thermal, high-

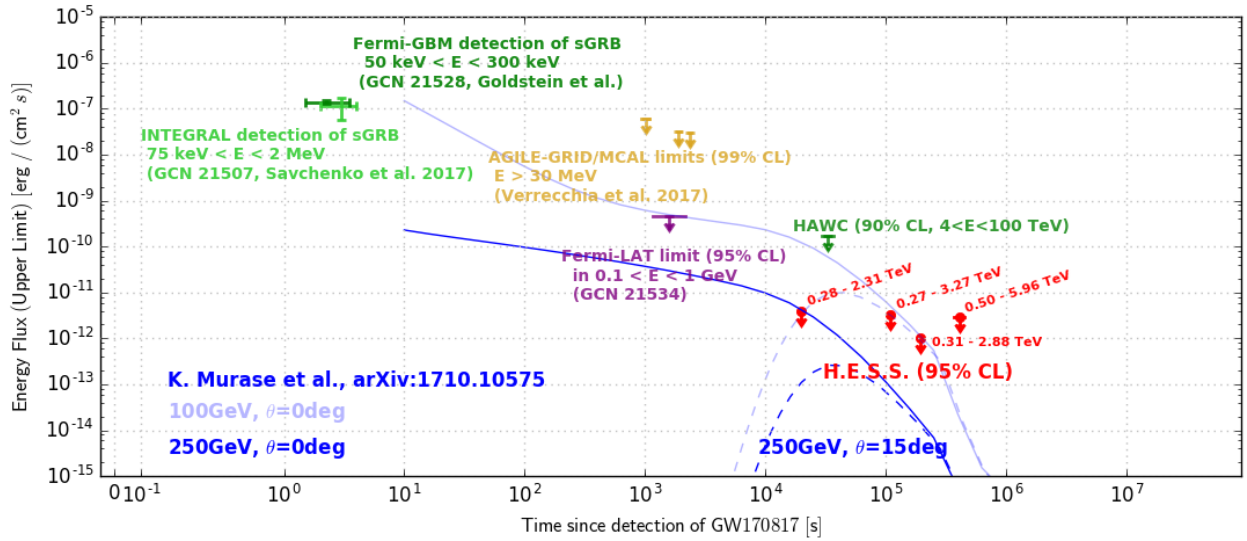


Figure 3.27: Same data as in Fig. 3.25 compared to model predictions for the high-energy afterglow emission proposed by [124] for various angles θ between the line-of-sight and the relativistic jet. Figure modified from [24].

energy emission following the merger of a confirmed binary neutron star system [24]. These results are clearly a highlight of the H.E.S.S. multi-messenger program and a milestone in high-energy multi-messenger astrophysics. Their use in multi-wavelength and multi-messenger models of mergers of compact object is only just starting. Comparing the obtained limits to model predictions from [124], one is for example able to rule out the presence of a face-on relativistic jet pointing directly at Earth (cf. Fig. 3.27), an observation that matches well with the late onset of the X-ray and radio afterglows.

The radio and X-ray emission of the remnant of GW170817 showed now spectral cooling feature and the flux continued to rise over timescales of several months. Assuming that this emission is electron synchrotron in origin, constraints on the magnetic field strengths can be derived from (non-)observations of the associated inverse Compton VHE gamma-rays [133]. These considerations led the H.E.S.S. multi-messenger group to conduct extended observations over several months starting in 12/2017. These observations cover the time period of the maximum emission observed in X-rays and the radio domain (cf. Fig. 3.28). The data is currently being analyzed and will allow constraining the magnetic field in the region of the relativistic jet that was emitted after the neutron star merger.

3.6 The Cherenkov Telescope Array

After more than a decade of preparation of the next generation, IACT based, high-energy gamma-ray observatory, the Cherenkov Telescope Array (CTA) is currently entering its construction phase. After completion, currently expected in the mid-2020s, the CTA observatory will operate more than 100 IACTs on two sites, one on each hemisphere. While the northern hemisphere array, located at the Observatorio del Roque de los Muchachos Roches on the island of La Palma, will be more limited in size and will focus on the low- and mid-energy range from 20 GeV to 20 TeV, the southern hemisphere array, located in Chile near the Paranal site of the European Southern Observatory, will span the entire energy range, covering gamma-ray energies from 20 GeV to 300 TeV. Three classes of telescope will be distributed across these two sites based on their sensitivity: the Small-Sized Telescopes (SST), Medium-Sized Telescopes (MST), and Large-Sized Telescopes (LST), cf. Fig. 3.29).

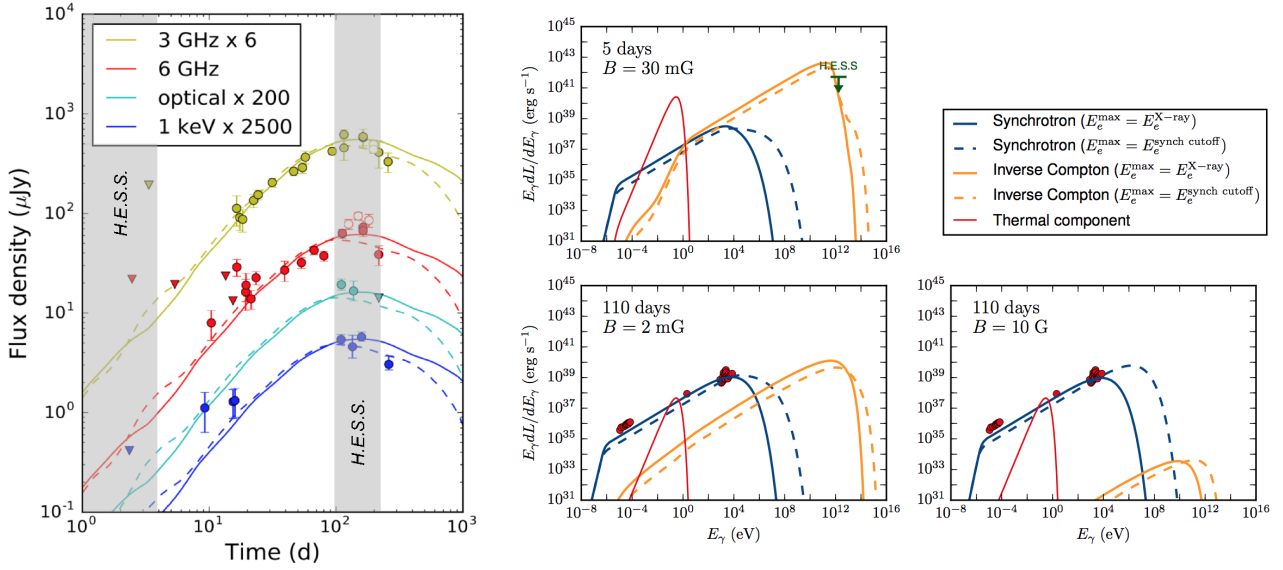


Figure 3.28: Left: Evolution of the radio and X-ray emission of GW170817 indicating the observation windows of the H.E.S.S. follow-up. Figure modified from [47]. Right: Theoretical luminosity spectrum produced by electron synchrotron emission at various times after a binary neutron star merger in comparison to the early H.E.S.S. observations [24] and radio-to-X-ray data from [113]. Further H.E.S.S. observations around 110 days will allow to constrain the strength of the magnetic field. Figure from [133].

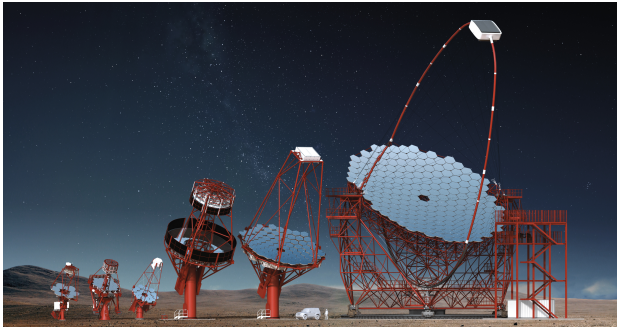
The SST array is optimized for the highest energies and will be only installed in the southern site which provides access to the Galactic plane and its wealth of high-energy sources. The MSTs and LSTs will be installed on both sites. Commissioning of the first LST has started in late 2018.

In addition to a low energy threshold, the LSTs are also able to slew within less than 30 seconds to any position in the sky. They therefore make CTA a very well suited observatory to react to observations and alerts from the multi-wavelength and multi-messenger community. Combining the fast reaction, the (comparably) low energy threshold and the high sensitivity CTA will be able to study the wealth of high-energy transient phenomena in unprecedented detail. Preparations for these exciting observations are ongoing within the CTA consortium and the CTA observatory through a variety of steps.

3.6.1 Preparations for the CTA transient program

Preparations for the CTA science operations started by defining the Key Science Projects (KSPs) [68]. During this process I participated in the outline of an observation program dedicated to transient phenomena, the “CTA Transients Key Science Project”. Based on and extending the current state-of-art multi-wavelength and multi-messenger follow-up programs by the current IACT experiments like H.E.S.S. (see for example Sec. 3.3.3 and 3.5), the Transient KSP will comprise observations of several interconnected source classes. The different sources, their priority as well as an estimate for the observation time that will be allocated by the CTA observatory for them is given in Tab. 3.3. With the start of science observations of the CTA observatory still some years in the future and given the extremely rapid evolution especially of the field of multi-messenger transients, one should note that these numbers can only be a very preliminary estimate. Significant adjustments and updates are currently being discussed.

After the outline of the KSPs, the details of the future operation and observations with CTA were defined as *use cases*. These were produced at all levels of the observatory and then combined in a



(a) CTA telescopes



(b) A global observatory

Figure 3.29: Left: Schematic view of the different telescope types that will form the Cherenkov Telescope Array observatory. Right: World map of the participating countries and the two sites of the observatory (red stars, modified from cta-observatory.org).

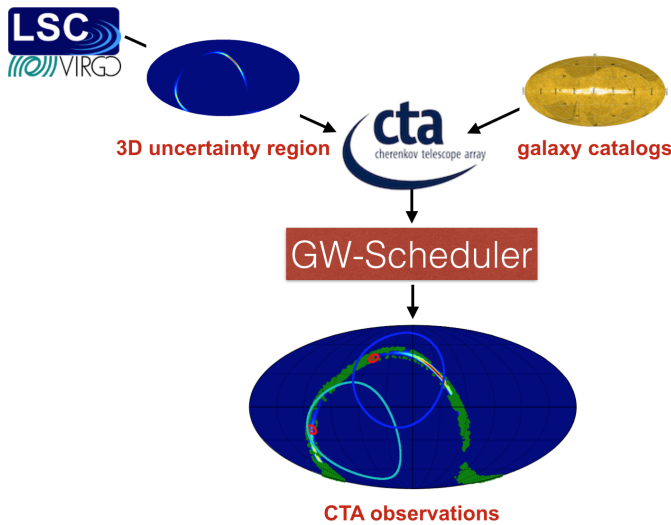
Table 3.3: Summary of proposed observations within the CTA Transients Key Science Project [68]

Priority	Observation times (h yr ⁻¹ site ⁻¹)	Target class		
		Early phase	Years 1–2	Years 3–10
1	GW transients	20	5	5
2	HE neutrino transients	20	5	5
3	Serendipitous detections	100	25	25
4	GRBs	50	50	50
5	MWL transients	50	10	10
6	Galactic	150	30	0
Total per site (h yr ⁻¹ site ⁻¹)		390	125	95
Total both sites (h yr ⁻¹)		780	250	190

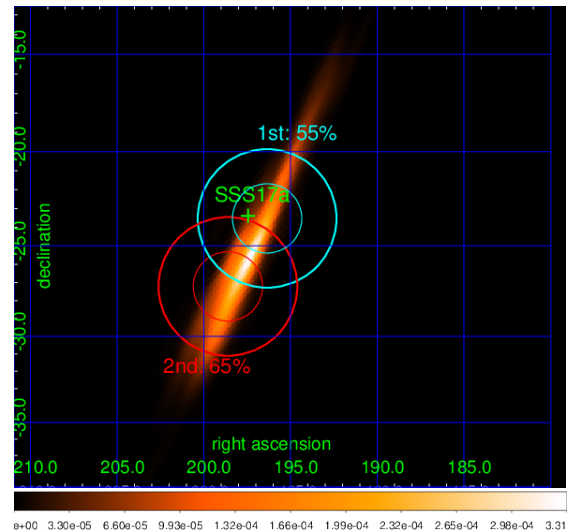
high-level layer, the *Top Level Use Cases (TLUCs)*. In addition to being co-responsible for the definition and validation of all CTA Science TLUCs, I also led the groups developing the specific TLUCs on “Gravitational wave follow-up” and “High-Energy neutrino follow-up”. Again based on our experience with current IACTs, we outlined detailed observation scenarios ranging from the reception of the alerts, their analysis, the reaction of the CTA infrastructure to the final physics observations.

A schematic view of the reception of gravitational wave alerts by CTA is given in Fig. 3.30a. As can be seen, the crucial component in this scheme is the *CTA GW-Scheduler*, which is the tool that combines all available information (e.g. the GW uncertainty map, galaxy catalog(s), status information of the CTA array, etc.) and derives an optimal observation strategy and schedule. A first version of this tool has been implemented and is being used to study the potential performance of the CTA GW follow-up. An illustration is given in figure 3.30b, where the simulated CTA response to the binary neutron star merger event GW170817 is given. The figure shows the two individual observations that would be necessary to cover the majority of the GW uncertainty region (individual coverages assuming the 8deg FoV of the CTA SSTs are given as percentage). Similar to the H.E.S.S. observations of GW170817 (cf. Sec. 3.5.3) the first pointing would already contain the (a-priori unknown) direction of the merger event.

Further quantifications of the CTA performance are currently being done by applying the developed scheduling tool to an extensive set of simulated neutron star mergers [127]. Including all known observational effects like the visibility from both CTA sites, observational constraints like dark-time



(a) Scheme of CTA reaction to GWs



(b) Simulated CTA follow-up of GW170817

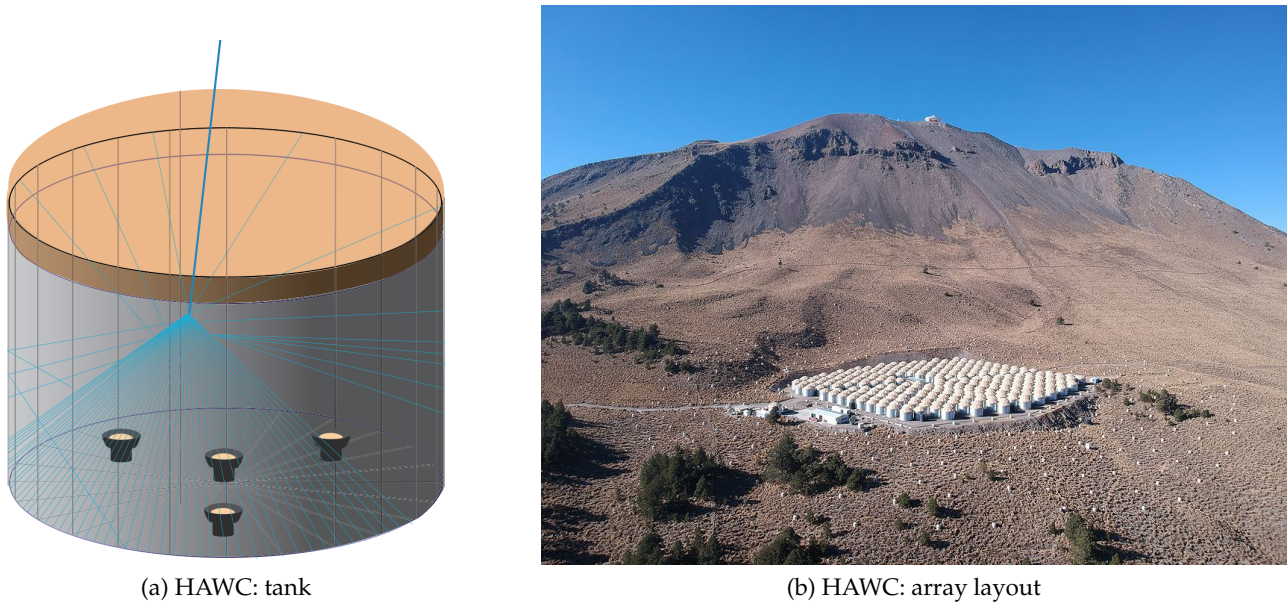
Figure 3.30: Left: The workflow of the reaction of CTA to the detection of a gravitational wave as outlined in the CTA Key Science Projects and the CTA Science Top Level Use Cases. Right: Simulated response of CTA to the binary neutron star merger GW170817 showing the two individual observations that would be necessary to cover the majority of the GW uncertainty region. From [142]

and moon-distance as well as the simulated response of CTA to an estimation of the flux and spectral evolution of the associated high-energy electromagnetic emission, the CTA Transient Science Working Group (Transient SWG) that I currently lead is working towards an estimate of the number of successful detections of high-energy counterparts of GW events.

3.7 The High Altitude Water Cherenkov Observatory (HAWC)

Building on the success of the MILAGRO observatory, the construction of the *High-Altitude Water Cherenkov Observatory* (HAWC) has been finalized in early 2015. The observatory is located near the mountains Pico de Orizaba and Sierra Negra at an altitude of 4150 m and consists of 300 water Cherenkov detectors (WCDs, cf. Fig. 3.31a), each holding 200 m³ of water monitored by three 8-inch and one 10-inch hemispherical photomultiplier tubes. This core detector covers an area of 20,000 m² and deployment of the full detector took about 2.5 years. During deployment, data taking with subsets of the full array allowed to verify the DAQ, prepare the reconstruction and analysis software and produce first physics results [26, 28]. In 2017/2018 an additional array of smaller, outrigger stations has been installed to improve the performance especially at high-energies. An overview over the HAWC observatory is shown in Fig. 3.31b.

The detector records the passage of the particles in extensive air showers which have been induced by cosmic rays and gamma-rays in the atmosphere above the array. The altitude and detector size make HAWC sensitive to air showers induced by primary particles with energies between about 100 GeV and 100 TeV. Due to the different development of hadronic and gamma-ray induced showers, the two components can be separated efficiently above a few hundred GeV. The angle of incidence of the primary particle and the location of the air shower core can be reconstructed from the timing of the individual PMTs with a resolution of better than 0.2° at the highest energies [29]. The total charge (recorded via a pair of time-over-threshold measurements for each PMT) and hit multi-



(a) HAWC: tank

(b) HAWC: array layout

Figure 3.31: Schematic view of a single HAWC WCD (left, from [29]) and the layout of the completed HAWC array (right, from [112]).

plicities provide access to the primary energy with a resolution of better than 50 % above 10 TeV.

Over the last years, HAWC illustrated the performance of the detection technique and provided significant new results about the highest energy gamma-ray sky (e.g. [30]). Its sensitivity to very extended emission regions allowed for example the unexpected detection of large halos around nearby pulsar wind nebulae and the measurement of the CR diffusion coefficients around these objects [27] thus shedding new light on the excess of positrons detected by AMS. Another striking result is the first detection of TeV gamma-ray emission from the microquasar SS 433 [31].

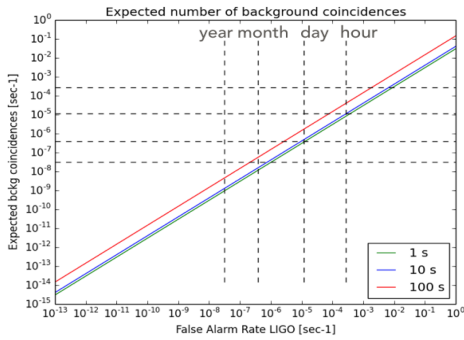
HAWC has an instantaneous aperture that covers more than 15 % of the sky. With this large field of view, the detector is exposed to 2/3 of the sky during a 24-hour period. Combined with its effective data taking duty cycle of greater than 95 %, HAWC is thus able to constantly monitor the high-energy sky. This capability is obviously especially important for transient events. These can be detected by HAWC itself (and then trigger detailed follow-up observations with IACTs or observatories at other wavelengths). An example for this scenario is the HAWC detection of a flaring activity of Mrk421 in January 2017. H.E.S.S. reacted to the information and was able to use its newly installed upgraded camera system to perform deep observations of the source (cf. [23]).

By storing all recorded data on disk, HAWC is also able to react to external alerts and especially is able to provide information on short timescales that reach below the alert distribution time. This is a significant advantage for example in the search for counterparts to GWs whose alerts are typically distributed only after delays reaching from several minutes to hours.

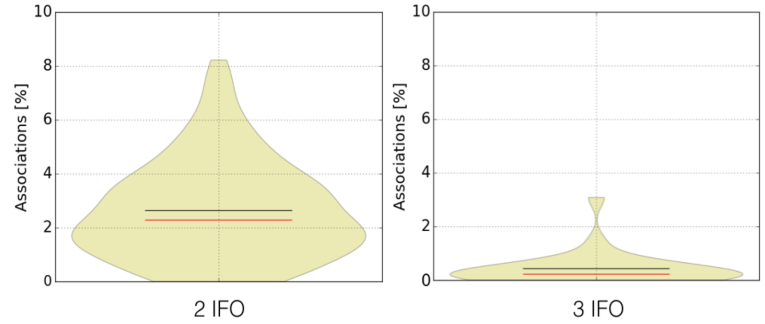
Another interesting possibility for all-sky monitoring observatories like HAWC is to combine their data at a low level with similar instruments observing in other wavelengths or detecting other astrophysical messengers.

3.7.1 Coincidences of sub-threshold events of Virgo/Ligo and HAWC

One of the main aims of the AMON network consist in combining sub-threshold events from different observatories through dedicated coincidence analyses (cf. Sec. 3.3.5). These coincidences could



(a) Temporal FAR



(b) Final HAWC-Virgo/Ligo chance coincidences

Figure 3.32: Left: False-Alarm-Rate of temporal coincidences between sub threshold HAWC and Virgo/Ligo events. Right: Percentage of HAWC-Virgo/Ligo background associations for GW events detected by two and three interferometers.

establish a connection between two signals unveil their common origin. The follow-up campaign on the high-energy neutrino event IC-170922A and the subsequent discovery of the flaring blazar TXS 0506+056 (cf. Sec. 3.3.4), can serve as an example for the promise of such searches. The triggering IceCube neutrino had a $\sim 44\%$ probability to be of atmospheric origin [165]. Only the connection with a flaring blazar, which, if taken on its own can be considered another insignificant event, made the multi-messenger event significant.

In an attempt to enhance the discovery space of searches of counterparts to gravitational wave events, the AMON framework has been extended with a likelihood based analysis searching for coincidences between GW events provided by Virgo/Ligo and VHE gamma-ray data from the HAWC observatory by Monica Seglar-Arroyo (PhD student under my co-supervision jointly with M. Mostafa, PennState). The Virgo/Ligo events can be both, highly significant public events as well as sub-threshold events. The latter are currently not distributed publicly and an agreement with the Virgo/Ligo collaboration to provide rapid access is still under discussion. The used HAWC data is resulting from an unbiased all-sky search method for short-timescale VHE transients that does not rely on external trigger information [104]. It searches for excesses in different time windows of 0.2, 1, 10 and 100 seconds, motivated by the typical timescales of short and long GRBs.

The developed likelihood framework uses realistic estimates of the background PDFs for both, the Virgo/LIGO and the HAWC data. The spatial correlation is treated on an event-by-event basis using the localization maps derived from the GW data, while the different time windows used in the HAWC searches are used to define coincidence time intervals. The expected False-Alarm-Rate (FAR) induced by chance temporal coincidences has been derived using the rate of sub-threshold short-timescale hotspots detected by HAWC over the first two years of operations. Its dependence on the FAR of the sub-threshold Virgo/Ligo events is illustrated in Fig. 3.32a. The rate of chance spatial coincidences depends strongly on the size of the localization region derived from the GW observations. As these depend on the number of interferometers that participated in the detection, the final fraction of events arising from from chance associations between HAWC and Virgo/Ligo is shown in Fig. 3.32b.

The sensitivity goal for O3 is a detection horizon for binary neutron star merger events around $D \approx 120$ Mpc. One can therefore expect 7.2 BNS per year are expected to be above the publication threshold. At the same time an extra 25.9 BNS event per year are expected to happen in the sub-threshold regime, i.e. at distances between 120 Mpc and 200 Mpc. The 70 % duty cycle for each interferometer implies that around 23 of these could be detected by either a single-interferometer or

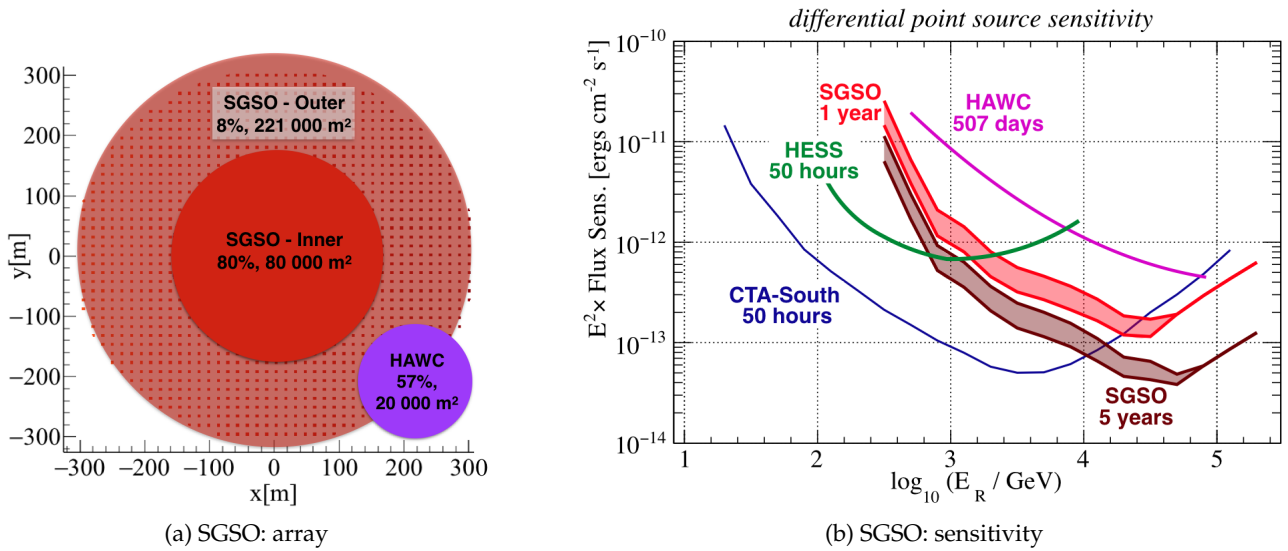


Figure 3.33: Schematic view of the SGSO observatory in comparison with HAWC (left, from [46]). The SGSO *straw-man* sensitivity to point-like gamma-ray sources has been derived by combining the SGSO array layout, the altitude of the observatory and the established performance figures of HAWC (right, from [46]).

by two-interferometers. Considering significant single-detector and sub-threshold events together, we expect 26.3 candidate BNS events that may be available for the outlined coincidence searches during O3. The HAWC duty cycle and FoV imply that about 25 % of these events will occur within the active field of view, thus implying useful data for 6.6 single-detector and sub-threshold BNS events conceivably observable by HAWC.

3.8 The Southern Gamma-ray Survey Observatory (SGSO)

As outlined in Sec. 3.6, I believe that the future of high-energy gamma-ray astronomy will be dominated by the Cherenkov Telescope Array. Its high sensitivity and unprecedented resolution will provide significant new insights into the highest energy phenomena of the universe, answer many of our current questions and (hopefully) create new ones. At the same time, the recent results provided by the HAWC observatory (cf. Sec. 3.7) highlight the maturity of the ground-based, particle detection technique for high-energy gamma-ray astronomy. Both techniques are largely complementary to each other:

- Ground based particle detectors are able to monitor the sky with a 100% duty-cycle and a field-of-view covering about 1 sr instantaneously. They are able to detect and measure very extended emission and provide real-time information on transient phenomena.
- Limited by their (15%) duty-cycle, IACTs are able to observe a limited number of pre-defined objects but provide detailed measurements on energy spectra, morphologies and variability.

Exploiting these complementary features, a promising way for future observations is thus the combination of both techniques. Accompanying the construction of CTA (providing significant improvements over current IACTs), a similar improvement over HAWC is expected to come from the installation of the LHAASO observatory in China. Unfortunately this next-generation large field-of-view



Figure 3.34: The SGSO-Alliance comprises currently more than 120 members from 18 countries (April 2019). The yellow circle illustrates the potential implementation region of the observatory.

observatory is (as HAWC) located on the northern hemisphere and is thus not able to provide full sky coverage to match CTA and lacks access to most of the wealth of Galactic sources. In addition, the LHAASO design is focussing on the highest energies and will therefore not be the prime observatory for transient, typically low-energy multi-messenger and multi-wavelength studies like searches for counterparts to GWs, high-energy neutrinos, etc.

These arguments motivated the initiation of a project that is now called the *Southern Gamma-ray Survey Observatory (SGSO)*. Since its formal installation in early 2018 a growing group of currently about 120 scientists from 18 countries have already joined the SGSO Alliance (sgso-alliance.org, cf. Fig. 3.34). Our aim is to develop a next-generation air shower detector located at a high-altitude site in the mountains of South America. Its design and location will enable SGSO to play an important role in the study the highest energy particle accelerators in our Galaxy (e.g. the full population of TeV halos around pulsar wind nebulae, proton accelerators reaching beyond PeV energies, etc.). Given its enormous advantage like the 100% duty cycle and its large field-of-view, SGSO will especially be a highly performant instrument for studies of transient, multi-messenger and multi-wavelength phenomena.

In its current design, the core array of SGSO will cover about 80.000 m² (cf. Fig. 3.33a) at a site of about 5000m above sea level in the Andes Mountains. A potential site has been identified near San Antonio de Los Cobres (Province of Salta, Argentina). Infrastructure is currently being developed on this site for the LLAMA and CUBIC instruments and a weather station is providing data since two years. Another option under consideration is the site of the ALMA observatory on the Chajnantor Plateau in Chili or high-altitude lakes in Peru or Bolivia. First estimates of the sensitivity that could be reached with this new observatory have been based on an extrapolation of the established HAWC performance figures (cf. Fig. 3.33b) extrapolated to higher altitudes and a larger and denser detector array.

Already this *straw-man* design (i.e. using monolithic, large water Cherenkov detector similar to HAWC) would provide significant sensitivity for multi-messenger studies. As illustrated in Fig. 3.35b, HESS J1745-290 [33] is an excellent target for instruments optimized in the TeV range, such as CTA, and for a highly sensitive instrument in the 10s of TeV range, such as SGSO. Especially the highest energy data will allow to understand the production of PeV particles at the first known Galactic PeV accelerator in detail. Another example is given in Fig. 3.36a where the potential of SGSO for

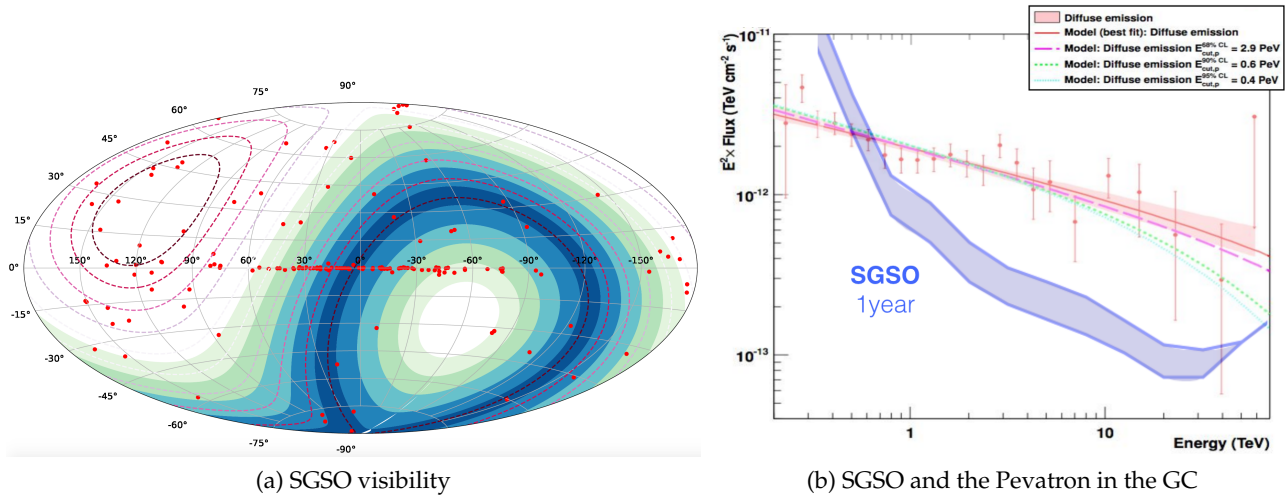
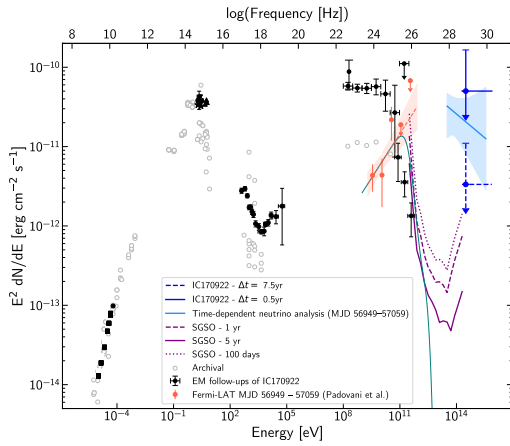


Figure 3.35: Sky-map in galactic coordinates showing the complementarity of the visibility ranges between HAWC (red lines) and SGSO (color bands). The red dots mark currently known TeV sources (right, from [46]). The first Pevatron detected by H.E.S.S. in the Galactic Center (J1745-290 [33]) is a prime target for SGSO searches (right, from [46]).

searches of high-energy gamma-ray sources in coincidence with high-energy neutrinos is illustrated using the first such detection, the IceCube-170922A vs TXS 0506+056 correlation (cf. Sec. 3.3.4, [165]). As discussed above, high-energy neutrinos travel through the universe unhindered but high-energy gamma-rays lose energy in interactions with the extragalactic infrared and microwave background radiation. To be able to probe correlations between different messengers like neutrinos and high-energy gamma rays, the sensitivity in the gamma-ray energy range starting at ≈ 100 GeV is crucial. This importance is further amplified by the fact that most emission scenarios (e.g. GRBs as GW counterparts, etc.) predict steeply falling energy spectra within this range. It is thus crucial to focus potential improvement to the detector and array design to improving the response of SGSO toward *low* energies, i.e. towards the 100 GeV range. At the same time, the installation of SGSO in South America allows to provide an unbiased view of the high-energy Southern sky, including the central part of the Galactic Plane with its multitude of TeV sources (cf. Fig. 3.35a) reaching to extreme energies above 100s of TeV. SGSO will thus certainly be extended by an outrigger array reaching a large effective area at high energies. A white paper on the detailed description of the expected science reach of SGSO has been finalized recently. Summaries have been presented for example in [60, 155] and are summarized in general white paper on the SGSO science case [46].

Thanks to its large field-of-view and duty-cycle, SGSO's continuous monitoring capability of the Southern sky will be unrivaled and SGSO will be a key player in the multi-wavelength and especially the multi-messenger community. Its unique monitoring capabilities will allow to alert observers around the world, across the full electromagnetic spectrum and all known messengers of new detections and phenomena. These alerts will be provided in real-time and will thus allow triggering detailed follow-up observations. While broad-band MWL information will be an important ingredient to the SGSO science, the expected performance is to a significant extent complementary to and beneficial for the science of the upcoming CTA. SGSO will for example act as a high-duty cycle, large FoV finder scope for deep and high-resolution CTA observations for many sources, including transient phenomena in various multi-wavelength and multi-messenger contexts. In addition to providing real-time "triggers" to CTA, SGSO may also provide important input for detailed CTA analysis on extended sources like PWNe, their TeV halos, the Fermi Bubbles or the diffuse Galactic emission.



(a) Multi-messenger observations with SGSO



(b) Potential SGSO design

Figure 3.36: The multi-messenger spectrum of TXS 0506+056 and Icecube-170922A illustrating the potential of SGSO (left, from [46]). A potential design of the individual SGSO stations using a layered WCD in order to increase the identification of muon-rich hadronic background events and improving the performance of the energy and timing/directional reconstruction.

The ambitious goals of SGSO will be made possible by important developments and design studies. Various detector and array designs are currently studied with simulations and validated with prototypes. In parallel, several candidates for an optimal site for the future observatory have been identified and are being assessed. One of the crucial parameters for many science cases is the low energy performance, which in ground based gamma-ray detectors like SGSO is dominated by the capability to separate the gamma ray induced air showers from the hadronic cosmic ray background. Various possibilities exist for this task: hadronic interactions with high transverse momentum create sub-showers at large distances from the main shower core, i.e. reflected by a more distributed pattern of signals at ground level which can be exploited by a fine segmentation of the detector array. Another striking feature is the presence of penetrating muons in hadronic air showers. Tagging of muons within the detector stations is thus a highly efficient way to select and veto cosmic ray backgrounds and thus achieve a significantly lower energy threshold and thus physics reach. One of several ideas on a possible technical implementation of enhanced muon tagging is based on highly separated water Cherenkov detectors (WCD). Horizontal separation into individual stations will allow detecting the detailed pattern of particles within the recorded air showers. In addition a vertical separation of each WCD into two parts seem a promising option [105]: the upper part allows for detection of signals dominated by electromagnetic particles and the lower part would be dominated by penetrating muons. A schematic view of a potential detector design is shown in Fig. 3.36b. The main parameter like the optimal heights of both sections and the advantages of black vs. reflective interiors of such a detector are currently being determined both by simulations and measurements with prototypes.

4

Summary, outlook and acknowledgements

High-energy astrophysics has seen unprecedented revolutions in the last decade. To name just a few: we detected Gravitational Waves (GWs) and could link them to Gamma-Ray Bursts (GRBs), we detected high-energy neutrinos and could link (at least one of them) to a flaring blazar, we scanned the Galactic Plane discovering a wealth of new sources emitting VHE gamma-rays and we could finally observe VHE gamma-rays from a GRB. These and many more discoveries are not only great achievements of the past: more importantly they opened new windows to the high-energy universe and thus promise even more exciting observations and discoveries. To fully exploit these possibilities, we obviously need the right instruments and observatories. Fortunately the future is also bright in this respect: the VIRGO and LIGO interferometers are being improved continuously and will path the way towards 3rd generation instruments like the Einstein Telescope and LISA. The IceCube neutrino telescope is continuing operations while IceCube-Gen2, GVD and KM3NeT are being prepared and built. The SVOM and later the ATHENA (and hopefully the THESEUS) X-ray satellites are being constructed, the pathfinders of the Square Kilometer Array (SKA) radio observatory have started operations and the full SKA is approaching fast. In the VHE gamma-ray domain, operations of the current Imaging Air Cherenkov Telescopes (H.E.S.S., MAGIC and VERITAS) are assured for the next few years until the Cherenkov Telescope Array (CTA), which is currently entering its construction phase, will take over. The HAWC observatory is producing novel and surprising results at an amazing rate, while the next-generation observatory LHAASO is being constructed and planning for a complementary counterpart on the Southern hemisphere (SGSO) is progressing.

I am extremely grateful to have been able to participate to some of these leading instruments. Following the continuous and combined effort of myself and many friends and colleagues to promote transient multi-messenger programs, many observatories are currently shifting their focus more and more to transient and multi-messenger studies and operations. These often very technical and local changes are starting to induce an even more profound modification of how high-energy astrophysics is being done: an ever increasing number of joint efforts and analyses across multiple collaborations with very different origins and histories. Together with the apparently inevitable increase in the size of the collaborations, we are witnessing an ever increasing globalization of our field. For me, these extremely fruitful and enriching exchanges with colleagues and friends around the world are one of the main personal drivers and the true reason for my confidence in the bright future of multi-messenger astroparticle physics that lies ahead of us.

4.1 Acknowledgements

As outlined above I am fortunate enough to be working across the three main fields of high-energy astrophysics: cosmic rays, high-energy neutrinos and gamma-rays. Given the size and variety of the international collaborations that I am or was directly involved in (Pierre Auger Observatory, ANTARES, H.E.S.S., CTA, HAWC, SGSO) and the various observatories with which I am/was collaborating for particular projects (IceCube, Parkes, Fermi-LAT, SVOM, GRAND, etc.), I see no way of thanking all the friends and colleagues that I met along the way. If you are reading these lines you are certainly one of them and I thank you very much for your friendship and the help, input, and feedback you provided. The exciting and enthusiastic exchanges with you are essential to my work and life.

A particular thank you goes obviously to my family Magali, Antoine, Marie and Pierre. Your support, patience, and love mean everything to me.

Bibliography

- [1] A. Albert et al. (ANTARES Collaboration). “Long-term monitoring of the ANTARES optical module efficiencies using ^{40}K decays in sea water”. In: *The European Physical Journal C* 78.8 (Aug. 2018), p. 669.
- [2] A. Albert et al. (ANTARES Collaboration). “The cosmic ray shadow of the Moon observed with the ANTARES neutrino telescope”. In: *European Physical Journal C* 78, 1006 (Dec. 2018), p. 1006. arXiv: 1807.11815 [astro-ph.HE].
- [3] M.G. Aartsen et al. (IceCube Collaboration). “Evidence for High-Energy Extraterrestrial Neutrinos at the IceCube Detector”. In: *Science* 342, 1242856 (Nov. 2013), p. 1242856. arXiv: 1311.5238 [astro-ph.HE].
- [4] M.G. Aartsen et al. (IceCube Collaboration). “Search for time-independent neutrino emission from astrophysical sources with 3 years of IceCube data”. In: *Astrophysical Journal* 779 (2013). arXiv: arXiv:1307.6669v2.
- [5] M.G. Aartsen et al. (IceCube Collaboration). “Observation of High-Energy Astrophysical Neutrinos in Three Years of IceCube Data”. In: *Physical Review Letters* 113.101101 (2014), p. 8. arXiv: 1405.5303.
- [6] M.G. Aartsen et al. (IceCube Collaboration). “Atmospheric and astrophysical neutrinos above 1 TeV interacting in IceCube”. In: *Physical Review D* 022001 (2015), pp. 1–16.
- [7] M.G. Aartsen et al. (IceCube Collaboration). “The IceCube Realtime Alert System”. In: *Astroparticle Physics* 92 (Dec. 2016), p. 30. eprint: 1612.06028.
- [8] M.G. Aartsen et al. (IceCube Collaboration). “Very high-energy gamma-ray follow-up program using neutrino triggers from IceCube”. In: *Journal of Instrumentation* 11 (Nov. 2016), P11009. arXiv: 1610.01814 [hep-ex].
- [9] M.G. Aartsen et al. (IceCube Collaboration). “All-sky Search for Time-integrated Neutrino Emission from Astrophysical Sources with 7 yr of IceCube Data”. In: *Astrophysical Journal* 835, 151 (Feb. 2017), p. 151. arXiv: 1609.04981 [astro-ph.HE].
- [10] M.G. Aartsen et al. (IceCube-Gen2 Collaboration). “IceCube-Gen2: A Vision for the Future of Neutrino Astronomy in Antarctica”. In: *arXiv: 1412.5106* (Dec. 2014). arXiv: 1412.5106 [astro-ph.HE].
- [11] R. Abbasi et al. (AMANDA Collaboration). “Search for point sources of high energy neutrinos with final data from AMANDA-II”. In: *Physical Review D* 79 (2009), pp. 1–11. arXiv: 0809.1646.
- [12] B. P. Abbott et al. (LIGO and VIRGO Collaborations). “Binary Black Hole Mergers in the First Advanced LIGO Observing Run”. In: *Physical Review X* 6, 041015 (Oct. 2016), p. 041015.
- [13] B. P. Abbott et al. (LIGO and VIRGO Collaborations). “GW151226: Observation of Gravitational Waves from a 22-Solar-Mass Binary Black Hole Coalescence”. In: *Phys. Rev. Lett.* 116.24, 241103 (June 2016), p. 241103.

- [14] B. P. Abbott et al. (LIGO and VIRGO Collaborations). “Observation of Gravitational Waves from a Binary Black Hole Merger”. In: *Physical Review Letters* 116.6, 061102 (Feb. 2016), p. 061102. arXiv: 1602.03837 [gr-qc].
- [15] B. P. Abbott et al. (LIGO and VIRGO Collaborations). “GW170104: Observation of a 50-Solar-Mass Binary Black Hole Coalescence at Redshift 0.2”. In: *Phys. Rev. Lett.* 118 (22 June 2017), p. 221101.
- [16] B. P. Abbott et al. (LIGO and VIRGO Collaborations). “GW170814: A Three-Detector Observation of Gravitational Waves from a Binary Black Hole Coalescence”. In: *Phys. Rev. Lett.* 119 (14 Oct. 2017), p. 141101.
- [17] B. P. Abbott et al. (LIGO and VIRGO Collaborations). “GW170817: Observation of Gravitational Waves from a Binary Neutron Star Inspiral”. In: *Phys. Rev. Lett.* 119 (16 Oct. 2017), p. 161101.
- [18] B. P. Abbott et al. (LIGO and VIRGO Collaborations). “Multi-messenger Observations of a Binary Neutron Star Merger”. In: *ApJ Letters* 848, L12 (Oct. 2017), p. L12. arXiv: 1710.05833 [astro-ph.HE].
- [19] B. P. Abbott et al. (LIGO and VIRGO Collaborations). “GWTC-1: A Gravitational-Wave Transient Catalog of Compact Binary Mergers Observed by LIGO and Virgo during the First and Second Observing Runs”. In: *arXiv e-prints* (Nov. 2018). arXiv: 1811.12907 [astro-ph.HE].
- [20] B. P. Abbott et al. “LIGO: the Laser Interferometer Gravitational-Wave Observatory”. In: *Reports on Progress in Physics* 72.7, 076901 (July 2009), p. 076901. arXiv: 0711.3041 [gr-qc].
- [21] H. Abdalla et al. (H.E.S.S. Collaboration). “First limits on the very-high energy gamma-ray afterglow emission of Fast Radio Bursts”. In: *Astronomy & Astrophysics* 597 (Jan. 2017), A115.
- [22] H. Abdalla et al. (H.E.S.S. Collaboration). “HGPS”. In: *Astronomy & Astrophysics* 123 (2017).
- [23] H. Abdalla et al. (H.E.S.S. Collaboration). *New eyes for the H.E.S.S. I cameras*. <https://www.mpi-hd.mpg.de/hfm/HESS/pages/home/som/2017/03/>. 2017.
- [24] H. Abdalla et al. (H.E.S.S. Collaboration). “TeV Gamma-Ray Observations of the Binary Neutron Star Merger GW170817 with H.E.S.S.” In: *ApJ Letters* 850, L22 (Dec. 2017), p. L22. arXiv: 1710.05862 [astro-ph.HE].
- [25] H. Abdalla et al. (H.E.S.S. Collaboration). “A search for very high-energy flares from the microquasars GRS 1915+105, Circinus X-1, and V4641 Sgr using contemporaneous H.E.S.S. and RXTE observations”. In: *Astronomy & Astrophysics* 612, A10 (Apr. 2018), A10. arXiv: 1607.04613 [astro-ph.HE].
- [26] A.U. Abeysekara et al. (HAWC Collaboration). “HAWC Contributions to the 34th International Cosmic Ray Conference (ICRC2015)”. In: *ArXiv: 1508.03327* (Aug. 2015). arXiv: 1508.03327 [astro-ph.HE].
- [27] A.U. Abeysekara et al. (HAWC Collaboration). “Extended gamma-ray sources around pulsars constrain the origin of the positron flux at Earth”. In: *Science* 358 (Nov. 2017), pp. 911–914. arXiv: 1711.06223 [astro-ph.HE].
- [28] A.U. Abeysekara et al. (HAWC Collaboration). “HAWC Contributions to the 35th International Cosmic Ray Conference (ICRC2017)”. In: *ArXiv: 1508.03327* (Aug. 2017). arXiv: 1708.02572 [astro-ph.HE].
- [29] A.U. Abeysekara et al. (HAWC Collaboration). “Observation of the Crab Nebula with the HAWC Gamma-Ray Observatory”. In: *ApJ* 843, 39 (July 2017), p. 39. arXiv: 1701.01778 [astro-ph.HE].

- [30] A.U. Abeysekara et al. (HAWC Collaboration). “The 2HWC HAWC Observatory Gamma-Ray Catalog”. In: *ApJ* 843, 40 (July 2017), p. 40. arXiv: 1702.02992 [astro-ph.HE].
- [31] A.U. Abeysekara et al. (HAWC Collaboration). “Very high energy particle acceleration powered by the jets of the microquasar SS 433”. In: *ArXiv e-prints* (Oct. 2018). arXiv: 1810.01892 [astro-ph.HE].
- [32] A.U. Abeysekara et al. (VERITAS Collaboration). “VERITAS Observations of the BL Lac Object TXS 0506+056”. In: *ApJ Letters* 861, L20 (July 2018), p. L20. arXiv: 1807.04607 [astro-ph.HE].
- [33] Abramowski, A. et al. (H.E.S.S. Collaboration). “Acceleration of petaelectronvolt protons in the Galactic Centre”. In: *Nature* 531.7595 (Mar. 2016), pp. 476–479.
- [34] A. Abramowski et al. (H.E.S.S. Collaboration). “Measurement of the extragalactic background light imprint on the spectra of the brightest blazars observed with H.E.S.S.” In: *Astronomy & Astrophysics* 550 (2013), A4.
- [35] A. Abramowski et al. (H.E.S.S. Collaboration). “Acceleration of petaelectronvolt protons in the Galactic Centre”. In: *Nature* 531 (Mar. 2016), pp. 476–479. arXiv: 1603.07730 [astro-ph.HE].
- [36] F. Acernese et al. “Advanced Virgo: a second-generation interferometric gravitational wave detector”. In: *Classical and Quantum Gravity* 32.2, 024001 (Jan. 2015), p. 024001. arXiv: 1408.3978 [gr-qc].
- [37] M. Ackermann et al. (Fermi-LAT Collaboration). “The First Fermi-LAT Gamma-Ray Burst Catalog”. In: *ApJS* 209, 11 (Nov. 2013), p. 11. arXiv: 1303.2908 [astro-ph.HE].
- [38] M. Ackermann et al. (Fermi-LAT collaboration). “Detection of the Characteristic Pion-Decay Signature in Supernova Remnants”. In: *Science* 339 (Feb. 2013), pp. 807–811. arXiv: 1302.3307 [astro-ph.HE].
- [39] S. Adrián-Martínez et al. (ANTARES Collaboration). “First Search for Point Sources of High-energy Cosmic Neutrinos with the ANTARES Neutrino Telescope”. In: *Astrophys. Journal* 743 (Dec. 2011), p. L14.
- [40] S. Adrián-Martínez et al. (ANTARES Collaboration). “Search for a correlation between ANTARES neutrinos and Pierre Auger Observatory UHECRs arrival directions”. In: *Astrophysical Journal* 774 (2013), p. 19. arXiv: 1202.6661.
- [41] S. Adrián-Martínez et al. (ANTARES Collaboration). “Optical and X-ray early follow-up of ANTARES neutrino alerts”. In: *Journal of Cosmology and Astroparticle Physics* 02 (Feb. 2016), p. 62. arXiv: 1508.01180.
- [42] M. Ageron et al. (ANTARES Collaboration). “The ANTARES telescope neutrino alert system”. In: *Astroparticle Physics* 35 (2012), pp. 530–536.
- [43] Vivek Agrawal et al. “Atmospheric neutrino flux above 1 GeV”. In: *Physical Review D* 53.3 (1996), pp. 1314–1323. arXiv: 9509423 [hep-ph].
- [44] J.A. Aguilar et al. (ANTARES Collaboration). “A fast algorithm for muon track reconstruction and its application to the ANTARES neutrino telescope”. In: *Astroparticle Physics* 34 (Apr. 2011), pp. 652–662.
- [45] C.W. Akerlof et al. “The ROTSE-III Robotic Telescope System”. In: *PASP* 115 (2003), pp. 132–140.
- [46] A. Albert et al. (SGSO Alliance). “Science Case for a Wide Field-of-View Very-High-Energy Gamma-Ray Observatory in the Southern Hemisphere”. In: *arXiv e-prints* (Feb. 2019). arXiv: 1902.08429 [astro-ph.HE].

- [47] K. D. Alexander et al. “A Decline in the X-Ray through Radio Emission from GW170817 Continues to Support an Off-axis Structured Jet”. In: *ApJ Letters* 863, L18 (Aug. 2018), p. L18. arXiv: 1805.02870 [astro-ph.HE].
- [48] P. Allison et al. (ARA Collaboration). “Design and initial performance of the Askaryan Radio Array prototype EeV neutrino detector at the South Pole”. In: *Astroparticle Physics* 35 (Feb. 2012), pp. 457–477. arXiv: 1105.2854 [astro-ph.IM].
- [49] J. Alvarez-Muniz et al. (GRAND Collaboration). “The Giant Radio Array for Neutrino Detection (GRAND): Science and Design”. In: *arXiv e-prints*, arXiv:1810.09994 (Oct. 2018), arXiv:1810.09994. arXiv: 1810.09994 [astro-ph.HE].
- [50] S. Ando and J.F. Beacom. “Revealing the Supernova Gamma-Ray Burst Connection with TeV Neutrinos”. In: *Phys. Rev. Lett.* 95.6 (Aug. 2005), p. 061103.
- [51] S. Ansoldi et al. (MAGIC Collaboration). “The Blazar TXS 0506+056 Associated with a High-energy Neutrino: Insights into Extragalactic Jets and Cosmic-Ray Acceleration”. In: *ApJ Letters* 863, L10 (Aug. 2018), p. L10. arXiv: 1807.04300 [astro-ph.HE].
- [52] ANTARES Collaboration, IceCube Collaboration, The Pierre Auger Collaboration, and LIGO Scientific Collaboration and Virgo Collaboration. “Search for High-energy Neutrinos from Binary Neutron Star Merger GW170817 with ANTARES, IceCube, and the Pierre Auger Observatory”. In: *The Astrophysical Journal* 850.2 (Nov. 2017), p. L35. arXiv: 1710.05839.
- [53] A. Albert et al. (ANTARES Collaboration). “First all-flavour Neutrino Point-like Source Search with the ANTARES Neutrino Telescope”. In: *Phys. Rev. D* 96.082001 (June 2017). arXiv: 1706.01857.
- [54] ANTARES/TAToO Collaboration. In: *The Astronomer’s Telegrams* #9324, #9440, #9715, #10189, #10773, #10854 (2016-2017).
- [55] Hugo A. Ayala Solares et al. “The Astrophysical Multimessenger Observatory Network (AMON)”. In: *arXiv e-prints* (Mar. 2019). arXiv: 1903.08714 [astro-ph.IM].
- [56] P. Bagley et al. (KM3NeT Collaboration). “KM3NeT: Technical Design Report for a Deep-Sea Research Infrastructure in the Mediterranean Sea Incorporating a Very Large Volume Neutrino Telescope”. In: (2009).
- [57] S. W. Barwick et al. (ARIANNA Collaboration). “A first search for cosmogenic neutrinos with the ARIANNA Hexagonal Radio Array”. In: *Astroparticle Physics* 70 (Oct. 2015), pp. 12–26. arXiv: 1410.7352 [astro-ph.HE].
- [58] C.G. Bassa et al. “Optical and radio astrometry of the galaxy associated with FRB 150418”. In: *MNRAS* 463 (Nov. 2016), pp. L36–L40.
- [59] P.M. Bauleo and J.R. Martino. “The dawn of the particle astronomy era in ultra-high energy cosmic rays”. In: *Nature* 458 (2009), pp. 847–851.
- [60] S. BenZvi et al. “On the scientific motivation for a wide field-of-view TeV gamma-ray observatory in the Southern Hemisphere”. In: *Proceedings of the 35th International Cosmic Ray Conference (ICRC2017)* 851 (Aug. 2017).
- [61] D. Berge, S. Funk, and J. Hinton. “Background modelling in very-high-energy γ -ray astronomy”. In: *Astronomy and Astrophysics* 466 (May 2007), pp. 1219–1229. eprint: astro-ph/0610959.
- [62] M. Böttcher et al. “Leptonic and Hadronic Modeling of Fermi-detected Blazars”. In: *Astrophys. Journal* 768 (May 2013), p. 54.
- [63] D.N. Burrows et al. “The Swift X-Ray Telescope”. In: *Space Sci. Rev.* 120 (2005), pp. 165–195.

- [64] M. Caleb et al. “The first interferometric detections of fast radio bursts”. In: *MNRAS* 468 (July 2017), pp. 3746–3756. arXiv: 1703.10173 [astro-ph.HE].
- [65] L.I. Caramete and P.L. Biermann. “The mass function of nearby black hole candidates”. In: *Astronomy & Astrophysics* 521 (2009), A55. arXiv: 1107.2244.
- [66] I. Chakrabarty. “Gravitational Waves: An Introduction”. In: *ArXiv: physics/9908041* (Aug. 1999). eprint: physics/9908041.
- [67] T. Chaleil et al. “Results of PMT ageing studies”. In: *ANTARES internal note ANTARES-OPMO-2011-001* (2011).
- [68] Cherenkov Telescope Array Consortium. “Science with the Cherenkov Telescope Array”. In: *ArXiv: 1709.07997* (Sept. 2017).
- [69] G. Dály et al. “GLADE: A galaxy catalogue for multimessenger searches in the advanced gravitational-wave detector era”. In: *MNRAS* 479 (Sept. 2018), pp. 2374–2381. arXiv: 1804.05709 [astro-ph.HE].
- [70] B. de Lotto et al. (MAGIC Collaboration). “MAGIC electromagnetic follow-up of gravitational wave alerts”. In: *IAU Symp.* 324 (2016), pp. 287–290.
- [71] M. de Naurois et al. (H.E.S.S. Collaboration). “H.E.S.S. follow-up of IceCube-170922A”. In: *The Astronomer’s Telegram #10787* (2017).
- [72] M. de Naurois and L. Rolland. “A high performance likelihood reconstruction of γ -rays for imaging atmospheric Cherenkov telescopes”. In: *Astropart. Physics* 32.5 (2009), pp. 231–252. arXiv: 0907.2610.
- [73] A. et al. de Ugarte Postigo. “ANTARES neutrino detection: Optical/NIR spectroscopy of the Swift/XRT counterpart candidate from NOT”. In: *The Astronomer’s Telegram #7994* (2015).
- [74] C.D. Dermer and A. Atoyan. “High-Energy Neutrinos from Gamma Ray Bursts”. In: *Phys. Rev. Lett.* 91.7 (Aug. 2003), p. 071102.
- [75] S. Dichiara et al. “ANTARES neutrino detection: optical spectroscopy of X-ray counterpart candidate with SALT”. In: *The Astronomer’s Telegram #7993* (2015).
- [76] D. Dornic et al. (ANTARES/TAToO Collaboration). “ANTARES neutrino detection and possible Swift X-ray counterpart”. In: *The Astronomer’s Telegram #7987* (2015).
- [77] F. Schüssler. “Energy reconstruction of ANTARES events: the dE/dX energy estimator”. In: *ANTARES internal note ANTARES-Soft-2012-008* (2012).
- [78] F. Schüssler, K. Payet, G. Vannoni. “Analysis utilities for AntDSTs”. In: *ANTARES Internal Note ANTARES-SOFT-2010-004* (2010).
- [79] F. Schüssler, K. Payet, G. Vannoni. “Data Summary Trees for Reconstructed and Simulated Antares Events”. In: *ANTARES Internal Note ANTARES-SOFT-2010-003* (2010).
- [80] G.J. Feldman and R.D. Cousins. “Unified approach to the classical statistical analysis of small signals”. In: *Physical Review D* 57.7 (1998), pp. 3873–3889. arXiv: 9711021 [physics].
- [81] C.B. Finley and S. Westerhoff. “On the evidence for clustering in the arrival directions of AGASA’s ultrahigh energy cosmic rays”. In: *Astroparticle Physics* 21 (2004), pp. 359–367. arXiv: 0309159 [astro-ph].
- [82] A. Franceschini, G. Rodighiero, and M. Vaccari. “Extragalactic optical-infrared background radiation, its time evolution and the cosmic photon-photon opacity”. In: *Astronomy and Astrophysics* 487.3 (2008), pp. 837–852. arXiv: 0805.1841.
- [83] N. Gehrels et al. “The Swift Gamma-Ray Burst Mission”. In: *ApJ* 611 (2004), pp. 1005–1020.

- [84] R. C. Gilmore et al. “Semi-analytic modeling of the EBL and consequences for extragalactic gamma-ray spectra”. In: *MNRAS* 422 (2012), p. 3189. arXiv: 1104.0671 [astro-ph.CO].
- [85] P. W. Gorham et al. (ANITA Collaboration). “The Antarctic Impulsive Transient Antenna ultra-high energy neutrino detector: Design, performance, and sensitivity for the 2006-2007 balloon flight”. In: *Astroparticle Physics* 32 (Aug. 2009), pp. 10–41. arXiv: 0812.1920 [astro-ph].
- [86] R. Gracia Ruiz et al. (ANTARES Collaboration). “Search for signal emission from unresolved point sources with the ANTARES neutrino telescope”. In: *Proceedings of the 34th ICRC* (2015).
- [87] E. Gross and O. Vitells. “Trial factors for the look elsewhere effect in high energy physics”. In: *Eur. Phys. J. C* 70 (2010), pp. 525–530.
- [88] G. Hallinan et al. “Jansky VLA observation of the ANTARES neutrino detection region”. In: *The Astronomer’s Telegram* #7999 (2015).
- [89] A.M. Hillas. “The Origin of Ultra-High-Energy Cosmic Rays”. In: *Ann. Rev. Astron. Astrophys.* 22 (1984), pp. 425–444.
- [90] K. D. Hoffman. “High energy neutrino telescopes”. In: *New Journal of Physics* 11.5, 055006 (May 2009), p. 055006. arXiv: 0812.3809.
- [91] P. Hofverberg et al. (H.E.S.S. Collaboration). “Commissioning and initial performance of the H.E.S.S. II drive system”. In: *Proceedings of the 33rd ICRC* (July 2013). eprint: 1307.4550.
- [92] C. Hoischen et al. (H.E.S.S. Collaboration). In: *Baikal Three Messenger Conference* (2016).
- [93] C. Hoischen. “PhD thesis, private communication”. In: ().
- [94] A. Kappes et al. “Potential Neutrino Signals from Galactic Gamma-Ray Sources”. In: *The Astrophysical Journal* 656 (2007), pp. 870–878. arXiv: 0607286 [astro-ph].
- [95] D. Kasen et al. “Origin of the heavy elements in binary neutron-star mergers from a gravitational-wave event”. In: *Nature* 551 (Nov. 2017), pp. 80–84.
- [96] B. Katz et al. “The energy production rate density of cosmic rays in the local universe is $\sim 10^{44-45} \text{ergMpc}^{-3}\text{yr}^{-1}$ at all particle energies”. In: *arXiv* 1311.0287 (Nov. 2013), p. 5. arXiv: 1311.0287.
- [97] E. F. Keane et al. (SUPERB Collaboration). “The host galaxy of a fast radio burst”. In: *Nature* 530.7591 (2016), pp. 453–456. arXiv: 1602.07477.
- [98] E. F. Keane et al. (SUPERB Collaboration). “The SURvey for Pulsars and Extragalactic Radio Bursts - I. Survey description and overview”. In: *MNRAS* 473 (Jan. 2018), pp. 116–135. arXiv: 1706.04459 [astro-ph.IM].
- [99] A. Keivani et al. “A Multimessenger Picture of the Flaring Blazar TXS 0506+056: Implications for High-energy Neutrino Emission and Cosmic-Ray Acceleration”. In: *ApJ* 864.1 (Aug. 2018).
- [100] S. R. Kelner and F. A. Aharonian. “Energy spectra of gamma rays, electrons, and neutrinos produced at interactions of relativistic protons with low energy radiation”. In: *Phys. Rev. D* 78.3, 034013 (Aug. 2008), p. 034013. arXiv: 0803.0688.
- [101] S. R. Kelner, F. A. Aharonian, and V. V. Bugayov. “Energy spectra of gamma rays, electrons, and neutrinos produced at proton-proton interactions in the very high energy regime”. In: *Phys. Rev. D* 74.3, 034018 (Aug. 2006), p. 034018. eprint: astro-ph/0606058.
- [102] A. Klotz et al. “Early Optical Observations of Gamma-Ray Bursts by the TAROT Telescopes: Period 2001-2008”. In: *AJ* 137 (2009), pp. 4100–4108.
- [103] C. Kopper et al. (IceCube Collaboration). “Observation of Astrophysical Neutrinos in Four Years of IceCube Data”. In: *Proceedings of the 34th ICRC* 1081 (2015).

- [104] D. Lennarz et al. (HAWC Collaboration). “The HAWC GRB programme”. In: *6th International Symposium on High Energy Gamma-Ray Astronomy*. Vol. 1792. American Institute of Physics Conference Series. Jan. 2017, p. 050033.
- [105] A. Letessier-Selvon et al. “Layered water Cherenkov detector for the study of ultra high energy cosmic rays”. In: *NIM A* 767 (Dec. 2014), pp. 41–49. arXiv: 1405.5699 [astro-ph.IM].
- [106] T.-P. Li and Y.-Q. Ma. “Analysis methods for results in gamma-ray astronomy”. In: *Astrophysical Journal* 272 (1983), p. 317.
- [107] LIGO, VIRGO, Fermi-GBM, INTEGRAL Collaborations). “Gravitational Waves and Gamma-Rays from a Binary Neutron Star Merger: GW170817 and GRB 170817A”. In: *ApJ Letters* 848, L13 (Oct. 2017), p. L13. arXiv: 1710.05834 [astro-ph.HE].
- [108] D. R. Lorimer et al. “A Bright Millisecond Radio Burst of Extragalactic Origin”. In: *Science* 318 (Nov. 2007), p. 777. arXiv: 0709.4301.
- [109] Y. Lyubarsky. “A model for fast extragalactic radio bursts”. In: *MNRAS* 442 (July 2014), pp. L9–L13. arXiv: 1401.6674 [astro-ph.HE].
- [110] M. Ageron et al. (ANTARES Collaboration). “ANTARES: The first undersea neutrino telescope”. In: *NIM A* 656 (2011), pp. 11–38. arXiv: 1104.1607.
- [111] M. Santander (VERITAS), M. Dorner (FACT), J. Dumm (IceCube), K. Satalecka (MAGIC) and F. Schüssler (H.E.S.S.) “Searching for VHE gamma-ray emission associated with IceCube astrophysical neutrinos using FACT, H.E.S.S., MAGIC, and VERITAS”. In: *ArXiv e-prints* (Aug. 2017). arXiv: 1708.08945 [astro-ph.HE].
- [112] M. Schneider (private communication).
- [113] R. Margutti et al. “The Electromagnetic Counterpart of the Binary Neutron Star Merger LIGO/Virgo GW170817. V. Rising X-Ray Emission from an Off-axis Jet”. In: *ApJL* 848, L20 (Oct. 2017), p. L20. arXiv: 1710.05431 [astro-ph.HE].
- [114] I. Martinez et al. (HAWC Collaboration). “HAWC detection of further increase in TeV gamma-ray flux from Mrk 421”. In: *The Astronomer’s Telegram* #9946 (2017).
- [115] K. Masui et al. “Dense magnetized plasma associated with a fast radio burst”. In: *Nature* 528 (Dec. 2015), pp. 523–525. arXiv: 1512.00529 [astro-ph.HE].
- [116] K. Masui et al. “Dense magnetized plasma associated with a fast radio burst”. In: *Nature* 528 (Dec. 2015), pp. 523–525. arXiv: 1512.00529 [astro-ph.HE].
- [117] P. Meszaros and E. Waxman. “TeV Neutrinos from Successful and Choked Gamma-Ray Bursts”. In: *Phys. Rev. Lett.* 87.17 (Oct. 2001), p. 171102.
- [118] B. D. Metzger. “Kilonovae”. In: *Living Reviews in Relativity* 20, 3 (May 2017), p. 3. arXiv: 1610.09381 [astro-ph.HE].
- [119] R. Mirzoyan et al. (MAGIC Collaboration). “MAGIC detects very high energy gamma-ray emission from the blazar OT 081 (PKS 1749+096, 4C +09.57)”. In: *The Astronomer’s Telegram* #9267 (2016).
- [120] R. Mirzoyan et al. (MAGIC Collaboration). “First-time detection of VHE gamma rays by MAGIC from a direction consistent with the recent EHE neutrino event IceCube-170922A”. In: *The Astronomer’s Telegram* #10817 (2017).
- [121] R. et al. Mirzoyan. “MAGIC observation of the ANTARES-detected neutrino sky region”. In: *The Astronomer’s Telegram* #8203 (2015).

- [122] R. et al. Mirzoyan. “First time detection of a GRB at sub-TeV energies; MAGIC detects the GRB 190114C”. In: *The Astronomer’s Telegram #12390* (2019).
- [123] K. Murase, K. Kashiyama, and P. Meszaros. “A burst in a wind bubble and the impact on external matter: high-energy gamma-ray flares and implications for fast radio bursts and pulsar-driven supernovae”. In: *ArXiv e-prints* (Mar. 2016). arXiv: 1603.08875 [astro-ph.HE].
- [124] K. Murase et al. “Double Neutron Star Mergers and Short Gamma-ray Bursts: Long-lasting High-energy Signatures and Remnant Dichotomy”. In: *ApJ* 854, 60 (Feb. 2018), p. 60. arXiv: 1710.10757 [astro-ph.HE].
- [125] P.L. Nolan et al. (FermiLAT Collaboration). “Large Area Telescope Second Source Catalog”. In: *The Astrophysical Journal Supplement Series* 199 (2012), p. 31. eprint: 1108.1435.
- [126] K.A. Olive et al. (Particle Data Group). “Review of Particle Physics”. In: *Chin. Phys. C* 38 (2014), p. 090001.
- [127] B. Patricelli et al. “GW COSMoS: Gravitational Wave COmpact binary SysteM Simulations”. In: *figshare.com: GW COSMoS* ().
- [128] E. Petroff et al. “A real-time fast radio burst: polarization detection and multiwavelength follow-up”. In: *MNRAS* 447 (Feb. 2015), pp. 246–255. arXiv: 1412.0342 [astro-ph.HE].
- [129] E. Petroff et al. “FRBCAT: The Fast Radio Burst Catalogue”. In: *ArXiv e-prints* (Jan. 2016). arXiv: 1601.03547 [astro-ph.HE].
- [130] E. Petroff et al. “A polarized fast radio burst at low Galactic latitude”. In: *MNRAS* 469 (Aug. 2017), pp. 4465–4482. arXiv: 1705.02911 [astro-ph.HE].
- [131] R. Abbasi et al. (IceCube Collaboration). “An improved method for measuring muon energy using the truncated mean of dE/dx ”. In: *NIM A* 703 (2013), pp. 190–198. arXiv: 1208.3430v1.
- [132] S. Razzaque, P. Meszaros, and E. Waxman. “High Energy Neutrinos from Gamma-Ray Bursts with Precursor Supernovae”. In: *Phys. Rev. Lett.* 90.24 (June 2003), p. 241103.
- [133] X. Rodrigues et al. “Binary Neutron Star Merger Remnants as Sources of Cosmic Rays Below the “Ankle””. In: *ArXiv e-prints* (June 2018). arXiv: 1806.01624 [astro-ph.HE].
- [134] W.A. Rolke, A.M. Lopez, and J. Conrad. In: *NIM A* 551 (2005), p. 493.
- [135] S. Adrián-Martínez et al. (ANTARES Collaboration). “Search for cosmic neutrino point sources with four years of data from the ANTARES telescope”. In: *The Astrophysical Journal* 760.1 (Nov. 2012), p. 53. arXiv: 1207.3105.
- [136] S. Adrián-Martínez et al. (ANTARES Collaboration). “Measurement of the atmospheric ν_μ energy spectrum from 100 GeV to 200 TeV with the ANTARES telescope”. In: *European Physical Journal C* 73 (2013), pp. 1–12. arXiv: 1308.1599.
- [137] S. Adrián-Martínez et al. (ANTARES Collaboration). “Search for muon neutrinos from gamma-ray bursts with the ANTARES neutrino telescope using 2008 to 2011 data”. In: *Astronomy & Astrophysics* 559 (2013), A9. arXiv: 1307.0304.
- [138] S. Adrián-Martínez et al. (ANTARES Collaboration). “Searches for clustering in the time integrated skymap of the ANTARES neutrino telescope”. In: *Journal of Cosmology and Astroparticle Physics* 001 (2014). arXiv: arXiv:1402.2809v1.
- [139] M. Sanguineti et al. (ANTARES Collaboration). “Moon shadow observation with the ANTARES”. In: *Proceedings of the 34th ICRC* (2015).
- [140] K. Satalecka et al. (IceCube Collaboration). “Cluster Search for neutrino flares from pre-defined directions”. In: *ArXiv e-prints* (Nov. 2007). arXiv: 0711.0353.

- [141] F. Schüssler and M. Seglar-Arroyo et al. (H.E.S.S. Collaboration). “Target of Opportunity Observations of Blazars with H.E.S.S.”. In: *Proceedings of the 35th ICRC, arXiv:1708.01083* (Aug. 2017). arXiv: 1708.01083 [astro-ph.HE].
- [142] F. Schüssler (CTA Consortium). “The Transient program of the Cherenkov Telescope Array”. In: *TeVPA 2018 (Berlin, Germany)* (Aug. 2018).
- [143] F. Schüssler et al. (ANTARES Collaboration). “Autocorrelation analysis of ANTARES data”. In: *Proceedings of the 32nd ICRC* (2011).
- [144] F. Schüssler et al. (ANTARES Collaboration). “Search for a diffuse flux of high-energy muon neutrinos with the ANTARES neutrino telescope”. In: *Proceedings of the 32nd ICRC* (2011).
- [145] F. Schüssler et al. (ANTARES Collaboration). “2pt correlation analysis of ANTARES data”. In: *Proceedings of the 33rd ICRC* (2013).
- [146] F. Schüssler et al. (ANTARES Collaboration). “Energy reconstruction in neutrino telescopes”. In: *Proceedings of the 33rd ICRC* (2013).
- [147] F. Schüssler et al. (H. E. S. S. Collaboration). “Simultaneous H.E.S.S. and RXTE observations of the microquasars GRS 1915+105, Circinus X-1 and V4641 Sgr”. In: *Proceedings of the 34th ICRC 727* (2015).
- [148] F. Schüssler et al. (H. E. S. S. Collaboration). “The H.E.S.S. multi-messenger program: Searches for TeV gamma-ray emission associated with high-energy neutrinos”. In: *AIP Conference Proceedings 1792.1* (2017), p. 060006.
- [149] F. Schüssler et al. (H.E.S.S. Collaboration). “Multiwavelength study of the region around the ANTARES neutrino excess”. In: *Proceedings of the 33rd ICRC* (2013). arXiv: 1307.6074.
- [150] F. Schüssler et al. (H.E.S.S. Collaboration). “The H.E.S.S. multi-messenger program”. In: *Proceedings of the 34th ICRC* (Sept. 2015). arXiv: 1509.03035 [astro-ph.HE].
- [151] F. Schüssler et al. (H.E.S.S. Collaboration). “H.E.S.S. multi-messenger observations”. In: *Proceedings of the Rencontres de Moriond 2017 (Very High Energy Phenomena in the Universe)* (May 2017). arXiv: 1705.08258 [astro-ph.HE].
- [152] F. Schüssler et al. (H.E.S.S. Collaboration). “H.E.S.S. observations following multi-messenger alerts in real-time”. In: *Proceedings of the 35th ICRC* (Aug. 2017). arXiv: 1708.00466 [astro-ph.HE].
- [153] F. Schüssler et al. (H.E.S.S. Collaboration). “LIGO/Virgo G297595: H.E.S.S. very-high energy gamma-ray follow-up”. In: *GCN circular #21673* (2017).
- [154] F. Schüssler et al. (H.E.S.S. Collaboration). “H.E.S.S. searches for TeV gamma-rays associated to high-energy neutrinos”. In: *TeVPA 2018 (Berlin, Germany)* (Aug. 2018).
- [155] F. Schüssler et al. (SGSO Alliance). “Science with SGSO”. In: *TeVPA 2018 (Berlin, Germany)* (Aug. 2018).
- [156] F. Schüssler. “High-energy gamma-ray transients and multimessenger links”. In: *Highlight talk at the 35th ICRC* (2017).
- [157] M. Seglar-Arroyo and F. Schüssler (H.E.S.S. Collaboration). “Gravitational wave alert follow-up strategy in the H.E.S.S. multi-messenger framework”. In: *ArXiv e-prints* (May 2017). arXiv: 1705.10138 [astro-ph.IM].
- [158] M. Seglar-Arroyo and F. Schüssler (H.E.S.S. Collaboration). “New atmospheric profiles for H.E.S.S. data analysis”. In: *European Physical Journal Web of Conferences*. Vol. 144. European Physical Journal Web of Conferences. 2017, p. 01013.

- [159] M. Seglar-Arroyo et al. (AMON, HAWC and Virgo/Ligo). “AMON coincidence analysis of sub-threshold events from HAWC and LIGO-Virgo”. In: *TeVPA 2018 (Berlin, Germany)* (Aug. 2018).
- [160] Leo P. Singer et al. “The First Two Years of Electromagnetic Follow-up with Advanced LIGO and Virgo”. In: *ApJ* 795, 105 (Nov. 2014), p. 105. arXiv: 1404.5623 [astro-ph.HE].
- [161] M.W.E. Smith et al. “The Astrophysical Multimessenger Observatory Network (AMON)”. In: *Astroparticle Physics* 45 (2013), pp. 56–70.
- [162] L. G. Spitler et al. “Fast Radio Burst Discovered in the Arecibo Pulsar ALFA Survey”. In: *Astrophys. Journal* 790, 101 (Aug. 2014), p. 101. arXiv: 1404.2934 [astro-ph.HE].
- [163] T. Stanev. “High Energy Cosmic Rays”. In: *Springer-Verlag, Berlin* (2003).
- [164] Y. Tanaka et al. (Fermi-LAT Collaboration). “Fermi-LAT detection of increased gamma-ray activity of TXS 0506+056, located inside the IceCube-170922A error region”. In: *The Astronomer’s Telegram #10791* (2017).
- [165] The IceCube, Fermi-LAT, MAGIC, AGILE, ASAS-SN, HAWC, H.E.S.S, INTEGRAL, Kanata, Kiso, Kapteyn, Liverpool telescope, Subaru, Swift/NuSTAR, VERITAS, VLA/17B-403 Collaborations. “Multimessenger observations of a flaring blazar coincident with high-energy neutrino IceCube-170922A”. In: *Science* 361 (July 2018), eaat1378. arXiv: 1807.08816 [astro-ph.HE].
- [166] D. Thornton et al. “A Population of Fast Radio Bursts at Cosmological Distances”. In: *Science* 341 (July 2013), pp. 53–56. arXiv: 1307.1628 [astro-ph.HE].
- [167] H. K. Vedantham et al. “On associating Fast Radio Bursts with afterglows”. In: *ArXiv e-prints* (Mar. 2016). arXiv: 1603.04421 [astro-ph.HE].
- [168] S. P. Wakely and D. Horan. “TeVcat: An online catalog for Very High Energy Gamma-Ray Astronomy”. In: *International Cosmic Ray Conference* 3 (2008), pp. 1341–1344.
- [169] E. Waxman and J. Bahcall. “High Energy Neutrinos from Cosmological Gamma-Ray Burst Fireballs”. In: *Phys. Rev. Lett.* 78 (Mar. 1997), pp. 2292–2295.
- [170] E. Waxman and J. Bahcall. “High Energy Neutrinos from Astrophysical Sources: An Upper Bound”. In: *Physical Review D* 59, June (1998), pp. 1–8. arXiv: 9807282 [hep-ph].
- [171] T.C. Weekes et al. (Whipple Collaboration). “Observation of TeV gamma rays from the Crab nebula using the atmospheric Cerenkov imaging technique”. In: *Astrophysical Journal* 342 (July 1989), pp. 379–395.
- [172] D.J. White, E.J. Daw, and V.S. Dhillon. “A List of Galaxies for Gravitational Wave Searches”. In: *Class. Quantum Grav.* 28 (2011), p. 085016.
- [173] B. Zhang. “A Possible Connection between Fast Radio Bursts and Gamma-Ray Bursts”. In: *Astrophys. Journal* 780, L21 (Jan. 2014), p. L21. arXiv: 1310.4893 [astro-ph.HE].
- [174] B. Zhang. “On the Afterglow and Progenitor of FRB 150418”. In: *Astrophys. Journal* 822.1 (2016), p. L14.

Appendices



Curriculum Vitae

PERSONAL INFORMATION

Fabian Schüssler (31.01.1978) fabian.schussler@cea.fr

fabian.schussler@cea.fr

Website: astroparticle.weebly.com

DPhP/IRFU, CEA, Université Paris-Saclay
F-91191 Gif-sur-Yvette, France

Researcher ID: G-5313-2013 / h-index: 32

InspireHEP.net: F.Schüssler



EDUCATION

11/2008: **PhD in "Astroparticle physics"** (Universität Karlsruhe, Germany; supervisor: Prof. J. Blümer), "Measurement of the Energy Spectrum of Ultra-High Energy Cosmic Rays using Hybrid Data of the Pierre Auger Observatory", Grade *very good*

08/2005: **Master in Physics** (Universität Karlsruhe, Germany), "Top-Down Reconstruction of Ultra-High Energy Air Showers measured with the Pierre Auger Observatory", Grade *very good with honours*

07/2003: **Maîtrise de Physique-Recherche** (Université Joseph Fourier, Grenoble, France), "Precision measurements of CP-Violation in the channel $B_s \rightarrow J/\Psi \eta$ with the ATLAS detector at the LHC", Grade *very good*

CURRENT and PAST POSITIONS

2009-present: **Permanent researcher** at Irfu / CEA Paris-Saclay (Gif-sur-Yvette, France); Neutrino astronomy with ANTARES and high-energy gamma-ray astronomy with H.E.S.S. and CTA

2008-2009: **PostDoc** at Karlsruhe Institut of Technology (Karlsruhe, Germany); Ultra-High Energy Cosmic Rays with the Pierre Auger Observatory

2005-2008: **PhD** student at Karlsruhe Institut of Technology (Karlsruhe, Germany); Ultra-High Energy Cosmic Rays with the Pierre Auger Observatory

2003: Summer student at CERN; Simulations and detector construction for ATLAS

2000-2005: Research assistant at Universität Karlsruhe and Forschungszentrum Karlsruhe

SCIENTIFIC COLLABORATIONS

2018-present: SGSO Alliance

2018-present: HAWC Collaboration (associated)

2012-present: CTA Consortium

2012-present: H.E.S.S. Collaboration

2009-2012: KM3NeT Collaboration

2009-present: ANTARES Collaboration

2004-2010: Pierre Auger Collaboration

PRIZES, AWARDS AND FELLOWSHIPS

2010-2013: Fellowship “EuroTalents” (Marie-Curie COFUND)

2008: Participation at the 58th Lindau Meeting of Nobel Laureates

2006: **Helmholtz young scientist award**: best German diploma thesis in astroparticle physics

2005: **Edison-Award** (General Electric Foundation): outstanding diploma thesis

1998: Freudenstadt-Award (city of Freudenstadt): best baccalaureate 1998

SUPERVISION OF (UNDER)-GRADUATE STUDENTS AND POSTDOCTORAL FELLOWS

2018-present: PhD thesis director of H. Ashkar (Irfu/CEA Paris-Saclay)

2016-present: PhD thesis director of M. Seglar-Arroyo (Irfu/CEA Paris-Saclay + PennState/US)

2013-2016: member of PhD thesis committee (Rodrigo Gracia, APC/Paris, France)

since 2010: supervision of 3 Master students (Irfu/CEA-Saclay, France)

since 2009: co-supervision of 3 Postdoctoral fellows (Irfu/CEA-Saclay, France)

2007: supervision of an international undergraduate student internship via RISE/DAAD fellowship (KIT/Karlsruhe, Germany)

MEMBERSHIPS OF SCIENTIFIC SOCIETIES

2018-present: Member of the International Astronomical Union

2004-present: Member “Deutsche Physikalische Gesellschaft”

2002-2003: Member “Association Double-Diplôme Karlsruhe-Grenoble”

ORGANISATION OF SCIENTIFIC MEETINGS

Since 2018: Member of the Scientific Program Committee “Rencontres de Vietnam, Very High Phenomena in the Universe”

2017 + 2018: Member of the Scientific Program Committee “Transient Sky 2020” (Orsay 2017, Montpellier 2018)

2015 Member of the Scientific Program Committee of the 1st GRAND workshop (Paris, France)

2013 Co-organization of the AtmoHEAD workshop “Atmospheric Monitoring for High-Energy Astroparticle Detectors” (Saclay, France)

INSTITUTIONAL RESPONSIBILITIES

2017-present: Member of the “Comité Local de l’Institut Pascal, CLIP” (Université Paris-Saclay)
2010-present: Responsible for graduate and under-graduate student internships (Irfu/CEA-Saclay)
2006-2007: Student representative graduate school “High-energy and astroparticle physics”

SCIENTIFIC REVIEW PANELS AND COMMITTEES

2018-present: Founding member and science coordinator of the SGSO Alliance
2018-present: Convener of the Science Working Group “Transients/MWL” (CTA Consortium)
2017-present: Scientific Evaluator, Swiss National Science Foundation (Geneva, Switzerland)
2016-present: Member of the Scientific Council of the “Action Spécifique Observatoire Virtuel”
2016-present: Member of the Scientific Council of the “Programme National de Haute Energie”
2015-2018: co-coordinator Top Level Science Use Cases (CTA Collaboration)
2014-present: Multi-messenger coordinator (H.E.S.S. Collaboration)
2014-2018: Editorial Board Key Science Project “Transient Phenomena” (CTA Collaboration)
2013-present: Convener working groups “Neutrino alerts” and “Neutrino events” (H.E.S.S. Collaboration)
2013-present: Scientific Evaluator, National Science Centre (Krakow, Poland)
2012-2016: Member Publication Committee (Antares Collaboration)
2011-2012: Panel member “Univers haute énergie, ondes gravitationnelles” (Prospective IN2P3-Irfu, France)
2011-2015: Referee “Gravitational waves - High-energy neutrinos” (Antares and Virgo/LIGO Collaborations)
2010-present: Member Steering Committee, Convener “Analysis Tools” (Antares Collaboration)

FUNDING

2017-present: Grants from “Programme National de Haute Energie” : AMIGO/SGSO: preparations for a next-generation large FoV gamma-ray observatory
2015-present: Grants from “Programme National de Haute Energie” : multi-messenger analyses
2013: Grant from Académie des Sciences (France) for participation at the 27th Texas Symposium on Relativistic Astrophysics
2010-2013: Fellowship “EuroTalents” (Marie-Curie COFUND, FP7), Project “Searches for sources of astrophysical neutrinos with the Antares detector”
2007: RISE fellowship (DAAD, Germany): supervision of an international undergraduate internship (M. Greeno, Kansas University, USA)

PUBLICATIONS

Total publications: 147 (average citations per article: 39; source: WoS, date: 2019-04-17)
Researcher ID: G-5313-2013 / h-index: 32
InspireHEP.net / Astrophysics Data System (ADS)

MAJOR PUBLICATIONS

- IceCube, Fermi-LAT, MAGIC, H.E.S.S. et al., “Multimessenger observations of a flaring blazar coincident with high-energy neutrino IceCube-170922A” , Science eaat1378 (2018), Main result of multi-messenger activities, PI of the H.E.S.S. observations
- H. Abdalla et al. (H.E.S.S. Collaboration), “TeV Gamma-Ray Observations of the Binary Neutron Star Merger GW170817 with H.E.S.S.” , Astrophys. Journal Letters 850 (2017) L22; Main

result of recent multi-messenger activities; PI of the observations, corresponding author on behalf of the H.E.S.S. collaboration

- B.P. Abbott, et al., “Multi-messenger Observations of a Binary Neutron Star Merger” , *Astrophys. Journal Letters* 848 (2017) L12; responsible for H.E.S.S. contribution and co-responsible for general section on gamma-ray observations
- A. Abdalla et al. (H.E.S.S. + SUPERB Collaborations), “First limits on the very-high energy gamma-ray afterglow emission of a Fast Radio Burst” , *Astronomy and Astrophysics* 597 (2016), PI of the observations, corresponding author on behalf of the H.E.S.S. and SUPERB collaborations
- S. Adrian-Martinez et al. (Antares Collaboration), “Searches for clustering in the time integrated skymap of the Antares neutrino telescope” , *JCAP* 5 (2014); Main result of the EuroTalents project I conducted between 2010 and 2013, corresponding author on behalf of the ANTARES collaboration.
- S. Adrian-Martinez et al. (Antares Collaboration), “The Antares telescope neutrino alert system” , *APP* 35 (2012) 8; I am participating in the technical implementation of the alert system, its commissioning and maintenance and supervise the data analysis (treatment of the optical images, search for GRBs and supernovae).
- J. Abraham et al. (Pierre Auger Collaboration), “Measurement of the energy spectrum of cosmic rays above 10^{18} eV using the Pierre Auger Observatory” , *Phys. Lett. B* 685 (2010) 239; Citations: 244; Publication of the main result of my PhD thesis, corresponding author on behalf of the Pierre Auger Collaboration
- J. Abraham et al. (Pierre Auger Collaboration), “Correlation of the highest-energy cosmic rays with nearby extragalactic objects” , *Science* 318 (2007) 938; I contributed with a cross-check analysis using a different dataset based on measurements of the fluorescence detector whereas the main analysis used data from the surface detector only.

PRESENTATIONS

Invited Conferences and seminars

2019: Sexten School of Astrophysics (Sexten/Italy): “Transient Science with CTA”

2018: Plenary talk at the “Festival d’astronomie de Fleurance” (Fleurance/France): “Les Neutrinos: une nouvelle fenêtre vers l’univers violent”

2017: Plenary highlight talk at the 35th International Cosmic Ray Conference (Busan/South Korea): “Gamma-ray transients and multi-messenger links”

2016: The Baikal Three Messenger Conference (Irkutsk/Russia), “H.E.S.S. multi-messenger and real-time alert follow-up observations”

2014 + 2015 + 2016: AMON workshops, “The H.E.S.S. multi-messenger program”

2014: RICAP (Noto, Italy), “ANTARES and Baikal: recent results from underwater neutrino telescopes”

2014: Atelier perspectives CTA (Paris, France), “Synergies between neutrinos and gamma-rays”

2013: MODE (Orsay, France), “Recent results from neutrino telescopes: interpretations and prospects”

2012: International School of Cosmic Ray Astrophysics (Erice, Italy), "Neutrino Astronomy"
2011: Rencontres de Moriond EW (La Thuile, Italy): session chair "Astroparticle physics"
2011: Seminar at KIT (Karlsruhe, Germany): "Neutrino Astronomy"
2009: Seminar at Irfu (Saclay, France): "Quelques résultats de l'Observatoire Pierre Auger"
2009: Seminar at PennState (University Park, USA): "Measurement of the energy spectrum of ultra-high energy cosmic rays using hybrid data of the Pierre Auger Observatory"
2008: Atmospheric Monitoring for Astroparticle Physics (Prague, Czech Republic): "Use of atmospheric data in the event reconstruction of the Pierre Auger Observatory"
2008: Seminar at KIT (Karlsruhe, Germany): "Measurement of the energy spectrum of ultra-high energy cosmic rays using hybrid data of the Pierre Auger Observatory"
2006-2008: Various Seminars at the Graduate School "High-energy and astroparticle physics" (Karlsruhe, Germany)
2005: Seminar at Forschungszentrum Karlsruhe (Karlsruhe, Germany): "Top-down reconstruction of fluorescence measurements with the Pierre Auger Observatory"

Major conference contributions

2018: TeVPA-2018 (Berlin/Germany): "The Transient program of the Cherenkov Telescope Array", "H.E.S.S. searches for TeV gamma-rays associated to high-E neutrinos", "Science with SGO"
2018: EWASS-2018 (Liverpool/UK): "TeV gamma-ray observations of GW170817 with H.E.S.S."
2017: 35th International Cosmic Ray Conference (Busan, South Korea): "H.E.S.S. observations following multi-messenger alerts in real-time" + "Target of Opportunity Observations of Blazars with H.E.S.S." + "Searching for VHE gamma-ray emission associated with IceCube astrophysical neutrinos using FACT, H.E.S.S., MAGIC and VERITAS" + "On the scientific motivation for a wide field-of-view TeV gamma-ray observatory in the Southern Hemisphere"
Moriond VHEPU: "Gravitational waves follow-up strategies in the H.E.S.S. multi-messenger framework" + "H.E.S.S. multi-messenger observations"
2016: Gamma2016 (Heidelberg, Germany): "The H.E.S.S. multi-messenger program: searches for TeV gamma-ray emission associated with high-energy neutrinos" + "Limits on the TeV gamma-ray afterglow of Fast Radio Bursts with H.E.S.S."
2016: Neutrino2016 (London, UK): "H.E.S.S. searches for TeV gamma-ray emission associated with high-energy neutrinos"
2015: 34th International Cosmic Ray Conference (The Hague, Netherlands): "The H.E.S.S. Multi-messenger program" + "Simultaneous H.E.S.S. and RXTE observations of the microquasars GRS 1915+105, Circinus X-1 and V4641 Sgr" + "The On-Site Analysis of CTA"
2013: 27th Texas Symposium on Relativistic Astrophysics (Dallas, USA): "Results from the Antares neutrino telescope"
2013: 33rd International Cosmic Ray Conference (Rio de Janeiro, Brazil): "Multiwavelength study of the region around the Antares neutrino excess" + "2pt correlation of Antares data" + "Energy reconstruction in neutrino telescopes"
2012: UHECR 2012 (CERN, Switzerland): "Searches for the sources of cosmic rays with the Antares

neutrino telescope”

2011: 32nd International Cosmic Ray Conference (Beijing, China): “Search for a diffuse flux of high-energy muon neutrinos with the Antares neutrino telescope” + “Autocorrelation analysis of Antares data”

2010: ICATPP Conference on Cosmic Rays for Particle and Astroparticle Physics (Como, Italy): “Status and Results of the Antares Experiment”

2009: 31nd International Cosmic Ray Conference (Lodz, Poland): “Measurement of the energy spectrum of cosmic rays above 10^{18} eV using the Pierre Auger Observatory”

2009: Rencontres de Moriond EW (La Thuile, Italy): “The energy spectrum of cosmic rays measured with the Pierre Auger Observatory”

B

Major publications



Measurement of the energy spectrum of cosmic rays above 10^{18} eV using the Pierre Auger Observatory

Pierre Auger Collaboration ^a

J. Abraham ^h, P. Abreu ^{bl}, M. Aglietta ^{ay}, E.J. Ahn ^{ca}, D. Allard ^{aa}, J. Allen ^{cd}, J. Alvarez-Muñiz ^{bs}, M. Ambrosio ^{ar}, L. Anchordoqui ^{co}, S. Andringa ^{bl}, T. Antičić ^v, A. Anzalone ^{ax}, C. Aramo ^{ar}, E. Arganda ^{bp}, K. Arisaka ^{ci}, F. Arqueros ^{bp}, H. Asorey ^b, P. Assis ^{bl}, J. Aublin ^{ac}, M. Ave ^{ag,cj}, G. Avila ^j, T. Bäcker ^{am}, D. Badagnani ^f, M. Balzer ^{ah}, K.B. Barber ^k, A.F. Barbosa ^l, S.L.C. Barroso ^r, B. Baughman ^{cf}, P. Bauleo ^{by}, J.J. Beatty ^{cf}, B.R. Becker ^{cm}, K.H. Becker ^{af}, A. Bellétoile ^{ad}, J.A. Bellido ^k, S. BenZvi ^{cn}, C. Berat ^{ad}, T. Bergmann ^{ah}, X. Bertou ^b, P.L. Biermann ^{aj}, P. Billoir ^{ac}, O. Blanch-Bigas ^{ac}, F. Blanco ^{bp}, M. Blanco ^{bq}, C. Bleve ^{aq}, H. Blümer ^{ai,ag}, M. Boháčová ^{cj,x}, D. Boncioli ^{as}, C. Bonifazi ^{u,ac}, R. Bonino ^{ay}, N. Borodai ^{bj}, J. Brack ^{by}, P. Brogueira ^{bl}, W.C. Brown ^{bz}, R. Bruijn ^{bu}, P. Buchholz ^{am}, A. Bueno ^{br}, R.E. Burton ^{bw}, N.G. Busca ^{aa}, K.S. Caballero-Mora ^{ai}, L. Caramete ^{aj}, R. Caruso ^{at}, A. Castellina ^{ay}, O. Catalano ^{ax}, G. Cataldi ^{aq}, L. Cazon ^{bl,cj}, R. Cester ^{au}, J. Chauvin ^{ad}, A. Chiavassa ^{ay}, J.A. Chinellato ^p, A. Chou ^{ca,cd}, J. Chudoba ^x, R.W. Clay ^k, E. Colombo ^c, M.R. Coluccia ^{aq}, R. Conceição ^{bl}, F. Contreras ⁱ, H. Cook ^{bu}, M.J. Cooper ^k, J. Coppens ^{bf,bh}, A. Cordier ^{ab}, U. Cotti ^{bd}, S. Coutu ^{cg}, C.E. Covault ^{bw}, A. Creusot ^{bn}, A. Criss ^{cg}, J. Cronin ^{cj}, A. Curutiu ^{aj}, S. Dagoret-Campagne ^{ab}, R. Dallier ^{ae}, K. Daumiller ^{ag}, B.R. Dawson ^k, R.M. de Almeida ^p, M. De Domenico ^{at}, C. De Donato ^{be,ap}, S.J. de Jong ^{bf}, G. De La Vega ^h, W.J.M. de Mello Junior ^p, J.R.T. de Mello Neto ^u, I. De Mitri ^{aq}, V. de Souza ⁿ, K.D. de Vries ^{bg}, G. Decerprit ^{aa}, L. del Peral ^{bq}, O. Deligny ^z, A. Della Selva ^{ar}, C. Delle Fratte ^{as}, H. Dembinski ^{ak}, C. Di Giulio ^{as}, J.C. Diaz ^{cc}, M.L. Díaz Castro ^m, P.N. Diep ^{cp}, C. Dobrigkeit ^p, J.C. D'Olivo ^{be}, P.N. Dong ^{cp,z}, A. Dorofeev ^{by}, J.C. dos Anjos ^l, M.T. Dova ^f, D. D'Urso ^{ar}, I. Dutan ^{aj}, M.A. DuVernois ^{ck}, J. Ebr ^x, R. Engel ^{ag}, M. Erdmann ^{ak}, C.O. Escobar ^p, A. Etchegoyen ^c, P. Facal San Luis ^{cj,bs}, H. Falcke ^{bf,bi}, G. Farrar ^{cd}, A.C. Fauth ^p, N. Fazzini ^{ca}, A. Ferrero ^c, B. Fick ^{cc}, A. Filevich ^c, A. Filipčić ^{bm,bn}, I. Fleck ^{am}, S. Fliescher ^{ak}, C.E. Fracchiolla ^{by}, E.D. Fraenkel ^{bg}, U. Fröhlich ^{am}, W. Fulgione ^{ay}, R.F. Gamarra ^c, S. Gambetta ^{an}, B. García ^h, D. García Gámez ^{br}, D. Garcia-Pinto ^{bp}, X. Garrido ^{ag,ab}, G. Gelmini ^{ci}, H. Gemmeke ^{ah}, P.L. Ghia ^{z,ay}, U. Giaccari ^{aq}, M. Giller ^{bk}, H. Glass ^{ca}, L.M. Goggin ^{co}, M.S. Gold ^{cm}, G. Golup ^b, F. Gomez Albarracin ^f, M. Gómez Berisso ^b, P. Gonçalves ^{bl}, D. Gonzalez ^{ai}, J.G. Gonzalez ^{br,cb}, D. Góra ^{ai,bj}, A. Gorgi ^{ay}, P. Gouffon ^o, S.R. Gozzini ^{bu}, E. Grashorn ^{cf}, S. Grebe ^{bf}, M. Grigat ^{ak}, A.F. Grillo ^{az}, Y. Guardincerri ^e, F. Guarino ^{ar}, G.P. Guedes ^q, J.D. Hague ^{cm}, V. Halenka ^y, P. Hansen ^f, D. Harari ^b, S. Harmsma ^{bg,bh}, J.L. Harton ^{by}, A. Haungs ^{ag}, T. Hebbeker ^{ak}, D. Heck ^{ag}, A.E. Herve ^k, C. Hojvat ^{ca}, V.C. Holmes ^k, P. Homola ^{bj}, J.R. Hörandel ^{bf}, A. Horneffer ^{bf}, M. Hrabovský ^{y,x}, T. Huege ^{ag}, M. Hussain ^{bn}, M. Iarlori ^{ao}, A. Insolia ^{at}, F. Ionita ^{cj}, A. Italiano ^{at}, S. Jiraskova ^{bf}, K. Kadija ^v, M. Kaducak ^{ca}, K.H. Kampert ^{af}, T. Karova ^x, P. Kasper ^{ca}, B. Kégl ^{ab}, B. Keilhauer ^{ag}, A. Keivani ^{cb}, J. Kelley ^{bf}, E. Kemp ^p, R.M. Kieckhafer ^{cc}, H.O. Klages ^{ag}, M. Kleifges ^{ah}, J. Kleinfeller ^{ag}, R. Knapik ^{by}, J. Knapp ^{bu}, D.-H. Koang ^{ad}, A. Krieger ^c, O. Krömer ^{ah}, D. Kruppke-Hansen ^{af}, F. Kuehn ^{ca}, D. Kuempel ^{af}, K. Kulbartz ^{al}, N. Kunka ^{ah}, A. Kusenko ^{ci}, G. La Rosa ^{ax}, C. Lachaud ^{aa}, B.L. Lago ^u, P. Lautridou ^{ae}, M.S.A.B. Leão ^t, D. Lebrun ^{ad}, P. Lebrun ^{ca}, J. Lee ^{ci}, M.A. Leigui de Oliveira ^t, A. Lemiere ^z, A. Letessier-Selvon ^{ac}, I. Lhenry-Yvon ^z, R. López ^{bb}, A. Lopez Agüera ^{bs}, K. Louedec ^{ab}, J. Lozano Bahilo ^{br}, A. Lucero ^{ay}, M. Ludwig ^{ai}, H. Lyberis ^z, M.C. Maccarone ^{ax}, C. Macolino ^{ac,ao}, S. Maldera ^{ay}, D. Mandat ^x, P. Mantsch ^{ca}, A.G. Mariazzi ^f,

V. Marin^{ae}, I.C. Maris^{ac,ai}, H.R. Marquez Falcon^{bd}, G. Marsella^{av}, D. Martello^{aq}, O. Martínez Bravo^{bb}, H.J. Mathes^{ag}, J. Matthews^{cb,ch}, J.A.J. Matthews^{cm}, G. Matthiae^{as}, D. Maurizio^{au}, P.O. Mazur^{ca}, M. McEwen^{bq}, G. Medina-Tanco^{be}, M. Melissas^{ai}, D. Melo^{au}, E. Menichetti^{au}, A. Menshikov^{ah}, C. Meurer^{ak}, S. Mičanović^v, M.I. Micheletti^c, W. Miller^{cm}, L. Miramonti^{ap}, S. Mollerach^b, M. Monasor^{cj,bp}, D. Monnier Ragaigne^{ab}, F. Montanet^{ad}, B. Morales^{be}, C. Morello^{ay}, E. Moreno^{bb}, J.C. Moreno^f, C. Morris^{cf}, M. Mostafá^{by}, S. Mueller^{ag}, M.A. Muller^p, R. Mussa^{au}, G. Navarra^{ay,1}, J.L. Navarro^{br}, S. Navas^{br}, P. Necasal^x, L. Nellen^{be}, P.T. Nhung^{cp}, N. Nierstenhoefer^{af}, D. Nitz^{cc}, D. Nosek^w, L. Nožka^x, M. Nyklicek^x, J. Oehlschläger^{ag}, A. Olinto^{cj}, P. Oliva^{af}, V.M. Olmos-Gilbaja^{bs}, M. Ortiz^{bp}, N. Pacheco^{bq}, D. Pakk Selmi-Dei^p, M. Palatka^x, J. Pallotta^d, N. Palmieri^{ai}, G. Parente^{bs}, E. Parizot^{aa}, S. Parlati^{az}, A. Parra^{bs}, J. Parrisius^{ai}, R.D. Parsons^{bu}, S. Pastor^{bo}, T. Paul^{ce}, V. Pavlidou^{cj,2}, K. Payet^{ad}, M. Pech^x, J. Pękala^{bj}, R. Pelayo^{bs}, I.M. Pepe^s, L. Perrone^{av}, R. Pesce^{an}, E. Petermann^{cl}, S. Petrera^{ao,aw}, P. Petrinca^{as}, A. Petrolini^{an}, Y. Petrov^{by}, J. Petrovic^{bh}, C. Pfendner^{cn}, R. Piegai^e, T. Pierog^{ag}, M. Pimenta^{bl}, V. Pirronello^{at}, M. Platino^c, V.H. Ponce^b, M. Pontz^{am}, P. Privitera^{cj}, M. Prouza^x, E.J. Quel^d, J. Rautenberg^{af}, O. Ravel^{ae}, D. Ravignani^c, A. Redondo^{bq}, B. Revenu^{ae}, F.A.S. Rezende^l, J. Ridky^x, S. Riggi^{at}, M. Risse^{am,af}, P. Ristori^d, C. Rivière^{ad}, V. Rizi^{ao}, C. Robledo^{bb}, G. Rodriguez^{bs,as}, J. Rodriguez Martino^{i,at}, J. Rodriguez Rojoⁱ, I. Rodriguez-Cabo^{bs}, M.D. Rodríguez-Frías^{bq}, G. Ros^{bq}, J. Rosado^{bp}, T. Rossler^y, M. Roth^{ag}, B. Rouillé-d'Orfeuil^{cj,aa}, E. Roulet^b, A.C. Rovero^g, F. Salamida^{ag,ao}, H. Salazar^{bb,3}, G. Salina^{as}, F. Sánchez^{c,be}, M. Santanderⁱ, C.E. Santo^{bl}, E. Santos^{bl}, E.M. Santos^u, F. Sarazin^{bx}, S. Sarkar^{bt}, R. Satoⁱ, N. Scharf^{ak}, V. Scherini^{af}, H. Schieler^{ag}, P. Schiffer^{ak}, A. Schmidt^{ah}, F. Schmidt^{cj}, T. Schmidt^{ai}, O. Scholten^{bg}, H. Schoorlemmer^{bf}, J. Schovancova^x, P. Schovánek^x, F. Schroeder^{ag}, S. Schulte^{ak}, F. Schüssler^{ag,*}, D. Schuster^{bx}, S.J. Sciutto^f, M. Scuderi^{at}, A. Segreto^{ax}, D. Semikoz^{aa}, M. Settimo^{aq}, R.C. Shellard^{l,m}, I. Sidelnik^c, B.B. Siffert^u, G. Sigl^{al}, A. Śmiałkowski^{bk}, R. Šmída^{ag,x}, G.R. Snow^{cl}, P. Sommers^{cg}, J. Sorokin^k, H. Spinka^{bv,ca}, R. Squartiniⁱ, J. Stasielak^{bj}, M. Stephan^{ak}, E. Strazzeri^{ax,ab}, A. Stutz^{ad}, F. Suarez^c, T. Suomijärvi^z, A.D. Supanitsky^{be}, T. Šušva^v, M.S. Sutherland^{cf}, J. Swain^{ce}, Z. Szadkowski^{af,bk}, A. Tamashiro^g, A. Tamburro^{ai}, A. Tapia^c, T. Tarutina^f, O. Taşcau^{af}, R. Tcaciuc^{am}, D. Tcherniakhovskii^{ah}, D. Tegolo^{at,ba}, N.T. Thao^{cp}, D. Thomas^{by}, J. Tiffenberg^e, C. Timmermans^{bh,bf}, W. Tkaczyk^{bk}, C.J. Todero Peixoto^t, B. Tomé^{bl}, A. Tonachini^{au}, P. Travnicek^x, D.B. Tridapalli^o, G. Tristram^{aa}, E. Trovato^{at}, M. Tueros^f, R. Ulrich^{cg,ag}, M. Unger^{ag}, M. Urban^{ab}, J.F. Valdés Galicia^{be}, I. Valiño^{ag}, L. Valore^{ar}, A.M. van den Berg^{bg}, J.R. Vázquez^{bp}, R.A. Vázquez^{bs}, D. Veberič^{bn,bm}, T. Venters^{cj}, V. Verzi^{as}, M. Videla^h, L. Villaseñor^{bd}, S. Vorobiov^{bn}, L. Voyvodic^{ca,1}, H. Wahlberg^f, P. Wahrlich^k, O. Wainberg^c, D. Warner^{by}, A.A. Watson^{bu}, S. Westerhoff^{cn}, B.J. Whelan^k, G. Wiczorek^{bk}, L. Wiencke^{bx}, B. Wilczyńska^{bj}, H. Wilczyński^{bj}, C. Williams^{cj}, T. Winchen^{ak}, M.G. Winnick^k, B. Wundheiler^c, T. Yamamoto^{cj,4}, P. Younk^{by}, G. Yuan^{cb}, A. Yushkov^{ar}, E. Zas^{bs}, D. Zavrtnik^{bn,bm}, M. Zavrtnik^{bm,bn}, I. Zaw^{cd}, A. Zepeda^{bc}, M. Ziolkowski^{am}

^a Observatorio Pierre Auger, Av. San Martín Norte 304, 5613 Malargüe, Argentina

^b Centro Atómico Bariloche and Instituto Balseiro (CNEA-UNCuyo-CONICET), San Carlos de Bariloche, Argentina

^c Centro Atómico Constituyentes (Comisión Nacional de Energía Atómica/CONICET/UTN-FRBA), Buenos Aires, Argentina

^d Centro de Investigaciones en Láseres y Aplicaciones, CITEFA and CONICET, Argentina

^e Departamento de Física, FCEyN, Universidad de Buenos Aires y CONICET, Argentina

^f IFLP, Universidad Nacional de La Plata and CONICET, La Plata, Argentina

^g Instituto de Astronomía y Física del Espacio (CONICET), Buenos Aires, Argentina

^h National Technological University, Faculty Mendoza (CONICET/CNEA), Mendoza, Argentina

ⁱ Pierre Auger Southern Observatory, Malargüe, Argentina

^j Pierre Auger Southern Observatory and Comisión Nacional de Energía Atómica, Malargüe, Argentina

^k University of Adelaide, Adelaide, S.A., Australia

^l Centro Brasileiro de Pesquisas Físicas, Rio de Janeiro, RJ, Brazil

^m Pontifícia Universidade Católica, Rio de Janeiro, RJ, Brazil

ⁿ Universidade de São Paulo, Instituto de Física, São Carlos, SP, Brazil

^o Universidade de São Paulo, Instituto de Física, São Paulo, SP, Brazil

^p Universidade Estadual de Campinas, IFGW, Campinas, SP, Brazil

^q Universidade Estadual de Feira de Santana, Brazil

^r Universidade Estadual do Sudoeste da Bahia, Vitoria da Conquista, BA, Brazil

^s Universidade Federal da Bahia, Salvador, BA, Brazil

^t Universidade Federal do ABC, Santo André, SP, Brazil

^u Universidade Federal do Rio de Janeiro, Instituto de Física, Rio de Janeiro, RJ, Brazil

^v Rudjer Bošković Institute, 10000 Zagreb, Croatia

^w Charles University, Faculty of Mathematics and Physics, Institute of Particle and Nuclear Physics, Prague, Czech Republic

^x Institute of Physics of the Academy of Sciences of the Czech Republic, Prague, Czech Republic

^y Palacký University, Olomouc, Czech Republic

- ^z Institut de Physique Nucléaire d'Orsay (IPNO), Université Paris 11, CNRS-IN2P3, Orsay, France
- ^{aa} Laboratoire AstroParticule et Cosmologie (APC), Université Paris 7, CNRS-IN2P3, Paris, France
- ^{ab} Laboratoire de l'Accélérateur Linéaire (LAL), Université Paris 11, CNRS-IN2P3, Orsay, France
- ^{ac} Laboratoire de Physique Nucléaire et de Hautes Energies (LPNHE), Universités Paris 6 et Paris 7, CNRS-IN2P3, Paris, France
- ^{ad} Laboratoire de Physique Subatomique et de Cosmologie (LPSC), Université Joseph Fourier, INPG, CNRS-IN2P3, Grenoble, France
- ^{ae} SUBATECH, CNRS-IN2P3, Nantes, France
- ^{af} Bergische Universität Wuppertal, Wuppertal, Germany
- ^{ag} Karlsruhe Institute of Technology – Campus North – Institut für Kernphysik, Karlsruhe, Germany
- ^{ah} Karlsruhe Institute of Technology – Campus North – Institut für Prozessdatenverarbeitung und Elektronik, Karlsruhe, Germany
- ^{ai} Karlsruhe Institute of Technology – Campus South – Institut für Experimentelle Kernphysik (IEKP), Karlsruhe, Germany
- ^{aj} Max-Planck-Institut für Radioastronomie, Bonn, Germany
- ^{ak} RWTH Aachen University, III. Physikalisches Institut A, Aachen, Germany
- ^{al} Universität Hamburg, Hamburg, Germany
- ^{am} Universität Siegen, Siegen, Germany
- ^{an} Dipartimento di Fisica dell'Università and INFN, Genova, Italy
- ^{ao} Università dell'Aquila and INFN, L'Aquila, Italy
- ^{ap} Università di Milano and Sezione INFN, Milan, Italy
- ^{aq} Dipartimento di Fisica dell'Università del Salento and Sezione INFN, Lecce, Italy
- ^{ar} Università di Napoli "Federico II" and Sezione INFN, Napoli, Italy
- ^{as} Università di Roma II "Tor Vergata" and Sezione INFN, Roma, Italy
- ^{at} Università di Catania and Sezione INFN, Catania, Italy
- ^{au} Università di Torino and Sezione INFN, Torino, Italy
- ^{av} Dipartimento di Ingegneria dell'Innovazione dell'Università del Salento and Sezione INFN, Lecce, Italy
- ^{aw} Gran Sasso Center for Astroparticle Physics, Italy
- ^{ax} Istituto di Astrofisica Spaziale e Fisica Cosmica di Palermo (INAF), Palermo, Italy
- ^{ay} Istituto di Fisica dello Spazio Interplanetario (INAF), Università di Torino and Sezione INFN, Torino, Italy
- ^{az} INFN, Laboratori Nazionali del Gran Sasso, Assergi (L'Aquila), Italy
- ^{ba} Università di Palermo and Sezione INFN, Catania, Italy
- ^{bb} Benemérita Universidad Autónoma de Puebla, Puebla, Mexico
- ^{bc} Centro de Investigación y de Estudios Avanzados del IPN (CINVESTAV), México, D.F., Mexico
- ^{bd} Universidad Michoacana de San Nicolás de Hidalgo, Morelia, Michoacan, Mexico
- ^{be} Universidad Nacional Autónoma de México, México, D.F., Mexico
- ^{bf} IMAPP, Radboud University, Nijmegen, Netherlands
- ^{bg} Kernfysisch Versneller Instituut, University of Groningen, Groningen, Netherlands
- ^{bh} NIKHEF, Amsterdam, Netherlands
- ^{bi} ASTRON, Dwingeloo, Netherlands
- ^{bj} Institute of Nuclear Physics PAN, Krakow, Poland
- ^{bk} University of Łódź, Łódź, Poland
- ^{bl} LIP and Instituto Superior Técnico, Lisboa, Portugal
- ^{bm} J. Stefan Institute, Ljubljana, Slovenia
- ^{bn} Laboratory for Astroparticle Physics, University of Nova Gorica, Slovenia
- ^{bo} Instituto de Física Corpuscular, CSIC-Universitat de València, Valencia, Spain
- ^{bp} Universidad Complutense de Madrid, Madrid, Spain
- ^{bq} Universidad de Alcalá, Alcalá de Henares (Madrid), Spain
- ^{br} Universidad de Granada & C.A.F.P.E., Granada, Spain
- ^{bs} Universidad de Santiago de Compostela, Spain
- ^{bt} Rudolf Peierls Centre for Theoretical Physics, University of Oxford, Oxford, United Kingdom
- ^{bu} School of Physics and Astronomy, University of Leeds, United Kingdom
- ^{bv} Argonne National Laboratory, Argonne, IL, USA
- ^{bw} Case Western Reserve University, Cleveland, OH, USA
- ^{bx} Colorado School of Mines, Golden, CO, USA
- ^{by} Colorado State University, Fort Collins, CO, USA
- ^{bz} Colorado State University, Pueblo, CO, USA
- ^{ca} Fermilab, Batavia, IL, USA
- ^{cb} Louisiana State University, Baton Rouge, LA, USA
- ^{cc} Michigan Technological University, Houghton, MI, USA
- ^{cd} New York University, New York, NY, USA
- ^{ce} Northeastern University, Boston, MA, USA
- ^{cf} Ohio State University, Columbus, OH, USA
- ^{cg} Pennsylvania State University, University Park, PA, USA
- ^{ch} Southern University, Baton Rouge, LA, USA
- ^{ci} University of California, Los Angeles, CA, USA
- ^{cj} University of Chicago, Enrico Fermi Institute, Chicago, IL, USA
- ^{ck} University of Hawaii, Honolulu, HI, USA
- ^{cl} University of Nebraska, Lincoln, NE, USA
- ^{cm} University of New Mexico, Albuquerque, NM, USA
- ^{cn} University of Wisconsin, Madison, WI, USA
- ^{co} University of Wisconsin, Milwaukee, WI, USA
- ^{cp} Institute for Nuclear Science and Technology (INST), Hanoi, Viet Nam

ARTICLE INFO

Article history:

Received 26 November 2009

Accepted 4 February 2010

Available online 10 February 2010

Editor: S. Dodelson

ABSTRACT

We report a measurement of the flux of cosmic rays with unprecedented precision and statistics using the Pierre Auger Observatory. Based on fluorescence observations in coincidence with at least one surface detector we derive a spectrum for energies above 10^{18} eV. We also update the previously published energy spectrum obtained with the surface detector array. The two spectra are combined addressing the systematic uncertainties and, in particular, the influence of the energy resolution on the spectral shape.

Keywords:

Pierre Auger Observatory
Cosmic rays
Energy spectrum

The spectrum can be described by a broken power law $E^{-\gamma}$ with index $\gamma = 3.3$ below the ankle which is measured at $\log_{10}(E_{\text{ankle}}/\text{eV}) = 18.6$. Above the ankle the spectrum is described by a power law with index 2.6 followed by a flux suppression, above about $\log_{10}(E/\text{eV}) = 19.5$, detected with high statistical significance.

© 2010 Elsevier B.V. All rights reserved.

1. Introduction

The flux of ultra-high energy cosmic rays exhibits two important features. At energies above 4×10^{19} eV a suppression of the flux with respect to a power law extrapolation is found [1,2], which is compatible with the predicted Greisen–Zatsepin–Kuz'min (GZK) effect [3,4], but could also be related to the maximum energy that can be reached at the sources. A break in the power law, called the ankle, is observed at an energy of about 3×10^{18} eV [5–8]. This break in the energy spectrum has traditionally been attributed to the transition from the galactic component of the cosmic ray flux to a flux dominated by extragalactic sources [9,10]. In recent years it became clear that a similar feature in the cosmic ray spectrum could also result from the propagation of protons from extragalactic sources, placing the transition from galactic to extragalactic cosmic rays at a much lower energy [11,12]. In this model the ankle is produced by the modification of the source spectrum of primary protons. This is caused by e^{\pm} pair production of protons with the photons of the cosmic microwave background, leading to a well-defined prediction of the shape of the flux in the ankle region.

Accurate measurement of the cosmic ray flux in the ankle region is expected to help determine the energy range of the transition between galactic and extragalactic cosmic rays and to constrain model scenarios.

Two complementary techniques are used at the Pierre Auger Observatory to detect extensive air showers initiated by ultra-high energy cosmic rays (UHECR): a *surface detector array* (SD) and a *fluorescence detector* (FD). The SD of the southern observatory in Argentina consists of an array of 1600 water Cherenkov detectors covering an area of about 3000 km² on a triangular grid with 1.5 km spacing. Electrons, photons and muons in air showers are sampled at ground level with a on-time of almost 100%. In addition the atmosphere above the surface detector is observed during clear, dark nights by 24 optical telescopes grouped in 4 buildings. These detectors are used to observe the longitudinal development of extensive air showers by detecting the fluorescence light emitted by excited nitrogen molecules and the Cherenkov light induced by the shower particles. Details of the design and status of the Observatory are given elsewhere [13–15].

The energy spectrum of ultra-high energy cosmic rays at energies greater than 2.5×10^{18} eV has been derived using data from the surface detector array of the Pierre Auger Observatory [2]. This measurement provided evidence for the suppression of the flux above 4×10^{19} eV and is updated here. In this work we extend the previous measurements to lower energies by analysing air showers measured with the fluorescence detector that also triggered at least one of the stations of the surface detector array. Despite the limited event statistics due to the fluorescence detector on-time of about 13%, the lower energy threshold and the good energy resolu-

tion of these *hybrid* events allow us to measure the flux of cosmic rays in the region of the ankle.

The energy spectrum of hybrid events is determined from data taken between November 2005 and May 2008, during which the Auger Observatory was still under construction. Using selection criteria that are set out below, the exposure accumulated during this period was computed and the flux of cosmic rays above 10^{18} eV determined. The spectrum obtained with the surface detector array, updated using data until the end of December 2008, is combined with the hybrid one to obtain a spectrum measurement over a wide energy range with the highest statistics available.

2. Hybrid energy spectrum

The hybrid approach to shower observation is based on the shower detection with the FD in coincidence with at least one SD station. The latter condition, though insufficient to establish an independent SD trigger [2,16], enables the shower geometry and consequently the energy of the primary particle to be determined accurately. The reconstruction accuracy of hybrid events is much better than what can be achieved using SD or FD data independently [17]. For example, the energy resolution of these hybrid measurements is better than 6% above 10^{18} eV compared with about 15% for the surface detector data.

Event reconstruction proceeds in two steps. First the shower geometry is found by combining information from the shower image and timing measured with the FD with the trigger time of the surface detector station that has the largest signal [18]. In the second step the profile of energy deposition of the shower is reconstructed [19] and shower parameters such as depth of shower maximum and primary particle energy are calculated together with their uncertainties.

2.1. Event selection and reconstruction

To ensure good energy reconstruction only events that satisfy the following quality criteria are accepted:

- Showers must have a reconstructed zenith angle smaller than 60°.
- In the plane perpendicular to the shower axis, the reconstructed shower core must be within 1500 m of the station used for the geometrical reconstruction.
- The contribution of Cherenkov light to the overall signal of the FD must be less than 50%.
- The Gaisser–Hillas fit [19,20] of the reconstructed longitudinal profile must be successful with $\chi^2/\text{ndof} < 2.5$.
- The maximum of the shower development, X_{max} , must be observed in the field of view of the telescopes.
- The uncertainty in the reconstructed energy, which includes light flux and geometrical uncertainties, must be $\sigma(E)/E < 20\%$.
- Only periods during which no clouds were detected above the Observatory are used.

To avoid a possible bias in event selection due to the differences between shower profiles initiated by primaries of different

* Corresponding author.

E-mail address: fabian.schuessler@ik.fzk.de (F. Schüssler).

¹ Deceased.

² At Caltech, Pasadena, USA.

³ On leave of absence at the Instituto Nacional de Astrofísica, Óptica y Electrónica.

⁴ At Konan University, Kobe, Japan.

mass, only showers with geometries that would allow the observation of all primaries in the range from proton to iron are retained in the data sample. The corresponding fiducial volume in shower-telescope distance and zenith angle range is defined as a function of the reconstructed energy and has been verified with data [21]. About 1700 events fulfill the selection criteria for quality and for fiducial volume.

A detailed simulation of the detector response has shown that every FD trigger above $E = 10^{18}$ eV passing all the described selection criteria is accompanied by a SD trigger of at least one station, independent of the mass and direction of the incoming primary particle [22].

2.2. Exposure calculation

During the time period discussed here the southern Auger Observatory was in its construction phase with the number of available SD stations increasing from around 630 to a nearly fully completed instrument with 1600 detectors. Over the same period the FD was enlarged from 12 to 24 telescopes. In addition to these large scale changes, smaller but important changes occur on much shorter timescales due, for example, to hardware failures. The data-taking of the fluorescence detector is furthermore influenced by weather effects such as storms or rainfall. These and other factors that affect the efficiency of the data-taking must be taken into account in the determination of the aperture.

The total exposure is the integral over the instantaneous aperture and can be written as

$$\mathcal{E}(E) = \int_T \int_{\Omega} \int_{S_{\text{gen}}} \varepsilon(E, t, \theta, \phi, x, y) \cos \theta \, dS \, d\Omega \, dt, \quad (1)$$

where $d\Omega = \sin \theta \, d\theta \, d\phi$ and Ω are respectively the differential and total solid angles, θ and ϕ are the zenith and azimuth angles and $dS = dx \times dy$ is the horizontal surface element. The final selection efficiency ε includes the efficiencies of the various steps of the analysis, namely the trigger, reconstruction and selection efficiencies and also the evolution of the detector during the time period T . It has been derived from Monte Carlo simulations that scan an area S_{gen} large enough to enclose the full detector array.

The changing configuration of the SD array is taken into account for the determination of the hybrid on-time. In addition, within time intervals of 10 min, the status of all detector components of the Pierre Auger Observatory down to the level of single PMTs of the fluorescence detector is determined. Moreover all known inefficiencies such as DAQ read-out deadtimes are considered.

The longitudinal profile of the deposition of energy simulated with the QGSJet-II [23,24] and Sibyll 2.1 [25,26] hadronic interaction models and the CONEX [27] air shower simulation program are the basis for an extensive set of Monte Carlo simulations. The exact data taking conditions are reproduced by means of a detailed detector simulation within the Auger analysis framework [28]. All atmospheric measurements, e.g. scattering and absorption lengths, as well as monitoring information such as the noise caused by night sky background light and PMT trigger thresholds are taken into account.

The reconstruction of the simulated showers is then performed in exactly the same way as for the data and good agreement between data and Monte Carlo simulations is obtained. As an example, we show in Fig. 1 the distribution of events observed with the fluorescence detector as a function of the distance of the shower core from the telescopes.

Fig. 2 shows the hybrid exposure of events fulfilling all of the quality and fiducial volume cuts that have been applied, for proton and iron primaries. As can be seen, the cuts adopted lead to

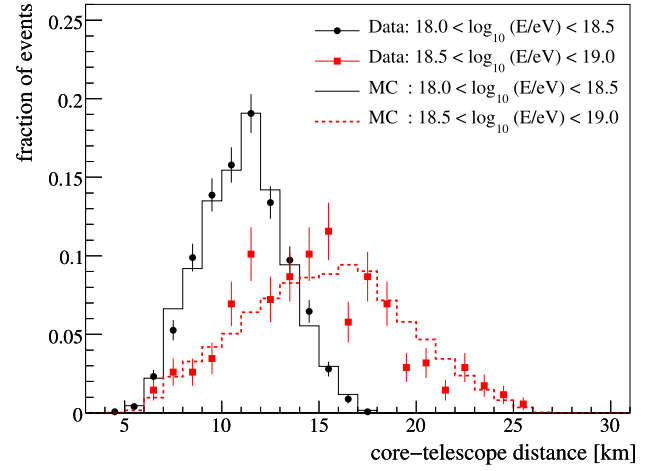


Fig. 1. Distribution of events observed with the fluorescence detector as a function of the distance of the shower core from the telescopes for data and Monte Carlo simulation.

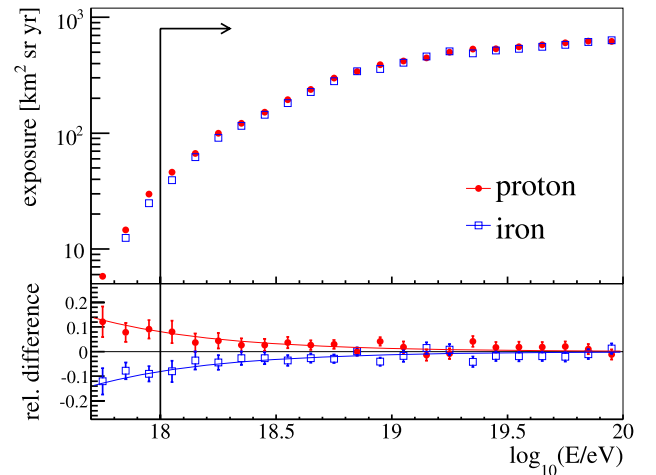


Fig. 2. The hybrid exposure for different primary particles together with the difference to the mixed composition used for the flux measurement.

only a small dependence of the exposure on the mass composition which can be assumed to be dominated by hadrons [29,30]. The systematic uncertainty arising from our lack of knowledge of the mass composition is about 8% at 10^{18} eV and decreases to less than 1% above 10^{19} eV. We assume a mixed composition of 50% proton and 50% iron nuclei for the flux determination and include the remaining composition dependence in the systematic uncertainty. The dependence of the exposure on the assumed model of hadronic interactions was found to be less than 2% over all the energy range.

The full MC simulation chain has been cross-checked with air shower observations and the analysis of laser shots that are fired from the Central Laser Facility [31] and detected with the fluorescence detector. Following this analysis the exposure has been reduced by 8% to account for lost events and an upper limit to the remaining systematic uncertainty of 5% was derived [32]. By combination with the uncertainty related to mass composition the total systematic uncertainty of the hybrid exposure is estimated as 10% (6%) at 10^{18} eV ($> 10^{19}$ eV).

2.3. Energy spectrum from hybrid data

The flux of cosmic rays J as a function of energy is given by

$$J(E) = \frac{d^4 N_{\text{inc}}}{dE dA d\Omega dt} \approx \frac{\Delta N_{\text{sel}}(E)}{\Delta E} \frac{1}{\mathcal{E}(E)}, \quad (2)$$

where N_{inc} is the number of cosmic rays with energy E incident on a surface element dA , within a solid angle $d\Omega$ and time dt . $\Delta N_{\text{sel}}(E)$ is the number of detected events passing the quality cuts in the energy bin centered around E and having width ΔE . $\mathcal{E}(E)$ is the energy-dependent exposure defined above.

The measured flux as function of energy is shown in Fig. 3. A break in the power law of the derived energy spectrum is clearly visible. The position of this feature, known as the ankle, has been determined by fitting two power laws $J = kE^{-\gamma}$ with a free break between them in the energy interval from 10^{18} eV to $10^{19.5}$ eV. The upper end of this interval was defined by the flux suppression observed in the spectrum derived using surface detector data [2]. The ankle is found at $\log_{10}(E_{\text{ankle}}/\text{eV}) = 18.65 \pm 0.09(\text{stat})_{-0.10}^{+0.10}(\text{sys})$ and the two power law indices have been determined as $\gamma_1 = 3.28 \pm 0.07(\text{stat})_{-0.10}^{+0.11}(\text{sys})$ and $\gamma_2 = 2.65 \pm 0.14(\text{stat})_{-0.14}^{+0.16}(\text{sys})$ ($\chi^2/\text{ndof} = 10.2/11$), where the systematic uncertainty is due to the residual effect of the unknown mass composition.

The energy estimation of fluorescence measurements relies on the knowledge of the fluorescence yield. Here we adopt the same absolute calibration [33] and the wavelength and pressure dependence [34] as in Ref. [2]. This is currently one of the dominant sources of systematic uncertainty (14%). The fraction of the energy of the primary particle that is carried by muons and neutrinos and does not contribute to the fluorescence signal has been calculated based on air shower simulations and goes from about 14% at 10^{18} eV to about 10% at 10^{19} eV [35]. The systematic uncertainty depending on the choice of models and mass composition is about 8% [36]. Further systematic uncertainties in the absolute energy scale are related to the absolute detector calibration (9.5%) and its wavelength dependence (3%) [37]. Uncertainties of the lateral width of the shower image and other reconstruction uncertainties amount to about 10% systematic uncertainty in the energy determination. Atmospheric conditions play a crucial role for air shower observations with fluorescence detectors. An extensive program of atmospheric monitoring is conducted at the Pierre Auger Observatory allowing the determination of the relevant parameters and the associated uncertainties [31,38–40]. The total systematic uncertainty in the energy determination is estimated as 22% [41]. Indirect methods of determining the energy scale, which do not involve the fluorescence detector calibration, seem to indicate an energy normalisation that is higher than the one used here by an amount comparable to the uncertainty given above [42].

3. Update of surface detector spectrum

Here we update the published energy spectrum based on surface detector data [2] using data until the end of December 2008. The exposure is now $12790 \text{ km}^2 \text{ sryr}$. The event selection requires that the detector station with the highest signal be surrounded by operational stations and that the reconstructed zenith angle be smaller than 60° [16]. More than 35000 events fulfill these criteria.

The energy estimator of the surface detector is corrected for shower attenuation effects using a constant-intensity method. The calibration of this energy estimator with fluorescence measurements has been updated using the increased data set of high-quality hybrid events [41].

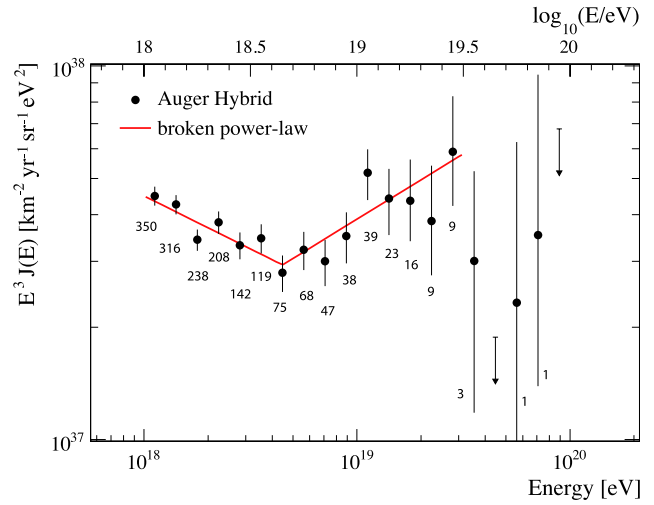


Fig. 3. The energy spectrum of ultra-high energy cosmic rays determined from hybrid measurements of the Pierre Auger Observatory. The number of events is given for each of the energy bins next to the corresponding data point. Only statistical uncertainties are shown. The upper limits correspond to the 68% CL. A fit with a broken power law is used to determine the position of the ankle.

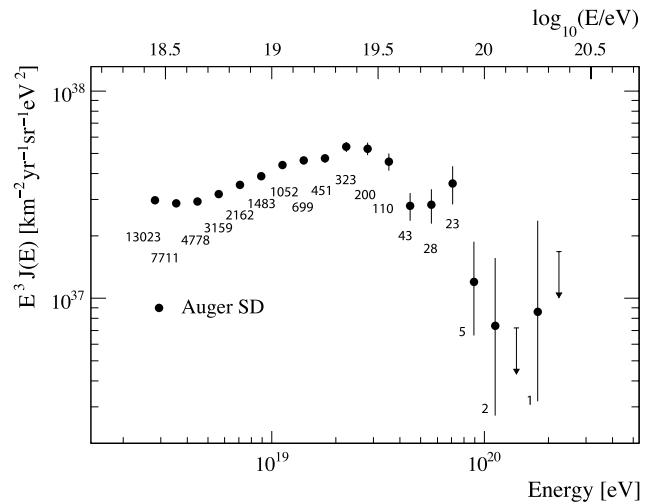


Fig. 4. Energy spectrum, corrected for energy resolution, derived from surface detector data calibrated with fluorescence measurements. The number of events is given for each of the energy bins next to the corresponding data point. Only statistical uncertainties are shown. The upper limits correspond to 68% CL.

Because of the energy resolution of the surface detector data (about 20% at the lowest energies, improving to about 10% at the highest energies), bin-to-bin migrations influence the reconstruction of the flux and spectral shape. To correct for these effects, a forward-folding approach is applied. MC simulations are used to determine the energy resolution of the surface detector and a bin-to-bin migration matrix is derived. The matrix is then used to find a flux parameterisation that matches the measured data after forward-folding. The ratio of this parameterisation to the folded flux gives a correction factor that is applied to the data. The correction to the flux is mildly energy dependent and is less than 20% over the full energy range. Details will be discussed in a forthcoming publication.

The energy spectrum, after correction for the energy resolution, is shown in Fig. 4 together with the event numbers of the un-

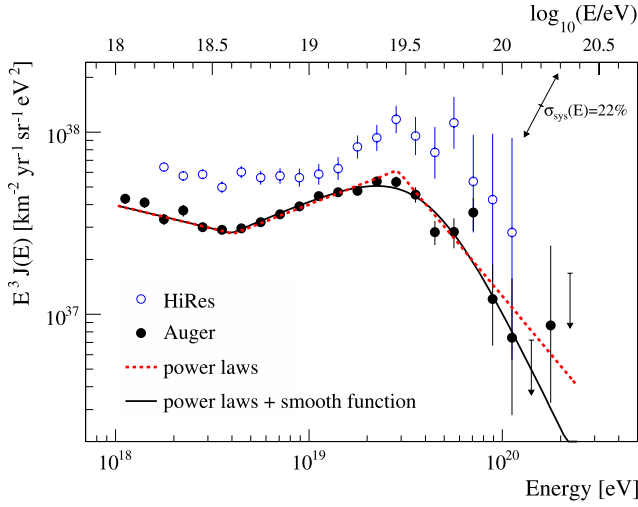


Fig. 5. The combined energy spectrum is fitted with two functions (see text) and compared to data from the HiRes instrument [43]. The systematic uncertainty of the flux scaled by E^3 due to the uncertainty of the energy scale of 22% is indicated by arrows. A table with the Auger flux values can be found at [44].

derlying raw distribution. Combining the systematic uncertainties of the exposure (3%) and of the forward folding assumptions (5%), the systematic uncertainty of the derived flux is 6%.

4. The combined Auger spectrum

The energy spectrum derived from hybrid data is combined with the one obtained from surface detector data using a maximum likelihood method. Since the surface detector energy estimator is calibrated with hybrid events, the two spectra have the same systematic uncertainty in the energy scale. On the other hand, the normalisation uncertainties are independent. They are taken as 6% for the SD and 10% (6%) for the hybrid flux at 10^{18} eV ($> 10^{19}$ eV). These normalisation uncertainties are used as additional constraints in the combination. This combination procedure is used to derive the scale parameters, k , for the fluxes that are to be applied to the individual spectra. These are $k_{SD} = 1.01$ and $k_{FD} = 0.99$ for the surface detector data and hybrid data respectively, showing that agreement between the measurements is at the 1% level.

The combined energy spectrum scaled with E^3 is shown in Fig. 5 in comparison with the spectrum obtained with stereo measurements of the HiRes instrument [43]. An energy shift within the current systematic uncertainties of the energy scale applied to one or both experiments could account for most of the difference between the spectra. The ankle feature seems to be somewhat more sharply defined in the Auger data. This is possibly due to a systematic energy offset between the experiments. However, for a complete comparison, care must also be taken to account for energy resolution and possible changes in aperture with energy.

The characteristic features of the combined spectrum are quantified in two ways. For the first method, shown as a dotted red line in Fig. 5, we have used three power laws with free breaks between them. A continuation of the power law above the ankle to highest energies can be rejected with more than 20σ . For the second characterisation we have adopted two power laws in the ankle region and a smoothly changing function at higher energies which is given by

$$J(E; E > E_{\text{ankle}}) \propto \frac{E^{-\gamma_2}}{1 + \exp\left(\frac{\log_{10} E - \log_{10} E_{1/2}}{\log_{10} W_c}\right)}, \quad (3)$$

Table 1

Fitted parameters and their statistical uncertainties characterising the combined energy spectrum.

Parameter	Power laws	Power laws + smooth function
$\gamma_1 (E < E_{\text{ankle}})$	3.26 ± 0.04	3.26 ± 0.04
$\log_{10}(E_{\text{ankle}}/\text{eV})$	18.61 ± 0.01	18.60 ± 0.01
$\gamma_2 (E > E_{\text{ankle}})$	2.59 ± 0.02	2.55 ± 0.04
$\log_{10}(E_{\text{break}}/\text{eV})$	19.46 ± 0.03	
$\gamma_3 (E > E_{\text{break}})$	4.3 ± 0.2	
$\log_{10}(E_{1/2}/\text{eV})$		19.61 ± 0.03
$\log_{10}(W_c/\text{eV})$		0.16 ± 0.03
χ^2/ndof	38.5/16	29.1/16

where $E_{1/2}$ is the energy at which the flux has fallen to one half of the value of the power-law extrapolation and W_c parametrizes the width of the transition region. It is shown as a black solid line in Fig. 5. The derived parameters (quoting only statistical uncertainties) are given in Table 1.

At high energies the combined spectrum is statistically dominated by the surface detector data. The agreement between the index of the power law above the ankle, γ_2 , measured with the combined spectrum (2.59 ± 0.02) and with hybrid data (2.65 ± 0.14), also demonstrates the good agreement between the two measurements.

5. Summary

We have measured the cosmic ray flux with the Pierre Auger Observatory by applying two different techniques. The fluxes obtained with hybrid events and from the surface detector array are in good agreement in the overlapping energy range. A combined spectrum has been derived with high statistics covering the energy range from 10^{18} eV to above 10^{20} eV. The dominant systematic uncertainty of the spectrum stems from that of the overall energy scale, which is estimated to be 22%.

The position of the ankle at $\log_{10}(E_{\text{ankle}}/\text{eV}) = 18.61 \pm 0.01$ has been determined by fitting the flux with a broken power law $E^{-\gamma}$. An index of $\gamma = 3.26 \pm 0.04$ is found below the ankle. Above the ankle the spectrum follows a power law with index 2.55 ± 0.04 . In comparison to the power law extrapolation, the spectrum is suppressed by a factor two at $\log_{10}(E_{1/2}/\text{eV}) = 19.61 \pm 0.03$. The significance of the suppression is larger than 20σ . The suppression is similar to what is expected from the GZK effect for protons or nuclei as heavy as iron, but could in part also be related to a change of the shape of the average injection spectrum at the sources.

Acknowledgements

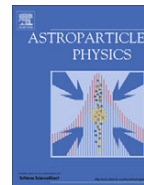
The successful installation and commissioning of the Pierre Auger Observatory would not have been possible without the strong commitment and effort from the technical and administrative staff in Malargüe.

We are very grateful to the following agencies and organizations for financial support: Comisión Nacional de Energía Atómica, Fundación Antorchas, Gobierno De La Provincia de Mendoza, Municipalidad de Malargüe, NDM Holdings and Valle Las Leñas, in gratitude for their continuing cooperation over land access, Argentina; the Australian Research Council; Conselho Nacional de Desenvolvimento Científico e Tecnológico (CNPq), Financiadora de Estudos e Projetos (FINEP), Fundação de Amparo à Pesquisa do Estado de Rio de Janeiro (FAPERJ), Fundação de Amparo à Pesquisa do Estado de São Paulo (FAPESP), Ministério de Ciência e Tecnologia (MCT), Brazil; AVCR AVOZ10100502 and AVOZ10100522, GAAV KJB300100801 and KJB100100904, MSMT-CR LA08016, LC527,

1M06002, and MSM0021620859, Czech Republic; Centre de Calcul IN2P3/CNRS, Centre National de la Recherche Scientifique (CNRS), Conseil Régional Ile-de-France, Département Physique Nucléaire et Corpusculaire (PNC-IN2P3/CNRS), Département Sciences de l'Univers (SDU-INSU/CNRS), France; Bundesministerium für Bildung und Forschung (BMBF), Deutsche Forschungsgemeinschaft (DFG), Finanzministerium Baden-Württemberg, Helmholtz-Gemeinschaft Deutscher Forschungszentren (HGF), Ministerium für Wissenschaft und Forschung, Nordrhein-Westfalen, Ministerium für Wissenschaft, Forschung und Kunst, Baden-Württemberg, Germany; Istituto Nazionale di Fisica Nucleare (INFN), Ministero dell'Istruzione, dell'Università e della Ricerca (MIUR), Italy; Consejo Nacional de Ciencia y Tecnología (CONACYT), Mexico; Ministerie van Onderwijs, Cultuur en Wetenschap, Nederlandse Organisatie voor Wetenschappelijk Onderzoek (NWO), Stichting voor Fundamenteel Onderzoek der Materie (FOM), Netherlands; Ministry of Science and Higher Education, Grant Nos. 1 P03 D 014 30, N202 090 31/0623, and PAP/218/2006, Poland; Fundação para a Ciência e a Tecnologia, Portugal; Ministry for Higher Education, Science, and Technology, Slovenian Research Agency, Slovenia; Comunidad de Madrid, Consejería de Educación de la Comunidad de Castilla La Mancha, FEDER funds, Ministerio de Ciencia e Innovación, Xunta de Galicia, Spain; Science and Technology Facilities Council, United Kingdom; Department of Energy, Contract Nos. DE-AC02-07CH11359, DE-FR02-04ER41300, National Science Foundation, Grant No. 0450696, The Grainger Foundation, USA; ALFA-EC/HELEN, European Union 6th Framework Program, Grant No. MEIF-CT-2005-025057, European Union 7th Framework Program, Grant No. PIEF-GA-2008-220240, and UNESCO.

References

- [1] R. Abbasi, et al., HiRes Collaboration, Phys. Rev. Lett. 100 (2008) 101101, astro-ph/0703099.
- [2] J. Abraham, et al., Pierre Auger Collaboration, Phys. Rev. Lett. 101 (2008) 061101, arXiv:0806.4302 [astro-ph].
- [3] K. Greisen, Phys. Rev. Lett. 16 (1966) 748.
- [4] G.T. Zatsepin, V.A. Kuz'min, Pis'ma Zh. Eksp. Teor. Fiz. 4 (1966) 114.
- [5] J. Linsley, Proc. of 8th Int. Cosmic Ray Conf., Jaipur 4 (1963) 77.
- [6] M.A. Lawrence, R.J.O. Reid, A.A. Watson, J. Phys. G 17 (1991) 733.
- [7] M. Nagano, et al., J. Phys. G 18 (1992) 423.
- [8] D.J. Bird, et al., Fly's Eye Collaboration, Phys. Rev. Lett. 71 (1993) 3401.
- [9] A.M. Hillas, J. Phys. G 31 (2005) R95.
- [10] T. Wibig, A.W. Wolfendale, J. Phys. G 31 (2005) 255, astro-ph/0410624.
- [11] V. Berezhinsky, A.Z. Gazizov, S.I. Grigorieva, Phys. Lett. B 612 (2005) 147, astro-ph/0502550.
- [12] R. Aloisio, V. Berezhinsky, P. Blasi, S. Ostapchenko, Phys. Rev. D 77 (2008) 025007, arXiv:0706.2834 [astro-ph].
- [13] J. Abraham, et al., Pierre Auger Collaboration, Nucl. Instrum. Methods A 523 (2004) 50.
- [14] I. Allekotte, et al., Pierre Auger Collaboration, Nucl. Instrum. Methods A 586 (2008) 409, arXiv:0712.2832 [astro-ph].
- [15] J. Abraham, et al., Pierre Auger Collaboration, arXiv:0907.4282 [astro-ph.IM], Nucl. Instrum. Methods A, submitted for publication.
- [16] J. Abraham, et al., Pierre Auger Collaboration, Nucl. Instrum. Methods A 613 (2010) 29.
- [17] B. Fick, et al., Pierre Auger Collaboration, 28th Int. Cosmic Ray Conf., Tsukuba (2003) 449, astro-ph/0308512; P. Sommers, Astropart. Phys. 3 (1995) 349.
- [18] M. Mostafa, Pierre Auger Collaboration, Nucl. Phys. B (Proc. Suppl.) 165 (2007) 50, astro-ph/0608670.
- [19] M. Unger, B.R. Dawson, R. Engel, F. Schüssler, R. Ulrich, Nucl. Instrum. Methods A 588 (2008) 433, arXiv:0801.4309 [astro-ph].
- [20] T.K. Gaisser, A.M. Hillas, Proc. of 15th Int. Cosmic Ray Conf., Plovdiv (1977) 358.
- [21] J. Abraham, et al., Pierre Auger Collaboration, Astropart. Phys. 27 (2007) 155, astro-ph/0606619.
- [22] L. Perrone, Pierre Auger Collaboration, Proc. of 30th Int. Cosmic Ray Conf., Merida 4 (2007) 331, arXiv:0706.2643 [astro-ph].
- [23] S. Ostapchenko, Phys. Rev. D 74 (2006) 014026, hep-ph/0505259.
- [24] S. Ostapchenko, Phys. Lett. B 636 (2006) 40, hep-ph/0602139.
- [25] R.S. Fletcher, T.K. Gaisser, P. Lipari, T. Stanev, Phys. Rev. D 50 (1994) 5710.
- [26] R. Engel, T.K. Gaisser, T. Stanev, P. Lipari, Proc. of 26th Int. Cosmic Ray Conf., Salt Lake City 1 (1999) 415.
- [27] T. Bergmann, et al., Astropart. Phys. 26 (2007) 420, astro-ph/0606564.
- [28] S. Argiro, et al., Nucl. Instrum. Methods A 580 (2007) 1485, arXiv:0707.1652 [astro-ph].
- [29] J. Abraham, et al., Pierre Auger Collaboration, Phys. Rev. D 79 (2009) 171101.
- [30] J. Abraham, et al., Pierre Auger Collaboration, Astropart. Phys. 31 (2009) 399; J. Abraham, et al., Pierre Auger Collaboration, Astropart. Phys. 29 (2008) 243.
- [31] B. Fick, et al., JINST 1 (2006) P11003.
- [32] F. Salamida, for the Pierre Auger Collaboration, Proc. 31th Int. Cosmic Ray Conf. (Lodz, Poland) (2009), arXiv:0906.2189 [astro-ph.HE].
- [33] M. Nagano, K. Kobayakawa, N. Sakaki, K. Ando, Astropart. Phys. 20 (2003) 293, astro-ph/0303193.
- [34] M. Ave, et al., AIRFLY Collaboration, Astropart. Phys. 28 (2007) 41, astro-ph/0703132.
- [35] H.M.J. Barbosa, et al., Astropart. Phys. 22 (2004) 159, astro-ph/0310234.
- [36] T. Pierog, R. Engel, D. Heck, S. Ostapchenko, K. Werner, Proc. of 30th Int. Cosmic Ray Conf., Merida 4 (2007) 625.
- [37] R. Knapik, et al., Pierre Auger Collaboration, Proc. of 30th Int. Cosmic Ray Conf., Merida 4 (2007) 343, arXiv:0708.1924 [astro-ph].
- [38] S.Y. BenZvi, et al., Nucl. Instrum. Methods A 574 (2007) 171, astro-ph/0609063.
- [39] B. Keilhauer, et al., Pierre Auger Collaboration, Proc. of 29th Int. Cosmic Ray Conf., Pune 7 (2005) 123, astro-ph/0507275.
- [40] S.Y. BenZvi, et al., Pierre Auger Collaboration, Proc. of 30th Int. Cosmic Ray Conf., Merida 4 (2007) 355, arXiv:0706.3236 [astro-ph].
- [41] C. Di Giulio, for the Pierre Auger Collaboration, Proc. 31th Int. Cosmic Ray Conf. (Lodz, Poland) (2009), arXiv:0906.2189 [astro-ph.HE].
- [42] A. Castellina, for the Pierre Auger Collaboration, Proc. 31th Int. Cosmic Ray Conf. (Lodz, Poland) (2009), arXiv:0906.2319 [astro-ph.HE].
- [43] R.U. Abbasi, et al., HiRes Collaboration, Astropart. Phys. 32 (2009) 53.
- [44] http://www.auger.org/combined_spectrum_icrc09.txt.



The ANTARES telescope neutrino alert system

M. Ageron^a, J.A. Aguilar^b, I. Al Samarai^a, A. Albert^c, M. André^d, M. Anghinolfi^e, G. Anton^f, S. Anvar^g, M. Ardid^h, A.C. Assis Jesusⁱ, T. Astraatmadja^{i,1}, J.-J. Aubert^a, B. Baret^j, S. Basa^k, V. Bertin^a, S. Biagi^{l,m}, A. Bigiⁿ, C. Bigongiari^b, C. Bogazziⁱ, M. Bou-Cabo^h, B. Bouhou^j, M.C. Bouwhuisⁱ, J. Brunner^{a,2}, J. Busto^a, F. Camarena^h, A. Capone^{o,p}, C. Cârloganu^q, G. Carminati^{l,m,3}, J. Carr^a, S. Cecchini^l, Z. Charif^a, Ph. Charvis^{r,s}, T. Chiarusi^l, M. Circella^t, R. Coniglione^v, H. Costantini^{e,a}, P. Coyle^a, C. Curtil^a, M.P. Decowskiⁱ, I. Dekeyser^u, A. Deschamps^r, C. Distefano^v, C. Donzaud^{j,w}, D. Dornic^b, Q. Dorosti^x, D. Drouhin^c, T. Eberl^f, U. Emanuele^b, A. Enzenhöfer^f, J.-P. Ernenwein^a, S. Escoffier^a, P. Fermani^{o,p}, M. Ferri^h, V. Flaminio^{n,y}, F. Folger^f, U. Fritsch^f, J.-L. Fuda^u, S. Galatà^a, P. Gay^q, G. Giacomelli^{l,m}, V. Giordano^v, J.P. Gómez-González^b, K. Graf^f, G. Guillard^q, G. Halladjian^a, G. Hallewell^a, H. van Haren^z, J. Hartmanⁱ, A.J. Heijboerⁱ, Y. Hello^{r,s}, J.J. Hernández-Rey^b, B. Herold^f, J. Hößl^f, C.C. Hsuⁱ, M. de Jong^{i,1}, M. Kadler^{aa}, O. Kalekin^f, A. Kappes^f, U. Katz^f, O. Kavatsyuk^x, P. Kooijman^{i,ab,ac}, C. Kopper^f, A. Kouchner^j, I. Kreykenbohm^{aa}, V. Kulikovskiy^{ad,e}, R. Lahmann^f, P. Lamare^g, G. Larosa^h, D. Lattuada^v, D. Lefèvre^u, G. Lim^{i,ac}, D. Lo Presti^{ae,af}, H. Loehner^x, S. Loucatos^{ag}, S. Mangano^b, M. Marcelin^k, A. Margiotta^{l,m}, J.A. Martínez-Mora^h, A. Meli^f, T. Montaruli^{t,ah}, L. Moscoso^{j,ag,4}, H. Motz^f, M. Neff^f, E. Nezri^k, D. Palioselitisⁱ, G.E. Pāvāļš^{ai}, K. Payet^{ag}, P. Payre^{a,4}, J. Petrovicⁱ, P. Piattelli^v, N. Picot-Clemente^a, V. Popa^{ai}, T. Pradier^{aj}, E. Presaniⁱ, C. Racca^c, C. Reedⁱ, C. Richardt^f, R. Richter^f, C. Rivièrè^a, A. Robert^t, K. Roensch^f, A. Rostovtsev^{ak}, J. Ruiz-Rivas^b, M. Rujoiu^{ai}, G.V. Russo^{ae,af}, F. Salesa^b, P. Sapienza^v, F. Schöck^f, J.-P. Schuller^{ag}, F. Schüssler^{ag}, R. Shanidze^f, F. Simeone^{o,p}, A. Spies^f, M. Spurio^{l,m}, J.J.M. Steijgerⁱ, Th. Stolarczyk^{ag}, A. Sánchez-Losa^b, M. Taiuti^{e,al}, C. Tamburini^u, S. Toscano^b, B. Vallage^{ag}, V. Van Elewyck^j, G. Vannoni^{ag}, M. Vecchi^{a,p,*}, P. Vernin^{ag}, G. Wijnkerⁱ, J. Wilms^{aa}, E. de Wolf^{i,ac}, H. Yepes^b, D. Zaborov^{ak}, J.D. Zornoza^b, J. Zúñiga^b

^a CPM, Aix-Marseille Université, CNRS/IN2P3, Marseille, France

^b IFIC – Instituto de Física Corpuscular, Edificios Investigación de Paterna, CSIC, Universitat de València, Apdo. de Correos 22085, 46071 Valencia, Spain

^c GRPHE – Institut universitaire de technologie de Colmar, 34 rue du Grillenbreit BP50568, 68008 Colmar, France

^d Technical University of Catalonia, Laboratory of Applied Bioacoustics, Rambla Exposició, 08800 Vilanova i la Geltrú, Barcelona, Spain

^e INFN – Sezione di Genova, Via Dodecaneso 33, 16146 Genova, Italy

^f Friedrich-Alexander-Universität Erlangen-Nürnberg, Erlangen Centre for Astroparticle Physics, Erwin-Rommel-Str. 1, 91058 Erlangen, Germany

^g Direction des Sciences de la Matière, Institut de recherche sur les lois fondamentales de l'Univers, Service d'Electronique des Détecteurs et d'Informatique, CEA Saclay, 91191 Gif-sur-Yvette Cedex, France

^h Institut d'Investigació per a la Gestió Integrada de les Zones Costaneres (IGIC), Universitat Politècnica de València. C/ Paranimf 1, 46730 Gandia, Spain

ⁱ Nikhef, Science Park, Amsterdam, The Netherlands

^j APC – Laboratoire AstroParticule et Cosmologie, UMR 7164, CNRS, Université Paris 7 Diderot, CEA, Observatoire de Paris, 10, rue Alice Domon et Léonie Duquet, 75205 Paris Cedex 13, France

^k LAM – Laboratoire d'Astrophysique de Marseille, Pôle de l'Étoile Site de Château-Gombert, rue Frédéric Joliot-Curie 38, 13388 Marseille Cedex 13, France

^l INFN – Sezione di Bologna, Viale Berti Pichat 6/2, 40127 Bologna, Italy

^m Dipartimento di Fisica dell'Università, Viale Berti Pichat 6/2, 40127 Bologna, Italy

ⁿ INFN – Sezione di Pisa, Largo B. Pontecorvo 3, 56127 Pisa, Italy

^o INFN – Sezione di Roma, P.le Aldo Moro 2, 00185 Roma, Italy

^p Dipartimento di Fisica dell'Università La Sapienza, P.le Aldo Moro 2, 00185 Roma, Italy

^q Clermont Université, Université Blaise Pascal, CNRS/IN2P3, Laboratoire de Physique Corpusculaire, BP 10448, 63000 Clermont-Ferrand, France

^r Géoazur, Université de Nice Sophia-Antipolis, CNRS/INSU, IRD, Observatoire de la Côte d'Azur, France

^s Université Pierre et Marie Curie, BP 48, 06235 Villefranche-sur-mer, France

^t INFN – Sezione di Bari, Via E. Orabona 4, 70126 Bari, Italy

^u COM – Centre d'Océanologie de Marseille, CNRS/INSU et Université de la Méditerranée, 163 Avenue de Luminy, Case 901, 13288 Marseille Cedex 9, France

^v INFN – Laboratori Nazionali del Sud (LNS), Via S. Sofia 62, 95123 Catania, Italy

^w Univ Paris-Sud, 91405 Orsay Cedex, France

^x Kernfysisch Versneller Instituut (KVI), University of Groningen, Zernikelaan 25, 9747 AA Groningen, The Netherlands

^y Dipartimento di Fisica dell'Università, Largo B. Pontecorvo 3, 56127 Pisa, Italy

^z Royal Netherlands Institute for Sea Research (NIOZ), Landsdiep 4, 1797 SZ 't Horntje (Texel), The Netherlands

^{aa} Dr. Reemis-Sternwarte and ECAP, Universität Erlangen-Nürnberg, Sternwartstr. 7, 96049 Bamberg, Germany

^{ab} Universiteit Utrecht, Faculteit Betawetenschappen, Princetonplein 5, 3584 CC Utrecht, The Netherlands

^{ac} Universiteit van Amsterdam, Instituut voor Hoge-Energie Fysika, Science Park 105, 1098 XG Amsterdam, The Netherlands

^{ad} Moscow State University, Skobeltsyn Institute of Nuclear Physics, Leninskie gory, 119991 Moscow, Russia

^{ae} INFN – Sezione di Catania, Viale Andrea Doria 6, 95125 Catania, Italy

^{af} Dipartimento di Fisica ed Astronomia dell'Università, Viale Andrea Doria 6, 95125 Catania, Italy

^{ag} Direction des Sciences de la Matière, Institut de recherche sur les lois fondamentales de l'Univers, Service de Physique des Particules, CEA Saclay, 91191 Gif-sur-Yvette Cedex, France

^{ah} University of Wisconsin–Madison, 53715, WI, USA

^{ai} Institute for Space Sciences, R-77125 Bucharest, Măgurele, Romania

^{aj} IPHC-Institut Pluridisciplinaire Hubert Curien, Université de Strasbourg et CNRS/IN2P3 23 rue du Loess, BP 28, 67037 Strasbourg Cedex 2, France

^{ak} ITEP – Institute for Theoretical and Experimental Physics, B. Chermushkinskaya 25, 117218 Moscow, Russia

^{al} Dipartimento di Fisica dell'Università, Via Dodecaneso 33, 16146 Genova, Italy

ARTICLE INFO

Article history:

Received 11 March 2011

Received in revised form 3 November 2011

Accepted 29 November 2011

Available online 20 December 2011

Keywords:

ANTARES

Neutrino astronomy

Transient sources

Optical follow-up

ABSTRACT

The ANTARES telescope has the capability to detect neutrinos produced in astrophysical transient sources. Potential sources include gamma-ray bursts, core collapse supernovae, and flaring active galactic nuclei. To enhance the sensitivity of ANTARES to such sources, a new detection method based on coincident observations of neutrinos and optical signals has been developed. A fast online muon track reconstruction is used to trigger a network of small automatic optical telescopes. Such alerts are generated for special events, such as two or more neutrinos, coincident in time and direction, or single neutrinos of very high energy.

© 2011 Elsevier B.V. All rights reserved.

1. Introduction

The detection of high energy cosmic neutrinos from a source would be direct evidence of the presence of hadronic acceleration within the source and provide important information on the origin of the high energy cosmic rays. Powerful sources of transient nature, such as gamma ray bursts or core collapse supernovae, offer one of the most promising perspectives for the detection of cosmic neutrinos as, due to their short duration, they are essentially background free. For example, several authors predict the emission of neutrinos in correlation with multi-wavelength signals, e.g. the Fireball model of GRBs [1]. As neutrino telescopes observe a full hemisphere of the sky (even the whole sky if downgoing events are considered) at all times, they are particularly well suited for the detection of transient phenomena.

In this paper, the implementation of a strategy for the detection of transient sources is presented. This method, earlier proposed in [2], is based on the optical follow-up of selected neutrino events very shortly after their detection (Section 3) by the ANTARES neutrino telescope [3]. The alert system, known as “TAToO” (Telescopes and ANTARES Target of Opportunity) [4], uses an online track reconstruction with a pointing accuracy of about 0.5 degrees. This reconstruction algorithm is described in Section 4. Its characteristics allow the triggering of small robotic optical telescopes such as those of TAROT [5] and ROTSE-III [6], which have slewing and settling time below 10 s. TAROT consists of two 25 cm telescopes with a large field of view of $1.98^\circ \times 1.98^\circ$ and magnitude limit of 18–19, located at Calern, France, and La Silla, Chile. ROTSE-III is an array of four 45 cm telescopes with field of view of $1.86^\circ \times 1.86^\circ$ and magnitude limit of 19, located at Sidings Springs Observatory, Australia, McDonald Observatory, Texas, Mt. Gamsberg, Namibia, and Bakiritepe, Turkey. In order to improve the precision of these alerts, an additional reconstruction algo-

rithm, described in Section 5, which takes into account the detailed detector geometry is used offline.

2. The ANTARES detector and data acquisition

The ANTARES neutrino telescope is located in the Mediterranean Sea, 40 km from the coast of Toulon, France, at a depth of 2475 m. The detector is an array of photomultiplier tubes (PMTs) arranged on 12 slender detection lines, anchored to the sea bed and kept taut by a buoy at the top. Each line comprises up to 25 storeys of triplets of optical modules (OMs), each housing a single $10''$ PMT. Since lines are subject to the sea current and can change shape and orientation, a positioning system comprising hydrophones and compass-tiltmeters is used to monitor the detector geometry. Data taking started in 2006 with the operation of the first line of the detector. The construction of the 12 line detector was completed in May 2008. The main goal of the experiment is to search for neutrinos of astrophysical origin by detecting high energy muons (≥ 100 GeV) induced by their neutrino charged current interaction in the vicinity of the detector. Due to the large background from downgoing cosmic ray induced muons, the detector is optimized for the detection of upgoing neutrino induced muon tracks.

2.1. Data acquisition

The task of the ANTARES data acquisition system (DAQ) [7] is to collect the data from all the individual PMTs of the detector and pass them to the filtering algorithms which search for a collection of signals compatible with a muon track crossing the detector.

From the DAQ point of view, each storey is an independent acquisition unit including a processor, buffering RAM and an Ethernet link to the shore station. Individual PMT pulses above a threshold of typically 0.3 photoelectron (referred to as ‘hits’) are digitized offshore in the form of ‘hit time’ and ‘charge’, and sent to a computer farm onshore for further processing. Due to bioluminescence activity and ^{40}K decays in the sea water, each PMT has an average counting rate of the order of 100 kHz, requiring large bandwidth for data transmission to shore. The data are transmitted through gigabit Ethernet links on single optical fibers to the computing farm where the filtering algorithms are executed, reducing the

* Corresponding author at: CPPM, Aix-Marseille Université, CNRS/IN2P3, Marseille, France.

E-mail address: vecchi@cppm.in2p3.fr (M. Vecchi).

¹ Also at University of Leiden, the Netherlands.

² On leave at DESY, Platanenallee 6, D-15738 Zeuthen, Germany.

³ Now at University of California – Irvine, 92697, CA, USA.

⁴ Deceased.

event rate to a few tens of hertz. The overall system is supervised by a state machine which handles the various commands needed to configure, start and stop the acquisition on both the offshore and onshore processors.

Data are time structured in the form of time slices of 104.85 ms, allowing the data of the full detector for the duration of one time slice to be sent to a single computing node. The synchronization of the 300 offshore processors is performed by a 20 MHz clock distribution system broadcasted to all storeys. In particular, the start of any data taking period is stamped using an external GPS signal giving the absolute timing at the location of the detector, allowing an absolute time accuracy better than 1 μ s [8].

2.2. Data filtering

The main goal of the filtering algorithm is to select hits compatible with the propagation of Cherenkov light emitted by a muon crossing the detector, among the background from bioluminescence and ^{40}K decays characterized by uncorrelated hits on single OMs. The filtering is based on local ‘clusters’, defined either as coincidence hits on OMs of the same storey within a narrow time window or as a single hit with a large amplitude. There are two main filtering algorithms running simultaneously, both searching for a combination of local clusters within a typical 2.2 μ s time window. The first algorithm requires five local causally connected clusters anywhere in the detector, while the second requires at least two local clusters in adjacent or next-to-adjacent storeys. All hits within a few microseconds around these clusters define an ‘event’ and are kept for further online and offline reconstructions.

2.3. The TAToO trigger

Once a single data filtering computer has processed its time slice, the resulting events are sent to a data distribution service to which the ‘Data Writer’ storing task, monitoring tasks and the online event reconstruction [9] are connected. The ‘alert’ application described in Section 4 analyses the data stream of reconstructed events, selects candidates fulfilling various criteria, and then generates the TAToO alerts.

An important performance parameter for the alert system is the time between the crossing of the detector by a high energy muon and the time at which an alert is sent. This time is the sum of the data dispatching time from the offshore photomultipliers to the onshore computing farm (1.5 s) and of the data processing time of an entire time slice by the filtering algorithm (≤ 5 s). For the time-being, the data transmission to the processors suffers from an additional latency of up to one minute, which will be removed after an upgrade of the acquisition to improve the performance of the alert sending capability. The time needed to reconstruct the event direction and verify the alert criteria typically amounts to a few milliseconds. Therefore, the total delay between an interesting particle crossing the detector and a TAToO alert is currently about one minute.

3. The TAToO run control

The TAToO Run Control (RC) is a stand-alone Qt control application⁵ which channels the triggers generated by the alert application to the optical telescope network.

The connections to this network are checked periodically and automatic reconnection is performed resulting in a fully autonomous and stable system. A veto prevents an alert to be sent if the ANTARES event counting rate exceeds a given threshold. In addition, if the alert criteria are fulfilled soon after a previous alert has

already been issued, the new alert is stored in a FIFO and sent only after a certain period of time. This time lag, currently set at one hour, is used to avoid alert pileup in the optical telescope network. Manual alerts can also be generated and sent. All alerts are sent using the Gamma-ray bursts Coordinates Network (GCN) [10] normalized format, allowing easy implementation of connections to additional telescopes. Information about the event that triggered the alert, i.e. a unique identifier, the time and the celestial coordinates, the number of hits used in the reconstruction and the track reconstruction quality are sent to the optical telescopes network at the time of the alert.

4. The alert criteria

The criteria for the TAToO trigger are based on the features of the neutrino signal from the expected sources. Several models predict the production of high energy neutrinos greater than 1 TeV from GRBs [11] and from Core Collapse Supernovae [12]. Under certain conditions, multiplet of neutrinos can be expected [13].

Two online neutrino trigger criteria are currently implemented in the TAToO alert system:

- the detection of at least two neutrino induced muons coming from similar directions within a predefined time window;
- the detection of a single high energy neutrino induced muon.

A basic requirement for the coincident observation of a neutrino and an optical counterpart is that the pointing accuracy of the neutrino telescope should be at least comparable to the field of view of the TAROT and ROTSE telescopes.

4.1. The online track reconstruction algorithm

To select the events which might trigger an alert, a fast and robust algorithm is used online to reconstruct tracks from the calibrated data. This algorithm uses an idealized detector geometry which does not rely on the dynamical positioning alignment. As a result, the hits of the three OMs of a storey are grouped and their location assigned to the barycenter of the storey. The storey orientations as well as the line-shape deviations from straight lines are not considered in the online reconstruction. A detailed description of this algorithm and its performance is found in Ref. [9]. The principle is to minimize a χ^2 which compares the times of selected hits with the expectation from a Cherenkov signal generated by a muon track. The resulting direction of the reconstructed muon track is available within 10 ms and the obtained reduced χ^2 , $\chi_{red}^2 = \chi_{min}^2/N_{dof}$ with N_{dof} the number of degrees of freedom, is used as a fit quality parameter to remove badly reconstructed tracks.

4.2. Neutrino selection criteria

Atmospheric muons, whose abundance at the ANTARES detector [14] is roughly six orders of magnitude larger than the one of muons induced by atmospheric neutrinos, are the main background for the alerts and have to be efficiently suppressed. Among the surviving events, neutrino candidates with an increased probability to be of cosmic origin are selected [15].

4.2.1. Atmospheric muon background rejection

Atmospheric muons resulting from the interaction of cosmic rays with nuclei in the atmosphere represent the main component of the background. Atmospheric muons propagate downgoing through the detector and can be suppressed with an elevation cut, selecting only the upgoing events. However, some badly reconstructed atmospheric muons classified as upgoing may remain, and

⁵ Software framework originally from Trolltech, now Nokia.

quality cuts are applied to reduce this contamination to an acceptable level.

In order to establish the criteria for our neutrino selection, we have analyzed a subsample of data taken by ANTARES after the completion of the 12-line detector, corresponding to a livetime of 70.3 days. During this period, around 350 upgoing neutrino candidates were reconstructed and have been compared to a Monte Carlo (MC) simulation of atmospheric muons and neutrinos using the same livetime. Downgoing atmospheric muons were simulated with Corsika [16], and normalized to match the data. The primary particle flux was composed of several nuclei according to Ref. [17] and the QGSJET hadronic model [18] was used for the shower development. Upgoing neutrinos were simulated according to the parameterization of the atmospheric neutrino flux from Ref. [19]. Only charged current interactions of neutrinos and antineutrinos were considered. The Cherenkov light produced in the vicinity of the ANTARES detector was propagated taking into account light absorption and scattering in sea water [20]. The angular acceptance, quantum efficiency and other characteristics of the optical modules were taken from Ref. [21].

Fig. 1 shows the distribution of the track fit quality (χ_{red}^2) of the minimization procedure for all upgoing events reconstructed with at least two lines. A cut on the track fit quality is applied to reduce the number of atmospheric muons reconstructed as upgoing in the final sample. Because the fit quality is correlated to the number of hits used in the fit, the selection cut on the fit quality parameter is set to a different value according to the number of hits used to reconstruct the event: $\chi_{red}^2 \leq 1.3 + [0.04 * (N_{hit} - 5)]^2$.

Fig. 2 shows the elevation distributions both for data and simulated atmospheric neutrino and muon samples, after the cut on the track fit quality. Atmospheric muons reconstructed as upgoing are efficiently rejected and a neutrino purity better than 90% is achieved.

Fig. 3 shows the angular resolution of the online algorithm as a function of the neutrino energy for events reconstructed with different number of lines. This resolution is defined as the median of the space angular difference between the incoming neutrino and the reconstructed neutrino-induced muon. For neutrinos with an energy higher than a few tens of TeV, an angular resolution of 0.4° is achieved, despite of the approximations related to the detector geometry. For example, the inclination of the ANTARES line for a typical sea current of 5 cm/s induces a systematic angular deviation of less than 0.2° .

4.2.2. Multi-neutrino trigger

The typical signature of the transient emission of high energy neutrinos is a neutrino burst, i.e. a multiplet of neutrino events

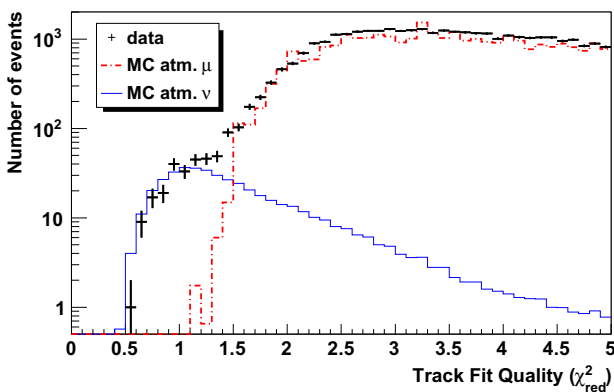


Fig. 1. Track fit quality (χ_{red}^2) distribution for all upgoing events reconstructed on at least 2 lines. The atmospheric muon Monte Carlo distribution has been rescaled to match the data.

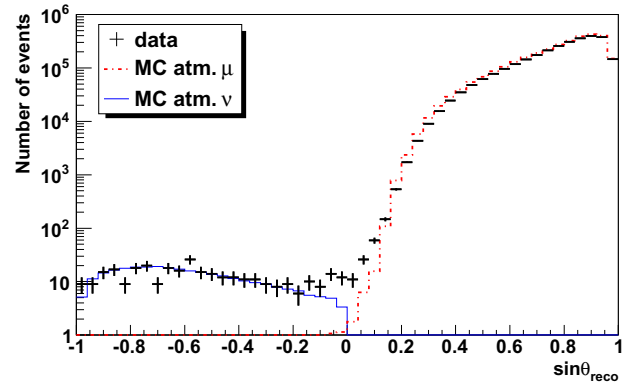


Fig. 2. Elevation angle distribution after a selection cut on the fit quality for all events reconstructed on at least 2 lines.

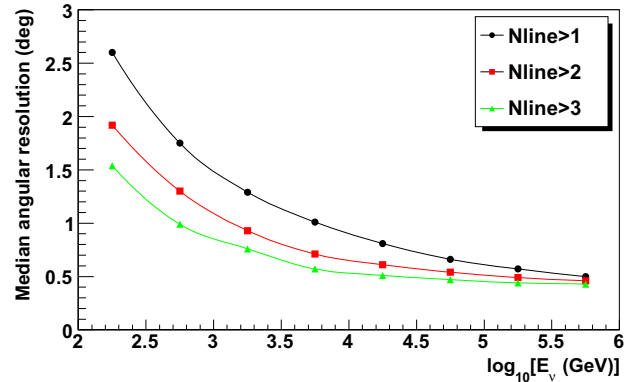


Fig. 3. Angular resolution as a function of the neutrino energy for events with tracks reconstructed with different number of lines.

originating from the source in a short time window. For the multi-neutrino trigger, the minimal cuts providing a pure neutrino sample are used to identify the single neutrinos which belong to the multiplet. This set of cuts is used as a reference for the evaluation of the efficiency for other triggers.

The time window was optimized to include most predictions of the neutrino emission by various models for transient sources. The 3° angular window was selected to match the convolution of the track reconstruction angular resolution and the field of view of the robotic optical telescopes ($\approx 2^\circ \times 2^\circ$). For the multi-neutrino trigger, the angular resolution is equal to the resolution of each single neutrino, divided by the square root of the multiplicity.

The accidental coincidence rate due to background events, from two uncorrelated upgoing atmospheric neutrinos, is estimated to be 7×10^{-3} coincidences per year with the full ANTARES detector. With such a small background, the detection of a doublet (triplet) in ANTARES would have a significance of about 3 (5) sigma.

4.2.3. High energy event trigger

Since the neutrino energy spectrum for signal events is expected to be harder than for atmospheric neutrinos, a cut on the reconstructed energy efficiently reduces the atmospheric neutrino background while most of the signal events are kept.

The selection of the alert candidates is based on two simple energy estimators: the number of storeys used in the track fit and the total amplitude (in photoelectrons) of the hits in the storeys. Figs. 4

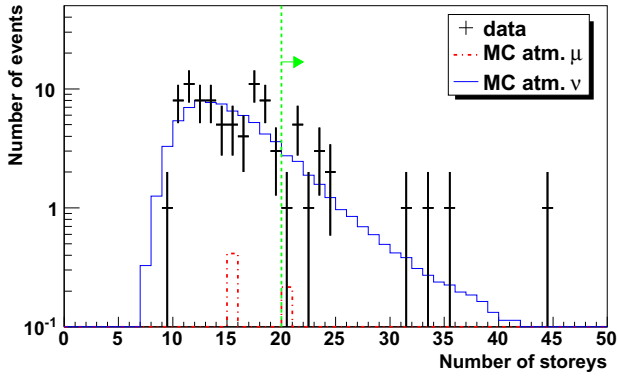


Fig. 4. Distribution of number of storeys having at least one hit used in the reconstruction, for data and Monte Carlo upgoing events reconstructed on at least three lines. The vertical line indicates the alert selection criterium.

and 5 show the distributions of the number of storeys and the amplitude, respectively, both for data and Monte Carlo samples.

The event selection for the high energy trigger has been tuned on atmospheric neutrinos in order to obtain a false alarm rate of about 25 alerts per year. This rate was agreed between ANTARES and the optical telescope collaborations. A requirement of at least 20 storeys on at least three lines and an amplitude greater than 180 photoelectrons will select around 25 high energy events per year with the full 12 line configuration of the ANTARES detector. These cuts allow to select around 86% of typical GRB neutrinos [11] and around 5% of typical core-collapse SNe neutrinos [12] while more than 98% of the atmospheric neutrino and muon background is rejected.

4.2.4. Trigger performance

The performance of these two triggers has been studied using a neutrino Monte Carlo generated with an E^{-2} energy spectrum. The TAToO alert criteria efficiently select neutrinos of energies above 1 TeV for the multi-neutrino trigger, and above 10 TeV for the single high energy trigger. Fig. 6 shows the ANTARES effective area for a neutrino passing both alert criteria.

The pointing accuracy of the neutrino telescope has two contributions: the angle between the incoming neutrino and the resulting muon, and the angle between the muon and the reconstructed trajectory. The former contribution is due to kinematics: the more energetic the neutrino, the more co-linear the resulting muon will tend to be with the neutrino direction. The latter contribution is

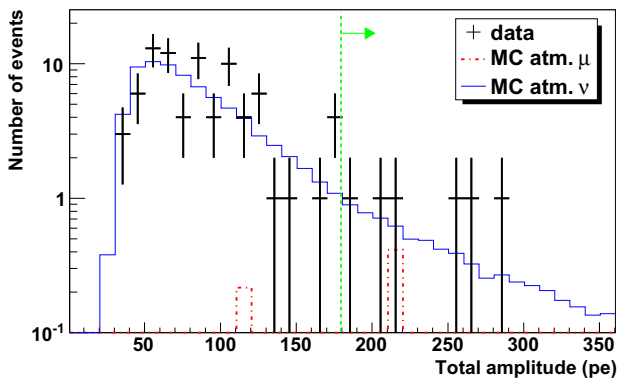


Fig. 5. Total amplitude distribution in photoelectrons (pe) for data and Monte Carlo upgoing events reconstructed on at least three lines. The vertical line indicates the alert selection criterium.

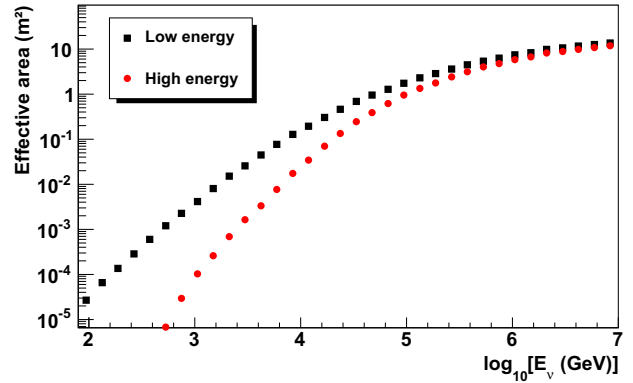


Fig. 6. Neutrino effective area as a function of the true neutrino energy for the events selected by the two alert triggers.

determined by the performance of the track reconstruction algorithm. The bidimensional point spread function expected for neutrino events selected by the single high energy trigger is shown in Fig. 7. As an illustration, $\sim 80\%$ of the events are reconstructed within the field of view (FOV) of the TAROT or ROTSE telescopes. Fig. 8 shows the dependence of this fraction on the neutrino energy.

5. Determination of the refined direction

Although the pointing accuracy of the online reconstruction algorithm is suitable for the field of view of the telescopes used for the follow-up, the use of the detailed knowledge of the detector geometry can further improve the determination of the neutrino direction. For this purpose, we use the standard ANTARES offline reconstruction algorithm [22].

Since the ANTARES lines are not rigid structures, sea currents can move the top buoy by several meters, and distort the line positions from a vertical line geometry, thus affecting the direction of the reconstructed muon trajectory.

In order to achieve the best track reconstruction performance, it is necessary to monitor the relative positions of all OMs with an

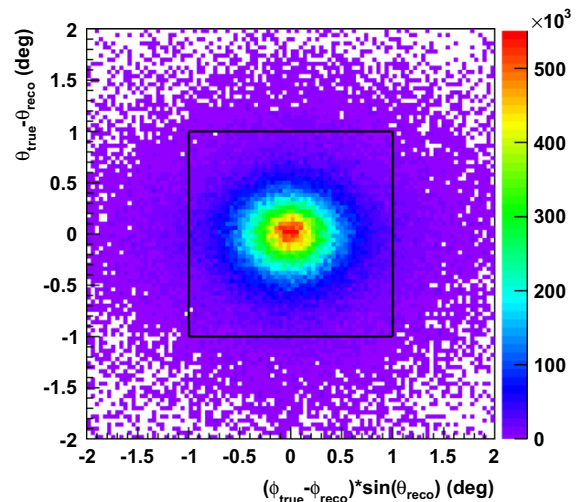


Fig. 7. Bidimensional point spread function. The black solid-line square corresponds to the TAROT field of view ($\approx 2^\circ \times 2^\circ$).

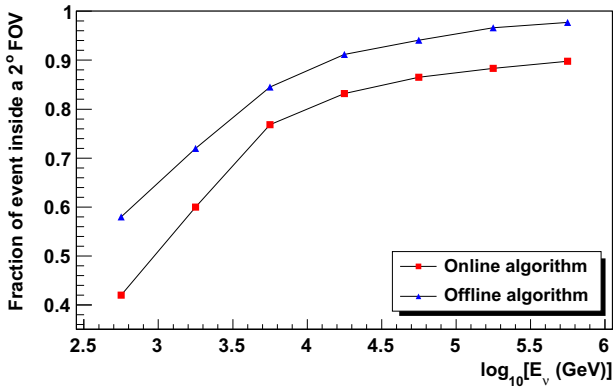


Fig. 8. Fraction of events inside a field of view of $2^\circ \times 2^\circ$ as a function of the energy of the event, assuming that the tracks originated from the center of the field of view, for both online and offline reconstruction algorithms.

accuracy of better than 20 cm, equivalent to 1 ns timing precision. In addition, a precise absolute orientation of the whole detector is necessary to point to individual neutrino sources in the sky. Two independent monitoring systems are used to attain the required accuracy:

- A high frequency long baseline acoustic system giving the 3D position of hydrophones placed along the line. These positions are obtained by triangulation from emitters anchored at the bases of the lines.
- A set of tiltmeter-compass sensors giving the local tilt angles of each OM storey with respect to the horizontal plane (pitch and roll) as well as its orientation with respect to the Earth’s magnetic field (heading).

In order to obtain a quasi-online precise detector geometry (within a delay of typically few tens of minutes), the shape of the detector lines is derived from a model which estimates the mechanical behavior under the influence of the sea water flow, obtained from online measurements of the sea current. The positions of the OMs are then calculated by combining the line shape with the measurements of the tilt and orientation angles of the storeys given by the tiltmeter-compass sensors.

5.1. The offline likelihood fit

The offline reconstruction algorithm derives the muon track parameters that maximize a likelihood function built from the difference between the expected and the measured arrival time of the hits from the Cherenkov photons emitted along the muon track. This maximization [22] takes into account the Cherenkov photons that scatter in the water and the additional photons that are generated by secondary particles (e.g. electromagnetic showers created along the muon trajectory).

The value of the log-likelihood per degree of freedom (Λ) from the track reconstruction fit is a measure of the track fit quality and is used to reject badly reconstructed events, such as atmospheric muons that are mis-reconstructed as upgoing tracks. The distribution of the variable Λ is shown in Fig. 9 for both data and Monte Carlo events. Only tracks reconstructed with $\Lambda > -5.2$ are kept for the determination of the refined track direction.

5.2. Offline reconstruction performance

Fig. 10 shows the median Monte Carlo computed angular resolution as a function of the neutrino energy for events selected by

the high energy alert trigger, for both online and offline algorithms. The improvement obtained with the offline algorithm is clearly visible at low energies. The angular resolution for neutrino energies above 10 TeV is 0.5° for the online algorithm and 0.35° for the offline algorithm. As illustrated in Fig. 7, $\sim 92\%$ of the signal events are reconstructed within a FOV of $2^\circ \times 2^\circ$.

6. Optical follow-up procedure

The optical follow-up strategy is based on short-term observations (for rapidly fading sources) and a long-term follow-up (mainly for core collapse SNe searches). Once the alert is sent at date T_0 , optical images are collected as soon as possible by the available telescopes. The fast slewing of the small robotic telescopes allow the collection of images from 5 to 10 s after the reception of the alert. The follow-up procedure, which extends over 1 month with images taken each night during the first week following the date T_0 of the alert, makes use of the refined direction. For these observations, an additional constraint is added: if the refined direction is more than 0.5° away from the initial direction and has a poor offline reconstruction quality, the follow-up of the alert is canceled. Otherwise, the pointing direction of the telescopes is updated with the refined coordinates and all subsequent images are centered around that direction.

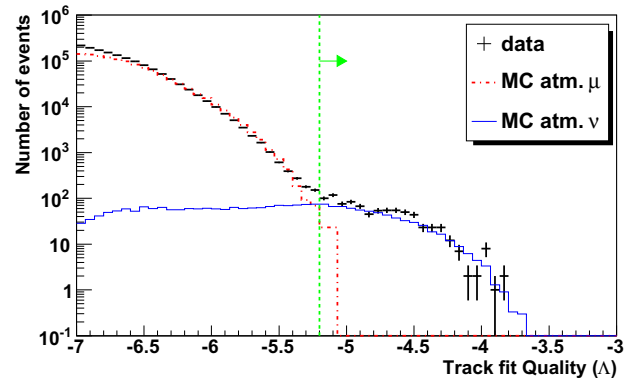


Fig. 9. Track fit quality (Λ) distribution for upgoing events in both data and atmospheric Monte Carlo samples.

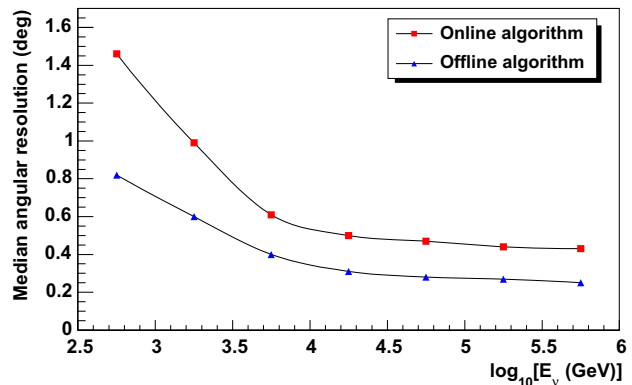


Fig. 10. Angular resolution obtained for both online and offline reconstructions as a function of the neutrino energy.

7. Summary

The method used by the ANTARES collaboration to implement the search for coincidence between high energy neutrinos and transient sources followed by small robotic telescopes has been presented. Of particular importance for this alert system are the ability to reconstruct online the neutrino direction and to reject efficiently the background. With the described ANTARES alert sending capability, the connected optical telescopes can start taking images with a latency of the order of one minute, which will be reduced to about 15 s in the near future. The precision of the direction of the alert is much better than one degree. The quasi-online availability of a refined direction obtained using the measured geometry of the ANTARES detector further improves the quality and efficiency of the alert system.

The alert system is operational since February 2009, and as of December 2010, 27 alerts have been sent, all of them triggered by the high energy selection criterium. No doublet trigger has been recorded yet. After a commissioning phase in 2009, all alerts had an optical follow-up in 2010, and the live time of the system over this year is strictly equal to the one of the ANTARES telescope, namely 87%. These numbers are consistent with the expected trigger rate, after accounting for the duty cycle of the neutrino telescope.

The optical follow-up of neutrino events significantly improves the perspective for the detection of transient sources. A confirmation by an optical telescope of a neutrino alert will not only provide information on the nature of the source but also improve the precision of the source direction determination in order to trigger other observatories (for example telescopes for spectroscopic redshift measurements). The program for the follow-up of ANTARES neutrino events is already operational with the TAROT and ROTSE telescopes and results based on analysis of the optical images will be presented in a forthcoming paper. This technique could be extended to observations in other wavelength regimes such as X-ray or radio.

Acknowledgments

The authors acknowledge the financial support of the funding agencies: Centre National de la Recherche Scientifique (CNRS), Commissariat à l'énergie atomique et aux énergies alternatives (CEA), Agence National de la Recherche (ANR), Commission Européenne (FEDER fund and Marie Curie Program), Région Alsace (contrat CPER), Région Provence-Alpes-Côte d'Azur, Département

du Var and Ville de La Seyne-sur-Mer, France; Bundesministerium für Bildung und Forschung (BMBF), Germany; Istituto Nazionale di Fisica Nucleare (INFN), Italy; Stichting voor Fundamenteel Onderzoek der Materie (FOM), Nederlandse organisatie voor Wetenschappelijk Onderzoek (NWO), the Netherlands; Council of the President of the Russian Federation for young scientists and leading scientific schools supporting grants, Russia; National Authority for Scientific Research (ANCS), Romania; Ministerio de Ciencia e Innovación (MICINN), Prometeo of Generalitat Valenciana and MultiDark, Spain. We also acknowledge the technical support of Ifremer, AIM and Foselev Marine for the sea operation and the CC-IN2P3 for the computing facilities.

This work has been financially supported by the GdR PCHE in France. We want to thank M. Kowalski for discussions on the neutrino triggers and the organization of the optical follow-up.

References

- [1] T. Piran, *Phys. Rep.* 314 (1999) 575.
- [2] M. Kowalski, A. Mohr, *Astropart. Phys.* 27 (2007) 533.
- [3] E. Aslanides et al., ANTARES Collaboration, <astro-ph/9907432>; P. Coyle et al., in: *Proc. 31st ICRC, Łódź 2009*. <arXiv:1002.0701v1>; M. Ageron et al., <arXiv:1104.1607v1[astro-ph.IM]>.
- [4] D. Dornic et al., *Nucl. Instrum. Methods A* 626–627 (2011) S183; S. Basa et al., *Nucl. Instrum. Methods A* 602 (2009) 275.
- [5] M. Boer et al., *Astron. Astrophys. Suppl. Ser.* 138 (1999) 579.
- [6] C.W. Akerlof et al., *Public. Astron. Soc. Pac.* 115 (2003) 132.
- [7] J.A. Aguilar et al., ANTARES Collaboration, *Nucl. Instrum. Methods A* 570 (2007) 107.
- [8] J.A. Aguilar et al., ANTARES Collaboration, *Astropart. Phys.* 34 (2011) 539.
- [9] J.A. Aguilar et al., ANTARES Collaboration, *Astropart. Phys.* 34 (2011) 652.
- [10] GCN network. <<http://www.gcn.gsfc.nasa.gov>>.
- [11] E. Waxman, J. Bahcall, *Phys. Rev. Lett.* 78 (1997) 2292; P. Meszaros, E. Waxman, *Phys. Rev. Lett.* 87 (2001) 171102; C. Dermer, A. Atoyan, *Phys. Rev. Lett.* 91 (2003) 071102; S. Razzaque, P. Meszaros, E. Waxman, *Phys. Rev. Lett.* 90 (2003) 241103.
- [12] S. Ando, J. Beacom, *Phys. Rev. Lett.* 95 (2005) 061103.
- [13] S. Razzaque, P. Meszaros, E. Waxman, *Phys. Rev. Lett.* 94 (2005) 109903.
- [14] J.A. Aguilar et al., ANTARES Collaboration, *Astropart. Phys.* 34 (2010) 179.
- [15] J.A. Aguilar et al., ANTARES Collaboration, *Phys. Lett.* B696 (2011) 16.
- [16] D. Heck et al., Report FZKA 6019, Forschungszentrum Karlsruhe, 1998.
- [17] J.R. Hörandel, *Astropart. Phys.* 19 (2003) 193.
- [18] N.N. Kalmykov, S.S. Ostapchenko, *Yad. Fiz.* 56 (1993) 105; N.N. Kalmykov, S.S. Ostapchenko, *Phys. At. Nucl.* 56 (3) (1993) 346.
- [19] G. Barr et al., *Phys. Rev. D* 39 (1989) 3532; V. Agrawal et al., *Phys. Rev. D* 53 (1996) 1314.
- [20] J.A. Aguilar et al., ANTARES Collaboration, *Astropart. Phys.* 23 (2005) 131.
- [21] P. Amram et al., *Nucl. Instrum. Methods A* 484 (2002) 369.
- [22] A. Heijboer, Ph.D. thesis, Universiteit van Amsterdam, Amsterdam, The Netherlands. <<http://www.antes.in2p3.fr/Publications/thesis/2004/Aart-Heijboer-phd.pdf>>.

Searches for clustering in the time integrated skymap of the ANTARES neutrino telescope

The ANTARES collaboration

E-mail: fabian.schussler@cea.fr

Received February 13, 2014

Accepted April 1, 2014

Published May 5, 2014

Abstract. This paper reports a search for spatial clustering of the arrival directions of high energy muon neutrinos detected by the ANTARES neutrino telescope. An improved two-point correlation method is used to study the autocorrelation of 3058 neutrino candidate events as well as cross-correlations with other classes of astrophysical objects: sources of high energy gamma rays, massive black holes and nearby galaxies. No significant deviations from the isotropic distribution of arrival directions expected from atmospheric backgrounds are observed.

Keywords: neutrino astronomy, neutrino detectors

ArXiv ePrint: [1402.2809](https://arxiv.org/abs/1402.2809)

JCAP05(2014)001

Contents

1	Introduction	1
1.1	The ANTARES neutrino telescope	2
1.2	Dataset	3
2	Autocorrelation analysis	4
2.1	Method	4
2.2	Reference autocorrelation distribution and comparison with data	4
2.3	Performance and sensitivity	6
2.4	Autocorrelation results and discussion	6
3	Two-point cross-correlation with external catalogues	7
3.1	High-energy gamma rays	8
3.2	The local universe	8
3.3	Massive black holes	9
4	Summary	9
	The ANTARES collaboration	12

1 Introduction

The key question to resolve the long standing mystery of the origin of cosmic rays is to locate their sources and understand the mechanisms that accelerate these particles up to energies orders of magnitude above the energies reached by man-made accelerators. Over the last years it has become obvious that multiple messengers will be needed to achieve this task. Fundamental particle physics processes like the production and subsequent decay of pions in interactions of high energy particles predict that the acceleration sites of cosmic rays should also be sources of high energy gamma rays and neutrinos. The detection of astrophysical neutrinos and the identification of their sources is one of the main goals of neutrino telescopes operated at the South Pole (IceCube [1]), in Lake Baikal [2] and in the Mediterranean Sea (ANTARES [3]).

Despite significant effort, no clear signature for point-like sources of astrophysical neutrinos has been found so far [4–9]. Currently, both the spatial distribution as well as the morphologies of sources potentially emitting neutrinos in the TeV energy range are unknown. Similar to the distribution of observed sources emitting high energy gamma rays, they are supposed to be distributed very inhomogeneously throughout our cosmic neighbourhood. A significant fraction of them should be located in the Galactic disk and be spatially extended (e.g. shell-type supernova remnants). It is therefore interesting to study the intrinsic clustering of the arrival directions of neutrino candidates.

In this analysis an improved autocorrelation method is used to this end. As no prior information about the potential sources is required biases are naturally reduced. Since it covers a large angular range, i.e. neutrino emission regions of very different sizes, this study complements the searches for point-like sources and could provide hints for underlying, yet

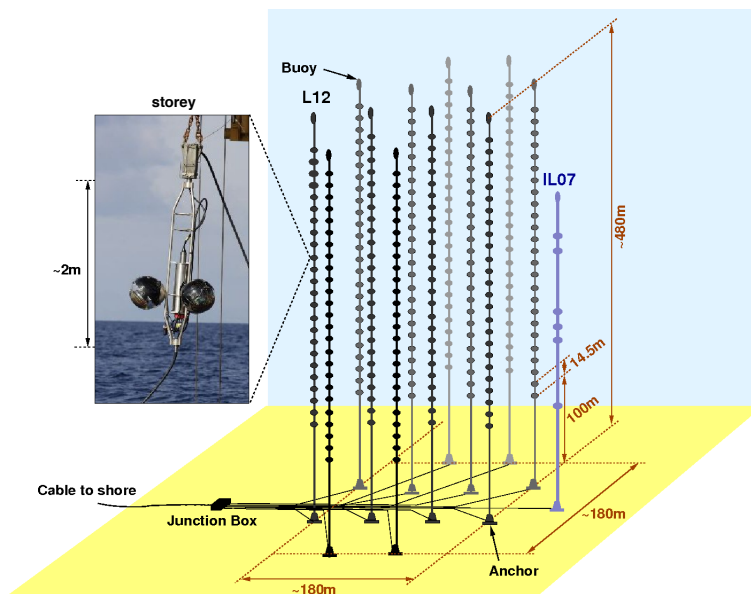


Figure 1. Schematic view of the ANTARES telescope. The inset shows a photograph of an optical storey.

unresolved, source morphologies and source distributions. Exploiting the expected multi-messenger signatures of potential sources the introduced method is extended to searches for correlations between the arrival directions of neutrino candidates and other classes of astrophysical objects: sources of high energy gamma rays, massive black holes and nearby galaxies.

1.1 The ANTARES neutrino telescope

The ANTARES telescope [3] became fully operational in 2008. The detector comprises twelve detection lines anchored at a depth of 2475 m and 40 km off the French coast near Toulon. The detector lines are about 450 m long and host a total of 885 optical modules (OMs), each comprising a 17" glass sphere which houses a 10" photomultiplier tube. The OMs look downward at 45° in order to optimise the detection of upgoing, i.e. neutrino induced, tracks. The geometry and size of the detector make it sensitive to extraterrestrial neutrinos in the TeV-PeV energy range. A schematic layout of the telescope is shown in figure 1.

The neutrino detection is based on the induced emission of Cherenkov light by high energy muons originating from charged current neutrino interactions inside or near the instrumented volume. All detected signals (*hits*) are transmitted via an optical cable to a shore station, where a computer farm filter the data for coincident signals in several adjacent OMs. The muon direction is then determined by maximising a likelihood which compares the time of the hits with the expectation from the Cherenkov signal of a muon track. Details on the event reconstruction are given in ref. [7, 10].

Two main backgrounds for the search for astrophysical neutrinos can be identified: downgoing atmospheric muons which have been mis-reconstructed as upgoing and atmospheric neutrinos originating in cosmic ray induced air showers at the opposite side of the Earth. Depending on the requirements of the analysis both backgrounds can, at least partially, be discriminated using various parameters such as the quality of the event reconstruction.

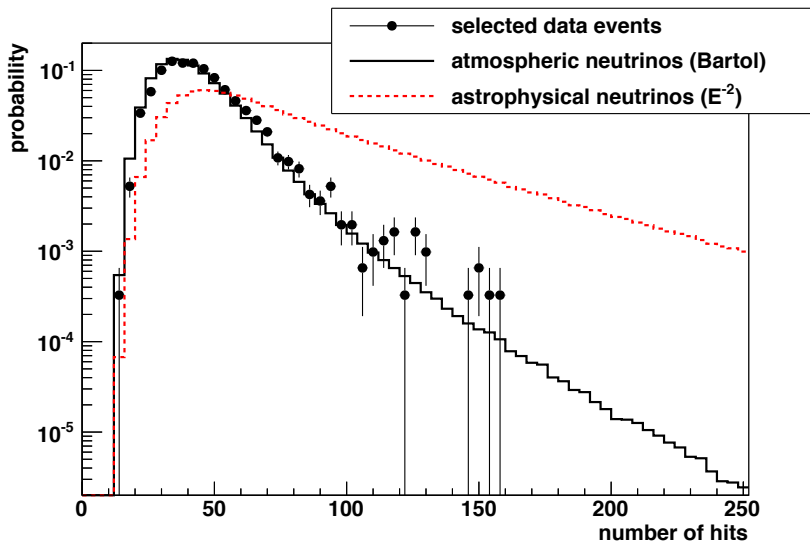


Figure 2. Normalised distribution of the number of hits used in the event reconstruction for data (black markers) and Monte Carlo simulations (atmospheric neutrinos following the parametrisation from ref. [11]: black histogram; astrophysical neutrinos: red, dotted histogram).

tion or an estimator of the energy of the muon, e.g. the number of hits used in the track reconstruction. The latter, being strongly correlated with the energy of the original neutrino, helps to discriminate events of atmospheric origin from neutrinos produced in astrophysical sources. Atmospheric neutrinos have a much softer energy spectrum ($\propto E^{-3.7}$) compared to the generic E^{-2} spectrum expected from Fermi acceleration in astrophysical sources. As illustrated in figure 2 this difference affects the distribution of energy dependent parameters (or *energy estimators*) and can therefore be used to enhance the background discrimination. In addition, analysing the reconstructed arrival directions of the events allows to search for an excess over the isotropic atmospheric backgrounds. Both features will be exploited in the analysis described in this paper.

1.2 Dataset

The data analysed here has been recorded by the ANTARES neutrino telescope between 2007 and 2010. During the beginning of this period (2007-2008) the detector was in its commissioning phase, increasing from five active detection lines to the full detector with twelve lines by mid 2008. After imposing basic data quality requirements, the event selection criteria have been optimised by means of Monte Carlo simulations to yield the best average upper limit on the neutrino flux in a search for point-like sources [7]. These criteria are mainly a cut on the reconstructed zenith angle, $\theta > 90^\circ$, a requirement on the reconstruction quality parameter, Λ , as well as a cut on the estimated angular uncertainty of the track reconstruction, $\beta < 1^\circ$. A total of 3058 neutrino candidates are found in 813 days of effective lifetime. Monte Carlo simulations show that the contribution from misreconstructed atmospheric muons is about 15% in this dataset. A skymap in galactic coordinates of these events is shown in the upper left plot of figure 7.

2 Autocorrelation analysis

2.1 Method

The most commonly used method to detect intrinsic clusters within a set of N events is the standard two-point autocorrelation distribution. It is defined as the differential distribution of the number of observed event pairs, N_p , in the dataset as a function of their mutual angular distance, $\Delta\Omega$. This technique has already been applied to the first two years of ANTARES data. No significant clustering has been detected [12]. Here, an improvement of this method by using an estimator of the neutrino energy is presented. To suppress statistical fluctuations that would reduce the sensitivity of the method, the cumulative autocorrelation distribution is used. It is defined as

$$\mathcal{N}_{\hat{E}}(\Delta\Omega) = \sum_{i=1}^N \sum_{j=i+1}^N w_{ij} \cdot [1 - H(\Delta\Omega_{ij} - \Delta\Omega)], \quad (2.1)$$

where H is the Heaviside step function. The weights $w_{ij} = w_i \cdot w_j$ are calculated using the individual event weights $w_i = \int_0^{\hat{E}_i} f(\hat{E}) d\hat{E}$, where $f(\hat{E})$ is the cumulative distribution of the energy estimator \hat{E} for the background. Astrophysical neutrinos are more likely to produce events with a higher value of the energy estimator \hat{E}_i than atmospheric neutrinos. This is represented by a higher event weight w_i . The used distribution is built from large statistics Monte Carlo simulations reproducing the actual data taking conditions, including, for example, the time dependent background fluctuations induced by bioluminescence. These simulations have been validated by extensive comparisons with data. An example is shown in figure 2, where the number of hits used in the event reconstruction is depicted (see [7, 10] for further details). The simulated events used to build the $f(\hat{E})$ distribution follow an energy spectrum as expected for atmospheric neutrinos [11] (black histogram in figure 2). Modifying the standard autocorrelation by these weights leads to a significant increase of the sensitivity to detect clustering of (astrophysical) events following a harder energy spectrum. This improvement is illustrated in figure 3. Various possibilities exist for the estimation of the energy and the definition of the weights. As crosscheck of the stability and performance of the method, the full analysis has been performed using two different energy estimators: the number of hits used during the final step of the event reconstruction, n_{Hit} , as in the search for point-like sources [7], as well as a recently developed estimator exploiting the correlation between the energy deposit, dE/dX , and the primary energy [10, 13]. Both provide very similar results. As shown in figure 3, the n_{Hit} energy estimator shows a slightly better performance for weak sources and is therefore retained for the final analysis.

Pseudo-experiments as described below are used to determine the optimal size of the angular steps $\Delta\Omega$. Increasing the number of angular steps enhances the angular resolution of the method but degrades the sensitivity due to the increasing number of trials (*look-elsewhere-effect* [14]). Taking into account the median angular resolution of 0.5° [7], an optimum has been found for angular steps of about 0.1° .

2.2 Reference autocorrelation distribution and comparison with data

To detect structures in the sky distribution of the selected events, a reference autocorrelation distribution to compare with is needed. This reference is determined by scrambling the data themselves, a method which allows the reduction of systematic uncertainties potentially introduced by the use of Monte Carlo simulations. The scrambling is performed keeping

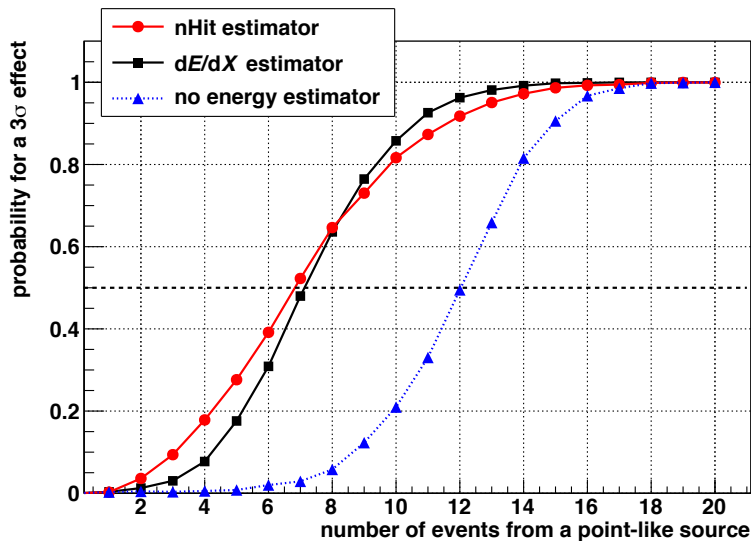


Figure 3. Probability to detect with a 3σ significance a single point-like source following an E^{-2} energy spectrum as a function of its neutrino luminosity, i.e. the number of detected neutrinos. The blue triangles denote the standard autocorrelation method without an energy estimator. The black squares show the performance including the dE/dX energy estimator [13] and the red circles denote the finally used method using the n_{Hit} estimator.

the pairs of local coordinates (zenith, azimuth) in order to avoid losing information about possible correlations between them. The detection time is drawn randomly from another event within the same detector configuration to keep track of the changing layout of the detector due to its construction and maintenance. This method is applied to all selected events and a randomised sky map naturally reproducing the coverage of the unscrambled ANTARES data is constructed.

This randomised sky is then analysed in exactly the same way as the data to derive the autocorrelation function. The randomisation process is performed about 10^6 times and the derived autocorrelation distributions are averaged in order to reduce statistical fluctuations.

Structures in the sky distribution of the data will show up as differences between the autocorrelation distribution of the data and the reference distribution. The comparison is performed by using the formalism introduced by Li and Ma [15]. This formalism provides a raw test statistic, t , as a function of the cumulative angular scale. As the comparison is performed bin-by-bin and as the scan is made over different angular scales, this result has to be corrected for the corresponding trial factor. To limit the number of trials the scan is performed only up to 25° , a scale which includes most known extended sources and emission regions.

Finally, the method proposed by Finley and Westerhoff [16] is applied by performing about 10^6 pseudo experiments in which the autocorrelation distributions of randomised sky maps are compared with the reference distribution. For each simulated map the maximum value of the test statistic is calculated. The obtained distribution is shown as black solid line in figure 4. To reach high significances the tail of the obtained distribution is fitted and extrapolated with an exponential function. The final p-value of the analysis is then calculated as the probability to obtain the same or a higher value of t from these background-only pseudo-experiments.

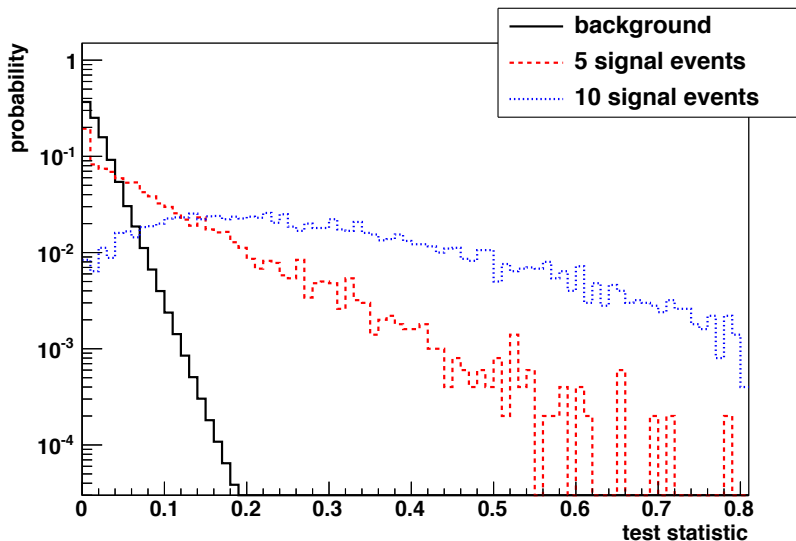


Figure 4. Normalized distribution of the maximum value of the test statistic derived from pseudo-experiments with scrambled data (black solid line). The red dashed (blue dotted) line corresponds to pseudo-datasets including a point-like source of 5 (10) events.

2.3 Performance and sensitivity

The performance of the algorithm is determined using mock datasets built by scrambling the selected data events as described above. While keeping the total number of events constant, predefined source structures with various sizes and source luminosities are added. The angular resolution of the detector is taken into account by convolving the intrinsic source size with a two dimensional Gaussian with a width of $\sigma = 0.5^\circ$. The energy estimator for the injected signal events is drawn randomly from distributions weighted to follow an E^{-2} energy spectrum (see red dotted line in figure 2). These mock datasets are then analysed in exactly the same way as described in section 2.2.

Compared to a dedicated likelihood-based search for a point-like excess in the same dataset [7], the sensitivity of the autocorrelation analysis is slightly worse for a single source. The present method indeed requires about 7 signal events to obtain a 3σ detection with a 50% probability, compared to about 6 events required in the likelihood search. On the other hand, it outperforms the algorithm optimised for the localisation of point-like sources as soon as several weak sources are present, which underlines the complementarity of the two methods. Another advantage is the sensitivity of the autocorrelation method to extended source regions. The performance of the algorithm for both cases is illustrated in figure 5.

2.4 Autocorrelation results and discussion

Following eq. (2.1), the improved cumulative autocorrelation analysis using the n_{Hit} energy estimator is applied to the 3058 selected neutrino candidate events recorded by the ANTARES neutrino telescope between 2007 and 2010. The obtained distribution is shown as the red markers in figure 6 and compared with the reference corresponding to the expectation from an isotropic distribution of the arrival directions (black histogram). The maximum deviation between the data and the reference distribution is found for an angular scale $\leq 1.1^\circ$. Cor-

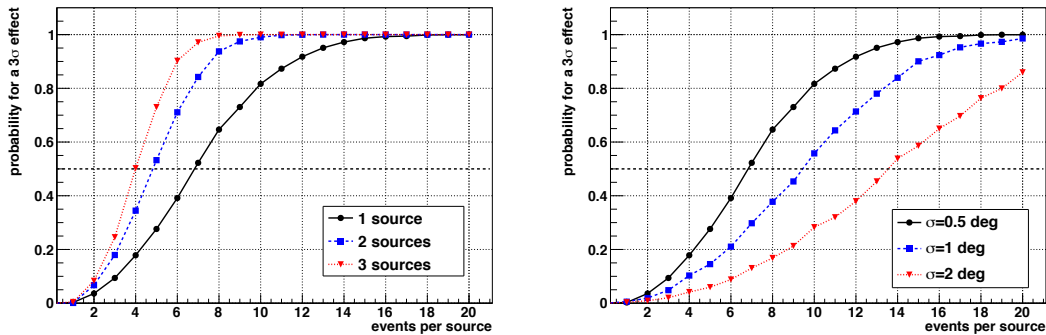


Figure 5. Probability for a 3σ effect using the autocorrelation method exploiting the n_{Hit} energy estimator. Left plot: dependence on the number of injected point-like sources in the visible sky. Right plot: dependence on the extension of a single source modelled by a 2-dimensional Gaussian.

recting for the scanning trial factor this corresponds to a p-value of 9.6% and is therefore not significant. In addition, it is known that the dataset analysed here contains a slight excess of events around (R.A., Dec) = $(-46.5^\circ, -65.0^\circ)$, where a cluster of 5 events within one degree has been found [7]. This cluster resulted in a 2.2σ effect and the region has been studied in detail in ref. [8]. Replacing these events by randomised events increases the post-trial p-value of the autocorrelation analysis to 35%. Therefore the analysed ANTARES dataset does not contain significant clusters in addition to the small point-like excess that had already been observed in the dedicated search.

3 Two-point cross-correlation with external catalogues

One way to improve the sensitivity of searches for sources of high-energy astrophysical neutrinos is to rely on the connection with other messengers. Based on phenomenological source scenarios, observations in certain wavelengths and catalogues of interesting astrophysical objects can provide valuable additional information. This approach is followed here through a first search for a global correlation between neutrinos detected by the ANTARES telescope and high energy gamma rays as well as the matter distribution in the local universe represented by the distribution of galaxies. The latter correlation with extragalactic sources, is complemented by a correlation with a catalogue of massive black holes. A dedicated correlation analysis between ultra-high energy cosmic rays detected by the Pierre Auger Observatory and neutrino candidates recorded by ANTARES has been published in ref. [17].

For this purpose, the autocorrelation function described in eq. (2.1) is extended to measure the two-point cross-correlation between the N neutrino candidates and an external dataset of n astrophysical objects:

$$\mathcal{N}_p(\Delta\Omega) = \sum_{i=1}^N \sum_{j=1}^n w_i \cdot \hat{w}_j \cdot [1 - H(\Delta\Omega_{ij} - \Delta\Omega)], \quad (3.1)$$

Here, w_i denotes the weights derived for each neutrino candidate event as described in section 2.1. The weights related to the external dataset, \hat{w}_j , are calculated in a similar way, i.e. by integrating the normalized distribution $f(\hat{x})$ of the discriminant parameter \hat{x} :

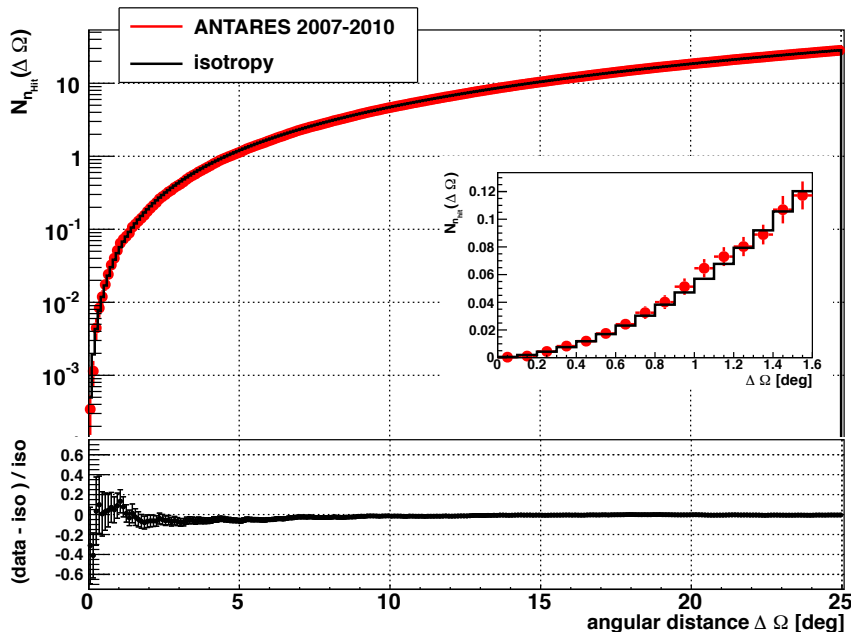


Figure 6. Cumulative autocorrelation function of data taken with the ANTARES neutrino telescope in 2007-2010. The red markers denote the ANTARES data and the black histogram represents the reference distribution expected for an isotropic dataset. The inset shows an enlarged view for small angular distances and the lower panel depicts the relative difference between data and reference distribution.

$\hat{w}_j = \int_0^{\hat{x}_j} f(\hat{x}) d\hat{x}$. The methods for the calculation of the reference distribution expected from an isotropic neutrino dataset, the comparison with the data and the correction for trial factors using pseudo experiments is performed in the same way as described in section 2 for the autocorrelation analysis.

3.1 High-energy gamma rays

Data from two years of observation of high-energy gamma rays with the Fermi-LAT satellite is used to compile the 2FGL point source catalogue [18]. It is shown in the upper right plot of figure 7. The full catalogue, containing 1873 gamma ray sources, is used for a two-point correlation analysis with the selected ANTARES neutrino candidates. It should be noted that a small subset of these sources are also included in the candidate list used in a dedicated search for point-like sources [7]. Each 2FGL source is weighted with its gamma ray flux 1 – 100 GeV as given in the Fermi catalogue and the ANTARES events are weighted based on the n_{Hit} energy estimator. The minimum post-trial p-value of 68% is found for angular scales smaller than 0.6° .

3.2 The local universe

The locations of the yet unknown cosmic ray accelerators are likely correlated with the matter distribution in the local universe. To exploit this connection, the ‘Gravitational Wave Galaxy Catalogue’ (GWGC) which provides a rather complete set of galaxies within a distance of $D < 100\text{Mpc}$, is used as description of the local extra-galactic matter distribution [19]. Their distribution is shown in the lower left plot figure 7. Assuming the simplest case of

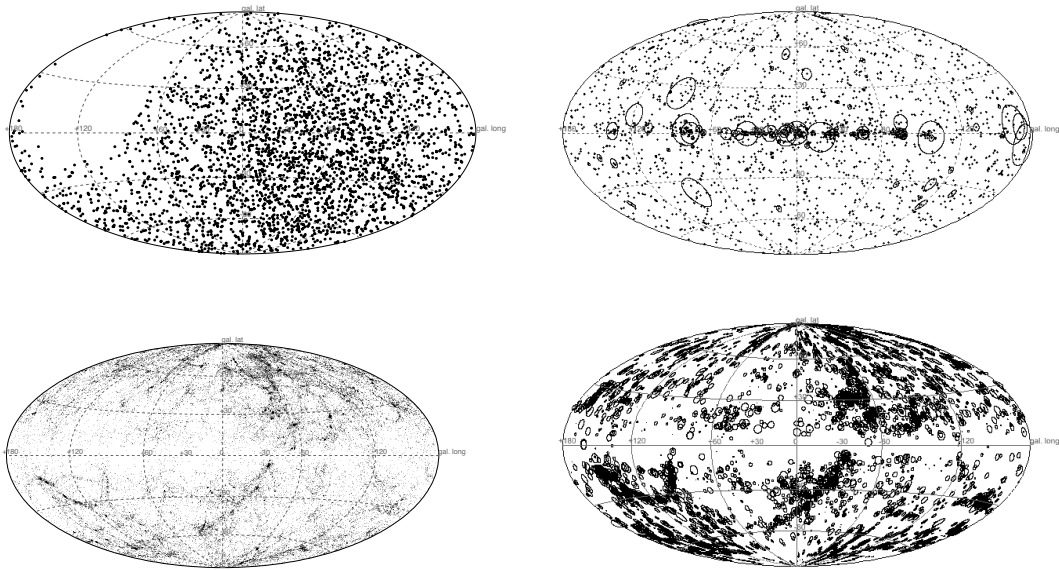


Figure 7. Upper left plot: skymap in galactic coordinates of the 3058 selected neutrino candidates used for this analysis [7]. Upper right plot: high-energy gamma ray sources given in the 2FGL catalogue from Fermi-LAT [18]. The size of the circles indicates the gamma ray flux in the 1–100 GeV energy range. Lower left plot: galaxies within 100 Mpc as given in the GWGC catalogue [19]. Lower right plot: massive black holes as given in [21]. The size of the circles indicates the mass of the objects.

equal neutrino luminosity from all given 53295 galaxies, a D^{-2} weighting for the galaxies and the n_{Hit} neutrino weights for the neutrino candidates are used. The two-point correlation analysis finds the most significant clustering at scales smaller than 0.3° with a post-trial p-value of 96%.

3.3 Massive black holes

A refinement of this largely unbiased analysis is the introduction of selection criteria that favour cosmic ray accelerator candidates among the neighbouring galaxies. For example, the sub-class of galaxies housing massive black holes at their centers has been discussed as efficient accelerators of cosmic rays up to ultra-high energies (for a summary of proposed acceleration sites, see e.g. ref. [20]). Here this scenario is exploited by searching for correlations between the neutrino candidates detected by the ANTARES telescope and massive black holes given in ref. [21] (see lower right plot of figure 7). The weighting the 5894 objects in the catalogue according to their mass reflects the energetics of the black hole systems and thus their acceleration power. Again, the neutrino events are weighted using the n_{Hit} estimator. The minimum post-trial p-value of 56% is found for angles smaller than 8.6° .

4 Summary

In the search for the sources of high-energy cosmic rays, the detection of astrophysical neutrino sources may play a crucial role. Here a search for intrinsic clustering of data recorded with the ANTARES neutrino telescope is presented. This analysis uses an improved two-point correlation technique exploiting an estimate of the energy of the neutrino candidates.

The arrival directions of the selected neutrino candidates neither show evidence for clustering of events on top of the isotropic distribution expected for the background of atmospheric neutrinos, nor correlate with catalogues of gamma rays, nearby galaxies or massive black holes.

Acknowledgments

The authors acknowledge the financial support of the funding agencies: Centre National de la Recherche Scientifique (CNRS), Commissariat à l'énergie atomique et aux énergies alternatives (CEA), Commission Européenne (FEDER fund and Marie Curie Program), Région Alsace (contrat CPER), Région Provence-Alpes-Côte d'Azur, Département du Var and Ville de La Seyne-sur-Mer, France; Bundesministerium für Bildung und Forschung (BMBF), Germany; Istituto Nazionale di Fisica Nucleare (INFN), Italy; Stichting voor Fundamenteel Onderzoek der Materie (FOM), Nederlandse organisatie voor Wetenschappelijk Onderzoek (NWO), the Netherlands; Council of the President of the Russian Federation for young scientists and leading scientific schools supporting grants, Russia; National Authority for Scientific Research (ANCS), Romania; Ministerio de Ciencia e Innovación (MICINN), Prometeo of Generalitat Valenciana and MultiDark, Spain; Agence de l'Oriental and CNRST, Morocco. We also acknowledge the technical support of Ifremer, AIM and Foselev Marine for the sea operation and the CC-IN2P3 for the computing facilities.

References

- [1] ICECUBE collaboration, A. Achterberg et al., *First Year Performance of The IceCube Neutrino Telescope*, *Astropart. Phys.* **26** (2006) 155 [[astro-ph/0604450](#)] [[INSPIRE](#)].
- [2] BAIKAL collaboration, A.V. Avrorin et al., *Search for astrophysical neutrinos in the Baikal neutrino project*, *Phys. Part. Nucl. Lett.* **8** (2011) 704 [[INSPIRE](#)].
- [3] ANTARES collaboration, M. Ageron et al., *ANTARES: the first undersea neutrino telescope*, *Nucl. Instrum. Meth. A* **656** (2011) 11 [[arXiv:1104.1607](#)] [[INSPIRE](#)].
- [4] ICECUBE collaboration, R. Abbasi et al., *Search for Point Sources of High Energy Neutrinos with Final Data from AMANDA-II*, *Phys. Rev. D* **79** (2009) 062001 [[arXiv:0809.1646](#)] [[INSPIRE](#)].
- [5] ICECUBE collaboration, M.G. Aartsen et al., *Search for Time-independent Neutrino Emission from Astrophysical Sources with 3 yr of IceCube Data*, *Astrophys. J.* **779** (2013) 132 [[arXiv:1307.6669](#)] [[INSPIRE](#)].
- [6] THE ICECUBE collaboration, M.G. Aartsen et al., *The IceCube Neutrino Observatory Part I: Point Source Searches*, Proceedings aof the 33rd ICRC (2013), [[arXiv:1309.6979](#)] [[INSPIRE](#)].
- [7] ANTARES collaboration, S. Adrian-Martinez et al., *Search for Cosmic Neutrino Point Sources with Four Year Data of the ANTARES Telescope*, *Astrophys. J.* **760** (2012) 53 [[arXiv:1207.3105](#)] [[INSPIRE](#)].
- [8] H.E.S.S. collaboration F. Schüssler et al., *Multiwavelength study of the region around the ANTARES neutrino excess*, proceedings of the 33rd ICRC, Rio de Janeiro (2013), [[arXiv:1307.6074](#)] [[INSPIRE](#)].
- [9] ANTARES collaboration, *Update on the ANTARES full-sky neutrino point source search*, Proceedings of the 33rd ICRC, Rio de Janeiro (2013), [[arXiv:1312.4308](#)] [[INSPIRE](#)].
- [10] ANTARES collaboration, S. Adrian-Martinez et al., *Measurement of the atmospheric ν_μ energy spectrum from 100 GeV to 200 TeV with the ANTARES telescope*, *Eur. Phys. J. C* **73** (2013) 2606 [[arXiv:1308.1599](#)] [[INSPIRE](#)].

- [11] G.D. Barr, T.K. Gaisser, P. Lipari, S. Robbins and T. Stanev, *A three-dimensional calculation of atmospheric neutrinos*, *Phys. Rev. D* **70** (2004) 023006 [[astro-ph/0403630](#)] [[INSPIRE](#)].
- [12] ANTARES collaboration, F. Schüssler, *Autocorrelation analysis of ANTARES data*, Proceedings of the 32nd ICRC (2011), [doi:10.7529/ICRC2011/V04/0238](#).
- [13] ANTARES collaboration, *Energy reconstruction in neutrino telescopes*, Proceedings of the 33rd ICRC, Rio de Janeiro (2013), [[arXiv:1312.4308](#)] [[INSPIRE](#)].
- [14] E. Gross and O. Vitells, *Trial factors or the look elsewhere effect in high energy physics*, *Eur. Phys. J. C* **70** (2010) 525 [[arXiv:1005.1891](#)] [[INSPIRE](#)].
- [15] T.-P. Li and Y.-Q. Ma, *Analysis methods for results in gamma-ray astronomy*, *Astrophys. J.* **272** (1983) 317 [[INSPIRE](#)].
- [16] C.B. Finley and S. Westerhoff, *On the evidence for clustering in the arrival directions of agasa's ultrahigh energy cosmic rays*, *Astropart. Phys.* **21** (2004) 359 [[astro-ph/0309159](#)] [[INSPIRE](#)].
- [17] ANTARES collaboration, S. Adrián-Martínez et al., *Search for a correlation between ANTARES neutrinos and Pierre Auger Observatory UHECRs arrival directions*, *Astrophys. J.* **774** (2013) 19 [[arXiv:1202.6661](#)] [[INSPIRE](#)].
- [18] FERMI-LAT collaboration, *Fermi Large Area Telescope Second Source Catalog*, *Astrophys. J. Suppl.* **199** (2012) 31 [[arXiv:1108.1435](#)] [[INSPIRE](#)].
- [19] D.J. White, E.J. Daw and V.S. Dhillon, *A List of Galaxies for Gravitational Wave Searches*, *Class. Quant. Grav.* **28** (2011) 085016 [[arXiv:1103.0695](#)] [[INSPIRE](#)].
- [20] T. Stanev, *High Energy Cosmic Rays*, Springer-Verlag, Berlin Germany, (2003).
- [21] L.I. Caramete and P.L. Biermann, *The mass function of nearby black hole candidates*, *Astron. Astrophys.* **521** (2010) A55 [[arXiv:0908.2764](#)] [[INSPIRE](#)].

The ANTARES collaboration

S. Adrián-Martínez^a A. Albert^b M. André^c G. Anton^e M. Ardid^a J.-J. Aubert^f B. Baret^g
 J. Barrios-Martí^h S. Basaⁱ V. Bertin^f S. Biagi^{j,k} C. Bogazzi^l R. Bormuth^{l,m} M. Bou-Cabo^g
 M.C. Bouwhuis^l R. Bruijn^l J. Brunner^f J. Busto^f A. Capone^{n,o} L. Caramete^p J. Carr^f
 S. Cecchini^j T. Chiarusi^j M. Circella^q R. Coniglione^v L. Core^f H. Costantini^f P. Coyle^f
 A. Creusot^g C. Curtin^f G. De Rosa^{s,t} I. Dekeyser^r A. Deschamps^u G. De Bonis^{n,o}
 C. Donzaud^{g,w} D. Dornic^f Q. Dorosti^x D. Drouhin^b A. Dumas^y T. Eberl^e D. Elsässer^z
 A. Enzenhöfer^e S. Escoffier^f K. Fehn^e I. Felis^a P. Fermani^{n,o} F. Folger^e L.A. Fusco^{j,k}
 S. Galatà^g P. Gay^y S. Geißelsöder^e K. Geyer^e V. Giordano^{aa} A. Gleixner^e
 J.P. Gómez-González^h K. Graf^e G. Guillard^y H. van Haren^{ab} A.J. Heijboer^l Y. Hello^u J.J.
 Hernández-Rey^h B. Herold^e A. Herrero^a J. Höbbl^e J. Hofestädt^e C. Hugon^d C.W James^e
 M. de Jong^{l,m} M. Kadler^z O. Kalekin^e U. Katz^e D. Kießling^e P. Kooijman^{l,ac,ad} A. Kouchner^g
 I. Kreykenbohm^{ae} V. Kulikovskiy^{af,d} R. Lahmann^e E. Lambard^f G. Lambard^h D. Lattuada^v
 D. Lefèvre^r E. Leonora^{aa,ag} H. Loehner^x S. Loucatos^{ah} S. Mangano^h M. Marcellinⁱ
 A. Margiotta^{j,k} J.A. Martínez-Mora^a S. Martini^r A. Mathieu^f T. Michael^l P. Migliozi^s
 C. Mueller^{ae} M. Neff^e E. Nezriⁱ D. Palioselitis^l G.E. Pāvālas^p C. Perrina^{n,o} P. Piattelli^v
 V. Popa^p T. Pradier^{ai} C. Racca^b G. Riccobene^v R. Richter^e K. Roensch^e A. Rostovtsev^{aj}
 M. Saldaña^a D.F.E. Samtleben^{l,m} A. Sánchez-Losa^h M. Sanguineti^{d,ak} J. Schmid^e J. Schnabel^e
 S. Schulte^l F. Schüssler^{l,ah} T. Seitz^e C. Sieger^e A. Spies^e M. Spurio^{j,k} J.J.M. Steijger^l
 Th. Stolarczyk^{ah} M. Taiuti^{d,ak} C. Tamburini^r Y. Tayalati^{al} A. Trovato^v B. Vallage^{ah} C. Vallée^f
 V. Van Elewyck^g E. Visser^l D. Vivolo^{s,t} S. Wagner^e J. Wilms^{ae} E. de Wolf^{l,ad} K. Yarkin^f
 H. Yepes^h J.D. Zornoza^h J. Zúñiga^h

^a Institut d'Investigació per a la Gestió Integrada de les Zones Costaneres (IGIC) - Universitat Politècnica de València. C/ Paranimf 1, 46730 Gandia, Spain.

^b GRPHE - Institut universitaire de technologie de Colmar, 34 rue du Grillenbreit BP 50568 - 68008 Colmar, France

^c Technical University of Catalonia, Laboratory of Applied Bioacoustics, Rambla Exposició, 08800 Vilanova i la Geltrú, Barcelona, Spain

^d INFN - Sezione di Genova, Via Dodecaneso 33, 16146 Genova, Italy

^e Friedrich-Alexander-Universität Erlangen-Nürnberg, Erlangen Centre for Astroparticle Physics, Erwin-Rommel-Str. 1, 91058 Erlangen, Germany

^f CPPM, Aix-Marseille Université, CNRS/IN2P3, Marseille, France

^g APC, Université Paris Diderot, CNRS/IN2P3, CEA/IRFU, Observatoire de Paris, Sorbonne Paris Cité, 75205 Paris, France

^h IFIC - Instituto de Física Corpuscular, Edificios Investigación de Paterna, CSIC - Universitat de València, Apdo. de Correos 22085, 46071 Valencia, Spain

ⁱ LAM - Laboratoire d'Astrophysique de Marseille, Pôle de l'Étoile Site de Château-Gombert, rue Frédéric Joliot-Curie 38, 13388 Marseille Cedex 13, France

^j INFN - Sezione di Bologna, Viale Berti-Pichat 6/2, 40127 Bologna, Italy

^k Dipartimento di Fisica dell'Università, Viale Berti Pichat 6/2, 40127 Bologna, Italy

^l Nikhef, Science Park, Amsterdam, The Netherlands

^m Huygens-Kamerlingh Onnes Laboratorium, Universiteit Leiden, The Netherlands

ⁿ INFN - Sezione di Roma, P.le Aldo Moro 2, 00185 Roma, Italy

^o Dipartimento di Fisica dell'Università La Sapienza, P.le Aldo Moro 2, 00185 Roma, Italy

^p Institute for Space Sciences, R-77125 Bucharest, Măgurele, Romania

^q INFN - Sezione di Bari, Via E. Orabona 4, 70126 Bari, Italy

^r Mediterranean Institute of Oceanography (MIO), Aix-Marseille University, 13288, Marseille, Cedex 9, France; Université du Sud Toulon-Var, 83957, La Garde Cedex, France CNRS-INSU/IRD UM 110

^s INFN - Sezione di Napoli, Via Cintia 80126 Napoli, Italy

^t Dipartimento di Fisica dell'Università Federico II di Napoli, Via Cintia 80126, Napoli, Italy

^u Géoazur, Université Nice Sophia-Antipolis, CNRS, IRD, Observatoire de la Côte d'Azur, Sophia Antipolis, France

¹corresponding author

- ^v INFN - Laboratori Nazionali del Sud (LNS), Via S. Sofia 62, 95123 Catania, Italy
- ^w Univ. Paris-Sud , 91405 Orsay Cedex, France
- ^x Kernfysisch Versneller Instituut (KVI), University of Groningen, Zernikelaan 25, 9747 AA Groningen, The Netherlands
- ^y Laboratoire de Physique Corpusculaire, Clermont Université, Université Blaise Pascal, CNRS/IN2P3, BP 10448, F-63000 Clermont-Ferrand, France
- ^z Institut für Theoretische Physik und Astrophysik, Universität Würzburg, Emil-Fischer Str. 31, 97074 Würzburg, Germany
- ^{aa} INFN - Sezione di Catania, Viale Andrea Doria 6, 95125 Catania, Italy
- ^{ab} Royal Netherlands Institute for Sea Research (NIOZ), Landsdiep 4, 1797 SZ 't Horntje (Texel), The Netherlands
- ^{ac} Universiteit Utrecht, Faculteit Betawetenschappen, Princetonplein 5, 3584 CC Utrecht, The Netherlands
- ^{ad} Universiteit van Amsterdam, Instituut voor Hoge-Energie Fysica, Science Park 105, 1098 XG Amsterdam, The Netherlands
- ^{ae} Dr. Remeis-Sternwarte and ECAP, Universität Erlangen-Nürnberg, Sternwartstr. 7, 96049 Bamberg, Germany
- ^{af} Moscow State University, Skobeltsyn Institute of Nuclear Physics, Leninskie gory, 119991 Moscow, Russia
- ^{ag} Dipartimento di Fisica ed Astronomia dell'Università, Viale Andrea Doria 6, 95125 Catania, Italy
- ^{ah} Direction des Sciences de la Matière - Institut de recherche sur les lois fondamentales de l'Univers - Service de Physique des Particules, CEA Saclay, 91191 Gif-sur-Yvette Cedex, France
- ^{ai} IPHC-Institut Pluridisciplinaire Hubert Curien - Université de Strasbourg et CNRS/IN2P3 23 rue du Loess, BP 28, 67037 Strasbourg Cedex 2, France
- ^{aj} ITEP - Institute for Theoretical and Experimental Physics, B. Cheremushkinskaya 25, 117218 Moscow, Russia
- ^{ak} Dipartimento di Fisica dell'Università, Via Dodecaneso 33, 16146 Genova, Italy
- ^{al} University Mohammed I, Laboratory of Physics of Matter and Radiations, B.P.717, Oujda 6000, Morocco

First limits on the very-high energy gamma-ray afterglow emission of a fast radio burst

H.E.S.S. observations of FRB 150418

H.E.S.S. Collaboration, H. Abdalla¹, A. Abramowski², F. Aharonian^{3,4,5}, F. Ait Benkhali³, A. G. Akhperjanian^{†,6,5}, T. Andersson¹⁰, E. O. Angüner²¹, M. Arakawa⁴¹, M. Arrieta¹⁵, P. Aubert²³, M. Backes⁸, A. Balzer⁹, M. Barnard¹, Y. Becherini¹⁰, J. Becker Tjus¹¹, D. Berge¹², S. Bernhard¹³, K. Bernlöhr³, R. Blackwell¹⁴, M. Böttcher¹, C. Boisson¹⁵, J. Bolmont¹⁶, P. Bordas³, J. Bregeon¹⁷, F. Brun²⁵, P. Brun¹⁸, M. Bryan⁹, M. Büchele³⁴, T. Bulik¹⁹, M. Capasso²⁷, J. Carr²⁰, S. Casanova^{21,3}, M. Cerruti¹⁶, N. Chakraborty³, R. Chalme-Calvet¹⁶, R. C. G. Chaves¹⁷, A. Chen²², J. Chevalier²³, M. Chretien¹⁶, M. Coffaro²⁷, S. Colafrancesco²², G. Cologna²⁴, B. Condon²⁵, J. Conrad²⁶, Y. Cui²⁷, I. D. Davids^{1,8}, J. Decock¹⁸, B. Degrange²⁸, C. Deil¹³, J. Devin¹⁷, P. deWilt¹⁴, L. Dirson², A. Djannati-Atai²⁹, W. Domainko³, A. Donath³, L. O'C. Drury⁴, K. Dutton³¹, J. Dyks³², T. Edwards³, K. Egberts³³, P. Eger³, J.-P. Ernenwein²⁰, S. Eschbach³⁴, C. Farnier^{26,10}, S. Fegan²⁸, M. V. Fernandes², A. Fiasson²³, G. Fontaine²⁸, A. Förster³, S. Funk³⁴, M. Fülling³⁵, S. Gabici²⁹, M. Gajdus⁷, Y. A. Gallant¹⁷, T. Garrigoux¹, G. Giavitto³⁵, B. Giebels²⁸, J. F. Glicenstein¹⁸, D. Gottschall²⁷, A. Goyal³⁶, M.-H. Grondin²⁵, J. Hahn³, M. Haupt³⁵, J. Hawkes¹⁴, G. Heinzlmann², G. Henri³⁰, G. Hermann³, O. Hervet^{15,46}, J. A. Hinton³, W. Hofmann³, C. Hoischen³³, M. Holler²⁸, D. Horns², A. Ivascenko¹, H. Iwasaki⁴¹, A. Jacholkowska¹⁶, M. Jamrozy³⁶, M. Janiak³², D. Jankowsky³⁴, F. Jankowsky²⁴, M. Jingo²², T. Jogler³⁴, L. Jouvin²⁹, I. Jung-Richardt³⁴, M. A. Kastendieck², K. Katarzyński³⁷, M. Katsuragawa⁴², U. Katz³⁴, D. Kerszberg¹⁶, D. Khangulyan⁴¹, B. Khélifi²⁹, M. Kieffer¹⁶, J. King^{3,*}, S. Klepser³⁵, D. Klochkov²⁷, W. Kluźniak³², D. Kolitzus¹³, Nu. Komin²², K. Kosack¹⁸, S. Krakau¹¹, M. Kraus³⁴, P. P. Krüger¹, H. Laffon²⁵, G. Lamanna²³, J. Lau¹⁴, J.-P. Lees²³, J. Lefaucheur¹⁵, V. Lefranc¹⁸, A. Lemière²⁹, M. Lemoine-Goumard²⁵, J.-P. Lenain¹⁶, E. Leser³³, T. Lohse⁷, M. Lorentz¹⁸, R. Liu³, R. López-Coto³, I. Lyova³⁵, V. Marandon³, A. Marcowith¹⁷, C. Mariaud²⁸, R. Marx³, G. Maurin²³, N. Maxted¹⁴, M. Mayer⁷, P. J. Meintjes³⁸, M. Meyer²⁶, A. M. W. Mitchell³, R. Moderski³², M. Mohamed²⁴, L. Mohrmann³⁴, K. Morá²⁶, E. Moulin¹⁸, T. Murach⁷, S. Nakashima⁴², M. de Naurois²⁸, F. Niederwanger¹³, J. Niemiec²⁰, L. Oakes⁷, P. O'Brien³¹, H. Odaka⁴², S. Öttl¹³, S. Ohm³⁵, M. Ostrowski³⁶, I. Oya³⁵, M. Padovani¹⁷, M. Panter³, R. D. Parsons³, N. W. Pekeur¹, G. Pelletier³⁰, C. Perennes¹⁶, P.-O. Petrucci³⁰, B. Peyaud¹⁸, Q. Piel²³, S. Pita²⁹, H. Poon³, D. Prokhorov¹⁰, H. Prokoph¹⁰, G. Pühlhofer²⁷, M. Punch^{29,10}, A. Quirrenbach²⁴, S. Raab³⁴, A. Reimer¹³, O. Reimer¹³, M. Renaud¹⁷, R. de los Reyes³, S. Richter¹, F. Rieger^{3,39}, C. Romoli⁴, G. Rowell^{14,*}, B. Rudak³², C. B. Rulten¹⁵, V. Sahakian^{6,5}, S. Saito⁴¹, D. Salek⁴⁰, D. A. Sanchez²³, A. Santangelo²⁷, M. Sasaki²⁷, R. Schlickeiser¹¹, F. Schüssler^{18,*}, A. Schulz³⁵, U. Schwanke⁷, S. Schwemmer²⁴, M. Seglar-Arroyo¹⁸, M. Settimo¹⁶, A. S. Seyffert¹, N. Shafi²², I. Shilon³⁴, R. Simoni⁹, H. Sol¹⁵, F. Spanier¹, G. Spengler²⁶, F. Spies², Ł. Stawarz³⁶, R. Steenkamp⁸, C. Stegmann^{33,35}, K. Stycz³⁵, I. Sushch¹, T. Takahashi⁴², J.-P. Tavernet¹⁶, T. Tavernier²⁹, A. M. Taylor⁴, R. Terrier²⁹, L. Tibaldo³, D. Tiziani³⁴, M. Tluczykont², C. Trichard²⁰, N. Tsujii⁴¹, R. Tuffs³, Y. Uchiyama⁴¹, D. J. van der Walt¹, C. van Eldik³⁴, C. van Rensburg¹, B. van Soelen³⁸, G. Vasileiadis¹⁷, J. Veh³⁴, C. Venter¹, A. Viana³, P. Vincent¹⁶, J. Vink⁹, F. Voisin¹⁴, H. J. Völk³, T. Vuillaume²³, Z. Wadiasingh¹, S. J. Wagner²⁴, P. Wagner⁷, R. M. Wagner²⁶, R. White³, A. Wierzchowska²¹, P. Willmann³⁴, A. Wörnlein³⁴, D. Wouters¹⁸, R. Yang³, V. Zabalza³¹, D. Zaborov²⁸, M. Zacharias²⁴, R. Zanin³, A. A. Zdziarski³², A. Zech¹⁵, F. Zefi²⁸, A. Ziegler³⁴, N. Żywucka³⁶, SUPERB Collaboration, F. Jankowski⁴³, E. F. Keane⁴⁴, and E. Petroff^{12,45}

(Affiliations can be found after the references)

Received 14 June 2016 / Accepted 15 November 2016

ABSTRACT

Aims. Following the detection of the fast radio burst FRB150418 by the SUPERB project at the Parkes radio telescope, we aim to search for very-high energy gamma-ray afterglow emission.

Methods. Follow-up observations in the very-high energy gamma-ray domain were obtained with the H.E.S.S. imaging atmospheric Cherenkov telescope system within 14.5 h of the radio burst.

Results. The obtained 1.4 h of gamma-ray observations are presented and discussed. At the 99% C.L. we obtained an integral upper limit on the gamma-ray flux of $\Phi_\gamma(E > 350 \text{ GeV}) < 1.33 \times 10^{-8} \text{ m}^{-2} \text{ s}^{-1}$. Differential flux upper limits as function of the photon energy were derived and used to constrain the intrinsic high-energy afterglow emission of FRB 150418.

Conclusions. No hints for high-energy afterglow emission of FRB 150418 were found. Taking absorption on the extragalactic background light into account and assuming a distance of $z = 0.492$ based on radio and optical counterpart studies and consistent with the FRB dispersion, we constrain the gamma-ray luminosity at 1 TeV to $L < 5.1 \times 10^{47} \text{ erg/s}$ at 99% C.L.

Key words. gamma rays: general – astroparticle physics

1. Introduction

Fast radio bursts (FRBs) are one of the major astronomical mysteries that have emerged in the last decade. First noticed in 2007 in archival data taken with the Parkes radio telescope (Lorimer et al. 2007), seventeen of these millisecond-duration bursts have been detected so far (Thornton et al. 2013; Petroff et al. 2015). The majority were found with the Parkes

telescopes, although additional bursts have been detected with the Arecibo telescope (Spitler et al. 2014) and the Green Bank Telescope (GBT; Masui et al. 2015). A summary of known FRBs including the details of the observations can be found in the on-line catalog FRBCAT¹ (Petroff et al. 2016).

The frequency-dependent dispersion properties of FRBs have constrained their distance to $z \sim 0.1-1$ (Petroff et al. 2016). Distance confusion can, however, arise due to the unknown plasma density within the supposed host galaxy of the FRB, and

[†] Deceased.

* Corresponding authors.

e-mail: contact.hess@hess-experiment.eu

¹ <http://www.astronomy.swin.edu.au/frbcats/>

that of our own Galaxy (the latter is especially relevant in cases where the FRB was observed toward the Galactic plane).

The typical radio energy output of a few $10^{39} D_{1\text{Gpc}}^2$ erg, assuming isotropic emission at distance $D_{1\text{Gpc}} = D/1$ Gpc, and the millisecond duration of FRBs have led to proposed scenarios involving compact objects – white dwarfs (WDs), neutron stars (NSs) and/or black holes (BHs). A review of potential sources can be found for example in Kulkarni et al. (2014). The merger of various combinations of WDs, NSs and/or BHs are generally favoured (e.g., Totani 2013; Zhang 2014; Kashiyama et al. 2013; Mingarelli et al. 2015) in what would be a cataclysmic event similar to short gamma-ray bursts (sGRBs). Other models involve young pulsars created in core-collapse supernovae of massive stars (Connor et al. 2016) and blitzars (BH forming rapidly from a NS via accretion, Falcke & Rezzolla 2014). The recent discovery of repeating bursts from FRB121102 (Spitler et al. 2016; Scholz et al. 2016) has renewed attention in non-cataclysmic scenarios such as flares and giant pulses from NSs and/or magnetars (Lyubarsky 2014; Katz 2016; Pen & Connor 2015; Cordes & Wasserman 2016).

A potentially significant advance in our understanding of FRBs came with the detection of a radio afterglow at the location of FRB150418 with the Australia Telescope Compact Array (ATCA, Keane et al. 2016). The burst FRB150418 was initially detected at Parkes on the 18th April 2015 by the SUPERB team. The fading radio afterglow lasted up to six days after the FRB, and could be linked to an elliptical host galaxy at $z = 0.492 \pm 0.008$ (WISE J071634.59–190039.2). If connected to the afterglow, the energetics of FRB150418 suggest a cataclysmic origin of the bursts (e.g. Zhang 2016). However, alternative explanations for the temporal behavior of the radio flux have been suggested in the form of an unrelated active galactic nucleus (AGN) activity in the host galaxy (Williams & Berger 2016), or interstellar scintillation (Akiyama & Johnson 2016). Several other possible scenarios could also explain the ATCA source, including an AGN related to the FRB (Vedantham et al. 2016), a magnetar (so the FRB repeats at the same dispersion measure as FRB150418), localized star formation, a long GRB afterglow (as seen in GRB130925A, Horesh et al. 2015), or a yet unknown mechanism. Ongoing radio monitoring may resolve the issue in the future.

FRBs release enormous amounts of energy in the radio domain (e.g., FRB150418 released $8_{-5}^{+1} \times 10^{38}$ erg at the position of the potential host galaxy with a luminosity greater than 1.3×10^{42} erg/s) and their potential origins are thought to be similar to other transients seen in the X-ray and multi-GeV gamma-ray bands such as short and/or long GRBs (Zhang 2014). Several FRB models have also specifically suggested the existence of flares in the TeV band (e.g., Lyubarsky 2014; Murase et al. 2016) and proposed follow-ups of FRBs at very high energies.

In this paper, we report the first follow-up observations of FRBs in very high energy (VHE) gamma-rays of TeV (10^{12} eV) energies. We present observations searching for the very high-energy afterglow of FRB150418 with the High Energy Stereoscopic System (H.E.S.S.) following an alert from the SUPERB collaboration.

2. Observations from H.E.S.S. and data analysis

Dedicated follow-up observations of FRB150418 were obtained in the very-high energy gamma-ray domain with the H.E.S.S. imaging atmospheric Cherenkov telescope array. H.E.S.S. is located on the Khomas Highland plateau of Namibia ($23^{\circ}16'18''$ South, $16^{\circ}30'00''$ East), at an elevation of 1800 m above sea

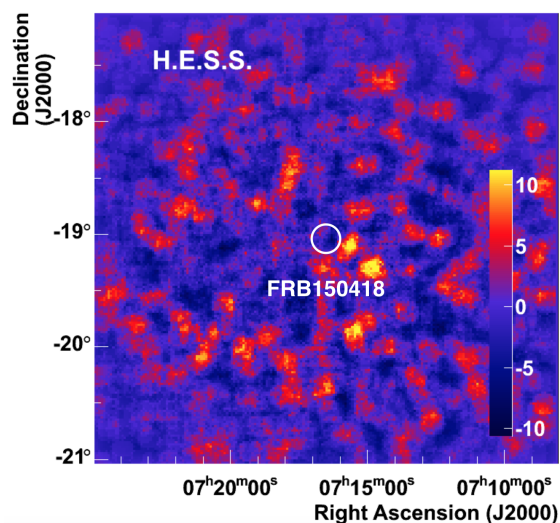


Fig. 1. VHE gamma-ray emission around the direction of FRB150418 illustrated by the event counts exceeding the background. The circle in the center has a diameter of 0.24° and denotes the width of the Parkes beam in which the burst has been observed.

level. With its original four-telescope array, H.E.S.S. is sensitive to cosmic and gamma-rays in the 100 GeV to 100 TeV energy range and is capable of detecting a Crab-like source close to zenith and under good observational conditions at the 5σ level within less than one minute (Aharonian et al. 2006). In 2012 a fifth telescope with 28 m diameter was commissioned, extending the covered energy range toward lower energies. This fifth telescope was unavailable at the time of the observation and data for the follow-up presented here have therefore been obtained with the four 12 m H.E.S.S. telescopes.

The notification of FRB150418 was received from the SUPERB team on 2015-04-18 during daytime at the site of the H.E.S.S. experiment, thus prohibiting prompt follow-up observations. The necessary observation conditions were reached the evening of the same day at 17:55 UTC (about 14.5 h after the FRB) and 1.4 h of data could be recorded until the source set below an elevation of 45° , which is the typical horizon for observations retaining a relatively low energy threshold. The data, taken in standard wobble mode operations with source offsets of 0.7° , fulfill all standard data quality criteria including requirements on atmospheric conditions, and detector stability. The zenith angle of the observations ranged from 21° to 42° . After correcting for acceptance effects due to the wobble source offsets, a total effective live-time of 1.1 h at the FRB position was available for analysis.

The data were analyzed using Model Analysis (de Naurois & Rolland 2009), an advanced Cherenkov image reconstruction method in which the recorded shower images of all triggered telescopes are compared to a semi-analytical model of gamma ray showers by means of a log-likelihood optimization. The “standard cuts” of Model Analysis were adopted. These cuts require, among other criteria, the total charge in the shower image to be greater than 60 photoelectrons. The resulting energy threshold, defined as the energy where the acceptance is 20% of its maximum value, is 350 GeV for this dataset.

The robustness and stability of the described analysis have been verified with an independent analysis relying on an independent data calibration chain and using the Image Pixel-wise fit for Atmospheric Cherenkov Telescopes (ImPACT, Parsons & Hinton 2014) reconstruction method. The results

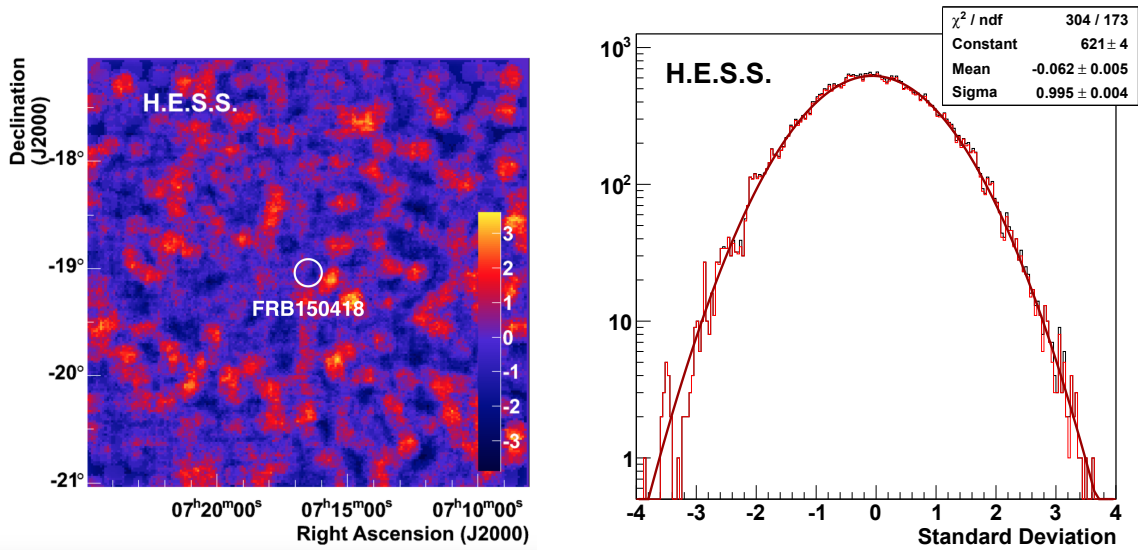


Fig. 2. *Left plot:* map of significances of the gamma ray emission using the formalism proposed by Li & Ma (1983) in the region around FRB150418. The circle in the center has a diameter of 0.24° and denotes the width of the Parkes beam in which the burst was observed. *Right plot:* distribution of significances (black histogram) compared to the distribution obtained by excluding a circular region of 0.25° radius (red histogram). The red line and the shown parameters correspond to a Gaussian function fit to the latter distribution.

from this cross-check analysis are consistent with the ones presented here.

The H.E.S.S. field-of-view (FoV) with a diameter of 5° easily covers the Parkes beam with a FWHM of 0.24° (Keane et al. 2016). The H.E.S.S. observations therefore cover all potential locations of FRB150418 within the Parkes beam in which the FRB was detected. On the other hand, the H.E.S.S. point-spread function has a diameter of $\sim 0.12^\circ$ (68% containment), that is, half the Parkes beam size. We can therefore, based solely on H.E.S.S. data, not expect to easily resolve the origin of a potential afterglow within the Parkes beam and would not be able to discriminate between the potential host galaxy discussed by Keane et al. (2016) and other locations within the beam.

No high-energy gamma ray source has been detected within the region of interest in the four-year long observations by the LAT instrument onboard the Fermi satellite (Acerro et al. 2015). Also no emission at very-high gamma-ray energies has been reported so far from the region².

The background level in the FoV was determined from the dataset itself using the standard “ring background” technique (Berge et al. 2007), a robust method ideally suited to deriving gamma-ray emission maps in FoVs with low numbers of sources. In order to derive the acceptance function required as input to the ring background method we exploited the azimuthal symmetry of the acceptance across the field-of-view of the telescopes. We derive the acceptance from the same dataset and, in order to reduce systematic uncertainties due to the limited statistics, we refrained from a detailed modeling of the zenith angle dependence of the acceptance function and use the acceptance derived at the average zenith angle of 32° .

3. Results

The map of gamma-ray events exceeding the background is shown for the full region of interest (ROI) around FRB150418 in Fig. 1. We then converted the excess counts into significance levels using the formalism described by Li & Ma (1983). The resulting map of significances is shown in the left plot of Fig. 2.

It should be noted that trial factors due to the large number of individual bins are not accounted for in this representation. For an ROI dominated by statistical fluctuations of the background the distribution of the significances should follow a Gaussian with a mean at zero and a width of one. The right plot in Fig. 2 shows the corresponding distribution (black histogram). The distribution obtained by excluding a circular “signal” region of 0.25° radius around the FRB position is shown in red. Both histograms agree very well. In addition, when fitting the latter distribution with a Gaussian shape, very good agreement with the “background only” hypothesis was found. It can be noted that the errors on the obtained parameters are underestimated due to correlations in the entries of the significance distributions which are introduced by the background estimation on overlapping regions. We conclude that the ROI is well described and clearly dominated by background events.

As the obtained results were fully compatible with the background expectation we conclude that no significant gamma-ray afterglow was detected from the direction of FRB150418 (cf. Fig. 2). Consequently we derive 99% C.L. upper limits on the gamma-ray flux as function of energy following the approach by Feldman & Cousins (1998). Assuming a generic E^{-2} energy spectrum for the potential emission and integrating above the threshold of 350 GeV we obtain $\Phi_\gamma(E > 350 \text{ GeV}) < 1.33 \times 10^{-8} \text{ m}^{-2} \text{ s}^{-1}$. Assuming a E^{-4} energy spectrum, we obtain $\Phi_\gamma(E > 350 \text{ GeV}) < 2.12 \times 10^{-8} \text{ m}^{-2} \text{ s}^{-1}$. Differential upper limits as function of the energy are shown as black arrows in Fig. 3. Due to the small size of the bins, the influence of the assumed spectrum (e.g. E^{-2} vs. E^{-4}) on the differential upper limits is less than 1.3%.

While propagating through the extragalactic radiation fields, high-energy gamma rays interact with the extragalactic background light (EBL) via e^+e^- pair-creation processes. This leads to the collective effect of an absorption of gamma-rays at the highest energies. The resulting gamma-ray opacity depends on the energy as well as on the distance of the source. Using the EBL model published in Gilmore et al. (2012) we were able to correct the derived upper limits on the gamma-ray flux measured on Earth for EBL absorption effects and thus derive

² <http://tevcat.uchicago.edu>

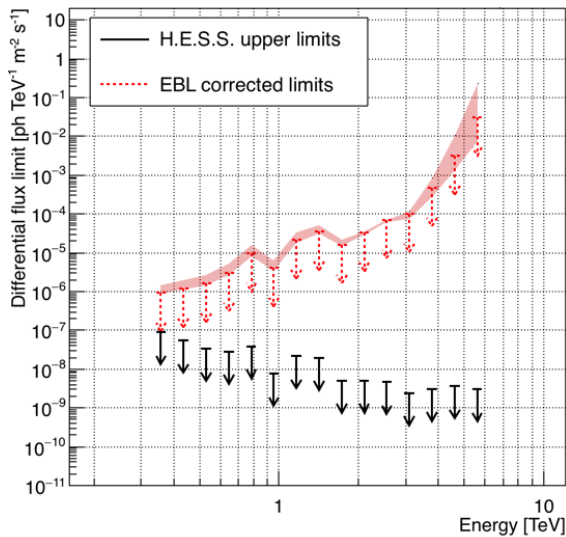


Fig. 3. Limits (99% CL) on the very high energy gamma-ray flux derived from the H.E.S.S. follow-up on FRB150418 assuming an E^{-2} energy spectrum. The EBL de-absorption is based on the model from Gilmore et al. (2012) and assumes the FRB distance of $z = 0.492$ (Keane et al. 2016). The uncertainty induced by different EBL models is shown as red band.

energy dependent intrinsic flux limits of the FRB. The result shown in Fig. 3 has been derived using the redshift of the potential host galaxy of FRB150418, $z = 0.492$ (Keane et al. 2016). While this distance is consistent with the one derived from the dispersion measure of the FRB, there is still controversy as to the relationship between FRB150418 and WISEJ071634.59–190039.2. The intrinsic limits shown should therefore not be taken as definitive, but rather as an illustration of how the EBL absorption impacts the constraints as a function of energy. The red band in Fig. 3 illustrates the effect of different EBL models (e.g. Gilmore et al. 2012; Franceschini et al. 2008; Dominguez et al. 2011) on the EBL correction of the derived flux limits.

4. Discussion and conclusion

We have reported the first follow-up observations of fast radio bursts in the very high-energy gamma-ray domain. The origin of FRBs remains elusive, and observational constraints such as those presented here are crucial pieces for solving this puzzle. In addition to an enlarged wavelength coverage, timely observations are essential in order to be able to cover as many of the potentially very rapid emission scenarios as possible.

The luminosity in the radio domain of FRB150408 has been estimated to $L > 1.3 \times 10^{42}$ erg/s (Keane et al. 2016). The first non-radio observations of the emission region of FRB150418 were carried out 8 h after the radio burst by the Swift X-ray satellite and a 3σ upper limit on the X-ray flux of $\Phi_X < 7.1 \times 10^{-14}$ erg cm $^{-2}$ s $^{-1}$ has been derived (Keane et al. 2016). Our VHE gamma-ray observations constrain emission at slightly longer timescales (starting 14.5 h after the burst, due to the inability of Imaging Atmospheric Cherenkov Telescopes to observe during daytime) and provide valuable input to models specifically suggesting flares in the TeV band (Lyubarsky 2014; Murase et al. 2016). Taking absorption on the extragalactic background light into account, as shown in Fig. 3, and assuming a distance of $z = 0.492$ based on radio and optical counterpart

studies and consistent with the FRB dispersion, we constrain the gamma-ray luminosity of the afterglow of FRB150418 at 1 TeV to $L < 5.1 \times 10^{47}$ erg/s at 99% C.L.

Acknowledgements. The support of the Namibian authorities and of the University of Namibia in facilitating the construction and operation of H.E.S.S. is gratefully acknowledged, as is the support by the German Ministry for Education and Research (BMBF), the Max Planck Society, the German Research Foundation (DFG), the French Ministry for Research, the CNRS-IN2P3 and the Astroparticle Interdisciplinary Programme of the CNRS, the UK Science and Technology Facilities Council (STFC), the IPNP of the Charles University, the Czech Science Foundation, the Polish Ministry of Science and Higher Education, the South African Department of Science and Technology and National Research Foundation, the University of Namibia, the Innsbruck University, the Austrian Science Fund (FWF), and the Austrian Federal Ministry for Science, Research and Economy, and by the University of Adelaide and the Australian Research Council. We appreciate the excellent work of the technical support staff in Berlin, Durham, Hamburg, Heidelberg, Palaiseau, Paris, Saclay, and in Namibia in the construction and operation of the equipment. This work benefited from services provided by the H.E.S.S. Virtual Organisation, supported by the national resource providers of the EGI Federation.

References

- Acero, F., Ackermann, M., Ajello, M., et al. 2015, *ApJ*, **218**, 23
 Aharonian, F., Akhperjanian, A. G., Bazer-Bachi, A. R., et al. 2006, *A&A*, **457**, 899
 Akiyama, K., & Johnson, M. D. 2016, *ApJ*, **824**, L3
 Berge, D., Funk, S., & Hinton, J. 2007, *A&A*, **466**, 1219
 Connor, L., Sievers, J., & Pen, U.-L. 2016, *MNRAS*, **458**, L19
 Cordes, J. M., & Wasserman, I. 2016, *MNRAS*, **457**, 232
 de Naurois, M., & Rolland, L. 2009, *Astropart. Phys.*, **32**, 231
 Dominguez, A., Primack, J. R., Rosario, D. J., et al. 2011, *MNRAS*, **410**, 2556
 Falcke, H., & Rezzolla, L. 2014, *A&A*, **562**, A137
 Feldman, G. J., & Cousins, R. D. 1998, *Phys. Rev. D*, **57**, 3873
 Franceschini, A., Rodighiero, G., & Vaccari, M. 2008, *A&A*, **487**, 837
 Gilmore, R. C., Somerville, R. S., Primack, J. R., & Dominguez, A. 2012, *MNRAS*, **422**, 3189
 Horesh, A.,enko, S. B., Perley, D. A., et al. 2015, *ApJ*, **812**, 86
 Kashiyama, K., Ioka, K., & Mészáros, P. 2013, *ApJ*, **776**, L39
 Katz, J. I. 2016, *ApJ*, **826**, 226
 Keane, E. F., Johnston, S., Bhandari, S., et al. 2016, *Nature*, **530**, 453
 Kulkarni, S. R., Ofek, E. O., Neill, J. D., Zheng, Z., & Juric, M. 2014, *ApJ*, **797**, 70
 Li, T.-P., & Ma, Y.-Q. 1983, *ApJ*, **272**, 317
 Lorimer, D. R., Bailes, M., McLaughlin, M. A., Narkevic, D. J., & Crawford, F. 2007, *Science*, **318**, 777
 Lyubarsky, Y. 2014, *MNRAS*, **442**, L9
 Masui, K., Lin, H.-H., Sievers, J., et al. 2015, *Nature*, **528**, 523
 Mingarelli, C. M. F., Levin, J., & Lazio, T. J. W. 2015, *ApJ*, **814**, L20
 Murase, K., Kashiyama, K., & Meszaros, P. 2016, *MNRAS*, **461**, 1498
 Parsons, R. D., & Hinton, J. A. 2014, *Astropart. Phys.*, **56**, 26
 Pen, U.-L., & Connor, L. 2015, *ApJ*, **807**, 179
 Petroff, E., Bailes, M., Barr, E. D., et al. 2015, *MNRAS*, **447**, 246
 Petroff, E., Barr, E. D., Jameson, A., et al. 2016, *PASA*, **33**, e045
 Scholz, P., Spitler, L. G., Hessels, J. W. T., et al. 2016, *ApJ*, **833**, 177
 Spitler, L. G., Cordes, J. M., Hessels, J. W. T., et al. 2014, *ApJ*, **790**, 101
 Spitler, L. G., Scholz, P., Hessels, J. W. T., et al. 2016, *Nature*, **531**, 202
 Thornton, D., Stappers, B., Bailes, M., et al. 2013, *Science*, **341**, 53
 Totani, T. 2013, *Publ. Astron. Soc. Japan*, **65**, 12
 Vedantham, H. K., Ravi, V., Mooley, K., et al. 2016, *ApJ*, **824**, L9
 Williams, P. K. G., & Berger, E. 2016, *ApJ*, **821**, L22
 Zhang, B. 2014, *ApJ*, **780**, L21
 Zhang, B. 2016, *ApJ*, **822**, L14

- 1 Centre for Space Research, North-West University, Potchefstroom 2520, South Africa
- 2 Universität Hamburg, Institut für Experimentalphysik, Luruper Chaussee 149, 22761 Hamburg, Germany
- 3 Max-Planck-Institut für Kernphysik, PO Box 103980, 69029 Heidelberg, Germany
- 4 Dublin Institute for Advanced Studies, 31 Fitzwilliam Place, Dublin 2, Ireland

- ⁵ National Academy of Sciences of the Republic of Armenia, Marshall Baghramian Avenue, 24, 0019 Yerevan, Republic of Armenia
- ⁶ Yerevan Physics Institute, 2 Alikhanian Brothers St., 375036 Yerevan, Armenia
- ⁷ Institut für Physik, Humboldt-Universität zu Berlin, Newtonstr. 15, 12489 Berlin, Germany
- ⁸ University of Namibia, Department of Physics, Private Bag 13301, Windhoek, Namibia
- ⁹ GRAPPA, Anton Pannekoek Institute for Astronomy, University of Amsterdam, Science Park 904, 1098 XH Amsterdam, The Netherlands
- ¹⁰ Department of Physics and Electrical Engineering, Linnaeus University, 351 95 Växjö, Sweden
- ¹¹ Institut für Theoretische Physik, Lehrstuhl IV: Weltraum und Astrophysik, Ruhr-Universität Bochum, 44780 Bochum, Germany
- ¹² GRAPPA, Anton Pannekoek Institute for Astronomy and Institute of High-Energy Physics, University of Amsterdam, Science Park 904, 1098 XH Amsterdam, The Netherlands
- ¹³ Institut für Astro- und Teilchenphysik, Leopold-Franzens-Universität Innsbruck, 6020 Innsbruck, Austria
- ¹⁴ School of Physical Sciences, University of Adelaide, Adelaide 5005, Australia
- ¹⁵ LUTH, Observatoire de Paris, PSL Research University, CNRS, Université Paris Diderot, 5 place Jules Janssen, 92190 Meudon, France
- ¹⁶ Sorbonne Universités, UPMC Université Paris 06, Université Paris Diderot, Sorbonne Paris Cité, CNRS, Laboratoire de Physique Nucléaire et de Hautes Énergies (LPNHE), 4 place Jussieu, 75252 Paris Cedex 5, France
- ¹⁷ Laboratoire Univers et Particules de Montpellier, Université Montpellier, CNRS/IN2P3, CC 72, Place Eugène Bataillon, 34095 Montpellier Cedex 5, France
- ¹⁸ DSM/Irfu, CEA Saclay, 91191 Gif-Sur-Yvette Cedex, France
- ¹⁹ Astronomical Observatory, The University of Warsaw, Al. Ujazdowskie 4, 00-478 Warsaw, Poland
- ²⁰ Aix-Marseille Université, CNRS/IN2P3, CPPM UMR 7346, 13288 Marseille, France
- ²¹ Instytut Fizyki Jądrowej PAN, ul. Radzikowskiego 152, 31-342 Kraków, Poland
- ²² School of Physics, University of the Witwatersrand, 1 Jan Smuts Avenue, Braamfontein, Johannesburg 2050, South Africa
- ²³ Laboratoire d'Annecy-le-Vieux de Physique des Particules, Université Savoie Mont-Blanc, CNRS/IN2P3, 74941 Annecy-le-Vieux, France
- ²⁴ Landessternwarte, Universität Heidelberg, Königstuhl, 69117 Heidelberg, Germany
- ²⁵ Université Bordeaux, CNRS/IN2P3, Centre d'Études Nucléaires de Bordeaux Gradignan, 33175 Gradignan, France
- ²⁶ Oskar Klein Centre, Department of Physics, Stockholm University, Albanova University Center, 10691 Stockholm, Sweden
- ²⁷ Institut für Astronomie und Astrophysik, Universität Tübingen, Sand 1, 72076 Tübingen, Germany
- ²⁸ Laboratoire Leprince-Ringuet, École Polytechnique, CNRS/IN2P3, 91128 Palaiseau, France
- ²⁹ APC, AstroParticule et Cosmologie, Université Paris Diderot, CNRS/IN2P3, CEA/Irfu, Observatoire de Paris, Sorbonne Paris Cité, 10 rue Alice Domon et Léonie Duquet, 75205 Paris Cedex 13, France
- ³⁰ Univ. Grenoble Alpes; CNRS, IPAG, 38000 Grenoble, France
- ³¹ Department of Physics and Astronomy, The University of Leicester, University Road, Leicester, LE1 7RH, UK
- ³² Nicolaus Copernicus Astronomical Center, Polish Academy of Sciences, ul. Bartycka 18, 00-716 Warsaw, Poland
- ³³ Institut für Physik und Astronomie, Universität Potsdam, Karl-Liebknecht-Strasse 24/25, 14476 Potsdam, Germany
- ³⁴ Friedrich-Alexander-Universität Erlangen-Nürnberg, Erlangen Centre for Astroparticle Physics, Erwin-Rommel-Str. 1, 91058 Erlangen, Germany
- ³⁵ DESY, 15738 Zeuthen, Germany
- ³⁶ Obserwatorium Astronomiczne, Uniwersytet Jagielloński, ul. Orła 171, 30-244 Kraków, Poland
- ³⁷ Centre for Astronomy, Faculty of Physics, Astronomy and Informatics, Nicolaus Copernicus University, Grudziadzka 5, 87-100 Torun, Poland
- ³⁸ Department of Physics, University of the Free State, PO Box 339, Bloemfontein 9300, South Africa
- ³⁹ Heisenberg Fellow (DFG), ITA Universität Heidelberg, Germany
- ⁴⁰ GRAPPA, Institute of High-Energy Physics, University of Amsterdam, Science Park 904, 1098 XH Amsterdam, The Netherlands
- ⁴¹ Department of Physics, Rikkyo University, 3-34-1 Nishi-Ikebukuro, Toshima-ku, Tokyo 171-8501, Japan
- ⁴² Japan Aerospace Exploration Agency (JAXA), Institute of Space and Astronautical Science (ISAS), 3-1-1 Yoshinodai, Chuo-ku, Sagami-hara, Kanagawa 229-8510, Japan
- ⁴³ Centre for Astrophysics and Supercomputing, Swinburne University of Technology, Mail H30, PO Box 218, VIC 3122, Australia; ARC Centre of Excellence for All-sky Astrophysics (CAASTRO), USA
- ⁴⁴ SKA Organisation, Jodrell Bank Observatory, Cheshire, SK11 9DL, UK; ARC Centre of Excellence for All-sky Astrophysics (CAASTRO), USA
- ⁴⁵ ASTRON, The Netherlands Institute for Radio Astronomy, Postbus 2, 7990 AA Dwingeloo, The Netherlands
- ⁴⁶ Now at Santa Cruz Institute for Particle Physics and Department of Physics, University of California at Santa Cruz, Santa Cruz, CA 95064, USA

A search for very high-energy flares from the microquasars GRS 1915+105, Circinus X-1, and V4641 Sgr using contemporaneous H.E.S.S. and RXTE observations

H.E.S.S. Collaboration: H. Abdalla¹, A. Abramowski², F. Aharonian^{3,4,5}, F. Ait Benkhali³, A. G. Akhperjanian^{6,5}, E. O. Angüner⁷, M. Arrieta¹⁵, P. Aubert²⁴, M. Backes⁸, A. Balzer⁹, M. Barnard¹, Y. Becherini¹⁰, J. Becker Tjus¹¹, D. Berge¹², S. Bernhard¹³, K. Bernlöhr³, E. Birsin⁷, R. Blackwell¹⁴, M. Böttcher¹, C. Boisson¹⁵, J. Bolmont¹⁶, P. Bordas^{*,3}, J. Bregeon¹⁷, F. Brun¹⁸, P. Brun¹⁸, M. Bryan⁹, T. Bulik¹⁹, M. Capasso²⁹, J. Carr²⁰, S. Casanova^{21,3}, P. M. Chadwick^{*,43}, N. Chakraborty³, R. Chalme-Calvet¹⁶, R. C.G. Chaves^{17,22}, A. Chen²³, J. Chevalier²⁴, M. Chrétiens¹⁶, S. Colafrancesco²³, G. Colonna²⁵, B. Condon²⁶, J. Conrad^{27,28}, C. Couturier¹⁶, Y. Cui²⁹, I. D. Davids^{1,8}, B. Degrange³⁰, C. Deil³, P. deWilt¹⁴, H. J. Dickinson^{*,44}, A. Djannati-Atai³¹, W. Domajko³, A. Donath³, L.O'C. Drury⁴, G. Dubus³², K. Dutton³³, J. Dyks³⁴, M. Dyrda²¹, T. Edwards³, K. Egberts³⁵, P. Eger³, J.-P. Ernenwein^{*,20}, S. Eschbach³⁶, C. Farnier^{27,10}, S. Fegan³⁰, M. V. Fernandes², A. Fiasson²⁴, G. Fontaine³⁰, A. Förster³, S. Funk³⁶, M. Füßling³⁷, S. Gabici³¹, M. Gajdus⁷, Y. A. Gallant¹⁷, T. Garrigoux¹, G. Giavitto³⁷, B. Giebels³⁰, J. F. Glicenstein¹⁸, D. Gottschall²⁹, A. Goyal³⁸, M.-H. Grondin²⁶, M. Grudzińska¹⁹, D. Hadasch¹³, J. Hahn³, J. Hawkes¹⁴, G. Heinzlmann², G. Henri³², G. Hermann³, O. Hervet¹⁵, A. Hillert³, J. A. Hinton³, W. Hofmann³, C. Hoischen³⁵, M. Holler³⁰, D. Horns², A. Ivascenko¹, A. Jacholkowska¹⁶, M. Jamroz³⁸, M. Janiak³⁴, D. Jankowsky³⁶, F. Jankowsky²⁵, M. Jingo²³, T. Jogler³⁶, L. Jouvin³¹, I. Jung-Richardt³⁶, M. A. Kastendieck², K. Katarzyński³⁹, U. Katz³⁶, D. Kerszberg¹⁶, B. Khélifi³¹, M. Kieffer¹⁶, J. King³, S. Klepser³⁷, D. Klochkov²⁹, W. Kluźniak³⁴, D. Kolitzus¹³, Nu. Komin²³, K. Kosack¹⁸, S. Krakau¹¹, M. Kraus³⁶, F. Krayzel²⁴, P. P. Krüger¹, H. Laffon²⁶, G. Lamanna²⁴, J. Lau¹⁴, J.-P. Lees²⁴, J. Lefaucheur³¹, V. Lefranc¹⁸, A. Lemièrre³¹, M. Lemoine-Goumard²⁶, J.-P. Lenain¹⁶, E. Leser³⁵, T. Lohse⁷, M. Lorentz¹⁸, R. Liu³, I. Lytova³⁷, V. Marandon³, A. Marcowith¹⁷, C. Mariaud³⁰, R. Marx³, G. Maurin²⁴, N. Maxted¹⁷, M. Mayer⁷, P. J. Meintjes⁴⁰, U. Menzler¹¹, M. Meyer²⁷, A. M.W. Mitchell³, R. Moderski³⁴, M. Mohamed²⁵, K. Morá²⁷, E. Moulin¹⁸, T. Murach⁷, M. de Naurois³⁰, F. Niederwanger¹³, J. Niemiec²¹, L. Oakes⁷, H. Odaka³, S. Öttl¹³, S. Ohm³⁷, M. Ostrowski³⁸, I. Oya³⁷, M. Padovani¹⁷, M. Panter³, R. D. Parsons³, M. Paz Arribas⁷, N. W. Pekeur¹, G. Pelletier³², P.-O. Petrucci³², B. Peyaud¹⁸, S. Pita³¹, H. Poon³, D. Prokhorov¹⁰, H. Prokoph¹⁰, G. Pühlhofer²⁹, M. Punch^{31,10}, A. Quirrenbach²⁵, S. Raab³⁶, A. Reimer¹³, O. Reimer¹³, M. Renaud¹⁷, R. de los Reyes³, F. Rieger^{3,41}, C. Romoli⁴, S. Rosier-Lees²⁴, G. Rowell¹⁴, B. Rudak³⁴, C. B. Rulten¹⁵, V. Sahakian^{6,5}, D. Salek⁴², D. A. Sanchez²⁴, A. Santangelo²⁹, M. Sasaki²⁹, R. Schlickeiser¹¹, F. Schüssler^{*,18}, A. Schulz³⁷, U. Schwanke⁷, S. Schwemmer²⁵, A. S. Seyffert¹, N. Shafi²³, I. Shilon³⁶, R. Simoni⁹, H. Sol¹⁵, F. Spanier¹, G. Spengler²⁷, F. Spies², L. Stawarz³⁸, R. Steenkamp⁸, C. Stegmann^{35,37}, F. Stinzing^{†,36}, K. Stycz³⁷, I. Sushch¹, J.-P. Tavernet¹⁶, T. Tavernier³¹, A. M. Taylor⁴, R. Terrier³¹, M. Tluczykont², C. Trichard²⁴, R. Tufts³, J. van der Walt¹, C. van Eldik³⁶, B. van Soelen⁴⁰, G. Vasileiadis¹⁷, J. Veh³⁶, C. Venter¹, A. Viana³, P. Vincent¹⁶, J. Vink⁹, F. Voisin¹⁴, H. J. Völk³, T. Vuillaume²⁴, Z. Wadiasingh¹, S. J. Wagner²⁵, P. Wagner⁷, R. M. Wagner²⁷, R. White³, A. Wiercholska²¹, P. Willmann³⁶, A. Wörnlein³⁶, D. Wouters¹⁸, R. Yang³, V. Zabalza³³, D. Zaborov³⁰, M. Zacharias²⁵, A. A. Zdziarski³⁴, A. Zech¹⁵, F. Zefi³⁰, A. Ziegler³⁶, and N. Żywucka³⁸

(Affiliations can be found after the references)

Received 17 November 2015 / Accepted 28 February 2016

ABSTRACT

Context. Microquasars are potential γ -ray emitters. Indications of transient episodes of γ -ray emission were recently reported in at least two systems: Cyg X-1 and Cyg X-3. The identification of additional γ -ray-emitting microquasars is required to better understand how γ -ray emission can be produced in these systems.

Aims. Theoretical models have predicted very high-energy (VHE) γ -ray emission from microquasars during periods of transient outburst. Observations reported herein were undertaken with the objective of observing a broadband flaring event in the γ -ray and X-ray bands.

Methods. Contemporaneous observations of three microquasars, GRS 1915+105, Circinus X-1, and V4641 Sgr, were obtained using the High Energy Spectroscopic System (H.E.S.S.) telescope array and the *Ross* X-ray Timing Explorer (RXTE) satellite. X-ray analyses for each microquasar were performed and VHE γ -ray upper limits from contemporaneous H.E.S.S. observations were derived.

Results. No significant γ -ray signal has been detected in any of the three systems. The integral γ -ray photon flux at the observational epochs is constrained to be $I(>560 \text{ GeV}) < 7.3 \times 10^{-13} \text{ cm}^{-2} \text{ s}^{-1}$, $I(>560 \text{ GeV}) < 1.2 \times 10^{-12} \text{ cm}^{-2} \text{ s}^{-1}$, and $I(>240 \text{ GeV}) < 4.5 \times 10^{-12} \text{ cm}^{-2} \text{ s}^{-1}$ for GRS 1915+105, Circinus X-1, and V4641 Sgr, respectively.

Conclusions. The γ -ray upper limits obtained using H.E.S.S. are examined in the context of previous Cherenkov telescope observations of microquasars. The effect of intrinsic absorption is modelled for each target and found to have negligible impact on the flux of escaping γ -rays. When combined with the X-ray behaviour observed using RXTE, the derived results indicate that if detectable VHE γ -ray emission from microquasars is commonplace, then it is likely to be highly transient.

Key words. gamma rays: general – X-rays: binaries – X-rays: individuals: GRS 1915+105 – X-rays: individuals: Circinus X-1 – X-rays: individuals: V4641 Sgr

* Corresponding authors: H.E.S.S. Collaboration, e-mail: contact.hess@hess-experiment.eu

† Deceased.

1. Introduction

Microquasars are X-ray binaries that exhibit spatially resolved, extended radio emission. The nomenclature is motivated by a structural similarity with the quasar family of active galactic nuclei (AGN). Both object classes are believed to comprise a compact central object embedded in a flow of accreting material, and both exhibit relativistic, collimated jets. In the current paradigm, both microquasars and AGN derive their power from the gravitational potential energy that is liberated as ambient matter falls onto the compact object. Notwithstanding their morphological resemblance, microquasars and radio-loud AGN represent complementary examples of astrophysical jet production on dramatically disparate spatial and temporal scales. Indeed, conditions of accretion and mass provision that pertain to the supermassive ($10^6 M_{\odot} \lesssim M_{\text{BH}} \lesssim 10^9 M_{\odot}$) black holes that power AGN and of the stellar-mass compact primaries of microquasars are markedly different. In the latter, a companion star (or donor) provides the reservoir of matter for accretion onto a compact stellar remnant (or primary), which can be either a neutron star or a black hole. Partial dissipation of the resultant power output occurs in a disk of material surrounding the primary, producing the thermal and non-thermal X-ray emission, which is characteristic of all X-ray binary systems. Microquasars are segregated on the basis of associated non-thermal radio emission, indicative of synchrotron radiation in a collimated outflow, which carries away a sizeable fraction of the accretion luminosity (Fender et al. 2004b). In AGN, superficially similar jet structures are known to be regions of particle acceleration and non-thermal photon emission. The resulting radiation spectrum can extend from radio wavelengths into the very high-energy (VHE; $E_{\gamma} > 100 \text{ GeV}$) γ -ray regime. Very high-energy γ -ray emission has been observed from many AGN in the blazar sub-class¹, where the jet axis is aligned close to the observer line-of-sight, as well as from a few radio galaxies (e.g. M 87, Aharonian et al. 2003; Cen A, Aharonian et al. 2009; NGC 1275, Aleksić et al. 2012) and starburst galaxies (e.g. M 82, Acciari et al. 2009; NGC 253, Abramowski et al. 2012).

If similar jet production and efficient particle acceleration mechanisms operate in microquasars and AGNs, this might imply that the former object class are plausible sources of detectable VHE γ -ray emission as well, assuming that appropriate environmental conditions prevail. The primarily relevant environmental conditions include the density of nearby hadronic material, which provides scattering targets for inelastic proton scattering interactions; these interactions produce pions that produce γ -rays when they subsequently decay. The ambient magnetic field strength is also important and influences the rate at which electrons lose energy via synchrotron radiation. Synchrotron photons contribute to the reservoir of soft photons that are available for inverse Compton (IC) up-scattering into the VHE γ -ray regime. The argument for phenomenological parity between AGN and microquasars, possibly related to their structural resemblance, has been strengthened in recent years as the spectral properties of both radio and X-ray emission are remarkably similar for both stellar mass and supermassive black holes. In recent years these similarities led to the postulation of a so-called fundamental plane, which describes a three-dimensional, phenomenological correlation between the radio (5 GHz) and X-ray (2–10 keV) luminosities and the black hole mass (Merloni et al. 2003; Falcke et al. 2004). However, the fundamental plane does not appear to extend into the TeV band. To date, only one well-established microquasar has been observed to emit in the

VHE γ -ray regime. This is the Galactic black hole Cygnus X-1, which was marginally detected (at the $\sim 4\sigma$ level) by the MAGIC telescope immediately prior to a 2–50 keV X-ray flare observed by the INTEGRAL satellite, the *Swift* Burst Alert Telescope (BAT), and the RXTE All-Sky Monitor (ASM; Albert et al. 2007; Malzac et al. 2008). Laurent et al. (2011) recently identified linear polarized soft γ -ray emission from Cygnus X-1 (see also Jourdain et al. 2012), thereby locating the emitter within the jets and identifying their capacity to accelerate particles to high energies (see however Romero et al. 2014). Further motivation for observing microquasars in the VHE band arises from the recent identification of the high-mass microquasar Cygnus X-3 as a transient high-energy (HE; $100 \text{ MeV} < E_{\gamma} < 100 \text{ GeV}$) γ -ray source by the *Fermi* (Abdo et al. 2009) and AGILE (Tavani et al. 2009) satellites. The identification of a periodic modulation of the HE signal is consistent with the orbital frequency of Cygnus X-3 and provides compelling evidence for effective acceleration of charged particles to GeV energies within the binary system (Abdo et al. 2009). Based on evidence from subsequent reobservations, the HE γ -ray flux from Cygnus X-3 appears to be correlated with transitions observed in X-rays in and out of the so-called ultra-soft state, which exhibits bright soft X-ray emission and low fluxes in hard X-rays and is typically associated with contemporaneous radio flaring activity (e.g. Corbel et al. 2012). Unfortunately, repeated observations of Cygnus X-3 using the MAGIC telescope did not yield a significant detection (Aleksić et al. 2010), despite the inclusion of data that were obtained simultaneously with the periods of enhanced HE emission detected using *Fermi*. However, the intense optical and ultraviolet radiation fields produced by the Wolf-Rayet companion star in Cygnus X-3 imply a large optical depth for VHE γ -rays due to absorption via e^+e^- pair production (e.g. Bednarek 2010; Zdziarski et al. 2012). Accordingly, particle acceleration mechanisms akin to those operating in Cygnus X-3 may yield detectable VHE γ -ray fluxes in systems with fainter or cooler donors.

Mechanisms for γ -ray production in microquasars have been widely investigated, resulting in numerous hadronic (see e.g. Romero et al. 2003) and leptonic (see e.g. Atoyan & Aharonian 1999; Georganopoulos et al. 2002; Bosch-Ramon et al. 2006; Dermer & Böttcher 2006; Dubus et al. 2010) models, describing the expected fluxes and spectra of microquasars in the GeV–TeV band. In both scenarios, a highly energetic population of the relevant particles is required and, consequently, emission scenarios generally localize the radiating region within the jet structures of the microquasar. Leptonic models rely upon IC scattering of photons from the primary star in the binary system or photons produced through synchrotron emission along the jet to produce VHE γ -ray emission. In this latter scenario, they closely resemble models of extragalactic jets (Königl 1981; Ghisellini & Maraschi 1989), but typically invoke internal magnetic fields that are stronger by factors ~ 1000 . Consideration of hadronic models is motivated by the detection of Doppler-shifted emission lines associated with the jets of the microquasar SS 433 (e.g. Margon 1984), indicating that at least some microquasar jets comprise a significant hadronic component. Models of VHE γ -ray production by hadronic particles generally invoke electromagnetic cascades initiated by both neutral and charged pion decays (Romero et al. 2003; Aharonian & Atoyan 1996; Romero et al. 2005).

Electron-positron pair production, $\gamma\gamma \rightarrow e^+e^-$ can absorb VHE γ -rays. In the case of 1 TeV γ -rays, the cross section for this process is maximised for ultraviolet target photons ($E_{\text{ph}} \sim 10 \text{ eV}$), where its value may be approximated in

¹ <http://tevcat.uchicago.edu/>

terms of the Thomson cross section as $\sigma_{\gamma\gamma} \approx \sigma_T/5$ (e.g. Gould & Schröder 1967). In high-mass systems, the companion star is expected to produce a dense field of these target photons to interact with the γ -rays (e.g. Protheroe & Stanev 1987; Moskalenko 1995; Böttcher & Dermer 2005; Dubus 2006). This process can be very significant and probably contributes to the observed orbital modulation in the VHE γ -ray flux from LS 5039 (Aharonian et al. 2006c). In contrast, the ultraviolet spectrum of low-mass microquasars is likely dominated by the reprocessing of X-ray emission in the cool outer accretion flow (van Paradijs & McClintock 1994; Gierliński et al. 2009), although jet emission might also be significant (Russell et al. 2006). Regardless of their origin, the observed optical and ultraviolet luminosities of low-mass X-ray binaries (LMXBs) are generally orders of magnitude lower than those of high-mass systems (Russell et al. 2006), and the likelihood of strong γ -ray absorption is correspondingly reduced.

However, microquasars may only become visible in the TeV band during powerful flaring events. These transient outbursts, characterised by the ejection of discrete superluminal plasma clouds, are usually observed at the transition between low- and high-luminosity X-ray states (Fender et al. 2004b). Monitoring black-hole X-ray binaries with radio telescopes and X-ray satellites operating in the last decade enabled a classification scheme of such events to be established (Homan & Belloni 2005). Hardness-intensity diagrams (HIDs) plot the source X-ray intensity against X-ray colour (or hardness) and have subsequently been extensively used to study the spectral evolution of black-hole outbursts. At the transition from the so-called low-hard state to the high-soft states through the hard-to-soft intermediate states, the steady jet associated with the low-hard state is disrupted. These transient ejections, produced once the accretion disk collapses inwards, are more relativistic than the steady low-hard jets (Fender et al. 2004b). Internal shocks can develop in the outflow, possibly accelerating particles that subsequently give rise to radio optically thin flares observed from black-hole systems; this phenomenological description is also extensible to neutron stars, although in that case jet radio power is lower by a factor 5–30 (Migliari & Fender 2006).

Outburst episodes have also been observed in cases in which the source remained in the hard state without transition to the soft state (Homan & Belloni 2005). The detection (at the $\sim 4\sigma$ level) by the MAGIC telescope of the high-mass, black-hole binary Cygnus X-1 took place during an enhanced 2–50 keV flux low-hard state as observed with the INTEGRAL satellite, the *Swift* BAT, and the RXTE ASM (Malzac et al. 2008). However, although the source X-ray spectrum remained unchanged throughout the TeV flare, such a bright hard state was unusually long when compared with previous observations of the source.

Here we report on contemporaneous observations with H.E.S.S. and RXTE of the three microquasars V4641 Sgr, GRS 1915+105, and Circinus X-1. Information on the targets, the H.E.S.S. and RXTE observations, and the corresponding trigger conditions are detailed in Sect. 2. Analysis results are reported in Sect. 3 and discussed in Sect. 4. In the appendix, detailed information on the X-ray analysis is reported, which in particular includes HIDs corresponding to the time of observations for the three studied sources.

2. Targets and observations

2.1. Observations

The H.E.S.S. Imaging Atmospheric Cherenkov Telescope (IACT) array is situated on the Khomas Highland plateau of

Table 1. Observationally established parameters of the target microquasars.

	GRS 1915+105	Circinus X-1	V4641 Sgr
P_{orb} [d]	33.85 ± 0.16 (1)	16.6 (2)	2.82 (3)
M_{\star} [M_{\odot}]	0.47 ± 0.27 (1)	3–10 (5)	2.9 ± 0.4 (10)
	0.28 ± 0.02 (4)		
M_{CO} [M_{\odot}]	$12.4^{+2.0}_{-1.8}$ (6)	≤ 1.4 (8)	6.4 ± 0.6 (10)
θ_{jet} [°]	60 ± 5 (6)	≤ 3 (9)	≤ 12 (3)
d [kpc]	$8.6^{+2.0}_{-1.6}$ (6,7)	$9.4^{+0.8}_{-1.0}$ (9)	6.2 ± 0.7 (10)

Notes. P_{orb} is the binary orbital period, M_{\star} is the mass of the companion star, M_{CO} is the compact object mass, θ_{jet} is the inclination of the observed jet with respect to the line of sight, and d is the estimated distance to the microquasar.

References. (1) Steeghs et al. (2013); (2) Nicolson (2007); (3) Orosz et al. (2001); (4) Ziolkowski (2015); (5) Johnston et al. (1999); Jonker et al. (2007); (6) Reid et al. (2014); (7) Zdziarski (2014); (8) Tennant et al. (1986b); Linares et al. (2010); (9) Heinz et al. (2015); (10) MacDonald et al. (2014).

Namibia (23°16′18″ south, 16°30′00″ east), at an elevation of 1800 m above sea level, and is capable of detecting a Crab-like source close to the zenith at the 5σ level within <5 min under good observational conditions (Aharonian et al. 2006a). The point source sensitivity of H.E.S.S. enables it to detect a $2.0 \times 10^{-13} \text{ cm}^{-2} \text{ s}^{-1}$ γ -ray flux above 1 TeV, at the 5σ level within 25 h, which, together with a low-energy threshold (~ 100 GeV), makes H.E.S.S. an invaluable instrument for studying the VHE γ -ray emission from microquasars. A fifth and larger telescope (commissioned in 2013) will allow the energy threshold to be lowered and will further increase the sensitivity of the instrument. For the analysis presented here, H.E.S.S. observations were carried out using the full, original four-telescope array. Owing to the diverse morphologies of the three binary systems, unique observational trigger criteria were established for each target employing various combinations of the observed X-ray state and radio flaring activity. Details are provided in subsequent paragraphs.

The *Rossi* X-ray Timing Explorer (RXTE) was a space-based X-ray observatory launched on 30 December 30 1995 and decommissioned on 5 January 2012. The primary mission of RXTE was to provide astrophysical X-ray data with high timing resolution. This observatory occupied a circular low-earth orbit with an orbital period of ~ 90 min and carried three separate X-ray telescopes. The Proportional Counter Array (PCA) on board RXTE comprised five copointing xenon and propane Proportional Counter Units (PCUs), which were nominally sensitive in the energy range ~ 2 –60 keV with an energy resolution of $<18\%$ at 6 keV (Zhang et al. 1993). For studies of rapidly varying sources like X-ray binaries, the PCA timing resolution of $\sim 1 \mu\text{s}$ can prove invaluable. However, rapid timing measurements also require a bright source to provide sufficient counting statistics within such short time bins. The High Energy X-ray-Timing Experiment (HEXTE) comprised two independent clusters of four phoswich scintillation detectors, which were sensitive to photons in the ~ 12 –250 keV energy range and had an energy resolution of ~ 9 keV at 60 keV. The maximum timing resolution of HEXTE was $\sim 8 \mu\text{s}$. The All-Sky Monitor (ASM) was a wide field-of-view instrument that monitored $\sim 80\%$ of the sky over the course of each ~ 90 min orbit. This instrument consisted of three identical scanning shadow cameras and was designed to provide near-continuous monitoring of bright X-ray sources. Nominally, the ASM was sensitive in the energy range

from 2–10 keV and had a rectangular field of view spanning $110^\circ \times 12^\circ$.

Contemporaneous X-ray (RXTE) and VHE γ -ray (H.E.S.S.) observations were performed at the epochs listed in Table 2. In the following, we briefly review the observational characteristics of the target microquasars, GRS 1915+105, Circinus X-1, and V4641 Sgr. Established system parameters that characterise the three target microquasars are collated in Table 1.

2.2. GRS 1915+105

GRS 1915+105 is a dynamically established black-hole binary first identified by the WATCH all-sky monitor on board the GRANAT satellite (Castro-Tirado et al. 1994). Observations in the optical and near-infrared using the Very Large Telescope succeeded in identifying the stellar companion as a low-mass KM III giant (Greiner et al. 2001). GRS 1915+105 gained a measure of celebrity as the prototype Galactic superluminal source (Mirabel & Rodriguez 1994).

In a detailed study of the X-ray light curves of GRS 1915+105, Belloni et al. (2000) succeeded in identifying 12 distinct variability classes, internally characterised by the duration and juxtaposition of three separate spectral states. Episodes of class χ behaviour, belonging to state C and lasting several days, are known as plateaux and are invariably terminated by flaring activity in the radio, infrared, and X-ray bands (Fender & Belloni 2004). In contrast with the evidence for self-absorbed synchrotron radiation seen in the spectrally hard, low-luminosity state C, and often associated with continuous relativistic jets (Klein-Wolt et al. 2002), radio spectra obtained during the end-plateau flaring episodes indicate optically thin synchrotron emission (Fender et al. 1997; Eikenberry et al. 1998). Occasionally, these flaring episodes are linked to powerful discrete plasma ejections with instantaneous power output reaching $\geq 10^{39}$ erg s $^{-1}$ (Mirabel & Rodriguez 1994; Zdziarski 2014). Modelling the emission from these discrete relativistic ejecta, Atoyan & Aharonian (1999) showed that inverse Comptonisation of emitted synchrotron photons into the GeV-TeV regime could produce significant and persistent γ -ray fluxes that remain detectable for several days.

Acero et al. (2009) and Saito et al. (2009) reported VHE γ -ray observations of GRS 1915+105; these authors derived integral flux upper limits of 6.1×10^{-13} cm $^{-2}$ s $^{-1}$ above 410 GeV and 1.17×10^{-12} cm $^{-2}$ s $^{-1}$ above 250 GeV, respectively.

For the analysis presented here, GRS 1915+105 was observed by H.E.S.S. between 28 April and 3 May 2004 in response to an apparent decrease in the 15 GHz radio flux, which was monitored by the Ryle Telescope during a ~ 50 day plateau state (Pooley 2006), as shown in Fig. A.2, in which coloured markers indicate the H.E.S.S. observation epochs. On the basis of previously observed behaviour, it was thought likely that the observed radio evolution signalled the end of the plateau state and, therefore, that flaring activity would begin within the subsequent 24 h. The RXTE observations of GRS 1915+105 comprised six individual pointings, contributing to accumulated PCA and HEXTE livetimes of 7.6 ks and 5176 s, respectively. Fifteen contemporaneous H.E.S.S. observations were obtained, constituting an overall livetime of 6.9 h.

2.3. Circinus X-1

Circinus X-1 (hereafter Cir X-1) has been extensively studied since its initial identification (Margon et al. 1971), reveal-

ing a somewhat confusing collection of complex observational characteristics.

Repeated observation of type I X-ray bursts (Tennant et al. 1986a,b; Linares et al. 2010) definitively identifies the compact primary in Cir X-1 as a low magnetic field ($B \lesssim 10^{11}$ G) neutron star. Further sub-classification as a Z or atoll source (see, for example, Done et al. 2007, for an explanation of the distinction between these two classes) is not possible since Cir X-1 exhibits several confusing spectral and timing properties, subsets of which are characteristic of both source types (see e.g. Shirey et al. 1999a; Oosterbroek et al. 1995). Accordingly, established paradigms for disk-jet coupling in X-ray binaries with neutron star primaries (e.g. Migliari & Fender 2006) cannot be reliably employed.

At radio wavelengths, the jets of Cir X-1 display notable structure on arcsecond scales, appearing as a bright core with significant extension along the axial direction of the arcminute jets (Fender et al. 1998). In fact, the observed extension is rather asymmetric with a ratio of at least two between the observed fluxes of the two opposing jets. Interpreted as pure relativistic aberration, this asymmetry implies a jet velocity $\geq 0.1c$. Cir X-1 has also been observed to eject condensations of matter with apparently superluminal velocities $\geq 15c$ (Fender et al. 2004a). These observations imply a physical velocity for the ejecta $v > 0.998c$ with a maximum angle between the velocity vector and the line of sight $\theta < 5^\circ$. These results identify Cir X-1 as a microblazar, a Galactic, small-scale analog of the blazar class of AGN, several of which are known sources of VHE γ -rays.

Definitive classification of the donor star in Cir X-1 is somewhat problematic. The low apparent magnitude of the detected optical counterpart implies a dereddened luminosity consistent with a low-mass or sub-giant companion, implying that Cir X-1 is a LMXB with a high orbital eccentricity $e \sim 0.7\text{--}0.9$ (e.g. Johnston et al. 1999). Nonetheless, recent near-infrared (Clark et al. 2003) and *I*-band optical (Jonker et al. 2007) observations reveal emission features that are consistent with a mid-B supergiant, suggesting a more moderate eccentricity $e \sim 0.45$.

Observations of Cir X-1 in the X-ray band reveal a long-term evolution of the average source brightness. Fluxes rose monotonically from near-undetectable in the early 1970s to a peak value of $\sim 1.5\text{--}2$ Crab (1.5–10 keV) at the turn of the millennium, before returning over a period of ~ 4 yr to their pre-rise levels (Parkinson et al. 2003). Various X-ray spectra, obtained during epochs of both high and low flux, display evidence of complex and variable emission and absorption processes.

A previous analysis of H.E.S.S. observations of Cir X-1 was presented by Nicholas & Rowell (2008), who derived a preliminary upper limit to the γ -ray flux above 1 TeV of 1.9×10^{-13} cm $^{-2}$ s $^{-1}$ corresponding to a detector livetime of 28 h.

The H.E.S.S. observations of Cir X-1 reported here began on 18 June 2004 and were scheduled to coincide with the periastron passage of the binary components. The previous observation of regular radio flares during this orbital interval were thought to provide a good chance of observing during a period of outburst with the associated possibility that superluminal ejections might occur. The RXTE observations of Cir X-1 comprised three individual pointings, corresponding to orbital phase intervals $0.0486 \leq \phi \leq 0.0498$, $0.1104 \leq \phi \leq 0.1112$, and $0.1718 \leq \phi \leq 0.1725$ (using the radio flare ephemeris of Nicolson 2007), and contributing to an accumulated PCA livetime of 2576 s. A data set comprising 12 contemporaneous H.E.S.S. observations yielded a combined livetime of 5.4 h.

Table 2. Observational epochs for each target microquasar.

Target	RXTE ObsId	RXTE Observations (MJD)	H.E.S.S. Observations (MJD)
GRS 1915+105	90108-01-01-00	53 123.091 → 53 123.109	53 123.067 → 53 123.150
	90108-01-02-00	53 124.074 → 53 124.094	53 124.079 → 53 124.162
	90108-01-03-00	53 125.130 → 53 125.149	53 125.083 → 53 125.148
	90108-01-04-00	53 126.114 → 53 126.129	53 126.109 → 53 126.132
	90108-01-05-00	53 127.097 → 53 127.114	53 127.106 → 53 127.165
	90108-01-06-00	53 128.150 → 53 128.165	53 128.149 → 53 128.165
Cir X-1	90124-02-01-00	53 174.749 → 53 174.761	53 174.748 → 53 174.832
	90124-02-02-00	53 175.768 → 53 175.780	53 175.735 → 53 175.822
	90124-02-03-00	53 176.781 → 53 176.793	53 176.772 → 53 176.858
V4641 Sgr	90108-03-01-00	53 193.904 → 53 193.924	Not Observed
	90108-03-02-00	53 194.887 → 53 194.908	53 194.883 → 53 194.926
	90108-03-03-00	53 195.871 → 53 195.892	53 195.890 → 53 195.931

2.4. V4641 Sgr

V4641 Sgr is the optical designation of the habitually weak X-ray source SAX J1819.3-2525 (XTE J1819-254), which was independently identified using the *BeppoSAX* (in 't Zand et al. 1999) and RXTE (Markwardt et al. 1999a) satellites. Optical spectroscopic measurements (Orosz et al. 2001; Lindström et al. 2005) strongly suggest a late B- or early A-type companion with an effective temperature $T_{\text{eff}} \approx 10\,500$ K. The mass of the compact primary, $6.4 \pm 0.6 M_{\odot}$ (MacDonald et al. 2014), categorises V4641 Sgr as a firm black hole candidate.

V4641 Sgr is probably best known for its exhibition of rapid and violent outbursts. Perhaps the most spectacular of these events was the super-Eddington flare detected by the RXTE ASM in September 1999. The observed X-ray fluxes (2–12 keV) increased sharply, reaching ≈ 12.2 Crab within eight hours before fading again to below 0.1 Crab in under two hours (Revnivtsev et al. 2002). Powerful contemporaneous flares were also observed at hard X-ray (McCullough et al. 1999), optical (Stubbings & Pearce 1999), and radio (Hjellming et al. 2000) wavelengths. In fact, Very Large Array (VLA) radio observations obtained within a day of the X-ray flare resolved a bright jet-like radio structure ≈ 0.25 arcsec in length (Hjellming et al. 2000). Assuming the most likely hypothesis, i.e., that the ejection is coincident with some phase of the X-ray flare, proper motions in the range $0.22 \lesssim \mu_{\text{jet}} \lesssim 1.1$ arcsec day $^{-1}$ are derived. At the minimum distance $d = 5.5$ kpc, the implied lower limit to the apparent velocity of the ejecta is $7c \lesssim v_{\text{min}} \lesssim 35c$, which is comparable with the extragalactic jets seen in blazars. Indeed, the remarkably high apparent velocities imply that V4641 Sgr may be a microblazar with a relativistic jet moving close to the line of sight ($\theta_{\text{jet}} \lesssim 12^{\circ}$; from Orosz et al. 2001). Subsequent, weaker broadband outbursts have also been observed, suggesting recurrent activity on a timescale ~ 1 – 2 yr (e.g. Hjellming 2000; Rupen et al. 2002, 2003; Swank 2004).

Observations of V4641 Sgr with H.E.S.S. were initiated on 7 July 2004 (MJD 53 193) in response to the source brightening rapidly in the radio (Rupen et al. 2004b), optical (Revnivtsev et al. 2004), and X-ray (Swank 2004) bands. The resultant RXTE exposure comprised three observations, each contributing to an accumulated PCA livetime of 5 ks. Two pairs of ~ 30 min H.E.S.S. observations were obtained contemporaneously with the final two RXTE pointings. In total, the four separate exposures constitute an overall livetime of 1.76 h.

3. Analysis and results

X-ray data reduction with the FT00LS 5.3.1 software suite employed the data selection criteria regarding elevation, offset, electron contamination, and proximity to the South Atlantic Anomaly recommended by the RXTE Guest Observer Facility website². For each observation, the PCA STANDARD2 data were extracted from all available PCUs. For all observations, HEXTE Archive mode data for both clusters were extracted following the recommended procedures for time filtering and background estimation. Spectral analysis was carried out using the XSPEC 12.6.0 package (Arnaud 1996). Spectral fits for GRS 1915+105 use both PCA and HEXTE data, including an energy range of 3–200 keV. For bright X-ray sources, such as GRS 1915+105, statistical errors on the number of counts per spectral bin become insignificant relative to dominant uncertainties in the instrument response. Accordingly, a 1% systematic error was added to all PCA channels. The remaining sources, Cir X-1 and V4641 Sgr, were not significantly detected by HEXTE and therefore only PCA data in the 3–20 keV range were considered to ensure good data quality. These targets were sufficiently faint that the spectral bin uncertainties were statistically dominated and the addition of a systematic error component was not required. In the case of GRS 1915+105, power density spectra (PDS) were derived using the *ftool* *powspec*. For each RXTE pointing of GRS 1915+105, individual PDS were extracted from 128 s intervals comprising 2^{14} bins. The resulting spectra were then averaged to produce a PDS for the total light curve with errors estimated using the standard deviation of the average of the power in each frequency bin. The overall PDS were logarithmically rebinned and normalised to represent the squared fractional RMS in each frequency bin (see e.g. Lewin et al. 1988). Corrections for instrument deadtime (see, for example, Revnivtsev et al. 2000) were applied (although this was found to have a negligible effect in the frequency range under consideration) and the expected white noise level was subtracted (Leahy et al. 1983). Similar temporal analyses for the remaining targets proved unfeasible because of insufficient count statistics at all but the lowest frequencies.

The γ -ray analysis followed the standard point-source procedure described in Aharonian et al. (2006b). The reflected background model (see, for example, Berge et al. 2007) was used to derive overall results in conjunction with both the *hard* and *standard* event selection cuts described by Aharonian et al. (2006b).

² http://heasarc.nasa.gov/docs/xte/xhp_proc_analysis.html

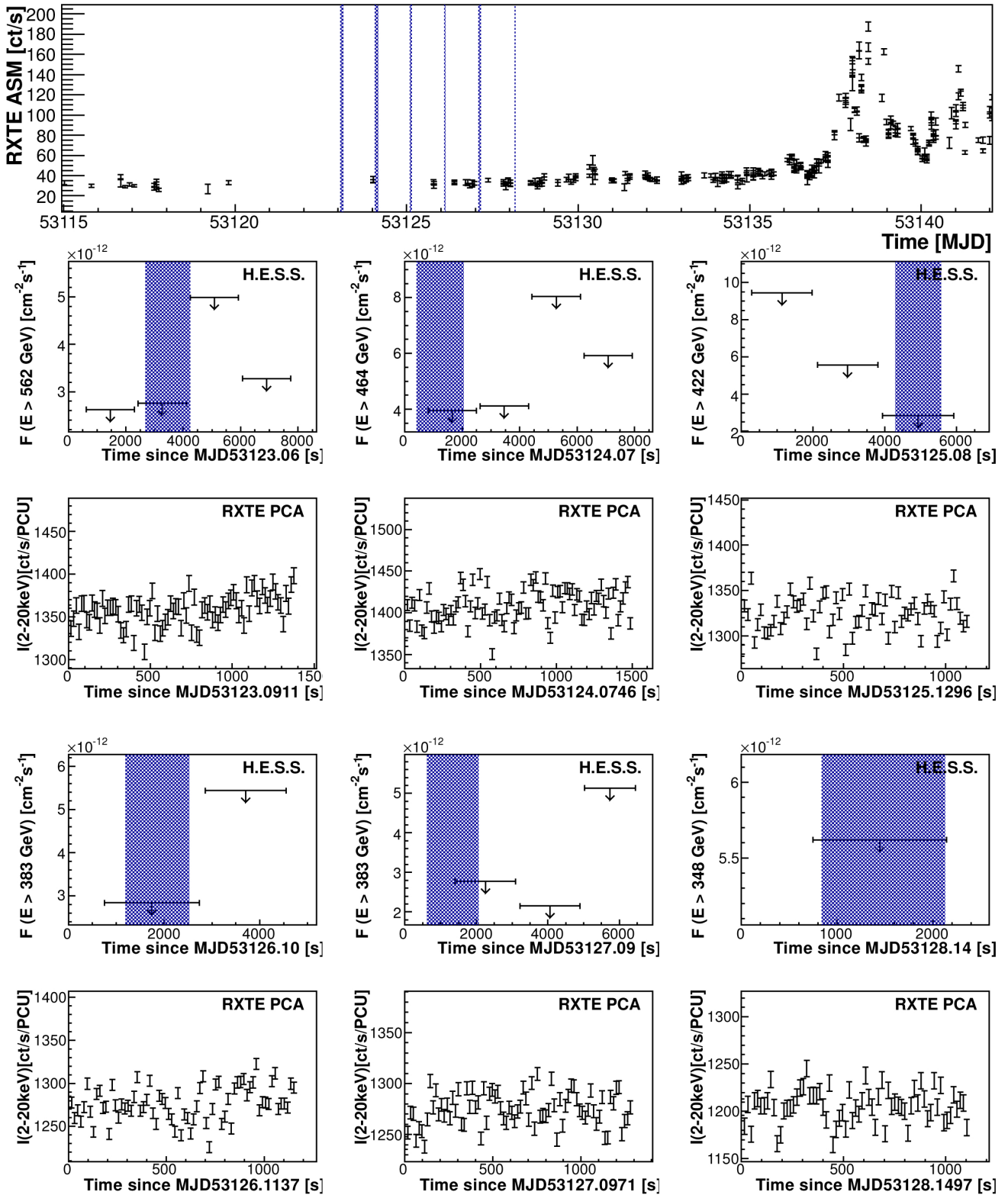


Fig. 1. RXTE ASM, and PCA light curves for GRS 1915+105 together with H.E.S.S. upper limits derived from individual ~ 28 min runs using standard event selection cuts. The blue shaded bands on the ASM light curve indicate the extent of the H.E.S.S. observations, while on the H.E.S.S. upper limit plots similar bands illustrate the duration of the contemporaneous PCA observations. The plotted H.E.S.S. upper limits correspond to different threshold energies and the vertical scale of each light curve has been optimised for the plotted data.

Table 3. H.E.S.S. VHE γ -ray significances corresponding to hard and standard event selection regimes.

Target	Image Cuts	N_{ON} [events]	N_{OFF} [events]	α	Excess [events]	Significance [σ]
GRS 1915+105	Standard	471	7127	0.073	-51.6	-2.2
	Hard	36	783	0.060	-10.9	-1.6
Cir X-1	Standard	385	5959	0.068	-20.1	-1.0
	Hard	45	648	0.056	9.1	1.4
V4641 Sgr	Standard	161	2373	0.067	1.2	0.1
	Hard	11	275	0.055	-4.2	-1.11

Table 4. H.E.S.S. VHE γ -ray integral flux upper limits above the telescope energy threshold corresponding to both event selection regimes.

Target	Cuts	T_{Live} [s]	\bar{Z}_{max} [$^{\circ}$]	E_{thresh} [GeV]	$I(>E_{\text{thresh}})$ [$\text{ph cm}^{-2} \text{s}^{-1}$]
GRS 1915+105	Standard	24681	40.6	562	$<7.338 \times 10^{-13}$
	Hard	24681	40.6	1101	$<1.059 \times 10^{-13}$
Cir X-1	Standard	19433	43.6	562	$<1.172 \times 10^{-12}$
	Hard	19433	43.6	1101	$<4.155 \times 10^{-13}$
V4641 Sgr	Standard	6335	8.4	237	$<4.477 \times 10^{-12}$
	Hard	6335	8.4	422	$<4.795 \times 10^{-13}$

Notes. The upper limits are derived at the 99% confidence level, assuming a power-law spectrum ($dN/dE \propto E^{-\Gamma}$) with the photon index $\Gamma_{\text{std}} = 2.6$ for standard cuts and $\Gamma_{\text{hard}} = 2.0$ for hard cuts. The rather high threshold energies derived for GRS 1915+105 and Cir X-1 are the result of large maximum observational zenith angles.

Hard cuts (image size ≥ 200 photoelectrons) tend to enhance the signal of sources with power-law spectral slopes that are harder in comparison to the dominant cosmic ray background. Standard cuts (image size ≥ 80 photoelectrons) provide less sensitivity in such cases but allow a lower energy threshold. No significant detection was obtained for any of the three targets. Upper limits to the VHE γ -ray flux above the instrumental threshold energy were therefore derived at the 99% confidence level using the profile likelihood method (Rolke et al. 2005).

3.1. GRS 1915+105

As illustrated by the PCA and ASM light curves shown in Fig. 1, the X-ray count rate was stable to within $\sim 10\%$ during each observation and varied by no more than $\sim 20\%$ between observations. Indeed, the long-term RXTE ASM light curve in Fig. 1 (top panel) clearly indicates that the H.E.S.S. observation epochs occurred during an extended and relatively faint plateau in the 2–10 keV flux.

The 3–200 keV X-ray spectra shown in Fig. A.4 also exhibit remarkable stability between observations. The individual spectra are dominated by a hard non-thermal component and strongly suggest class χ (in state C) behaviour (e.g. Zdziarski et al. 2001; Trudolyubov 2001), which is confirmed by the location of the observations in the HID of Fig. A.1, according to the classification of Belloni et al. (2000). Figure A.2 shows the contextual X-ray and 15 GHz radio light curves of GRS 1915+105 during a two-month period that brackets the H.E.S.S. observation epochs. It is evident from the figure that H.E.S.S. observed the target during an extended radio-loud plateau (~ 80 mJy; for historical flux comparison, a three-year monitoring campaign is presented in Pooley 2006). The plateau ended approximately ten days later with a combined radio and X-ray flaring episode. The assertion of radio-loud behaviour at the H.E.S.S. observation epochs is supported by the quasi-periodic oscillation (QPO) analysis presented in Fig. A.3. For a detailed discussion see Appendix A.1.

In summary, the combined spectral and temporal analyses indicate a robust association of the contemporaneous H.E.S.S.

observation with the radio-loud χ state, and the presence of steady, mildly relativistic jets at the time of observation may be confidently inferred.

The contemporaneous H.E.S.S. observations did not yield a significant VHE γ -ray detection. The significances corresponding to the total H.E.S.S. exposure are computed using Eq. (17) from Li & Ma (1983) and are listed in Table 3. Figure 1 plots runwise 99% confidence level upper limits to the integral VHE γ -ray flux above the instrumental threshold energy and illustrates the overlap between the RXTE and H.E.S.S. observations. Integral flux upper limits, which correspond to the overall H.E.S.S. exposure, are listed in Table 4.

3.2. Cir X-1

The ASM light curve shown in Fig. 2 reveals that the H.E.S.S. observation epochs occurred during an extended ~ 4 day dip in the 2–10 keV X-ray flux. Additionally, it should be noted that the observations reported here were obtained during an extremely faint episode in the secular X-ray flux evolution of Cir X-1 (Parkinson et al. 2003), which is also evident from the HID presented in Fig. A.5. As a consequence, the measured X-ray fluxes are significantly lower than most others reported for this source. As illustrated in Fig. 2, the individual PCA light curves obtained during the first two pointings are characterised by a relatively low count rate, which remains approximately constant throughout each observation. In marked contrast, the third observation exhibits clear variability with count rates doubling on timescales of ~ 50 s.

A detailed analysis of the obtained spectra (see Appendix A.2) reveals that the observed flux variability is accompanied by marked variations in spectral shape. These can be interpreted as hinting towards a strong mass transfer during the periastron passage and subsequent dramatic evolution of the local radiative environment.

H.E.S.S. observations obtained contemporaneously with the RXTE pointings yield a non-detection that is evident from the significances listed in Table 3. Figure 2 plots runwise 99% confidence level upper limits to the integral VHE γ -ray flux

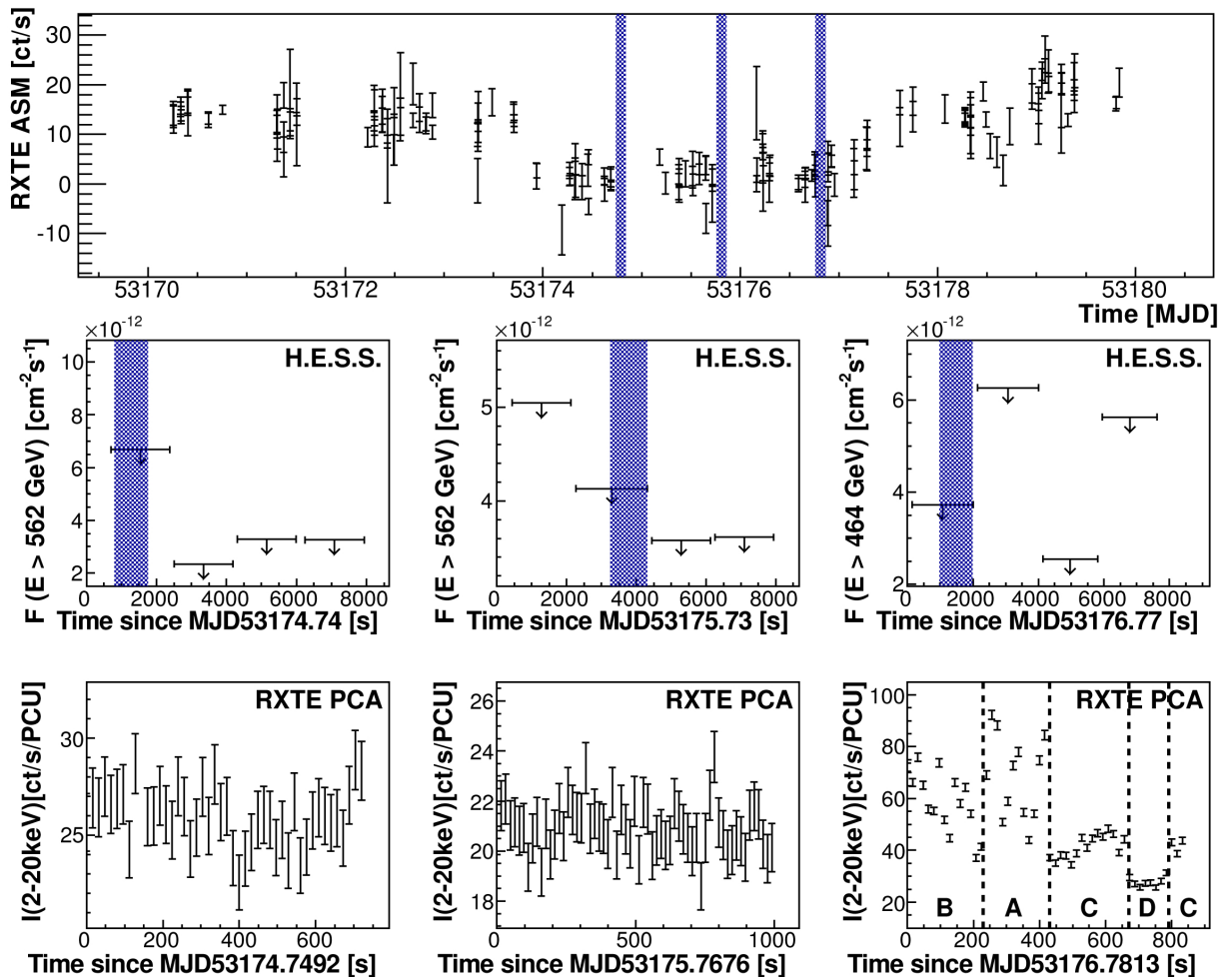


Fig. 2. RXTE ASM and PCA light curves for Cir X-1 together with H.E.S.S. upper limits derived from individual ~ 28 min runs using standard event selection cuts. The blue shaded bands on the ASM light curve indicate the extent of the H.E.S.S. observations, while on the H.E.S.S. upper limit plots similar bands illustrate the duration of the contemporaneous PCA observations (OBS 1–3). The partitioning of OBS 3 into sub-intervals A–D based on 2–20 keV X-ray flux is illustrated in the *bottom right panel*. The plotted H.E.S.S. upper limits correspond to different threshold energies, and the vertical scale of each light curve has been optimised for the plotted data.

above the instrumental threshold energy and illustrates complete overlap between the RXTE and H.E.S.S. observations. Integral flux upper limits, which correspond to the overall H.E.S.S. exposure, are listed in Table 4.

3.3. V4641 Sgr

Figure 3 shows RXTE PCA light curves derived from three pointed observations. The individual light curves indicate various degrees of X-ray variability with the clearest evidence for flaring visible as a sharp ~ 5 -fold count rate fluctuation during the first observation. In marked contrast, the second observation is uniformly faint with the χ^2 probability of constant count rate $P_{\text{const}} = 0.97$ and, hence, this observation is consistent with a period of steady, low-level emission. Subsequently, the third observation reveals a reemergence of mild variability ($P_{\text{const}} = 0.07$) with ~ 2 -fold count rate fluctuations occurring on timescales of ~ 500 s.

Radio data shown in Fig. A.7 right were obtained using the VLA and Australia Telescope Compact Array (ATCA) between MJD 53 190 and MJD 53 208. They indicate rapid variability with peak flux densities of ~ 30 mJy observed on MJD 53 193 (Rupen et al. 2004b; Senkbeil & Sault 2004;

Rupen et al. 2004a). An optically thin radio spectrum ($S_\nu \propto \nu^{-0.7}$) observed on MJD 53 191 was interpreted by Rupen et al. (2004b) as the signature of a decaying radio flare. Radio observations were triggered by an optical alert from VSNET (MJD 53 190) in combination with a RXTE PCA measurement during a Galactic bulge scan (MJD 53 189) that revealed a 2–10 keV X-ray flux equivalent to 8.2 mCrab. For comparison, the August 2003 flare of V4641 Sgr reached 66 mCrab, while quiescent fluxes are typically < 0.5 mCrab (Swank 2004). As shown in Fig. A.7 right, the dedicated RXTE PCA observation and H.E.S.S. observations took place between two radio flares, which is consistent with the X-ray variability evolution illustrated in Fig. 3.

While V4641 Sgr is evidently the most X-ray-faint binary in the studied sample, it simultaneously exhibits the hardest spectrum, as shown by the hardness values in Fig. A.7 (left-hand panel). Furthermore, the evolution of the hardness is consistent with contemporaneous observations of rapid flux evolution in the radio band (Senkbeil & Sault 2004)³ (Fig. A.7). To help place the H.E.S.S. and RXTE observations in a historical context, the HID for V4641 Sgr in Fig. A.8 displays the entire

³ <http://www.ph.unimelb.edu.au/~rsault/astro/v4641/>

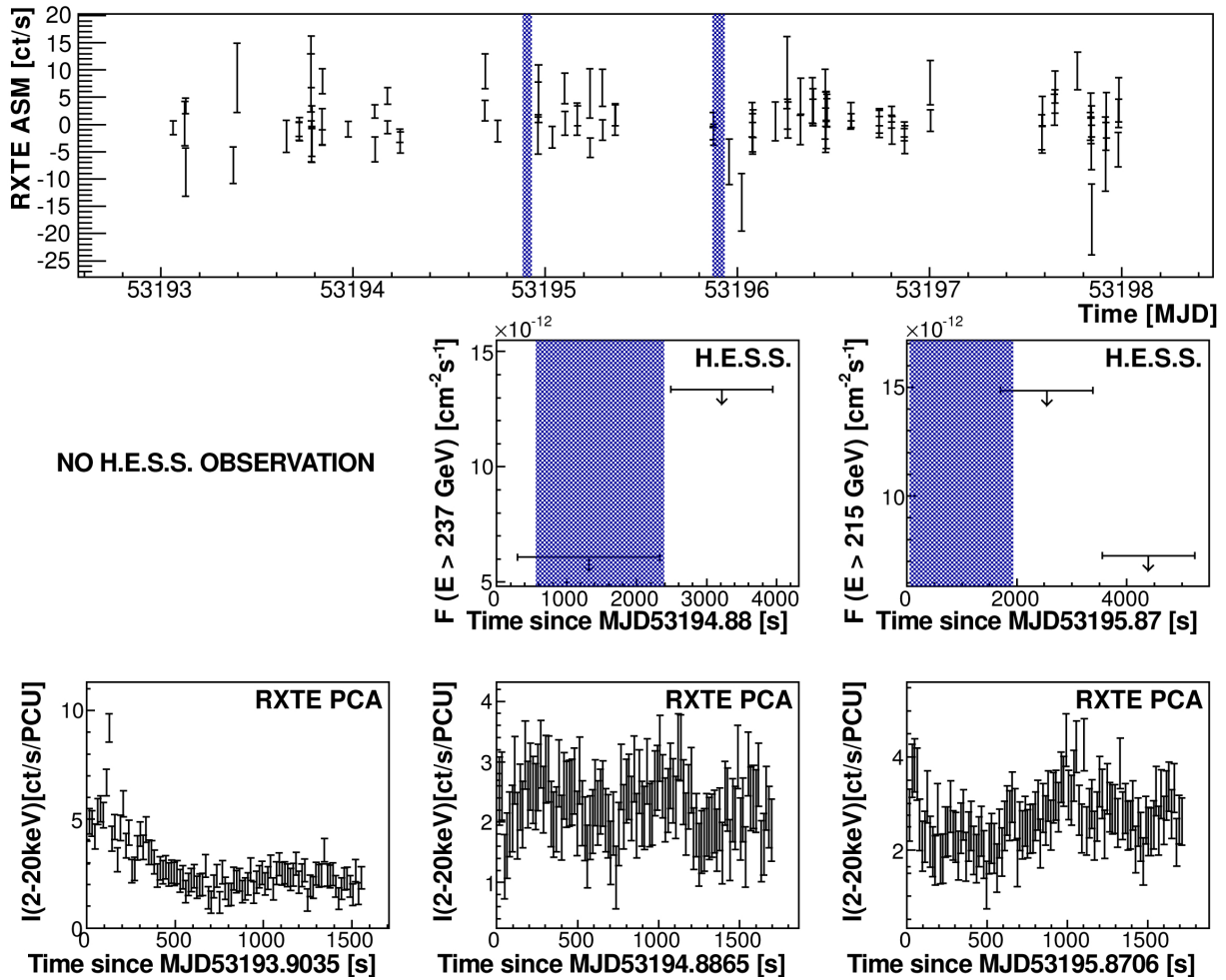


Fig. 3. RXTE ASM and PCA light curves for V4641 Sgr together with H.E.S.S. upper limits derived from individual ~ 28 min runs using standard event selection cuts. The blue shaded bands on the ASM light curve indicate the extent of the H.E.S.S. observations, while on the H.E.S.S. upper limit plots they illustrate the duration of the contemporaneous PCA observations. The plotted H.E.S.S. upper limits correspond to different threshold energies and the vertical scale of each light curve has been optimised for the plotted data.

archival RXTE PCA data set for this target, and compares the X-ray characteristics corresponding to the H.E.S.S. observation periods (different symbols are used to indicate observations obtained on each day in the range MJD 53 193-5) with three flaring episodes observed with RXTE. On 15 September 1999 (orange markers in Fig. A.8), a 1500 s RXTE observation revealed a source flux evolution that is characterised by rapid, large-amplitude variability before reverting to a soft, low intensity state after ~ 1000 s. An optical flare that preceded the RXTE observations likely corresponds with the onset of the short 10-hour outburst, which [Wijnands & van der Klis \(2000\)](#) associated with a low \dot{M} accretion event. Historically, flaring episodes exhibited by V4641 Sgr are often short, unpredictable, and relatively faint, which implies that many may go unnoticed.

Data corresponding to two longer outbursts, spanning the periods 24–26 May 2002 and 5–7 August 2003, are also illustrated in Fig. A.8. In the coordinates of the HID, both episodes are topologically similar to the 1999 outburst, but shifted towards fainter harder regions.

Evidently, the X-ray fluxes that correspond with H.E.S.S. observation epochs indicated in Fig. A.8 are substantially fainter than any of these historically remarkable outbursts.

In summary, in view of the various multiwavelength data, it seems likely that V4641 Sgr underwent a period of mild activity that spanned the H.E.S.S. observation epochs.

The contemporaneous H.E.S.S. data are consistent with non-detection with the corresponding γ -ray significances listed in Table 3. Technical issues prevented γ -ray data corresponding to the first RXTE observation from being obtained. Simultaneous γ -ray observations were obtained corresponding to the second RXTE exposure, which showed no indications of X-ray variability. Although the source began to show increased X-ray activity during the third RXTE observation, the degree of overlap with the corresponding H.E.S.S. observations was minimal. At radio, optical, and X-ray energies, V4641 Sgr exhibits rapid variability on timescales ~ 10 min or less (e.g. [Uemura et al. 2005](#); [Maitra & Bailyn 2006](#)). Optimistically, the compelling evidence for mild broadband flaring admits the possibility that the H.E.S.S. observations monitor a transient outburst event.

Integral flux upper limits above the instrumental threshold energy, which correspond to the overall H.E.S.S. exposure at the position of V4641 Sgr, are listed in Table 4.

Table 5. Estimated maximum VHE γ -ray luminosities of the target microquasars, which would still be consistent with a non-detection given the flux upper limits presented in Table 4.

Target	Maximum distance estimate [kpc]	E_{thresh} [GeV]	Luminosity above E_{thresh} [erg s ⁻¹]
GRS 1915+105	10.6	562	$<2.3 \times 10^{34}$
Cir X-1	10.2	562	$<3.4 \times 10^{34}$
V4641 Sgr	6.9	237	$<2.5 \times 10^{34}$

Notes. Source distances correspond to the largest estimate that was found in the literature (see Sect. 2). The energy threshold of Cherenkov telescope arrays increases with observational zenith angle.

4. Discussion

The principal aim of this investigation was to obtain contemporaneous X-ray and VHE γ -ray observations of three known superluminal microquasars during major flaring events. However, the results presented in Sect. 3 indicate that the interpretation of the VHE γ -ray non-detections cannot proceed under the assumption of energetic flaring or bulk superluminal ejections at the time of observation. Nonetheless, upper limits to the VHE γ -ray flux were derived and an analysis of the contemporaneous RXTE observations has helped to reveal the X-ray behaviour corresponding to the H.E.S.S. observation epochs. These data facilitate the straightforward derivation of constraints on the γ -ray luminosity of the target binary systems. In Table 5 the calculated flux upper limits were used to infer the maximum γ -ray luminosities above the target-specific, instrumental threshold energy for each target binary system by assuming the maximum source distance estimate presented in Table 1.

Analysis of the contemporaneous X-ray and radio observations conclusively places GRS 1915+105 in a radio-loud plateau state at the time of observation. In contrast with the superluminal flaring episodes, this state is characterised by the production of continuous, mildly relativistic radio jets with an estimated power of $\sim 3 \times 10^{38}$ erg s⁻¹ (Klein-Wolt et al. (2002), assuming a distance of 11 kpc). Theoretically, it seems unlikely that bright VHE γ -ray emission would be expected from the compact self-absorbed jets, which are typical of the plateau state of GRS 1915+105. For example, a leptonic emission model developed by Bosch-Ramon et al. (2006) to simulate the broadband emission of microquasar jets in the low-hard state predicts VHE γ -ray luminosities $\lesssim 10^{33}$ erg s⁻¹ that are consistent with the H.E.S.S. non-detection. Notwithstanding the plausibility of VHE γ -ray emission in the plateau state, a comparison of the estimated jet power with the maximum γ -ray luminosity listed in Table 5 reveals that the jet power conversion efficiency is constrained to be $\lesssim 0.008\%$ for γ -ray production above 562 GeV. For comparison, corresponding efficiency estimates for γ -ray production were derived for the steady, compact jets of other microquasars that were observed in appropriate states. The published MAGIC upper limit on the VHE γ -ray luminosity of Cygnus X-3 during its hard state implies a somewhat larger maximum conversion efficiency of 0.07% (Aleksić et al. 2010) and a similar value is obtained from MAGIC upper limits on the steady VHE emission from Cygnus X-1 (Albert et al. 2007). These efficiencies are inferred from the directly observed jet power, and should be distinguished from the higher jet powers that were indirectly derived from the observation of radio-emitting bubbles inflated by microquasar jets (see e.g. Gallo et al. 2005 for Cyg X-1; and Pakull et al. 2010; Soria et al. 2010 for S26 in NGC 7793).

We presented an analysis of the entire H.E.S.S. data set for GRS 1915+105 (Acero et al. 2009) and we derived an upper limit to the γ -ray flux above 0.41 TeV of 6.1×10^{-13} cm⁻² s⁻¹,

corresponding to a detector livetime of 24.1 h. The somewhat higher upper limits presented in Sect. 3.1 utilise a more limited data set and are therefore consistent with the previously published value. None of the H.E.S.S. observations of GRS 1915+105 coincide with bright flaring episodes at longer wavelengths.

Observations of Cir X-1 were obtained during an extended dip in the X-ray flux, at phase intervals close to the periastron passage of the binary components. Spectral analysis of the RXTE data showed some evidence for a recent increase in mass transfer, producing strong signatures of X-ray absorption. It was hoped that H.E.S.S. observations would coincide with one of the quasi-regular radio flares, which often accompany periastron passage in Cir X-1.

The ephemeris of Nicolson (2007) predicts the onset of a radio flare ~ 19 – 20 h before the first RXTE observation. Unfortunately, despite the undoubted occurrence of quasi-periodic radio flares from Cir X-1 near periastron, a robust correlation between the observed X-ray and radio behaviour is yet to be identified. Although rapid brightening of the X-ray continuum might indicate accompanying radio flares, evidence for a definitive association is far from clear (Soleri et al. 2007; Tudose et al. 2008). Recent radio observations of Cir X-1 (e.g. Fender et al. 2004a; Tudose et al. 2008) focus primarily on the ultrarelativistic ejection events that manifest as $\gtrsim 3$ day episodes of flaring on timescales of a few hours. In principle, the lack of contemporaneous radio data admits the possibility of such persistent outbursts at the time of observation. By analogy with canonical black hole binaries, it is possible that the inferred variation in the mass accretion rate between the first and second RXTE observations also implies an evolution of the jet properties (Migliari & Fender 2006), but this is far from clear in such an unusual system. Moreover, Tudose et al. (2008) report compelling evidence that prior to 2006, Cir X-1 underwent a ~ 6 yr episode of unusual radio quiescence, suggesting that jet formation was somewhat suppressed during the epochs of H.E.S.S. observation. Accordingly, without strictly simultaneous radio data indicating otherwise, the most likely scenario is that no outflows were present. In this context the absence of a detectable γ -ray signal is not surprising.

As a confirmed high-mass black hole binary, V4641 Sgr is the studied target that most closely resembles the Cygnus X-1 and Cygnus X-3 systems. Moreover, the H.E.S.S. observations were obtained during a period of sporadic broadband flaring, and comparing these observations with the results of Albert et al. (2007), VHE γ -ray emission might have been expected. The detection of Cyg X-1 using the MAGIC telescopes appeared to coincide with the rising part of a strong X-ray flare. In contrast, radio spectra obtained close to the H.E.S.S. observational epochs are indicative of the decay following a flaring episode (Senkbeil & Sault 2004). Assuming that the γ -ray emission mechanisms operating in Cyg X-1 also occur in V4641 Sgr,

the absence of a significant H.E.S.S. detection might be viewed as evidence that production of GeV and TeV photons is a highly transient process. This would further suggest that γ -ray emission originates in a spatially compact region that is at most a few light hours in size.

Absorption of γ -rays by pair production is expected to be negligible in GRS 1915+105, since the donor star is too cool and faint to produce a strong ultraviolet photon field. The same is true of Cir X-1 if the conventional assumption of a low-mass companion is adopted. For completeness, Fig. 4 plots the level of γ -ray absorption predicted by a numerical implementation of the model presented by Dubus (2006), assuming that the companion star in Cir X-1 is in fact a mid-B supergiant as proposed by Jonker et al. (2007). The separate curves are representative of the three orbital phase intervals corresponding to the H.E.S.S. observation epochs, and were derived using the system parameters derived by Jonker et al. (2007) in conjunction with typical values for the temperature ($T_{\text{eff}} \approx 20\,000$ K) and radius ($R \approx 9 R_{\odot}$) of a mid-B supergiant. It is evident that some non-negligible absorption is expected, particularly during the first observation interval. Nonetheless, it seems unlikely that the expected levels of attenuation ($\lesssim 20\%$) would suppress an otherwise detectable γ -ray flux sufficiently to yield the low significances listed in Table 3.

The situation with regard to γ -ray absorption is clearer in the case of V4641 Sgr, since the companion has been spectroscopically identified as a late B- or early A-type star. Using the system parameters derived by Orosz et al. (2001) and assuming a circularised orbit, the model presented by Dubus (2006) was used to predict the expected levels of γ -ray absorption as a function of orbital phase. As illustrated in Fig. 4 (bottom panel), absorption might have an important effect during the first H.E.S.S. observation interval, although as with Cir X-1 the predicted levels of absorption ($\lesssim 25\%$) would not attenuate a bright γ -ray signal so far below the detection threshold. During the second H.E.S.S. observation interval, when X-ray data show marginal indications of source activity, the predicted absorption due to pair production on the stellar radiation field is negligible. We note however that, as in the case of Cir X-1, the relative inclination of the jets from V4641 Sgr with respect to the accretion disk may be low (Schulz et al. 2006) and, therefore, further absorption of ~ 100 GeV–TeV γ -ray photons could occur via interaction with the disk thermal photon field (see e.g. Carraminana 1992).

It should also be noted that all the confirmed VHE γ -ray binaries lie at distances of 2–4 kpc. In contrast, the targets reported here have maximum distances in the range 7–11 kpc, resulting in flux dilution factors that are greater by one order of magnitude. Obviously, this has strong implications for the detectability of any emitted γ -ray signal.

5. Conclusions

Contemporaneous VHE γ -ray and X-ray observations of GRS 1915+105, Cir X-1, and V4641 Sgr were obtained using H.E.S.S. and RXTE. Analysis of the resultant H.E.S.S. data did not yield a significant detection for any of the target microquasars. However, X-ray binaries are dynamic systems and as such are likely to exhibit evolution of their radiative properties, both as a function of orbital phase and also in response to non-deterministic properties. It follows that the non-detections presented in this work do not indicate that the target binary systems do not emit detectable VHE γ -ray emission at phases other than those corresponding to the H.E.S.S. observations.

GRS 1915+105 appears to have been observed during an extended plateau state, the archival multiwavelength data sug-

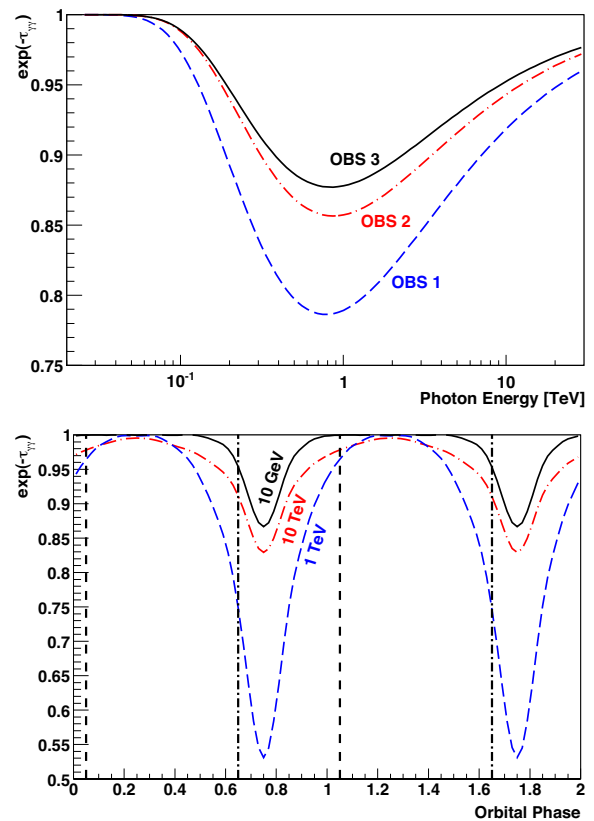


Fig. 4. Levels of γ -ray absorption due to pair production with stellar photons as predicted by the numerical model outlined by Dubus (2006). *Top panel:* expected γ -ray transmission as a function of photon energy for Cir X-1 assuming an inclination $i = 66^\circ$ and using the best-fit ephemeris derived by Jonker et al. (2007), which is appropriate for a mid-B supergiant companion. The individual curves correspond to the orbital phases of the first (blue dashed), second (red dot-dashed), and third (black solid) H.E.S.S. observation intervals. *Bottom panel:* expected γ -ray transmission for V4641 Sgr as a function of orbital phase derived using the orbital solution of Orosz et al. (2001) and assuming a circularised orbit. The individual curves represent photon energies of 10 GeV (black solid), 1 TeV (blue dashed), and 10 TeV (red dot-dashed). Vertical lines indicate the first (dot-dashed) and second (dashed) H.E.S.S. observation epochs.

gesting the presence of continuous, mildly relativistic radio jets at the time of observation. The RXTE observations of Cir X-1 yield data that are consistent with strongly varying obscuration of the X-ray source shortly after periastron passage, but these data are not indicative of bright flaring during the H.E.S.S. observation epochs. Conversely, V4641 Sgr appears to have been observed during an episode of mild, transient flaring, although rapid source variability, combined with the limited duration of the strictly simultaneous H.E.S.S. and RXTE exposure, complicates interpretation.

Microquasars continue to be classified as targets of opportunity for IACTs, requiring a rapid response to any external trigger to maximise the likelihood of obtaining a significant detection. These conditions are realised with the commissioning of the H.E.S.S. 28 m telescope, which aims to lower the energy threshold from 100 GeV to about 30 GeV (Parsons et al. 2015; Holler et al. 2015a,b) while simultaneously enabling very rapid follow-up observations (Hofverberg et al. 2013). To exploit these new opportunities and an increasing understanding of the behaviour of microquasars, the triggering strategies

for TeV follow-up observations have evolved significantly in recent years. In the future, alternative observational strategies, including continuous monitoring of candidate microquasars in the VHE γ -ray band, may become possible using dedicated sub-arrays of the forthcoming Cherenkov Telescope Array (CTA Consortium 2011).

Irrespective of the non-detections presented herein, the tantalising observations of Cygnus X-3 at GeV energies and Cygnus X-1 by the MAGIC telescope ensures that the motivations for observing microquasars using IACTs remain compelling. Indeed, by further constraining the γ -ray emission properties of microquasars, subsequent observations will inevitably yield an enhanced understanding of astrophysical jet production on all physical scales. More optimistically, the detection of additional γ -ray-bright microquasars would greatly facilitate a comprehensive characterisation of the particle acceleration and radiative emission mechanisms that operate in such systems.

Acknowledgements. The support of the Namibian authorities and of the University of Namibia in facilitating the construction and operation of H.E.S.S. is gratefully acknowledged, as is the support by the German Ministry for Education and Research (BMBF), the Max Planck Society, the German Research Foundation (DFG), the French Ministry for Research, the CNRS-IN2P3 and the Astroparticle Interdisciplinary Programme of the CNRS, the UK Science and Technology Facilities Council (STFC), the IPNP of the Charles University, the Czech Science Foundation, the Polish Ministry of Science and Higher Education, the South African Department of Science and Technology and National Research Foundation, and by the University of Namibia. We appreciate the excellent work of the technical support staff in Berlin, Durham, Hamburg, Heidelberg, Palaiseau, Paris, Saclay, and in Namibia in the construction and operation of the equipment.

References

- Abdo, A. A., et al. (Fermi LAT Collaboration) 2009, *Science*, **326**, 1512
- Abramowski, A., Acero, F., Aharonian, F., et al. 2012, *ApJ*, **757**, 158
- Acciari, V. A., Aliu, E., Arlen, T., et al. 2009, *Nature*, **462**, 770
- Acero, F., Aharonian, F., Akhperjanian, A. G., & H.E.S.S. Collaboration. 2009, *A&A*, **508**, 1135
- Aharonian, F. A., & Atoyan, A. M. 1996, *A&A*, **309**, 917
- Aharonian, F., Akhperjanian, A., Beilicke, M., et al. 2003, *A&A*, **403**, L1
- Aharonian, F., Akhperjanian, A. G., Bazer-Bachi, A. R., et al. 2006a, *A&A*, **457**, 899
- Aharonian, F., Akhperjanian, A. G., Bazer-Bachi, A. R., et al. 2006b, *A&A*, **449**, 223
- Aharonian, F., Akhperjanian, A. G., Bazer-Bachi, A. R., et al. 2006c, *A&A*, **460**, 743
- Aharonian, F., Akhperjanian, A. G., Anton, G., et al. 2009, *ApJ*, **695**, L40
- Albert, J., Aliu, E., Anderhub, H., et al. 2007, *ApJ*, **665**, L51
- Aleksić, J., Antonelli, L. A., Antoranz, P., et al. 2010, *ApJ*, **721**, 843
- Aleksić, J., Alvarez, E. A., Antonelli, L. A., et al. 2012, *A&A*, **539**, L2
- Arnaud, K. A. 1996, in *Astronomical Data Analysis Software and Systems V*, eds. G. H. Jacoby, & J. Barnes, *ASP Conf. Ser.*, **101**, 17
- Atoyan, A. M., & Aharonian, F. A. 1999, *MNRAS*, **302**, 253
- Bednarek, W. 2010, *MNRAS*, **406**, 689
- Belloni, T., Mendez, M., King, A. R., van der Klis, M., & van Paradijs, J. 1997, *ApJ*, **488**, L109
- Belloni, T., Klein-Wolt, M., Méndez, M., van der Klis, M., & van Paradijs, J. 2000, *A&A*, **355**, 271
- Belloni, T., Psaltis, D., & van der Klis, M. 2002, *ApJ*, **572**, 392
- Berge, D., Funk, S., & Hinton, J. 2007, *A&A*, **466**, 1219
- Bosch-Ramon, V., Romero, G. E., & Paredes, J. M. 2006, *A&A*, **447**, 263
- Böttcher, M., & Dermer, C. D. 2005, *ApJ*, **634**, L81
- Carraminana, A. 1992, *A&A*, **264**, 127
- Castro-Tirado, A. J., Brandt, S., Lund, N., et al. 1994, *ApJS*, **92**, 469
- Clark, J. S., Charles, P. A., Clarkson, W. I., & Coe, M. J. 2003, *A&A*, **400**, 655
- Coppi, P. S. 2000, *BAAS*, **32**, 1217
- Corbel, S., Dubus, G., Tomsick, J. A., et al. 2012, *MNRAS*, **421**, 2947
- CTA Consortium. 2011, *Exp. Astron.*, **32**, 193
- Dermer, C. D., & Böttcher, M. 2006, *ApJ*, **643**, 1081
- Done, C., Gierliński, M., & Kubota, A. 2007, *A&ARv*, **15**, 1
- Dubus, G. 2006, *A&A*, **451**, 9
- Dubus, G., Cerutti, B., & Henri, G. 2010, *MNRAS*, **404**, L55
- Eikenberry, S. S., Matthews, K., Morgan, E. H., Remillard, R. A., & Nelson, R. W. 1998, *ApJ*, **494**, L61
- Falcke, H., Körding, E., & Markoff, S. 2004, *A&A*, **414**, 895
- Fender, R., & Belloni, T. 2004, *ARA&A*, **42**, 317
- Fender, R. P., Pooley, G. G., Brocksopp, C., & Newell, S. J. 1997, *MNRAS*, **290**, L65
- Fender, R., Spencer, R., Tzioumis, T., et al. 1998, *ApJ*, **506**, L121
- Fender, R., Wu, K., Johnston, H., et al. 2004a, *Nature*, **427**, 222
- Fender, R. P., Belloni, T. M., & Gallo, E. 2004b, *MNRAS*, **355**, 1105
- Gallo, E., Fender, R., Kaiser, C., et al. 2005, *Nature*, **436**, 819
- Georganopoulos, M., Aharonian, F. A., & Kirk, J. G. 2002, *A&A*, **388**, L25
- Ghisellini, G., & Maraschi, L. 1989, *ApJ*, **340**, 181
- Gierliński, M., Done, C., & Page, K. 2009, *MNRAS*, **392**, 1106
- Gould, R. J., & Schröder, G. P. 1967, *Phys. Rev.*, **155**, 1404
- Greiner, J., Cuby, J. G., McCaughrean, M. J., Castro-Tirado, A. J., & Mennickent, R. E. 2001, *A&A*, **373**, L37
- Heinz, S., Burton, M., Braiding, C., et al. 2015, *ApJ*, **806**, 265
- Hjellming, R. M. 2000, *The Astronomer's Telegram*, **61**, 1
- Hjellming, R. M., Rupen, M. P., Hunstead, R. W., et al. 2000, *ApJ*, **544**, 977
- Hofverberg, P., Kankayan, R., Panter, M., et al. 2013, in *Proc. 33rd ICRC [arXiv:1307.4550]*
- Holler, M., Balzer, A., Chalmé-Calvet, R., de Naurois, M., & Zaborov, D. 2015a, *PoS(ICRC2015)980*
- Holler, M., Berge, D., van Eldik, C., et al. 2015b, *PoS(ICRC2015)847*
- Homan, J., & Belloni, T. 2005, *Ap&SS*, **300**, 107
- Iaria, R., Di Salvo, T., Burderi, L., & Robba, N. R. 2001, *ApJ*, **561**, 321
- in 't Zand, J., Heise, J., Bazzano, A., et al. 1999, *IAU Circ.*, **7119**, 1
- Johnston, H. M., Fender, R., & Wu, K. 1999, *MNRAS*, **308**, 415
- Jonker, P. G., Nelemans, G., & Bassa, C. G. 2007, *MNRAS*, **374**, 999
- Jourdain, E., Roques, J. P., Chauvin, M., & Clark, D. J. 2012, *ApJ*, **761**, 27
- Kalberla, P. M. W., Burton, W. B., Hartmann, D., et al. 2005, *A&A*, **440**, 775
- Klein-Wolt, M., Fender, R. P., Pooley, G. G., et al. 2002, *MNRAS*, **331**, 745
- Königl, A. 1981, *ApJ*, **243**, 700
- Laurent, P., Rodriguez, J., Wilms, J., et al. 2011, *Science*, **332**, 438
- Leahy, D. A., Darbro, W., Elsner, R. F., et al. 1983, *ApJ*, **266**, 160
- Lewin, W. H. G., van Paradijs, J., & van der Klis, M. 1988, *Space Sci. Rev.*, **46**, 273
- Li, T.-P., & Ma, Y.-Q. 1983, *ApJ*, **272**, 317
- Linares, M., Watts, A., Altamirano, D., et al. 2010, *ApJ*, **719**, L84
- Lindström, C., Griffin, J., Kiss, L. L., et al. 2005, *MNRAS*, **363**, 882
- MacDonald, R. K. D., Bailyn, C. D., Buxton, M., et al. 2014, *ApJ*, **784**, 2
- Maitra, D., & Bailyn, C. D. 2006, *ApJ*, **637**, 992
- Malzac, J., Lubiński, P., Zdziarski, A. A., et al. 2008, *A&A*, **492**, 527
- Margon, B. 1984, *ARA&A*, **22**, 507
- Margon, B., Lampton, M., Bowyer, S., & Cruddace, R. 1971, *ApJ*, **169**, L23
- Markoff, S., Nowak, M. A., & Wilms, J. 2005, *ApJ*, **635**, 1203
- Markwardt, C. B., Swank, J. H., & Morgan, E. H. 1999a, *IAU Circ.*, **7257**, 2
- Markwardt, C. B., Swank, J. H., & Taam, R. E. 1999b, *ApJ*, **513**, L37
- McCollough, M. L., Finger, M. H., & Woods, P. M. 1999, *IAU Circ.*, **7257**, 1
- Merloni, A., Heinz, S., & di Matteo, T. 2003, *MNRAS*, **345**, 1057
- Migliari, S., & Fender, R. P. 2006, *MNRAS*, **366**, 79
- Mirabel, I. F., & Rodríguez, L. F. 1994, *Nature*, **371**, 46
- Moskalenko, I. V. 1995, *Space Sci. Rev.*, **72**, 593
- Muno, M. P., Morgan, E. H., & Remillard, R. A. 1999, *ApJ*, **527**, 321
- Murdin, P., Jauncey, D. L., Lerche, I., et al. 1980, *A&A*, **87**, 292
- Nicholas, B., & Rowell, G. 2008, in *AIP Conf. Ser. 1085*, eds. F. A. Aharonian, W. Hofmann, & F. Rieger, 245
- Nicolson, G. D. 2007, *The Astronomer's Telegram*, **985**, 1
- Oosterbroek, T., van der Klis, M., Kuulkers, E., van Paradijs, J., & Lewin, W. H. G. 1995, *A&A*, **297**, 141
- Orosz, J. A., Kuulkers, E., van der Klis, M., et al. 2001, *ApJ*, **555**, 489
- Pakull, M., Soria, R., & Motch, C. 2010, *Nature*, **466**, 209
- Parkinson, P. M. S., Tournear, D. M., Bloom, E. D., et al. 2003, *ApJ*, **595**, 333
- Parsons, R. D., Gajdus, M., & Murach, T. 2015, *PoS(ICRC2015)826*
- Pooley, G. 2006, in *VI Microquasar Workshop: Microquasars and Beyond*, 9
- Protheroe, R. J., & Stanev, T. 1987, *ApJ*, **322**, 838
- Reid, M. J., McClintock, J. E., Steiner, J. F., et al. 2014, *ApJ*, **796**, 2
- Revnivtsev, M., Gilfanov, M., & Churazov, E. 2000, *A&A*, **363**, 1013
- Revnivtsev, M., Gilfanov, M., Churazov, E., & Sunyaev, R. 2002, *A&A*, **391**, 1013
- Revnivtsev, M., Khamitov, I., Burenin, R., et al. 2004, *The Astronomer's Telegram*, **297**, 1
- Rolke, W. A., López, A. M., & Conrad, J. 2005, *Nucl. Instrum. Meth. Phys. Res. A*, **551**, 493
- Romero, G. E., Torres, D. F., Kaufman Bernadó, M. M., & Mirabel, I. F. 2003, *A&A*, **410**, L1
- Romero, G. E., Christiansen, H. R., & Orellana, M. 2005, *ApJ*, **632**, 1093
- Romero, G. E., Vieyro, F. L., & Chaty, S. 2014, *A&A*, **562**, L7
- Rupen, M. P., Dhawan, V., & Mioduszewski, A. J. 2002, *IAU Circ.*, **7928**, 2
- Rupen, M. P., Mioduszewski, A. J., & Dhawan, V. 2003, *The Astronomer's Telegram*, **172**, 1

- Rupen, M. P., Dhawan, V., & Mioduszewski, A. J. 2004a, *The Astronomer's Telegram*, 303, 1
- Rupen, M. P., Mioduszewski, A. J., & Dhawan, V. 2004b, *The Astronomer's Telegram*, 296, 1
- Russell, D. M., Fender, R. P., Hynes, R. I., et al. 2006, *MNRAS*, 371, 1334
- Saito, T. Y., Zanin, R., Bordas, P., et al. 2009, in 31st ICRC (Łódź) [[arXiv:0907.1017](https://arxiv.org/abs/0907.1017)]
- Schulz, N. S., Brandt, W. N., Galloway, D. K., Chakrabarty, D., & Heinz, S. 2006, in *The X-ray Universe 2005*, ed. A. Wilson, *ESA SP*, 604, 201
- Schulz, N. S., Kallman, T. E., Galloway, D. K., & Brandt, W. N. 2008, *ApJ*, 672, 1091
- Senkbeil, C., & Sault, B. 2004, *The Astronomer's Telegram*, 302, 1
- Shirey, R. E., Bradt, H. V., & Levine, A. M. 1999a, *ApJ*, 517, 472
- Shirey, R. E., Levine, A. M., & Bradt, H. V. 1999b, *ApJ*, 524, 1048
- Soleri, P., Belloni, T., & Casella, P. 2006, in VI Microquasar Workshop: Microquasars and Beyond, 43
- Soleri, P., Tudose, V., Fender, R. P., & van der Klis, M. 2007, in *Proc. Bursts, Pulses and Flickering: wide-field monitoring of the dynamic radio sky*; 12–15 June, Kerastari, Tripolis, Greece, 37
- Soria, R., Pakull, M., Broderick, J., & Corbel, S. 2010, *MNRAS*, 409, 541
- Steghs, D., McClintock, J. E., Parsons, S. G., et al. 2013, *ApJ*, 768, 185
- Stubbings, R., & Pearce, A. 1999, *IAU Circ.*, 7253, 1
- Swank, J. 2004, *The Astronomer's Telegram*, 295, 1
- Tavani, M., Bulgarelli, A., Piano, G., et al. 2009, *Nature*, 462, 620
- Tennant, A. F., Fabian, A. C., & Shafer, R. A. 1986a, *MNRAS*, 221, 27P
- Tennant, A. F., Fabian, A. C., & Shafer, R. A. 1986b, *MNRAS*, 219, 871
- Trudolyubov, S. P. 2001, *ApJ*, 558, 276
- Tudose, V., Fender, R. P., Kaiser, C. R., et al. 2006, *MNRAS*, 372, 417
- Tudose, V., Fender, R. P., Tzioumis, A. K., Spencer, R. E., & van der Klis, M. 2008, *MNRAS*, 390, 447
- Uemura, M., Mennickent, R., Stubbings, R., et al. 2005, *Information Bulletin on Variable Stars*, 5626, 1
- Vadawale, S. V., Rao, A. R., & Chakrabarti, S. K. 2001, *A&A*, 372, 793
- van Oers, P., & Markoff, S. 2010, in *Jets at all Scales*, *Proc. IAU*, 6, 294
- van Paradijs, J., & McClintock, J. E. 1994, *A&A*, 290, 133
- Wijnands, R., & van der Klis, M. 2000, *ApJ*, 528, L93
- Zdziarski, A. A. 2014, *MNRAS*, 444, 1113
- Zdziarski, A. A., Grove, J. E., Poutanen, J., Rao, A. R., & Vadawale, S. V. 2001, *ApJ*, 554, L45
- Zdziarski, A. A., Lubinski, P., Gilfanov, M., & Revnivtsev, M. 2003, *MNRAS*, 342, 355
- Zdziarski, A. A., Sikora, M., Dubus, G., et al. 2012, *MNRAS*, 421, 2956
- Zhang, W., Giles, A. B., Jahoda, K., et al. 1993, in *SPIE Conf. Ser.* 2006, eds. O. H. Siegmund, 324
- Ziolkowski, J. 2015, *ArXiv e-prints* [[arXiv:1509.02819](https://arxiv.org/abs/1509.02819)]
- ¹ Centre for Space Research, North-West University, Potchefstroom 2520, South Africa
- ² Universität Hamburg, Institut für Experimentalphysik, Luruper Chaussee 149, 22761 Hamburg, Germany
- ³ Max-Planck-Institut für Kernphysik, PO Box 103980, 69029 Heidelberg, Germany
- ⁴ Dublin Institute for Advanced Studies, 31 Fitzwilliam Place, Dublin 2, Ireland
- ⁵ National Academy of Sciences of the Republic of Armenia, Marshall Baghramian Avenue, 24, 0019 Yerevan, Republic of Armenia
- ⁶ Yerevan Physics Institute, 2 Alikhanian Brothers St., 375036 Yerevan, Armenia
- ⁷ Institut für Physik, Humboldt-Universität zu Berlin, Newtonstr. 15, 12489 Berlin, Germany
- ⁸ University of Namibia, Department of Physics, Private Bag 13301, Windhoek, Namibia
- ⁹ GRAPPA, Anton Pannekoek Institute for Astronomy, University of Amsterdam, Science Park 904, 1098 XH Amsterdam, The Netherlands
- ¹⁰ Department of Physics and Electrical Engineering, Linnaeus University, 351 95 Växjö, Sweden
- ¹¹ Institut für Theoretische Physik, Lehrstuhl IV: Weltraum und Astrophysik, Ruhr-Universität Bochum, 44780 Bochum, Germany
- ¹² GRAPPA, Anton Pannekoek Institute for Astronomy and Institute of High-Energy Physics, University of Amsterdam, Science Park 904, 1098 XH Amsterdam, The Netherlands
- ¹³ Institut für Astro- und Teilchenphysik, Leopold-Franzens-Universität Innsbruck, 6020 Innsbruck, Austria
- ¹⁴ School of Chemistry & Physics, University of Adelaide, 5005 Adelaide, Australia
- ¹⁵ LUTH, Observatoire de Paris, PSL Research University, CNRS, Université Paris Diderot, 5 Place Jules Janssen, 92190 Meudon, France
- ¹⁶ Sorbonne Universités, UPMC Université Paris 06, Université Paris Diderot, Sorbonne Paris Cité, CNRS, Laboratoire de Physique Nucléaire et de Hautes Energies (LPNHE), 4 place Jussieu, 75252 Paris Cedex 5, France
- ¹⁷ Laboratoire Univers et Particules de Montpellier, Université Montpellier, CNRS/IN2P3, CC 72, Place Eugène Bataillon, 34095 Montpellier Cedex 5, France
- ¹⁸ DSM/Irfu, CEA Saclay, 91191 Gif-Sur-Yvette Cedex, France
- ¹⁹ Astronomical Observatory, The University of Warsaw, Al. Ujazdowskie 4, 00-478 Warsaw, Poland
- ²⁰ Aix Marseille Université, CNRS/IN2P3, CPPM UMR 7346, 13288 Marseille, France
- ²¹ Instytut Fizyki Jądrowej PAN, ul. Radzikowskiego 152, 31-342 Kraków, Poland
- ²² Funded by EU FP7 Marie Curie, grant agreement No. PIEF-GA-2012-332350.
- ²³ School of Physics, University of the Witwatersrand, 1 Jan Smuts Avenue, Braamfontein, 2050 Johannesburg, South Africa
- ²⁴ Laboratoire d'Annecy-le-Vieux de Physique des Particules, Université Savoie Mont-Blanc, CNRS/IN2P3, 74941 Annecy-le-Vieux, France
- ²⁵ Landessternwarte, Universität Heidelberg, Königstuhl, 69117 Heidelberg, Germany
- ²⁶ Université Bordeaux, CNRS/IN2P3, Centre d'Études Nucléaires de Bordeaux Gradignan, 33175 Gradignan, France
- ²⁷ Oskar Klein Centre, Department of Physics, Stockholm University, Albanova University Center, 10691 Stockholm, Sweden
- ²⁸ Wallenberg Academy Fellow
- ²⁹ Institut für Astronomie und Astrophysik, Universität Tübingen, Sand 1, 72076 Tübingen, Germany
- ³⁰ Laboratoire Leprince-Ringuet, École Polytechnique, CNRS/IN2P3, 91128 Palaiseau, France
- ³¹ APC, AstroParticule et Cosmologie, Université Paris Diderot, CNRS/IN2P3, CEA/Irfu, Observatoire de Paris, Sorbonne Paris Cité, 10, rue Alice Domon et Léonie Duquet, 75205 Paris Cedex 13, France
- ³² Univ. Grenoble Alpes, IPAG; CNRS, IPAG, 38000 Grenoble, France
- ³³ Department of Physics and Astronomy, The University of Leicester, University Road, Leicester, LE1 7RH, UK
- ³⁴ Nicolaus Copernicus Astronomical Center, ul. Bartycka 18, 00-716 Warsaw, Poland
- ³⁵ Institut für Physik und Astronomie, Universität Potsdam, Karl-Liebknecht-Strasse 24/25, 14476 Potsdam, Germany
- ³⁶ Universität Erlangen-Nürnberg, Physikalisches Institut, Erwin-Rommel-Str. 1, 91058 Erlangen, Germany
- ³⁷ DESY, 15738 Zeuthen, Germany
- ³⁸ Obserwatorium Astronomiczne, Uniwersytet Jagielloński, ul. Orla 171, 30-244 Kraków, Poland
- ³⁹ Centre for Astronomy, Faculty of Physics, Astronomy and Informatics, Nicolaus Copernicus University, Grudziadzka 5, 87-100 Torun, Poland
- ⁴⁰ Department of Physics, University of the Free State, PO Box 339, 9300 Bloemfontein, South Africa
- ⁴¹ Heisenberg Fellow (DFG), ITA Universität Heidelberg, 069120 Heidelberg, Germany
- ⁴² GRAPPA, Institute of High-Energy Physics, University of Amsterdam, Science Park 904, 1098 XH Amsterdam, The Netherlands
- ⁴³ University of Durham, Department of Physics, South Road, Durham DH1 3LE, UK
- ⁴⁴ Iowa State University, Ames, IA 50011, USA

Appendix A: Modelling and determination of the system X-ray states

A.1. GRS 1915+105

Figure A.1 shows the HID derived from the entire archival RXTE PCA data set for GRS 1915+105. Hardness is defined as the ratio of fluxes measured in the 2–9 keV and 9–20 keV bands, while intensity is defined as the sum of the band-limited fluxes in units of counts per second. The background has been subtracted and the light curves are sampled in 16 s intervals. These definitions are used consistently for the three HIDs presented in this paper. In the case of GRS 1915+105, the H.E.S.S. observation took place in a low-hard state (LHS; symbols for MJD 53 123–8 in top-left sector of Fig. A.1), in which compact jets are expected to be present and characterised by a potentially radio-loud χ X-ray variability class (belonging to state C following the classification of Belloni et al. 2000). For comparison, the orange points in Fig. A.1 correspond with data obtained on 17 December 1997. These data were studied by Soleri et al. (2006) who associated them with a hard-intermediate state (HIMS) to soft-intermediate state (SIMS) transition.

The power density spectra shown in Fig. A.3 show the presence of low frequency QPOs: following the approach of Belloni et al. (2002), a Lorentzian decomposition of the observed power spectra was performed using two broad continuum components and several narrower QPO peaks. Crucially, the characteristic frequency ($\nu_{\max} = \sqrt{\nu_0^2 + \Delta^2}$, see Belloni et al. 2002) of the higher frequency continuum component never exceeds ~ 4 Hz during our observations. This is far below the characteristic cut-off frequencies associated with previous observations of the radio-quiet χ state (e.g. Trudolyubov 2001). Radio-quiet observations (Belloni et al. 1997; Trudolyubov 2001) exhibit significant band-limited white noise extending to high frequencies $f \sim 60$ –80 Hz, while in radio-loud case such noise is either absent or exhibits an exponential cut-off at ~ 15 Hz (Trudolyubov 2001). Consequently, the absence of band limited noise at high frequencies is consistent with a radio-loud state C.

Figure A.4 illustrates the spectral analysis performed for each GRS 1915+105 RXTE observation. The simple model described by Vadawale et al. (2001) has been adopted: a continuum model comprising a disk black-body (DiskBB⁴) component, a hybrid thermal and a non-thermal Comptonisation component (COMPST), and a separate power law (POWERLAW) to model the high-energy emission. Interstellar absorption was modelled using the WABS model in XSPEC with the equivalent hydrogen column fixed to a value of $6 \times 10^{22} \text{ cm}^{-2}$ (Belloni et al. 1997; Markwardt et al. 1999b; Munro et al. 1999). A constant multiplicative factor was introduced to account for the normalisation of HEXTE relative to the PCA. The addition of a GAUSSIAN component with centroid energy E_{Line} fixed at 6.4 keV was found to significantly improve the resultant model fit.

As demonstrated by the reduced χ^2 values listed in Table A.1, the fitted model provides an adequate description of the RXTE data, and the derived model parameters correspond closely to those obtained by Vadawale et al. (2001) during earlier episodes of radio-loud χ -state behaviour, supporting the attribution of this state to the epochs of H.E.S.S. observation. However, insufficient event statistics prevent the inference of robust conclusions regarding the origin of the X-rays that were

observed in this study. A more sophisticated and physically well-motivated model, describing an X-ray corona (EQPAIR from Coppi 2000) gives a similar goodness-of-fit, after accounting for a larger parameter count. Physically, the power-law component could result from Comptonisation by energetic electrons in a corona or could be generated by synchrotron radiation at the base of a jet. The former scenario is discussed in a number of papers (e.g. Zdziarski et al. 2003), while the latter was studied by van Oers & Markoff 2010 in the context of a similar plateau state of GRS1915+105. They applied a leptonic jet model (Markoff et al. 2005) to X-ray, IR, and radio data. Although their model provided statistically convincing broadband fits, this was only achievable when adopting extreme parameter values. The power law with $\Gamma \approx 2.7$ that was derived in this study (Table A.1) cannot be extrapolated down to UV band without generating an inconsistency in subsequently inferred bolometric luminosity. It should be interpreted as a phenomenological approximation of a high-energy tail, which itself might only be partially accounted for by SSC radiation.

A similar plateau state of GRS 1915+105 (October 1997) was studied by Klein-Wolt et al. (2002), who attributed the observed radio emission to quasi-continuous ejecta forming the compact jet.

In Fig. A.2, the 15 GHz radio surface brightness and the X-ray hardness and intensity corresponding with the epochs of H.E.S.S. observation are illustrated in a broader historical context (Pooley 2006)⁵. The H.E.S.S. observations started approximately one week before the end of a long radio-loud plateau and were triggered by a transient dip in radio flux whilst the plateau end was not yet reached. The plateau ended about two days after the last H.E.S.S. observation, followed by a radio and X-ray flare ten days later.

In summary, GRS 1915+105 remained in a radio-loud χ state with steady, mildly relativistic jets at the time of H.E.S.S. observations without clear signs of a state transition.

A.2. Cir X-1

The HID for Cir X-1 is shown in Fig. A.5. An extensive study, examining ten days out of the 16.55 orbital period was performed by Shirey et al. (1999a) in 1997; the corresponding RXTE data are indicated with orange symbols in Fig. A.5. The study focused on the toroidally distributed data plotted in the lower right part of the HID. Shirey et al. (1999a), studied the spectral and temporal X-ray evolution of Cir X-1 along three distinct branches (horizontal, normal, flaring) in the HID. This evolution occurred during a half-day period, approximately one day after periastron and was repeated few days later. Such behaviour is typical of a “Z source”.

In Shirey et al. (1999a), the periastron passage corresponds to the data at low flux and hardness (dipping episode, lower-left part of the cycle). Data contemporaneous to the H.E.S.S. observations (MJD 53 174–6) are indicated by symbols and exhibit low X-ray intensity and hardness values. They span two days starting 19 h after the periastron, which coincides with the orbital range explored by Shirey et al. (1999a), but in a much fainter X-ray luminosity context.

Inspection of the 3–20 keV PCA spectra shown in Fig. A.6 reveals that the observed flux variability is accompanied by marked variations in spectral shape. For the third observation, individual spectra were extracted from the four regions (A to D) shown in Fig. 2 (bottom-right panel), segregated on

⁴ <http://heasarc.gsfc.nasa.gov/xanadu/xspec/manual/XspecModels.html>

⁵ <http://www.mrao.cam.ac.uk/~guy/>

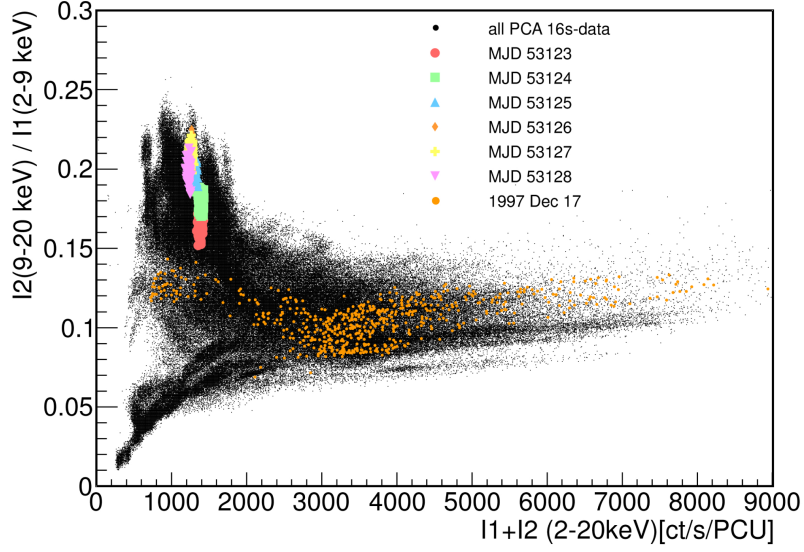


Fig. A.1. Hardness-intensity diagram of GRS 1915+105 derived from the entire archival RXTE PCA data set. The temporal sampling is 16 s. Hardness is defined as the ratio of fluxes measured in the 2–9 keV and 9–20 keV bands, while intensity is defined as the sum of the band-limited fluxes in units of counts per second. Data corresponding to H.E.S.S. observations are highlighted using symbols to identify the individual days of observation. For comparison, the data corresponding to noteworthy events such as known flares observed by RXTE are also plotted (see e.g. Soleri et al. 2006).

Table A.1. XSPEC model components and best-fit parameters for GRS 1915+105.

Component	Parameter	OBS 1	OBS 2	OBS 3
DISKBB	T_{in} [keV]	$1.695^{+0.42}_{-0.59}$	$1.137^{+0.6}_{-0.3}$	$1.698^{+0.63}_{-0.77}$
DISKBB	Norm	31.1^{+120}_{-17}	81.3^{+360}_{-78}	20.9^{+200}_{-16}
COMPST	kT_e [keV]	$4.195^{+2}_{-0.54}$	$5.057^{+1.1}_{-0.81}$	$4.460^{+0.54}_{-0.7}$
COMPST	τ	$13.145^{+6.9}_{-6.9}$	$7.801^{+3.7}_{-1.8}$	$10.959^{+4.7}_{-4.7}$
POWERLAW	Γ_{phot}	$2.714^{+0.058}_{-0.86}$	$2.668^{+0.12}_{-0.15}$	$2.644^{+0.077}_{-0.82}$
GAUSSIAN	E_{Line} [keV]	6.4*		
GAUSSIAN	σ [keV]	$0.776^{+0.24}_{-0.29}$	$0.891^{+0.15}_{-0.17}$	$0.730^{+0.22}_{-0.24}$
GAUSSIAN	W [eV]	66.44	87.76	70.44
χ^2_{ν} (NDF)		0.82 (77)	0.96 (78)	0.99 (80)
Component	Parameter	OBS 4	OBS 5	OBS 6
DISKBB	T_{in} [keV]	$1.350^{+0.63}_{-0.42}$	$1.415^{+0.63}_{-0.51}$	$1.713^{+0.51}_{-0.55}$
DISKBB	Norm	30.8^{+140}_{-28}	23.3^{+110}_{-23}	15.4^{+28}_{-13}
COMPST	kT_e [keV]	$5.130^{+0.77}_{-0.69}$	$4.888^{+0.73}_{-0.69}$	$5.118^{+0.83}_{-0.82}$
COMPST	τ	$8.516^{+4.4}_{-1.6}$	$8.870^{+6.1}_{-1.7}$	$9.028^{+14}_{-1.9}$
POWERLAW	Γ_{phot}	$2.503^{+0.12}_{-0.38}$	$2.521^{+0.026}_{-0.27}$	$2.441^{+0.13}_{-0.37}$
GAUSSIAN	E_{Line} [keV]	6.4*		
GAUSSIAN	σ [keV]	$0.894^{+0.16}_{-0.19}$	$0.902^{+0.16}_{-0.18}$	$0.928^{+0.19}_{-0.24}$
GAUSSIAN	W [eV]	91.15	91.78	86.93
χ^2_{ν} (NDF)		1.12 (80)	1.19 (83)	0.82 (80)

Notes. As discussed in the text, an additional W_{ABS} component (with equivalent hydrogen column density fixed to $N_{\text{H}} = 6 \times 10^{22} \text{ cm}^{-2}$) was used to model the effects of interstellar absorption. The parameter errors correspond to a $\Delta\chi^2$ of 2.71. Frozen parameters are indicated by *.

the basis of average 2–20 keV count rates. Fitting of the spectral data from the third observation employed a similar approach to that of Shirey et al. (1999b) with the unabsorbed continuum modelled using a disk black-body component (DISKBB in XSPEC) at low energies in combination with a single temperature black body (BBODY) that dominates above ~ 15 keV.

Previous observations of Cir X-1 during periastron dips (e.g. Shirey et al. 1999b; Schulz et al. 2008) reveal the evidence of strong, complex, and variable intrinsic X-ray absorption. Consequently, diagnosis of the system behaviour during the third RXTE observation is critically dependent upon whether the observed variability represents a genuine change in the underlying continuum emission or is simply an artefact of varying ab-

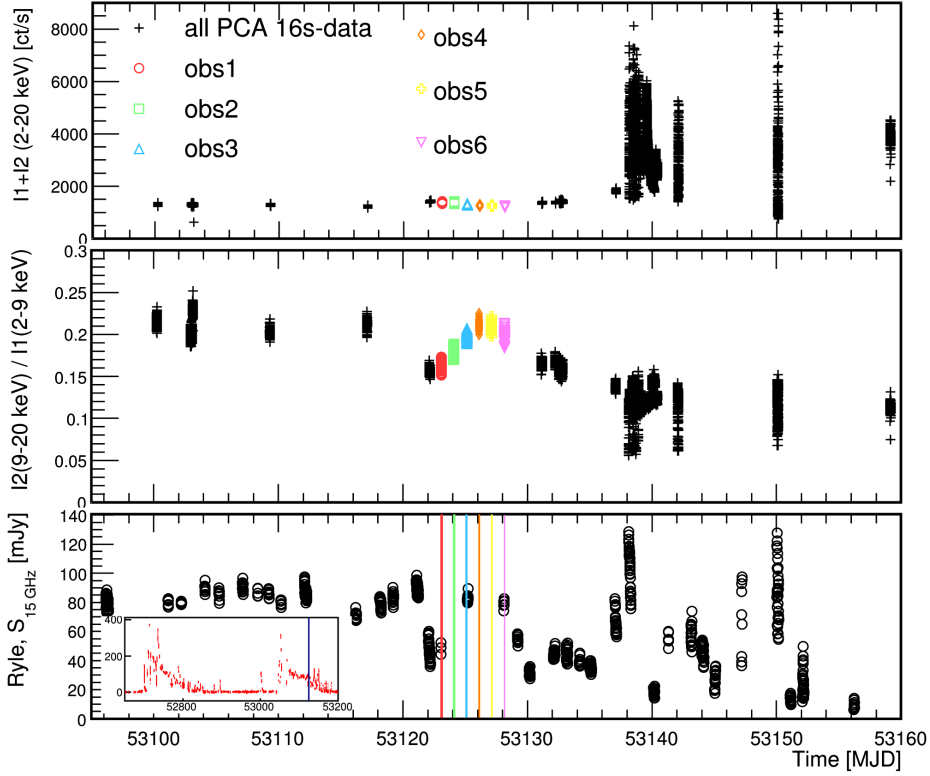


Fig. A.2. Evolution of GRS 1915+105 before and after H.E.S.S. observations. RXTE PCA intensity and hardness (defined in the caption of Fig. A.1) are plotted on the *top* and *middle* panels, respectively. The *bottom* panel presents contemporaneous 15 GHz radio data obtained using the Ryle Telescope (Pooley 2006). Long-term monitoring data in the 15 GHz radio band are illustrated in the *inset*. Coloured markers and lines indicate the H.E.S.S. observation epochs.

Table A.2. Spectral parameters for Cir X-1 during OBS 3 corresponding to the orbital phase interval $0.1718 \leq \phi \leq 0.1725$ (according to the ephemeris of Nicolson 2007).

Component	Parameter	OBS 3A	OBS 3B	OBS 3C	OBS 3D
DISKBB	T_{in} [keV]	$1.059^{+0.03}_{-0.04}$	Joint fit		
	Norm	$(1.914^{+0.63}_{-0.44}) \times 10^2$	Joint fit		
BBODY	kT [keV]	$2.954^{+0.67}_{-0.47}$	Joint fit		
	Norm	$(1.126^{+0.24}_{-0.18}) \times 10^{-3}$	$(9.373^{+2.09}_{-1.70}) \times 10^{-4}$	$(7.646^{+2.01}_{-1.62}) \times 10^{-4}$	$(4.992^{+2.61}_{-2.44}) \times 10^{-4}$
PCFABS	N_{H} [$\times 10^{22}$]	$(2.303^{+0.33}_{-0.34}) \times 10^1$	$(2.880^{+0.32}_{-0.32}) \times 10^1$	$(4.606^{+0.29}_{-0.29}) \times 10^1$	$(7.998^{+0.51}_{-0.48}) \times 10^1$
	CvrFract	$(8.630^{+0.22}_{-0.20}) \times 10^{-1}$	$(8.411^{+0.19}_{-0.20}) \times 10^{-1}$	$(8.726^{+0.15}_{-0.16}) \times 10^{-1}$	$(8.852^{+0.14}_{-0.15}) \times 10^{-1}$
χ^2_{ν} (NDF)		1.27 (145)	Joint fit		
Model flux	[$\text{erg cm}^{-2} \text{s}^{-1}$]	6.121×10^{-10}	5.512×10^{-10}	3.822×10^{-10}	2.515×10^{-10}

Notes. XSPEC model components, best-fit parameters, and 3–20 keV model fluxes are shown for the four separate sub-intervals illustrated in Fig. 2 in order of decreasing model flux. As discussed in the text, an additional W_{ABS} component (with equivalent hydrogen column density fixed to $N_{\text{H}} = 1.59 \times 10^{22} \text{ cm}^{-2}$) was used to model the effects of interstellar absorption. Jointly fitted parameters assume the values quoted for OBS 3A. The parameter errors correspond to a $\Delta\chi^2$ of 2.71.

sorption. Accordingly, two components are used to separately simulate intrinsic and extrinsic X-ray absorption characteristics. The bipartite intrinsic absorption is treated using a partial covering model (PCFABS), while a simple photoelectric model (W_{ABS}) simulates the absorbing effect of the interstellar medium. Adopting a weighted average of the neutral hydrogen data of Kalberla et al. (2005) calculated using the `nH ftool`, a fixed effective hydrogen column with $N_{\text{H}} = 1.59 \times 10^{22} \text{ cm}^{-2}$ was assumed for the W_{ABS} component. This assumption is consistent with an

estimate of the surrounding interstellar medium density used by Tudose et al. (2006) to model the evolution of the radio nebula of Cir X-1.

In order to constrain the origin of the observed spectral variability, a joint fit was performed using the complete best-fitting model. Initially, the continuum and extrinsic absorption components (DISKBB, BBODY, W_{ABS}) were constrained to be equal for all individual spectra, while the component related to intrinsic absorption (PCFABS) was allowed to vary

Table A.3. XSPEC model components, best-fit parameters, and 3–20 keV model fluxes for Cir X-1 during OBS 1 and OBS 2 corresponding to the orbital phase intervals $0.0486 \leq \phi \leq 0.0498$ and $0.1104 \leq \phi \leq 0.1112$, respectively (according to the ephemeris of [Nicolson 2007](#)).

Component	Parameter	OBS 1 ($0.0486 \leq \phi \leq 0.0498$)	OBS 2 ($0.1104 \leq \phi \leq 0.1112$)
DISKBB	T_{in} [keV]	$1.355^{+0.18}_{-0.08}$	1.059*
	Norm	$(3.798^{+3.42}_{-3.64}) \times 10^1$	$(1.914) \times 10^{12}$ *
BBODY	kT [keV]	–	$2.465^{+0.50}_{-0.39}$
	Norm	–	$(7.577^{+1.90}_{-1.22}) \times 10^{-4}$
PCFABS	N_{H} [$\times 10^{22}$]	$(1.353^{+0.44}_{-0.22}) \times 10^2$	$(9.545^{+0.25}_{-0.22}) \times 10^1$
	CvrFract	$(8.292^{+0.87}_{-2.01}) \times 10^{-1}$	$(9.191^{+0.01}_{-0.01}) \times 10^{-1}$
GAUSSIAN	E_{Line} [keV]	$6.696^{+0.09}_{-0.08}$	–
	σ [keV]	0.1^{\dagger}	–
	Norm	$(1.435^{+0.36}_{-0.33}) \times 10^{-3}$	–
χ^2_{ν} (NDF)		1.07 (34)	1.22 (36)
Model flux	[$\text{erg cm}^{-2} \text{s}^{-1}$]	2.722×10^{-10}	1.912×10^{-10}

Notes. As discussed in the text, an additional WABS component (with equivalent hydrogen column density fixed to $N_{\text{H}} = 1.59 \times 10^{22} \text{ cm}^{-2}$) was used to model the effects of interstellar absorption. Parameters marked by * are fixed to the best-fitting values from the third observation (see Table A.2). The value of the GAUSSIAN σ parameter (marked by a † symbol) was also fixed. The parameter errors correspond to a $\Delta\chi^2$ of 2.71.

independently. Although this model provides a reasonable fit to the observational data ($\chi^2_{\nu} = 1.38$), allowing the normalisation of the BBODY component to vary between observations improves the fit quality somewhat, yielding $\chi^2_{\nu} = 1.27$. The parameters that result from fitting this more relaxed model are listed in Table A.2. A statistical comparison of the alternative model fits using the F test yields a $\sim 1\%$ probability that the observed improvement in fit quality would be obtained even if the more restrictive model was correct. This marginal evidence for variation of the BBODY component normalisation might indicate rapid fluctuations of the X-ray continuum above ~ 10 keV. However, the available data cannot exclude an alternative scenario in which apparent changes in the fitted BBODY parameters arise purely from imperfect modelling of substantial variations in the intrinsic X-ray absorption with no requirement for genuine evolution of the underlying continuum.

Table A.3 lists the parameters of the spectral fits obtained from the first and second observations. A similar continuum model to that obtained from the third observation also provides a good fit ($\chi^2_{\nu} = 1.22$) to the spectrum obtained during the second observation. In contrast, the spectrum obtained during the first

observation is more appropriately described by a single, heavily absorbed disk black-body component with large correlated residuals around ~ 6.5 keV statistically favouring the addition of a GAUSSIAN line component. This continuum variability is consistent with the results of [Shirey et al. \(1999a\)](#) who found that significant variation of the continuum parameters could occur on timescales of a few hours.

Overall, the RXTE data reinforce the accepted paradigm of enhanced mass transfer during the periastron passage of the compact primary with the strong and variable intrinsic absorption attributed to obscuration by a turbulent accretion flow (see e.g. [Oosterbroek et al. 1995](#); [Murdin et al. 1980](#); [Iaria et al. 2001](#)). A marked disparity between best-fitting model components and parameters of the first and second observations implies a dramatic evolution of the local radiative environment. A $\sim 30\%$ decrease in continuum luminosity accompanied by a similar reduction of the intrinsic absorption column suggests a significant decrease in the mass transfer rate. Subsequent fluctuation in the inferred magnitude of the absorption column during the third observation is indicative of dispersion or reorganisation of the recently accreted material.

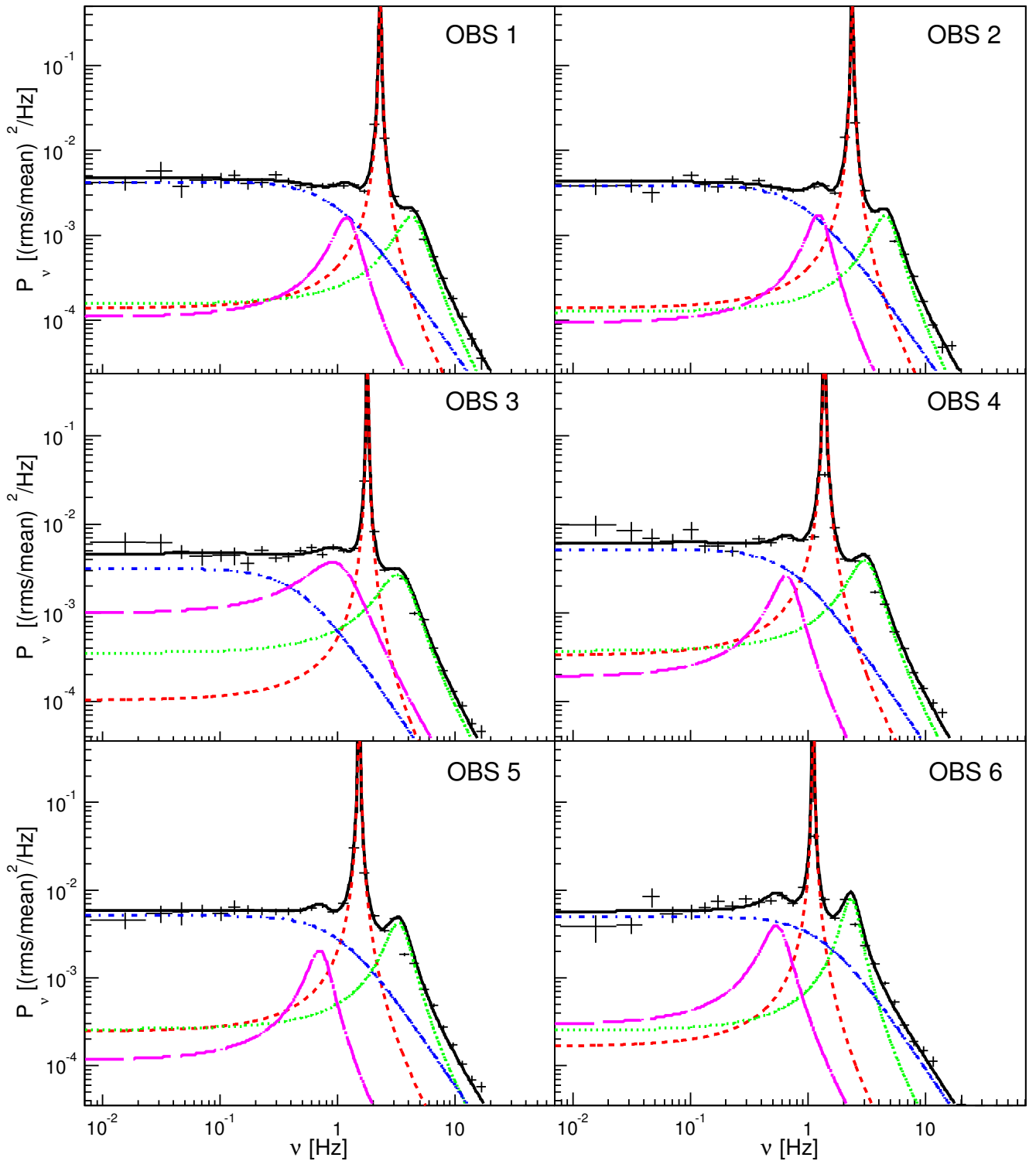


Fig. A.3. X-ray power density spectra (PDS) corresponding to the six RXTE observations of GRS 1915+105. The PDS were fitted using a superposition of Lorentzian functions comprising two broad continuum components (blue dot-dashed and green dotted curves) and several narrow QPO peaks (remaining curves). For all six observations, the derived properties of higher frequency continuum component are consistent with the radio-loud χ state.

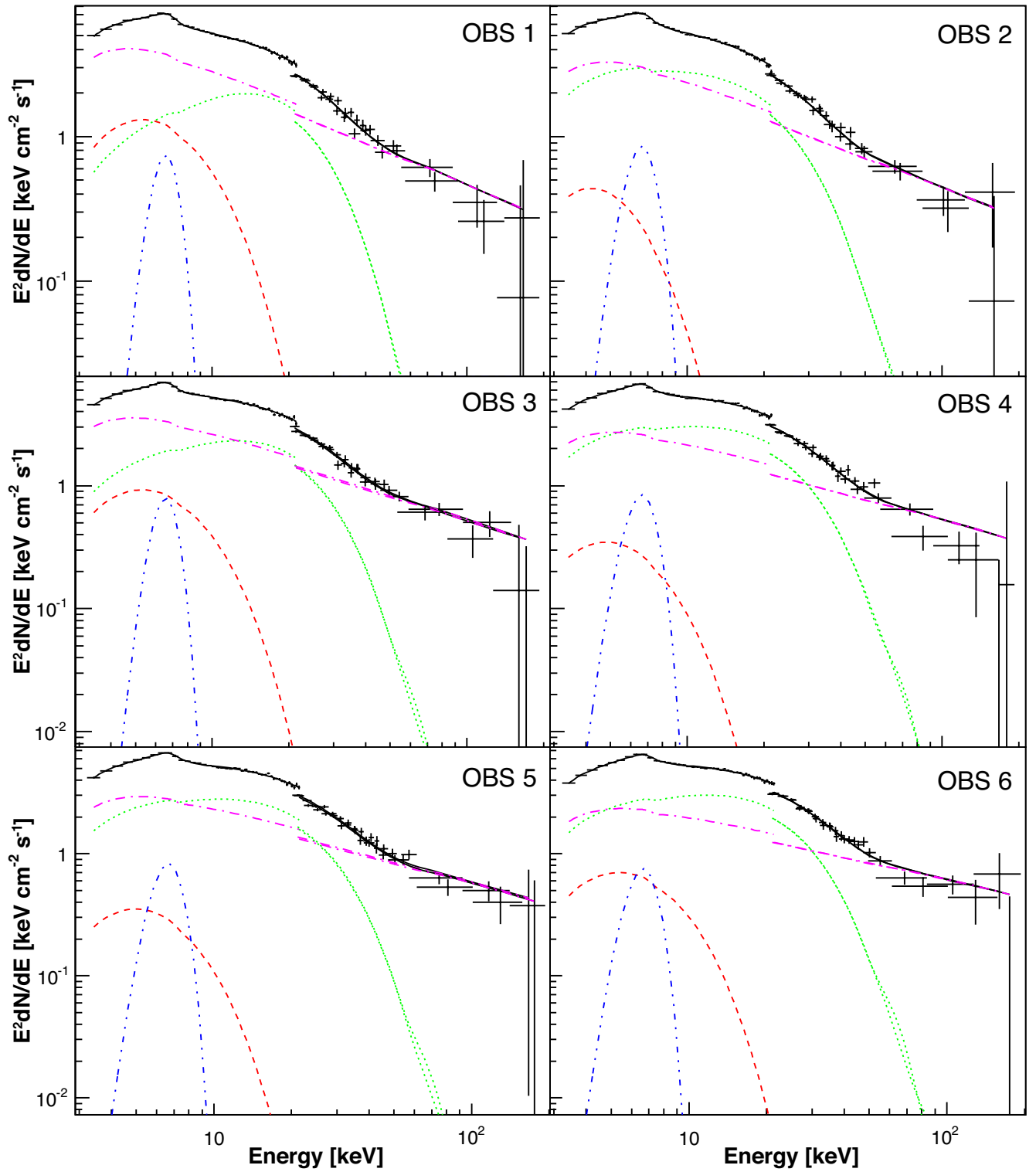


Fig. A.4. Unfolded RXTE 3–200 keV X-ray spectra of GRS 1915+105 showing the individual XSPEC model components: DiskBB (red dashes), COMPST (green dots), POWERLAW (magenta dot-dashed), GAUSSIAN (blue double-dot-dashed), and the total spectrum (black).

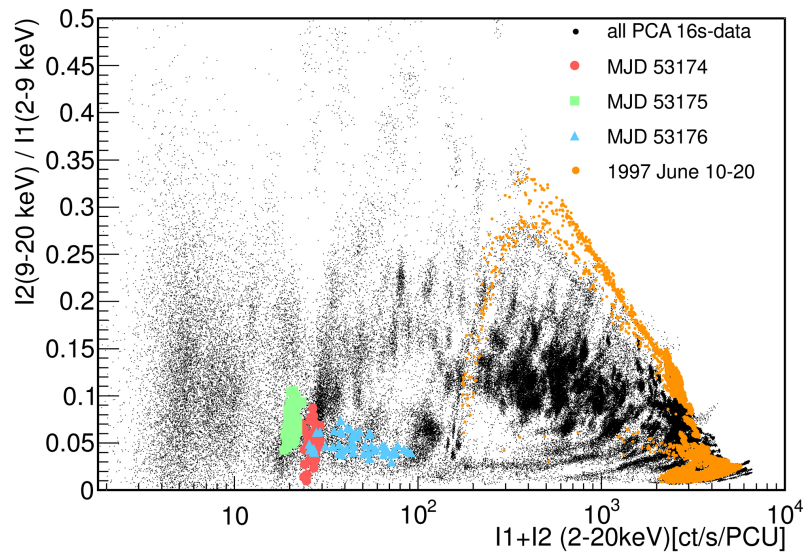


Fig. A.5. Hardness-intensity diagram derived from the entire archival RXTE PCA data set for Circinus X-1. Intensity and hardness are defined in the caption of Fig. A.1. Coloured markers indicate data that correspond with the H.E.S.S. observation epochs and historically noteworthy episodes of flaring activity (e.g. Shirey et al. 1999a).

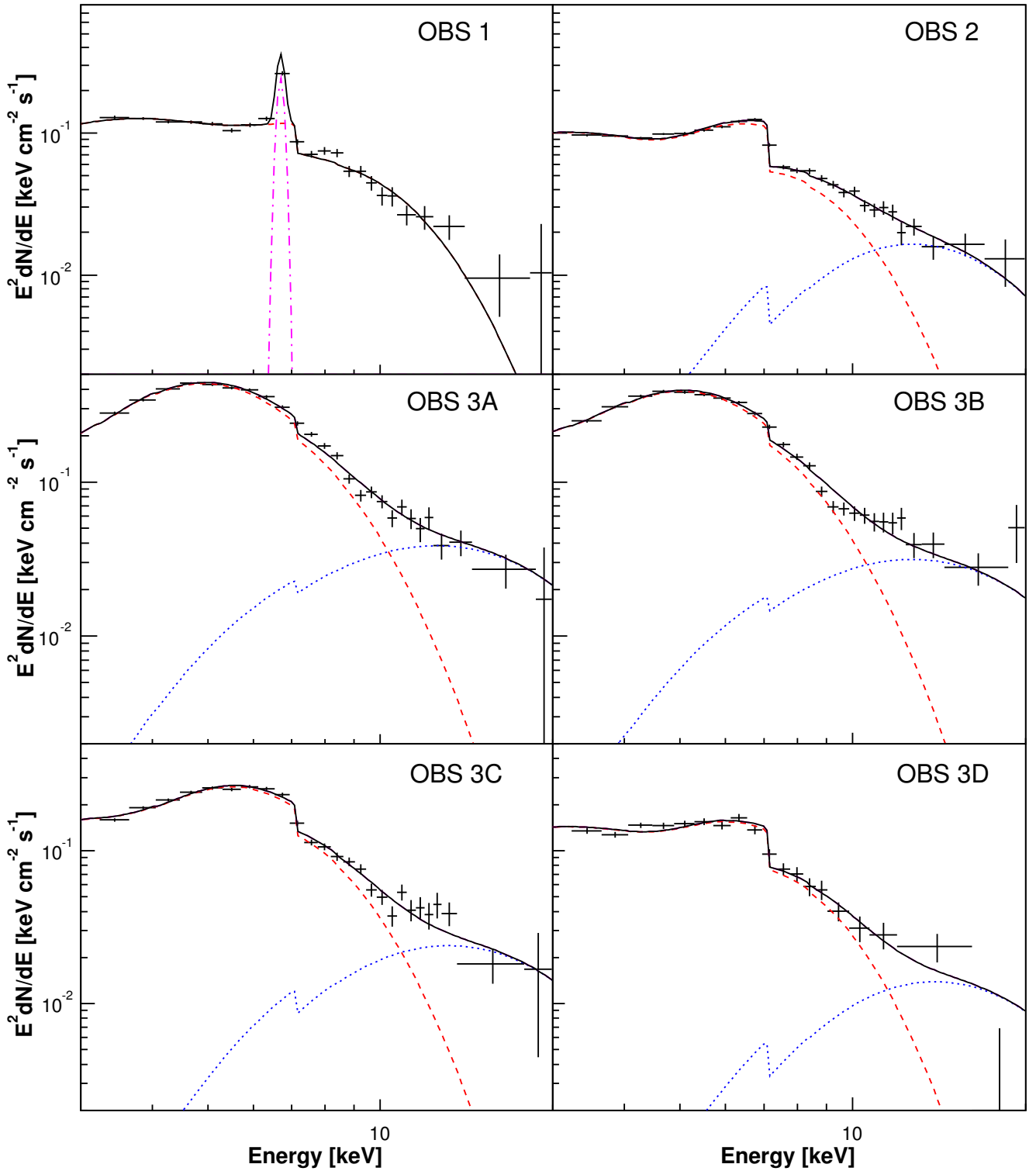


Fig. A.6. Unfolded 3–20 keV RXTE X-ray spectra of Cir X-1 for the first and second observations (*top two panels*), and the four sub-intervals of the third observation (*bottom four panels*). The solid black curves illustrate the total spectral model, while the individual components are represented as follows: DiskBB (red dashed), Bbody (blue dotted), GAUSSIAN (pink dot-dashed lines).

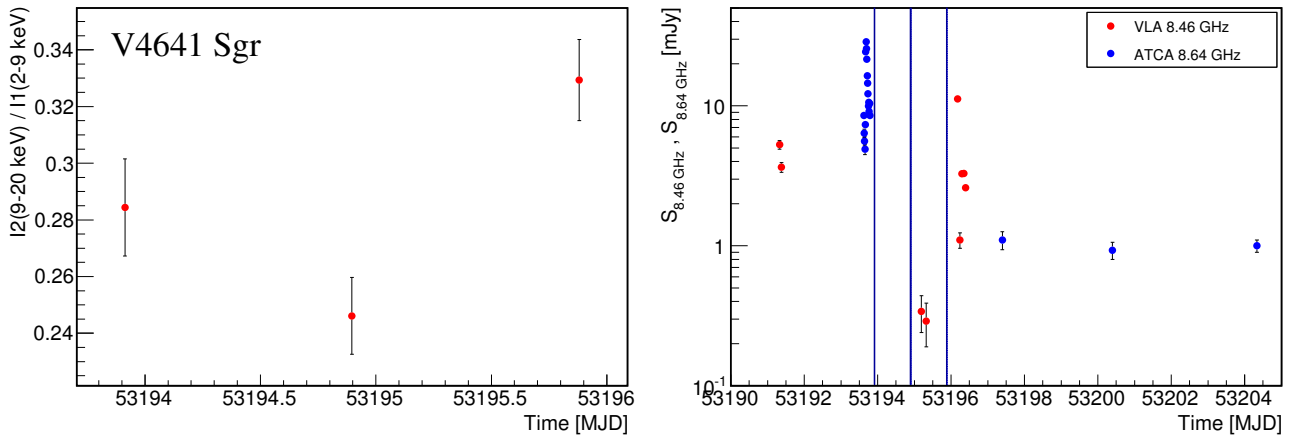


Fig. A.7. *Left:* hardness (ratio of bands 9–20 keV/2–9 keV) computed from RXTE-PCA data for the three observations of V4641 Sgr. Each point is the mean value of hardness and the error bar represents the standard error on the mean. *Right:* radio data for V4641 Sgr, from ATCA and VLA (Rupen et al. 2004b,a; Senkbeil & Sault 2004). RXTE-PCA and H.E.S.S. observation times are indicated by blue shaded bands.

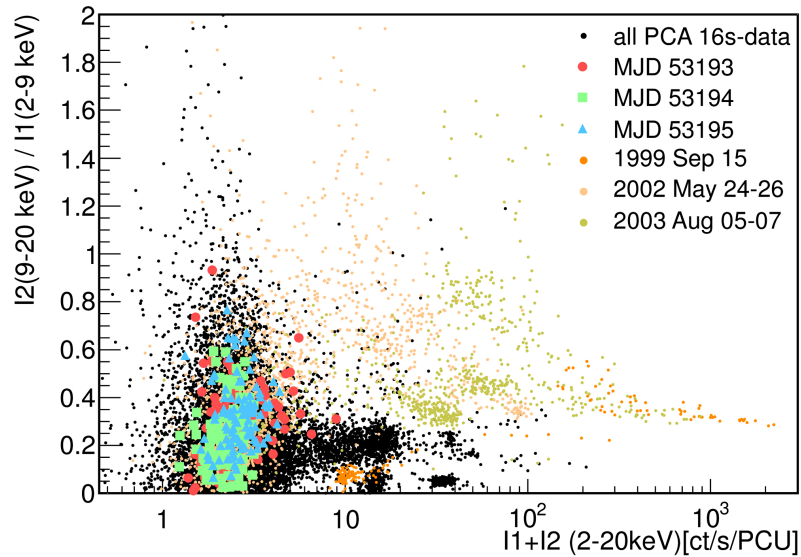


Fig. A.8. Hardness-Intensity diagram derived from the entire archival RXTE PCA data set for V4641 Sgr. Intensity and Hardness are defined in the caption of Fig. A.1. Coloured markers indicate data that correspond with the H.E.S.S. observation epochs, as well as historically noteworthy episodes of flaring activity (e.g. Wijnands & van der Klis 2000).



TeV Gamma-Ray Observations of the Binary Neutron Star Merger GW170817 with H.E.S.S.

H. Abdalla¹, A. Abramowski², F. Aharonian^{3,4,5}, F. Ait Benkhali³, E. O. Angüner⁶, M. Arakawa⁷, M. Arrieta⁸, P. Aubert⁹, M. Backes¹⁰, A. Balzer¹¹, M. Barnard¹, Y. Becherini¹², J. Becker Tjus¹³, D. Berge¹⁴, S. Bernhard¹⁵, K. Bernlöhr³, R. Blackwell¹⁶, M. Böttcher¹, C. Boisson⁸, J. Bolmont¹⁷, S. Bonnefoy¹⁸, P. Bordas³, J. Bregeon¹⁹, F. Brun²⁰, P. Brun²¹, M. Bryan¹¹, M. Büchele²², T. Bulik²³, M. Capasso²⁴, S. Caroff²⁵, A. Carosi⁹, S. Casanova^{6,3}, M. Cerruti¹⁷, N. Chakraborty³, R. C. G. Chaves^{19,41}, A. Chen²⁶, J. Chevalier⁹, S. Colafrancesco²⁶, B. Condon²⁰, J. Conrad^{27,42}, I. D. Davids¹⁰, J. Decock²¹, C. Deil³, J. Devin¹⁹, P. deWilt¹⁶, L. Dirson², A. Djannati-Atai²⁸, A. Donath³, L. O'C. Drury⁴, K. Dutson²⁹, J. Dyks³⁰, T. Edwards³, K. Egberts³¹, G. Emery¹⁷, J.-P. Ernenwein³², S. Eschbach²², C. Farnier^{27,12}, S. Fegan²⁵, M. V. Fernandes², A. Fiasson⁹, G. Fontaine²⁵, S. Funk²², M. Füssling^{18,47}, S. Gabici²⁸, Y. A. Gallant¹⁹, T. Garrigoux¹, F. Gaté⁹, G. Giavitto¹⁸, B. Giebels²⁵, D. Glawion³³, J. F. Glicenstein²¹, D. Gottschall²⁴, M.-H. Grondin²⁰, J. Hahn³, M. Haupt¹⁸, J. Hawkes¹⁶, G. Heinzlmann², G. Henri³⁴, G. Hermann³, J. A. Hinton³, W. Hofmann³, C. Hoischen^{31,47}, T. L. Holch³⁵, M. Holler¹⁵, D. Horns², A. Ivascenko¹, H. Iwasaki⁷, A. Jacholkowska¹⁷, M. Jamroz³⁶, D. Jankowsky²², F. Jankowsky³³, M. Jingo²⁶, L. Jouvin²⁸, I. Jung-Richardt²², M. A. Kastendieck², K. Katarzyński³⁷, M. Katsuragawa³⁸, U. Katz²², D. Kerszberg¹⁷, D. Khangulyan⁷, B. Khélifi²⁸, J. King³, S. Klepser¹⁸, D. Klochkov²⁴, W. Kluźniak³⁰, Nu. Komin²⁶, K. Kosack²¹, S. Krakau¹³, M. Kraus²², P. P. Krüger¹, H. Laffon²⁰, G. Lamanna⁹, J. Lau¹⁶, J.-P. Lees⁹, J. Lefaucheur⁸, A. Lemièrre²⁸, M. Lemoine-Goumard²⁰, J.-P. Lenain¹⁷, E. Leser³¹, T. Lohse³⁵, M. Lorentz²¹, R. Liu³, R. López-Coto³, I. Lypova¹⁸, D. Malyshev²⁴, V. Marandon³, A. Marcowith¹⁹, C. Mariaud²⁵, R. Marx³, G. Maurin⁹, N. Maxted^{16,43}, M. Mayer³⁵, P. J. Meintjes³⁹, M. Meyer^{27,44}, A. M. W. Mitchell³, R. Moderski³⁰, M. Mohamed³³, L. Mohrmann²², K. Morá²⁷, E. Moulin²¹, T. Murach¹⁸, S. Nakashima³⁸, M. de Naurois²⁵, H. Ndiyavala¹, F. Niederwanger¹⁵, J. Niemiec⁶, L. Oakes³⁵, P. O'Brien²⁹, H. Odaka³⁸, S. Ohm^{18,47}, M. Ostrowski³⁶, I. Oya¹⁸, M. Padovani¹⁹, M. Panter³, R. D. Parsons³, N. W. Pekeur¹, G. Pelletier³⁴, C. Perennes¹⁷, P.-O. Petrucci³⁴, B. Peyaud²¹, Q. Piel⁹, S. Pita²⁸, V. Poireau⁹, H. Poon³, D. Prokhorov¹², H. Prokoph¹⁴, G. Pühlhofer²⁴, M. Punch^{28,12}, A. Quirrenbach³³, S. Raab²², R. Rauth¹⁵, A. Reimer¹⁵, O. Reimer¹⁵, M. Renaud¹⁹, R. de los Reyes³, F. Rieger^{3,45}, L. Rinchiuso²¹, C. Romoli⁴, G. Rowell¹⁶, B. Rudak³⁰, C. B. Rulten⁸, V. Sahakian^{40,5}, S. Saito⁷, D. A. Sanchez⁹, A. Santangelo²⁴, M. Sasaki²², R. Schlickeiser¹³, F. Schüssler^{21,47}, A. Schulz¹⁸, U. Schwanke³⁵, S. Schwanmer³³, M. Seglar-Arroyo^{21,47}, M. Settimo¹⁷, A. S. Seyffert¹, N. Shafi²⁶, I. Shilon²², K. Shiningayamwe¹⁰, R. Simoni¹¹, H. Sol⁸, F. Spanier¹, M. Spir-Jacob²⁸, Ł. Stawarz³⁶, R. Steenkamp¹⁰, C. Stegmann^{31,18}, C. Steppa³¹, I. Sushch¹, T. Takahashi³⁸, J.-P. Tavernet¹⁷, T. Tavernier²⁸, A. M. Taylor¹⁸, R. Terrier²⁸, L. Tibaldo³, D. Tiziani²², M. Tluczykont², C. Trichard³², M. Tsiour¹⁹, N. Tsuboi⁷, R. Tuffs³, Y. Uchiyama⁷, D. J. van der Walt¹, C. van Eldik²², C. van Rensburg¹, B. van Soelen³⁹, G. Vasileiadis¹⁹, J. Veh²², C. Venter¹, A. Viana^{3,46}, P. Vincent¹⁷, J. Vink¹¹, F. Voisin¹⁶, H. J. Völk³, T. Vuillaume⁹, Z. Wadiasingh¹, S. J. Wagner³³, P. Wagner³⁵, R. M. Wagner²⁷, R. White³, A. Wiercholska⁶, P. Willmann²², A. Wörnlein²², D. Wouters²¹, R. Yang³, D. Zaborov²⁵, M. Zacharias¹, R. Zanin³, A. A. Zdziarski³⁰, A. Zech⁸, F. Zefi²⁵, A. Ziegler²², J. Zorn³, and N. Zywucka³⁶

(H.E.S.S. Collaboration)

¹ Centre for Space Research, North-West University, Potchefstroom 2520, South Africa

² Universität Hamburg, Institut für Experimentalphysik, Luruper Chaussee 149, D-22761 Hamburg, Germany

³ Max-Planck-Institut für Kernphysik, P.O. Box 103980, D-69029 Heidelberg, Germany

⁴ Dublin Institute for Advanced Studies, 31 Fitzwilliam Place, Dublin 2, Ireland

⁵ National Academy of Sciences of the Republic of Armenia, Marshall Baghramian Avenue, 24, 0019 Yerevan, Armenia

⁶ Instytut Fizyki Jądrowej PAN, ul. Radzikowskiego 152, 31-342 Kraków, Poland

⁷ Department of Physics, Rikkyo University, 3-34-1 Nishi-Ikebukuro, Toshima-ku, Tokyo 171-8501, Japan

⁸ LUTH, Observatoire de Paris, PSL Research University, CNRS, Université Paris Diderot, 5 Place Jules Janssen, F-92190 Meudon, France

⁹ Laboratoire d'Annecy-le-Vieux de Physique des Particules, Université Savoie Mont-Blanc, CNRS/IN2P3, F-74941 Annecy-le-Vieux, France

¹⁰ University of Namibia, Department of Physics, Private Bag 13301, Windhoek, Namibia

¹¹ GRAPPA, Anton Pannekoek Institute for Astronomy, University of Amsterdam, Science Park 904, 1098 XH Amsterdam, The Netherlands

¹² Department of Physics and Electrical Engineering, Linnaeus University, 351 95 Växjö, Sweden

¹³ Institut für Theoretische Physik, Lehrstuhl IV: Weltraum und Astrophysik, Ruhr-Universität Bochum, D-44780 Bochum, Germany

¹⁴ GRAPPA, Anton Pannekoek Institute for Astronomy and Institute of High-Energy Physics, University of Amsterdam, Science Park 904, 1098 XH Amsterdam, The Netherlands

¹⁵ Institut für Astro- und Teilchenphysik, Leopold-Franzens-Universität Innsbruck, A-6020 Innsbruck, Austria

¹⁶ School of Physical Sciences, University of Adelaide, Adelaide, SA 5005, Australia

¹⁷ Sorbonne Universités, UPMC Université Paris 06, Université Paris Diderot, Sorbonne Paris Cité, CNRS, Laboratoire de Physique Nucléaire et de Hautes Energies (LPNHE), 4 place Jussieu, F-75252, Paris Cedex 5, France

¹⁸ DESY, D-15738 Zeuthen, Germany

¹⁹ Laboratoire Univers et Particules de Montpellier, Université Montpellier, CNRS/IN2P3, CC 72, Place Eugène Bataillon, F-34095 Montpellier Cedex 5, France

²⁰ Université Bordeaux, CNRS/IN2P3, Centre d'Études Nucléaires de Bordeaux Gradignan, F-33175 Gradignan, France

²¹ IRFU, CEA, Université Paris-Saclay, F-91191 Gif-sur-Yvette, France

²² Friedrich-Alexander-Universität Erlangen-Nürnberg, Erlangen Centre for Astroparticle Physics, Erwin-Rommel-Str. 1, D-91058 Erlangen, Germany

²³ Astronomical Observatory, The University of Warsaw, Al. Ujazdowskie 4, 00-478 Warsaw, Poland

²⁴ Institut für Astronomie und Astrophysik, Universität Tübingen, Sand 1, D-72076 Tübingen, Germany

²⁵ Laboratoire Leprince-Ringuet, Ecole Polytechnique, CNRS/IN2P3, F-91128 Palaiseau, France

- ²⁶ School of Physics, University of the Witwatersrand, 1 Jan Smuts Avenue, Braamfontein, Johannesburg, 2050 South Africa
- ²⁷ Oskar Klein Centre, Department of Physics, Stockholm University, Albanova University Center, SE-10691 Stockholm, Sweden
- ²⁸ APC, AstroParticule et Cosmologie, Université Paris Diderot, CNRS/IN2P3, CEA/Irfu, Observatoire de Paris, Sorbonne Paris Cité, 10, rue Alice Domon et Léonie Duquet, F-75205 Paris Cedex 13, France
- ²⁹ Department of Physics and Astronomy, The University of Leicester, University Road, Leicester LE1 7RH, UK
- ³⁰ Nicolaus Copernicus Astronomical Center, Polish Academy of Sciences, ul. Bartycka 18, 00-716 Warsaw, Poland
- ³¹ Institut für Physik und Astronomie, Universität Potsdam, Karl-Liebknecht-Strasse 24/25, D-14476 Potsdam, Germany
- ³² Aix Marseille Université, CNRS/IN2P3, CPPM, Marseille, France
- ³³ Landessternwarte, Universität Heidelberg, Königstuhl, D-69117 Heidelberg, Germany
- ³⁴ Univ. Grenoble Alpes, CNRS, IPAG, F-38000 Grenoble, France
- ³⁵ Institut für Physik, Humboldt-Universität zu Berlin, Newtonstr. 15, D-12489 Berlin, Germany
- ³⁶ Obserwatorium Astronomiczne, Uniwersytet Jagielloński, ul. Orla 171, 30-244 Kraków, Poland
- ³⁷ Centre for Astronomy, Faculty of Physics, Astronomy and Informatics, Nicolaus Copernicus University, Grudziadzka 5, 87-100 Torun, Poland
- ³⁸ Japan Aerospace Exploration Agency (JAXA), Institute of Space and Astronautical Science (ISAS), 3-1-1 Yoshinodai, Chuo-ku, Sagami, Kanagawa 229-8510, Japan
- ³⁹ Department of Physics, University of the Free State, PO Box 339, Bloemfontein 9300, South Africa
- ⁴⁰ Yerevan Physics Institute, 2 Alikhanian Brothers Street, 375036 Yerevan, Armenia

Received 2017 October 17; revised 2017 November 1; accepted 2017 November 1; published 2017 November 22

Abstract

We search for high-energy gamma-ray emission from the binary neutron star merger GW170817 with the H.E.S.S. Imaging Air Cherenkov Telescopes. The observations presented here have been obtained starting only 5.3 hr after GW170817. The H.E.S.S. target selection identified regions of high probability to find a counterpart of the gravitational-wave event. The first of these regions contained the counterpart SSS17a that has been identified in the optical range several hours after our observations. We can therefore present the first data obtained by a ground-based pointing instrument on this object. A subsequent monitoring campaign with the H.E.S.S. telescopes extended over several days, covering timescales from 0.22 to 5.2 days and energy ranges between 270 GeV to 8.55 TeV. No significant gamma-ray emission has been found. The derived upper limits on the very-high-energy gamma-ray flux for the first time constrain non-thermal, high-energy emission following the merger of a confirmed binary neutron star system.

Key words: gamma-ray burst: individual (GRB 170817A) – gamma rays: general – gravitational waves

1. Introduction

Opening the era of gravitational-wave (GW) astronomy, the first direct detection of a GW signal from a binary black hole merger was reported by the LIGO–Virgo Scientific Collaboration (LVC) in 2015 September (Abbott et al. 2016) during the first science run (O1) of the Advanced LIGO interferometers. The second science run O2 started in the fall of 2016 with the two LIGO detectors taking data. The Advanced Virgo interferometer joined the observations on 2017 August 1.

Marking the beginning of GW multi-messenger astronomy, a GW signal compatible with that expected from the merger of a binary neutron star system was detected by the LIGO–Virgo Collaborations on 2017 August 17 (Abbott et al. 2017c). The event stands as the first direct detection of GWs coming from a system of this kind. As these events are assumed to be related to gamma-ray bursts (GRBs) or kilonovae (Metzger & Berger 2012), broadband emission of electromagnetic (EM) radiation as well as high-energy neutrinos (Eichler et al. 1989) can be expected in addition to the GW signal. Gamma-ray

detections in the GeV–TeV energy range have been argued to depend on the specifics of the progenitor’s ambient environment density, energy fraction in electrons and magnetic fields, the merger’s proximity, and the viewing angle with respect to the outflow by Takami et al. (2014) and Zhu & Wang (2016). An extensive observational campaign covering a very wide range of EM wavelengths from radio to high-energy gamma-rays and including high-energy neutrinos was launched immediately after the detection of the GW signal.

Gamma-ray bursts are short bursts of radiation with prompt emission typically detected in the tens of keV to GeV range (e.g., Zhang et al. 2006). The duration of the initial, or prompt, emission follows a bimodal distribution, with the divisional timescale between both types of bursts being around 2 s (Kouveliotou et al. 1993). This distinction enables their classification into *short* GRB (sGRB) and *long* GRB (lGRB). These classes have been linked to the association of the events with different cosmic progenitors. The lGRBs are usually associated with the core collapse of massive stars (Woosley et al. 2007; Piran et al. 2017), while the coalescence of compact binary systems, being either a neutron star–neutron star (NS–NS) or a neutron star–black hole, are thought to be the cosmic progenitors of sGRBs that have a hard spectrum (Piran 1994; Metzger & Berger 2012). In these systems, the orbit of the binary system steadily decays as a result of the energy loss through continuous GW emission, resulting in the objects spiraling inward at an increasing rate. At the final phase of the process, a characteristic burst of gravitation radiation is emitted, a prime signal for current GW instruments. In addition, the GW radiation is expected to be accompanied by both thermal and non-thermal emission in the form of EM radiation. Depending on the mass losses during the cataclysmic event, the residual compact object

⁴¹ Funded by EU FP7 Marie Curie, grant agreement No. PIEF-GA-2012-332350.

⁴² Wallenberg Academy Fellow.

⁴³ Now at The School of Physics, The University of New South Wales, Sydney, NSW 2052, Australia.

⁴⁴ Now at Kavli Institute for Particle Astrophysics and Cosmology, Department of Physics and SLAC National Accelerator Laboratory, Stanford University, Stanford, CA 94305, USA.

⁴⁵ Heisenberg Fellow (DFG), ITA Universität Heidelberg, Germany.

⁴⁶ Now at Instituto de Física de São Carlos, Universidade de São Paulo, Av. Trabalhador São-carlense, 400—CEP 13566-590, São Carlos, SP, Brazil.

⁴⁷ Author to whom any correspondence should be addressed (contact.hess@hess-experiment.eu).

left afterward will be a black hole or a neutron star. However, due to strong absorption at early times and the beaming effects associated with relativistic outflows of the post-merger ejecta, the EM radiation from the inner engine may be shrouded from view. Therefore, a GW observation of such an event provides substantial new information to characterize the progenitor system and the phenomena leading to the explosive merger.

One of the leading theoretical frameworks describing the phenomenology of GRBs is the so-called fireball model (Meszaros & Rees 1993; Piran 1999). After the formation of a new compact object, the central engine releases a huge amount of energy over a short time and within a small volume, giving rise to relativistic outflows and shocks. This *fireball* is considered to consist of an optically thick electron–positron/ photon plasma expanding with relativistic velocities.

Additionally, another class of EM transient counterpart to mergers of binary neutron stars has been proposed. These events are called macronovae (Kulkarni 2005) or kilonovae (Metzger et al. 2010), and their energy output lies between the novae and supernovae energy scales. Kilonovae produce delayed optical, UV, and infrared radiation on timescales of a few days, heated by the radioactive decay of r -process elements in the ejecta itself, or in the interaction of the ejecta with the interstellar medium (see, e.g., Tanvir et al. 2013, for a GRB–kilonova association). The ejecta in a kilonova are believed to have a mass of $\sim 10^{-2} M_{\odot}$ and are moving at mildly relativistic velocities of 0.1–0.2 c . Kilonovae produce rather isotropic emission that typically lasts for days after the merger event (see Baiotti & Rezzolla 2017 and references therein).

Clear evidence for a non-thermal emission from sGRBs has been found in the GeV energy range for only a handful of cases (Ackermann et al. 2013b), with the maximum observed photon energies exceeding 30 GeV (Ackermann et al. 2010). In principle, this gamma-ray emission may be produced via energy losses from particles accelerated at shocks present in the outflow or formed when the ejecta propagate through the interstellar medium. Given the ejected mass and ejecta velocities considered, this situation is reminiscent of a supernova remnant where diffusive shock acceleration would proceed in the non-relativistic to trans-relativistic regime (Ellison et al. 2013). With its superior sensitivity on short timescales above 50 GeV, relative to the *Fermi*-LAT instrument, the High Energy Stereoscopic System (H.E.S.S. II) is uniquely suited to probe the level of non-thermal emission produced by high-energy transient events (Hoischen et al. 2017).

High-energy observations of non-thermal emission in the GeV–TeV energy range thus provide an effective probe of non-thermal emission from both fireball and kilonovae classes of events. With the significant sensitivity achieved in this energy range, a detection of a cutoff in the spectral energy distribution of the emission is possible, which would provide hints on the environment of the cataclysmic event (Ackermann et al. 2011) and allow one to estimate the kinematic velocities of the outflow in which the γ -ray emission was produced. Moreover, the comparison between the highest and the low-energy photons from the same source can provide constraints on theories of Lorentz invariance violation (Biesiada & Piórkowska 2009).

This Letter is organized as follows. In Section 2, the GW event, the subsequent EM follow-up campaign, and the H.E.S.S. follow-up effort are discussed. Section 3 describes the data

and their analysis, and in Section 4 the results are described. Discussion and conclusion are presented in Section 5.

2. Neutron Star Merger Follow-up

2.1. Electromagnetic Follow-up of GW Alerts

In preparation of the physics data taking of the Advanced LIGO and Virgo interferometers, agreements with an extensive group of observatories interested in performing follow-up observations across the EM spectrum and using high-energy neutrinos have been set up by the LIGO–Virgo Collaborations. H.E.S.S. became a member of this group in early 2015 and the follow-up of GW alerts has been prepared (see Section 2.3.1 for details).

To rapidly alert the multi-wavelength (MWL) follow-up community, the LIGO–Virgo Collaborations have developed different low-latency pipelines searching for transient signals from compact binary mergers. The fastest pipeline is BAYESTAR (Singer & Price 2016). It is complemented by the LALInference algorithm, which is scanning a larger parameter space and marginalizing over calibration uncertainties and is thus providing a more robust estimate of the important event parameters (Veitch et al. 2015).

2.2. GW170817

A GW event was recorded on 2017 August 17, at 12:41:04 UTC by the Advanced LIGO and Advanced Virgo interferometers (Abbott et al. 2017c). Based on a BAYESTAR analysis using the data of the LIGO-Hanford instrument, an initial alert notice was issued at 13:08:16 UTC. A subsequent GCN circular reporting a highly significant detection of a binary neutron star signal was distributed among a wide range of follow-up observatories about 40 minutes after the event at 13:21:42 UTC (LIGO Scientific Collaboration & Virgo Collaboration 2017a). As only data from a single interferometer were used in this initial reconstruction, the sky location of the event could only be localized to within 24, 200 deg² (90% containment). Nevertheless, the timing of the alert allowed the team of the *Fermi* Gamma-Ray Burst Monitor (*Fermi*-GBM) to correlate the GW event with a gamma-ray burst (170817A; Connaughton et al. 2017; von Kienlin et al. 2017) observed ~ 1.7 s after the gravitational-wave candidate. The light curve of the GRB event shows a weak short pulse with a duration of 2 s, typical for sGRBs (Goldstein et al. 2017a). GRB 170817A has also been recorded by the SPI-ACS instrument on board the *INTEGRAL* satellite (Savchenko et al. 2017). Further details are given in Abbott et al. (2017b).

On 2017 August 17, at 17:54:51 UTC, the LIGO–Virgo Collaborations provided an update on the GW skymap, incorporating data from the LIGO Livingston detector (which had to be excluded in the initial analysis due to a noise artifact) as well as data from the Virgo detector in the BAYESTAR pipeline (LIGO Scientific Collaboration & Virgo Collaboration 2017c; BAYESTAR_HLV in the following). The result of this joint analysis reduced the 90% localization uncertainty of the GW event to about 31 deg². The data confirmed the binary neutron star origin and located the merger event at a distance of 40 ± 8 Mpc (50 ± 3 Mpc if assuming the binary to be face-on). A further analysis using the LALInference method was provided about six hours later (LIGO Scientific Collaboration & Virgo Collaboration 2017d; 2017 August 17, 23:54:40

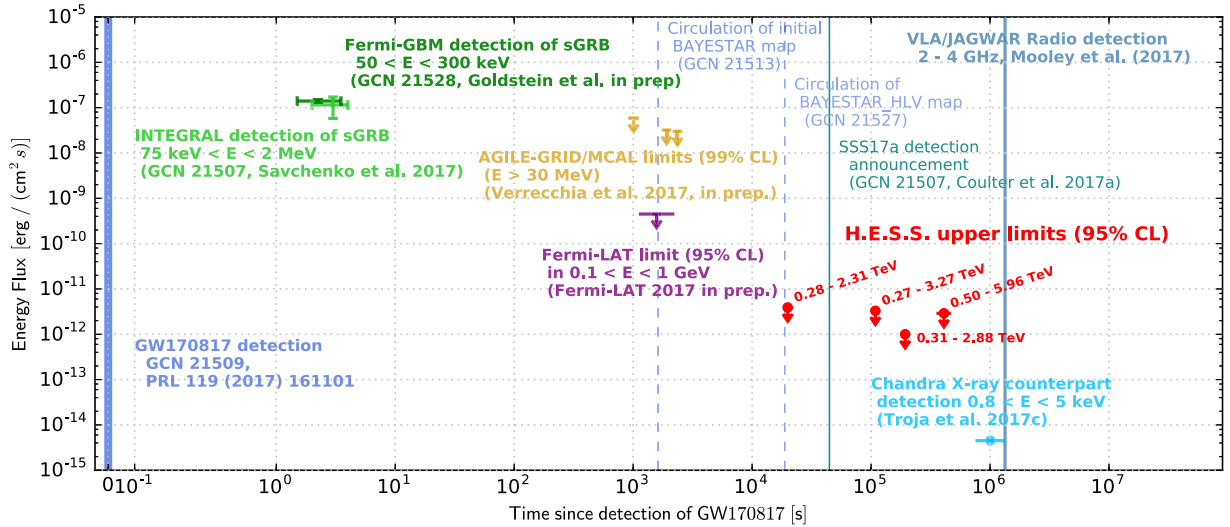


Figure 1. Timeline of the observations following the detection of GW170817 with a focus on the high-energy, non-thermal domain. A more complete picture of the multi-wavelength and multi-messenger campaign is given in Abbott et al. (2017a).

UTC). The 90% credible region of this map (see Figure 2) spans 34 deg^2 , overlapping with the 90% uncertainty region of GRB 170817A (Goldstein et al. 2017b). The final estimates of the source properties of GW170817 are given in Abbott et al. (2017c).

The first EM counterpart to GW170817 and GRB 170817A was detected in the near-infrared by the One-Meter Two-Hemisphere (1M2H) Collaboration with the 1 m Swope telescope at Las Campanas Observatory in Chile on August 17 at 23:33 UTC, i.e., 10.87 hr after GW170817 (Coulter et al. 2017a, 2017b). The source, located at $\alpha(\text{J2000.0}) = 13^{\text{h}}09^{\text{m}}48^{\text{s}}.085 \pm 0.018$, $\delta(\text{J2000.0}) = -23^{\circ}22'53''.343 \pm 0.218$, near the early-type galaxy NGC 4993 at a distance of 42.5 Mpc, got designated Swope Supernova Survey 2017a (SSS17a). It had an initial brightness of magnitude 17.3 ± 0.1 in the i band (Coulter et al. 2017c). The IAU designation of the source is AT 2017gfo. NGC 4993 is on the list of possible candidates that had been identified by “Global Relay of Observatories Watching Transients Happen” network (Cook et al. 2017) via cross-matching the GW localization with the “census of the local universe” catalog (Cook & Kasliwal 2016). The optical transient was detected independently by five different teams: the Distance Less Than 40 Mpc (DLT40) survey (Yang et al. 2017), by Tanvir et al. (VISTA), Lipunov et al. (MASTER), Allam et al. (DECam) and Arcavi et al. (Las Cumbres Observatory). Archival searches (e.g., ASAS-SN, Cowperthwaite et al. 2017; Hubble, Foley et al. 2017; etc.) did not show evidence of emission at this position in observations taken before the GW event.

The subsequent MWL follow-up campaign focused mainly on the optical transient SSS17a. The monitoring of the source in the UV, optical, and near-infrared domain allows the detailed description of its spectral evolution over timescales extending from hours to several days and weeks. The source has also been monitored in UV and X-rays by *Swift* (Evans et al. 2017) over several days. An X-ray source coincident with the location of SSS17a has been discovered by *Chandra* about 9 days after GW170817 (Troja et al. 2017). In the radio domain, the first counterpart consistent with the optical transient position was identified on 2017 September 2 and 3 (16 days after

GW170817) by two observations using the Jansky VLA (Corsi et al. 2017; Mooley et al. 2017).

This extensive monitoring campaign covering the full EM spectrum, including the high-energy (HE) and very-high-energy (VHE) gamma-ray domains (the latter reported in this Letter) and searches for high-energy neutrinos, allowed us to monitor the evolution of the source over several days. Focusing on the high-energy, non-thermal domain, a subset of the observations obtained during this campaign is shown in Figure 1. Further details of this unprecedented multi-wavelength and multi-messenger effort can be found in Abbott et al. (2017a and references therein).

2.3. H.E.S.S. Follow-up of GW170817

Here, we report on observations obtained in the very-high-energy gamma-ray domain with the H.E.S.S. imaging atmospheric Cherenkov telescope array. H.E.S.S. is located on the Khomas Highland plateau of Namibia ($23^{\circ}16'18''$ south, $16^{\circ}30'00''$ east), at an elevation of 1800 m above sea level. With its original four-telescope array, H.E.S.S. is sensitive to cosmic and gamma-rays in the 100 GeV to 100 TeV energy range and is capable of detecting a source with an energy spectrum similar to the Crab Nebula under good observational conditions close to zenith at the 5σ level within less than one minute (Aharonian et al. 2006). In 2012, a fifth telescope with 28 m diameter was commissioned, extending the covered energy range toward lower energies. The observations reported here were conducted jointly with three of the original 12 m telescopes and the 28 m telescope. One of the 12 m H.E.S.S. telescopes was not available due to a maintenance campaign.

2.3.1. Scheduling for GW Follow-up

The localization uncertainty derived from the data of the GW interferometers is significant for events detected by two interferometers (hundreds to thousands of square degrees) and still sizable for events with data from three detectors (tens to hundreds of square degrees). Although the field of view (FoV) of the large 28 m H.E.S.S. telescope and the four 12 m telescopes has a radius of about 1.5° and 2.5° , respectively, several pointings are typically necessary to cover the identified

region. An additional challenge is related to the limited duty-cycle of the observatory, operating only in astronomical darkness during moonless nights and the accessible range of zenith angles (usually $<60^\circ$). Since H.E.S.S. joined the EM follow-up group of the LIGO–Virgo Collaborations, several algorithms have been developed to optimize the follow-up of GW events while taking into account these constraints. The most straightforward and most general scheduling algorithms determine the pointing of the telescopes by maximizing the coverage of the two-dimensional localization probability provided with the GW alerts. In addition to these algorithms, we developed optimized strategies for events occurring at distances for which sufficient complete galaxy catalogs are available. For these we use the GLADE catalog (Dalya et al. 2016), a value-added full-sky galaxy catalog highly complete and specifically built in order to support EM follow-up of GW signals. It includes more than 3 million entries and is (outside the Galactic plane) complete up to ~ 70 Mpc, well matching the horizon of the current GW interferometers to detect mergers of binary neutron star systems.

Our approach follows the one outlined by Singer et al. (2016). We use the full three-dimensional information of the location of the GW event provided by the BAYESTAR and LALInference GW pipelines and correlate it with the location of galaxies within that volume. Several algorithms have been implemented to derive an optimized pointing scenario from this 3D GW-galaxies probability region. The *One-in-FoV* algorithm searches for the coordinates that provide the highest probability of hosting the event, while the *Gal-in-FoV* algorithm determines the center of a region on the sky that provides best coverage of neighboring high-probability regions falling in the same FoV. Both algorithms are taking into account observational constraints like the available time window and, trying to achieve a low energy threshold, optimize the pointing strategy favoring low-zenith angle observations. Both are complementary in terms of calculation speed and performance, with *One-in-FoV* being used for real-time follow-ups and the *Gal-in-FoV* for offline scheduling. Further details about the developed approaches and performance estimates based on Monte Carlo simulations of NS–NS merger events are given in Seglar-Arroyo et al. (2017).

2.3.2. Scheduling for GW170817

As outlined above, the first localization map for the event GW170817 was provided by the BAYESTAR pipeline and was made available to follow-up partners about 1.5 hr after the GW event (LIGO Scientific Collaboration & Virgo Collaboration 2017b). Due to its large uncertainty covering $24,200 \text{ deg}^2$ at 90% containment, it was not suitable for scheduling follow-up observations. An updated BAYESTAR-reconstructed GW map, BAYESTAR_HLV, using data from all three interferometers was received about 5 hr after the event, at 17:54 UTC (LIGO Scientific Collaboration & Virgo Collaboration 2017c). This map, with the 90% region of the localization uncertainty covering 31 deg^2 , was used for the scheduling of H.E.S.S. follow-up observations. With H.E.S.S. data taking starting on August 17 at 17:59 UTC, only about 5 minutes were available to derive a pointing strategy. A LALInference based skymap was made available about 9 hr after the GW event. Changes with respect to the low-latency BAYESTAR_HLV

Table 1
H.E.S.S. Follow-up Observations of GW170817

ID	Observation Time (UTC)	Pointing Coordinates (deg)	(zenith angle) (deg)
1a	2017 Aug 17 17:59	196.88, -23.17	59
1b	2017 Aug 17 18:27	198.19, -25.98	58
1c	2017 Aug 17 18:56	200.57, -30.15	62
2a	2017 Aug 18 17:55	197.75, -23.31	53
2b	2017 Aug 18 18:24	197.23, -23.79	60
3a	2017 Aug 19 17:56	197.21, -23.20	55
3b	2017 Aug 19 18:24	197.71, -23.71	60
5a	2017 Aug 21 18:15	197.24, -24.07	60
6a	2017 Aug 22 18:10	197.70, -24.38	60

Note. All pointings were taken with the default run duration of 28 minutes and are given in equatorial J2000 coordinates.

map were minimal (the 90% uncertainty region increased slightly to 34 deg^2).

Due to the limited time between the publication of the BAYESTAR_HLV map and the start of the visibility window we used the *One-in-FoV* approach to determine the H.E.S.S. pointing schedule for the night of August 17/18. Three observation runs of 28 minutes each were scheduled. They are given in Table 1 and illustrated in Figure 2. The three observations were taken between August 17, 17:59–19:30 UTC. For an effective FoV of 1.5° radius of the H.E.S.S. 28 m telescope, they cover about 56% of the GW uncertainty region of the final LALInference map. At the same time they include about 86% of the probability density region obtained by weighting the three-dimensional GW map with galaxies from the GLADE catalog. All three pointings are compatible with GRB 1707A within 2σ . Whereas the optical transient SSS17a had not been discovered at the time our observations took place, the focus on a region containing many galaxies compatible with the 3D-GW map allowed us to cover NGC 4993 and SSS17a with our first observation, i.e., starting 5.3 hr after the GW event. We note that our observations have the shortest time delay with respect to GW170817 by any ground-based pointing instrument participating in the follow-up of GW170817.

After the detection of SSS17a during the night of August 17/18 we discontinued further coverage of the GW uncertainty region and focused on monitoring the source in TeV gamma-rays. H.E.S.S. observations were scheduled at the beginning of the following nights around SSS17a as long as the location was visible from the H.E.S.S. site within a maximum zenith angle of about 60° and fulfilling the necessary observation conditions. The obtained observations are summarized in Table 1.

3. Data and Analysis

The obtained data were analyzed using Model Analysis (de Naurois & Rolland 2009), an advanced Cherenkov image reconstruction method in which the recorded shower images are compared to a semi-analytical model of gamma-ray showers by means of a log-likelihood optimization. The background level in the FoV was determined from the data set itself using the standard “ring background” technique (Berge et al. 2007). Relying on the azimuthal symmetry of the response of the telescopes, the required acceptance function has been derived from the data itself. We perform our analysis

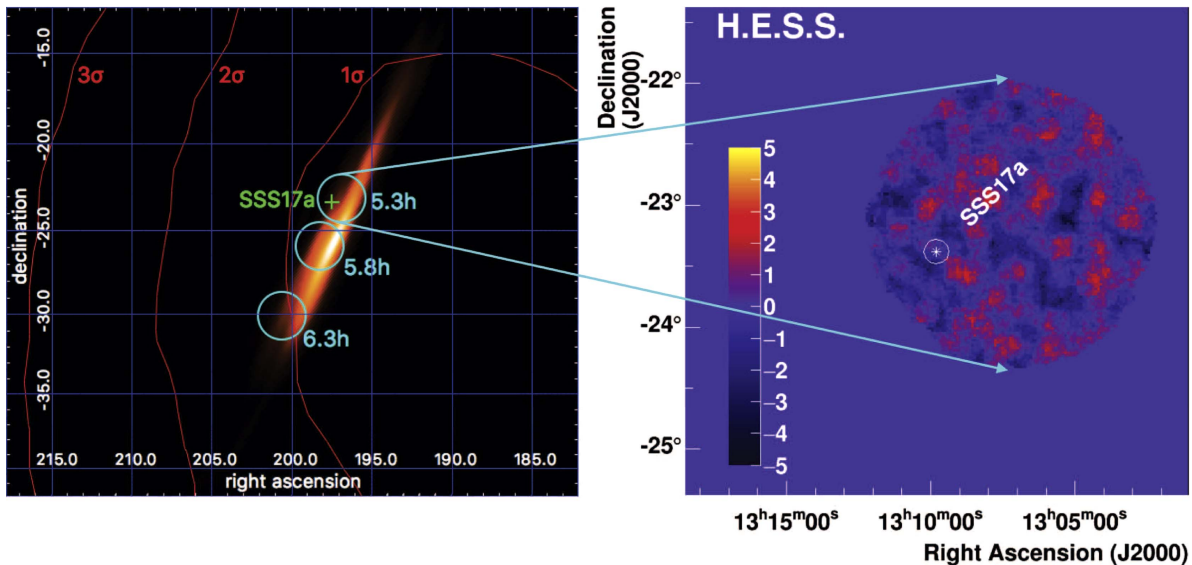


Figure 2. Left: pointing directions of the first night of H.E.S.S. follow-up observations starting 2017 August 17, at 17:59 UTC. The circles illustrate a FoV with a radius of $1^{\circ}5$ and the times shown are the starting times of each observation with respect to GW170817. The LALInference map of GW170817 is shown as a colored background, and the red lines denote the uncertainty contours of GRB 170817A. Right: map of significances of the gamma-ray emission in the region around SSS17a obtained during the first observation of GW170817. The white circle has a diameter of $0^{\circ}1$, corresponding to the H.E.S.S. point-spread function and also used for the oversampling of the map.

using only data from the 28 m telescope in the center of the H.E.S.S. array in order to achieve a low energy threshold. We adopted the “Loose cuts” of the Model Analysis, which, for example, require the total charge in the recorded shower image to be greater than 60 photoelectrons. This and additional quality selection criteria yield an energy threshold of 280 GeV for the first observation and 270 GeV for the combined data set on SSS17a. We note that the threshold is significantly influenced by the relatively high zenith angle of the observations. We further require that at least 10 events are available for the background estimation, a requirement that limits the energy range over which our results are valid. The derived energy ranges are given in Table 2. Further analyses exploiting the data from the full H.E.S.S. array will be published at a later time.

A second analysis using a fully independent data calibration chain and the Image Pixel-wise fit for Atmospheric Cherenkov Telescope (ImPACT; Parsons & Hinton 2014) reconstruction method was used to verify the results. The results of this cross-check analysis are consistent with the ones presented here, thus providing confidence in the robustness of the presented results.

High-energy gamma-rays interact with the extragalactic background light (EBL) via e^+/e^- pair-creation processes. At the highest energies gamma-rays are thus absorbed during the propagation through the extragalactic radiation fields. The resulting opacity depends on the gamma-ray energy and the distance of their source. We used the EBL model published in Franceschini et al. (2008) to calculate these energy-dependent EBL correction factors. Using the redshift of NGC 4993, $z = 0.009787$ (Wenger et al. 2000), these factors increase with energy and are about 10% (30%) at 1 TeV (10 TeV). These effects are therefore only of minor importance and we do not correct for them in this Letter.

The region covered by our observations contains several sources with emission in the GeV energy range. They are, for example, listed in the catalog compiled after four-year-long observations by the LAT instrument on board the *Fermi*

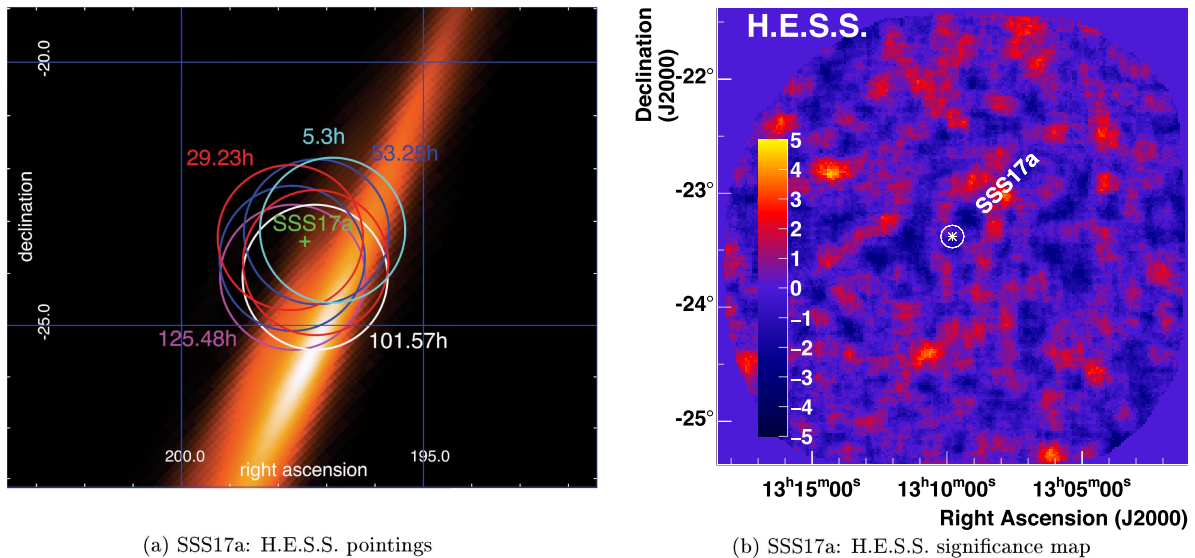
Table 2
Limits on the High-energy Gamma-Ray Flux at 95% C.L. and Assuming a E^{-2} Energy Spectrum Obtained During the Monitoring of SSS17a with H.E.S.S.

Pointings (See Table 1)	Time since GW170817 (days)	f_{γ} ($\text{erg cm}^{-2} \text{s}^{-1}$)	Energy Band (TeV)
1a	0.22	$<3.9 \times 10^{-12}$	0.28–2.31
2a+2b	1.22	$<3.3 \times 10^{-12}$	0.27–3.27
3a+3b	2.22	$<1.0 \times 10^{-12}$	0.31–2.88
5a+6a	4.23, 5.23	$<2.9 \times 10^{-12}$	0.50–5.96
all	0.22–5.23	$<1.5 \times 10^{-12}$	0.27–8.55

satellite (Acero et al. 2015). None of them is known to exhibit emission in the TeV range.⁴⁸ The most promising TeV candidate source in the region is likely PKS 1309-216, at an angular distance of $1^{\circ}58$ from NGC 4993/SSS17a. It has a flux in the 1–100 GeV range of about $2.0 \times 10^{-11} \text{ erg cm}^{-2} \text{ s}^{-1}$ and an energy spectrum following $E^{-2.07 \pm 0.05}$ in the same energy range. Extrapolating the emission to the higher energies relevant for our observations needs to account for EBL absorption effects: at the redshift of PKS 1309-216 ($z = 1.489$; Wenger et al. 2000) the initial flux is decreased by more than one order of magnitude at energies around 100 GeV and by a factor exceeding 10^9 at 1 TeV (Franceschini et al. 2008). Conservatively, we nevertheless excluded a region with a $0^{\circ}3$ radius around PKS 1309-216 from the background estimation used for the analysis presented here.

None of the GeV detected sources showed significant flux increases during the period of the observations presented here (Ackermann et al. 2013a). We therefore conclude that no TeV gamma-ray emission exceeding the level of the reached sensitivity, other than a potential signal related to GW170817 and GRB 170817A, is expected.

⁴⁸ <http://tevcat.uchicago.edu>



(a) SSS17a: H.E.S.S. pointings

(b) SSS17a: H.E.S.S. significance map

Figure 3. Left plot: H.E.S.S. pointing directions during the monitoring campaign of SSS17a. For details, see Table 1. The circles denote an FoV with a radius of $1^{\circ}.5$, and the times shown are the start times of each observation with respect to GW170817. Right plot: map of significances of the gamma-ray emission in the region around SSS17a combining all observations obtained during the H.E.S.S. monitoring campaign.

We note that archival H.E.S.S. observations on PKS 1309-216 have been obtained in 2013. After about 10 hr of observations, neither gamma-ray emission from the source nor from the region around NGC 4993/SSS17a could be detected. We therefore derive an archival upper limit on the gamma-ray flux at from SSS17a from these observations to $\Phi(170 \text{ GeV} < E < 47.2 \text{ TeV}) < 3.1 \times 10^{-12} \text{ erg cm}^{-2} \text{ s}^{-1}$ at 95% C.L. and assuming a spectral index of -2 . The differential upper limit as function of energy is shown in the left plot of Figure 4.

4. Results

As outlined above, our observations of SSS17a started 2017 August 17, at 17:59 UTC (pointing 1a), and were repeated during several nights (see Table 1). The different pointings, except 1b and 1c, which are not covering SSS17a but were taken during the initial scanning of the GW170817 uncertainty region, are shown in the left plot of Figure 3. The same color is used for pointings obtained successively during the same night, and the numbers indicate the time difference between the start of the observations and the time of GW170817. As the potential gamma-ray emission from an NS–NS merger is expected to be transient, we analyzed each of the obtained nightly data sets independently. For each of them we produce skymaps of the gamma-ray excess counts above the background derived from the data itself as described above. These excess maps have then been converted into significance maps using the formalism described by Li & Ma (1983).

As an example, we show the gamma-ray significance map derived from the first observation in Figure 2. An oversampling radius of $0^{\circ}.1$, roughly corresponding to the H.E.S.S. point-spread function, has been applied. No significant gamma-ray emission is found within any of the individual data sets, and all of the obtained results are fully compatible with the background-only expectation. We thus conclude that no significant VHE gamma-ray afterglow was detected from the direction of SSS17a. Consequently, we derive 95% C.L. upper limits on the

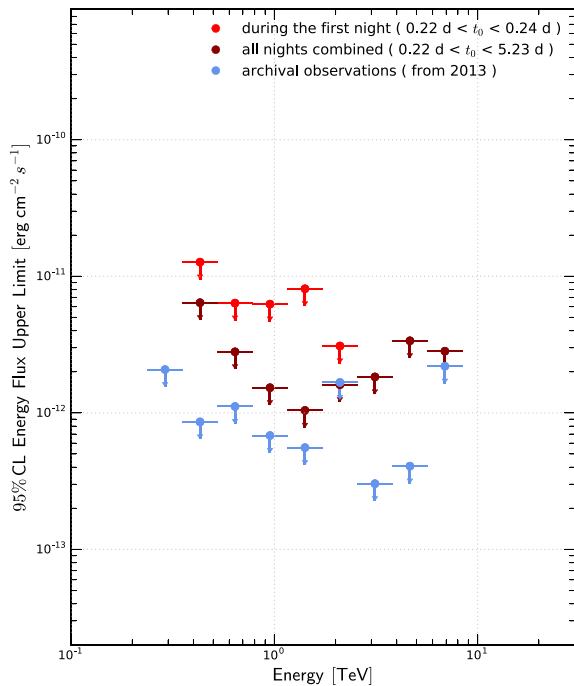
gamma-ray flux, following Feldman & Cousins (1998). The obtained flux limits, assuming a generic E^{-2} energy spectrum for the potential emission, are given together with the corresponding energy ranges in Table 2 and are shown in Figure 1.

In a search for fainter but temporally extended emission from SSS17a, we combined all data sets (except 1b and 1c). The obtained significance map (see the right plot of Figure 3) is again fully compatible with the background-only hypothesis. We obtain $\Phi_{\gamma} < 1.5 \times 10^{-12} \text{ erg cm}^{-2} \text{ s}^{-1}$ in the energy band $0.27 < E [\text{TeV}] < 8.55$. Assuming a radially symmetric emission, this flux limit corresponds to a limit on the VHE gamma-ray luminosity of SSS17a at a distance of 42.5 Mpc of $L_{\gamma} < 3.2 \times 10^{41} \text{ erg s}^{-1}$. We note the luminosity of the prompt phase of GRB 170817A that has been found to be around $2.2 \times 10^{46} \text{ erg s}^{-1}$ by *INTEGRAL* SPI-ACS (Savchenko et al. 2017). Differential upper limits as a function of the energy are shown in the left plot of Figure 4 for the first observation on SSS17a, the combined data set, and the archival observations obtained in 2013.

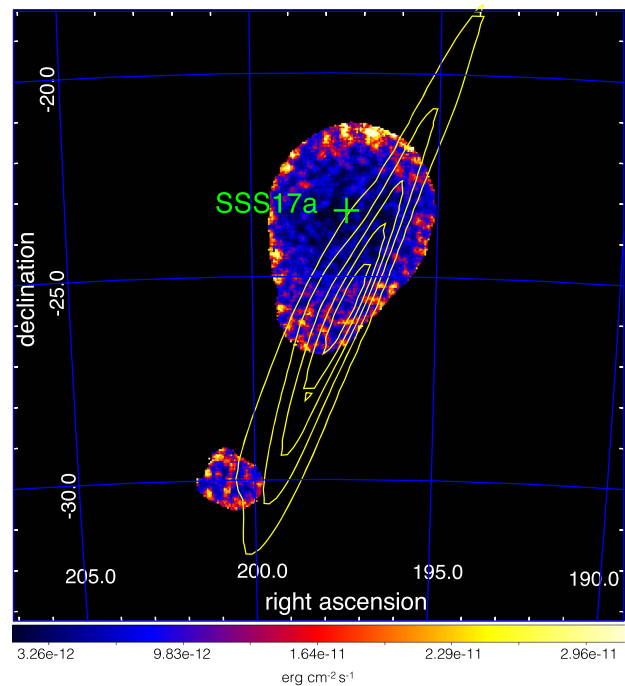
After combining all observations obtained with H.E.S.S. during the follow-up campaign of GW170817 we derive a skymap showing the integral upper limits in the 270 GeV to 8.55 TeV energy range. It is shown in the right plot of Figure 4. First of all, it illustrates the deep observations centered on SSS17a. Induced by the radially decreasing acceptance of the telescope, the obtained limits are less constraining when approaching the border of the FoV. The figure also illustrates the achieved $\approx 50\%$ coverage of the LALInference map of GW170817, which is depicted by the yellow contours.

5. Discussion and Conclusion

The observations presented here represent the first very-high-energy gamma-ray observations following the merger of a binary neutron star system. A prepared scheduling procedure allowed fast reaction to the event and provided efficient pointings within the GW uncertainty region, covering



(a) SSS17a: H.E.S.S. limits



(b) GW170817: H.E.S.S. flux limit map

Figure 4. Left plot: differential upper limits on the gamma-ray flux from SSS17a derived from the H.E.S.S. monitoring campaign and archival observations of the region. Right plot: map showing the integral upper limits in the 270 GeV to 8.55 TeV energy range (assuming an E^{-2} energy spectrum) derived from the H.E.S.S. follow-up observations of GW170817. The yellow contours outline the localization of the GW event as provided by the LALInference map.

observational fields including that of the multi-wavelength counterpart SSS17a even before it had been discovered from optical observations. Following the discovery of this counterpart in the optical band, subsequent extended monitoring allowed deep observations to be made of this source. Although the source was not detected within the energy range $0.27 < E[\text{TeV}] < 8.55$, the derived upper limits are the most stringent ones obtained on hour- to week-long timescales of non-thermal emission from GW170817 in the full gamma-ray domain ranging from keV to TeV energies. They allow for the first time a constraint to be placed on the level of early-time very-high-energy emission from the source, following the binary neutron star merger. With a potential connection to a kilonova-type event, expected to give rise to the ejection of mildly relativistic outflows, further observations of this object should be performed to probe particle acceleration beyond TeV energies on longer timescales.

The support of the Namibian authorities and of the University of Namibia in facilitating the construction and operation of H.E.S.S. is gratefully acknowledged, as is the support by the German Ministry for Education and Research (BMBF), the Max Planck Society, the German Research Foundation (DFG), the French Ministry for Research, the CNRS-IN2P3 and the Astroparticle Interdisciplinary Programme of the CNRS, the U.K. Science and Technology Facilities Council (STFC), the IPNP of the Charles University, the Czech Science Foundation, the Polish Ministry of Science and Higher Education, the South African Department of Science and Technology and National Research Foundation, the University of Namibia, the Innsbruck University, the

Austrian Science Fund (FWF), and the Austrian Federal Ministry for Science, Research and Economy, and by the University of Adelaide and the Australian Research Council. We appreciate the excellent work of the technical support staff in Berlin, Durham, Hamburg, Heidelberg, Palaiseau, Paris, Saclay, and in Namibia in the construction and operation of the equipment. This work benefited from services provided by the H.E.S.S. Virtual Organisation, supported by the national resource providers of the EGI Federation.

References

- Abbott, B. P., Abbott, R., Abbott, T. D., et al. (LVC) 2016, *PhRvL*, **116**, 061102
 Abbott, B. P., Abbott, R., Abbott, T. D., et al. (LVC et al.) 2017a, *ApJL*, **848**, L12
 Abbott, B. P., Abbott, R., Abbott, T. D., et al. (LVC, Fermi-GBM, & INTEGRAL) 2017b, *ApJL*, **848**, L13
 Abbott, B. P., Abbott, R., Abbott, T. D., et al. (LVC) 2017c, *PhRvL*, **119**, 161101
 Acero, F., Ackermann, M., Ajello, M., et al. 2015, *ApJ*, **218**, 23
 Ackermann, M., Ajello, M., Albert, A., et al. 2013a, *ApJ*, **771**, 57
 Ackermann, M., Ajello, M., Asano, K., et al. 2011, *ApJ*, **729**, 114
 Ackermann, M., Ajello, M., Asano, K., et al. 2013b, *ApJS*, **209**, 11
 Ackermann, M., Asano, K., Atwood, W. B., et al. 2010, *ApJ*, **716**, 1178
 Aharonian, F., Akhperjanian, A. G., Bazer-Bachi, A. R., et al. 2006, *A&A*, **457**, 899
 Allam, S., Annis, J., Berger, E., et al. (DECam) 2017, GCN, 21530
 Arcavi, I., Howell, D. A., McCully, C., et al. (Las Cumbres Observatory) 2017, GCN, 21538
 Baiotti, L., & Rezzolla, L. 2017, *RPPPh*, **80**, 096901
 Berge, D., Funk, S., & Hinton, J. 2007, *A&A*, **466**, 1219
 Biesiada, M., & Piórkowska, A. 2009, *CQGrA*, **26**, 125007
 Connaughton, V., Blackburn, L., Briggs, M. S., et al. (Fermi-GBM Collaboration) 2017, GCN, 21506
 Cook, D. O., & Kasliwal, M. M. 2016, AAS Meeting, **227**, 349.08

- Cook, D. O., Van Sistine, A., Singer, L., et al. (GROWTH Collaboration) 2017, GCN, 21519
- Corsi, A., Hallinan, G., Mooley, K., et al. (VLA) 2017, GCN, 21815
- Coulter, D. A., Foley, R. J., Kilpatrick, C. D., et al. 2017b, *Sci*, <https://doi.org/10.1126/science.aap9811>
- Coulter, D. A., Kilpatrick, C. D., Siebert, M. R., et al. (1M2H Collaboration) 2017a, GCN, 21529
- Coulter, D. A., Kilpatrick, C. D., Siebert, M. R., et al. (1M2H Collaboration) 2017c, GCN, 21567
- Cowperthwaite, P. S., Foley, R. J., & Berger, E. 2017, GCN, 21533
- Dalya, G., Frei, Z., Galgoczi, G., Raffai, P., & de Souza, R. 2016, *yCat*, 7275, 0
- de Naurois, M., & Rolland, L. 2009, *Aph*, 32, 231
- Eichler, D., Livio, M., Piran, T., & Schramm, D. N. 1989, *Natur*, 340, 126
- Ellison, D. C., Warren, D. C., & Bykov, A. M. 2013, *ApJ*, 776, 46
- Evans, P. A., Kennea, J. A., Breeveld, A. A., et al. (Swift) 2017, GCN, 21550
- Feldman, G. J., & Cousins, R. D. 1998, *PhRvD*, 57, 3873
- Foley, R. J., Kilpatrick, C. D., Nicholl, M., & Berger, E. 2017, GCN, 21536
- Franceschini, A., Rodighiero, G., Vaccari, M., et al. 2008, *A&A*, 487, 837
- Goldstein, A., Veres, P., Broida, J., et al. (Fermi-GBM Collaboration) 2017a, GCN, 21528
- Goldstein, A., Veres, P., Burns, E., et al. (Fermi-GBM Collaboration) 2017b, *ApJL*, 848, L14
- Hoischen, C., Balzer, A., Bissaldi, E., et al. (H.E.S.S. Collaboration) 2017, [arXiv:1708.01088](https://arxiv.org/abs/1708.01088)
- Kouveliotou, C., Meegan, C. A., Fishman, G. J., et al. 1993, *ApJL*, 413, L101
- Kulkarni, S. R. 2005, [arXiv:astro-ph/0510256](https://arxiv.org/abs/astro-ph/0510256)
- Li, T.-P., & Ma, Y.-Q. 1983, *ApJ*, 272, 317
- LIGO Scientific Collaboration & Virgo Collaboration 2017a, GCN, 21505
- LIGO Scientific Collaboration & Virgo Collaboration 2017b, GCN, 21509
- LIGO Scientific Collaboration & Virgo Collaboration 2017c, GCN, 21513
- LIGO Scientific Collaboration & Virgo Collaboration 2017d, GCN, 21527
- Lipunov, V. M., Gorbovskiy, E., Komilov, V. G., et al. (MASTER) 2017, GCN, 21546
- Meszaros, P., & Rees, M. 1993, *ApJ*, 405, 278
- Metzger, B. D., & Berger, E. 2012, *ApJ*, 746, 48
- Metzger, B. D., Martínez-Pinedo, G., Darbha, S., et al. 2010, *MNRAS*, 406, 2650
- Mooley, K. P., Hallinan, G., & Corsi, A. (JVLA/JAGWAR) 2017, GCN, 21814
- Parsons, R. D., & Hinton, J. A. 2014, *Aph*, 56, 26
- Piran, T. 1994, in AIP Conf. Proc. 307, Gamma-ray Bursts: Second Workshop, ed. G. J. Fishman, J. J. Brainerd, & K. Hurley (Melville, NY: AIP), 543
- Piran, T. 1999, *PhR*, 314, 575
- Piran, T., Nakar, E., Mazzali, P., & Pian, E. 2017, [arXiv:1704.08298](https://arxiv.org/abs/1704.08298)
- Savchenko, V., Mereghetti, S., Ferrigno, C., et al. (INTEGRAL) 2017, GCN, 21507
- Seglar-Arroyo, M., Schüssler, F. & (H.E.S.S. Collaboration) 2017, [arXiv:1705.10138](https://arxiv.org/abs/1705.10138)
- Singer, L. P., Chen, H.-Y., Holz, D. E., et al. 2016, *ApJL*, 829, L15
- Singer, L. P., & Price, L. R. 2016, *PhRvD*, 93, 024013
- Takami, H., Kyutoku, K., & Ioka, K. 2014, *PhRvD*, 89, 063006
- Tanvir, N. R., Levan, A. J., Fruchter, A. S., et al. 2013, *Natur*, 500, 547
- Tanvir, N. R., & Levan, A. J. (VISTA) 2017, GCN, 21544
- Troja, E., Piro, L., Sakamoto, T., et al. (Chandra) 2017, GCN, 21765
- Veitch, J., Raymond, V., Farr, B., et al. 2015, *PhRvD*, 91, 042003
- von Kienlin, A., Meegan, C., & Goldstein, A. (Fermi-GBM Collaboration) 2017, GCN, 21520
- Wenger, M., Ochsenein, F., Egret, D., et al. 2000, *A&AS*, 143, 9
- Woosley, S., Blinnikov, S., & Heger, A. 2007, *Natur*, 450, 390
- Yang, S., Valenti, S., Sand, D., Tartaglia, L., & Cappellaro, E. 2017, GCN, 21531
- Zhang, B., Fan, Y. Z., Dyks, J., et al. 2006, *ApJ*, 642, 354
- Zhu, Q.-Y., & Wang, X.-Y. 2016, *ApJL*, 828, 1